

การสังเคราะห์และศึกษาโครงสร้างของวานาเดตกับธาตุหมู่หลัก
ซึ่งถูกดัดแปลงด้วยสารออร์แกนิก



วิทยานิพนธ์นี้เป็นส่วนหนึ่งของการศึกษาตามหลักสูตรปริญญาวิทยาศาสตรดุษฎีบัณฑิต
สาขาวิชาเคมี
มหาวิทยาลัยเทคโนโลยีสุรนารี
ปีการศึกษา 2553

**SYNTHESES AND STRUCTURAL STUDIES OF
ORGANICALLY MODIFIED MAIN GROUP
VANADATES**



**A Thesis Submitted in Partial Fulfillment of the Requirements for the
Degree of Doctor of Philosophy in Chemistry
Suranaree University of Technology
Academic Year 2010**

**SYNTHESES AND STRUCTURAL STUDIES OF
ORGANICALLY MODIFIED MAIN GROUP VANADATES**

Suranaree University of Technology has approved this thesis submitted in partial fulfillment of the requirements for the Degree of Doctor of Philosophy

Thesis Examining Committee

(Asst. Prof. Dr. Kunwadee Rangriwatananon)

Chairperson

(Assoc. Prof. Dr. Kenneth J. Haller)

Member (Thesis Advisor)

(Assoc. Prof. Dr. David J. Harding)

Member

(Assoc. Prof. Dr. Adrian E. Flood)

Member

(Dr. Weenawan Somphon)

Member

(Prof. Dr. Sukit Limpijumnong)

Vice Rector for Academic Affairs

(Assoc. Prof. Dr. Prapun Manyum)

Dean of Institute of Science

สำเร็จ ครอบคลุม : การสังเคราะห์และศึกษาโครงสร้างของวานาเดตกับธาตุหมู่หลัก
ซึ่งถูกดัดแปลงด้วยสารออร์แกนิก (SYNTHESES AND STRUCTURAL STUDIES OF
ORGANICALLY MODIFIED MAIN GROUP VANADATES) อาจารย์ที่ปรึกษา :
รองศาสตราจารย์ ดร.เค็นเนท เจ แชลเลอร์, 200 หน้า.

วิทยานิพนธ์นี้เป็นการศึกษาอิทธิพลของสารออร์แกนิกไดเอมีนต่อโครงสร้างทางเคมีของ
วานาเดตกับธาตุหมู่หลัก โดยการสังเคราะห์ภายใต้เงื่อนไขวิธีไฮโดรเทอร์มัลของระบบ
 $V_2O_5-M(OAc)_2$ -ออร์แกนิกไดเอมีน-น้ำ เมื่อ M คือ Zn และ Cd

สารประกอบวัสดุผสมออร์แกนิก-อินออร์แกนิกวานาเดตใหม่ห้าชนิดถูกสังเคราะห์ขึ้นจาก
การเปลี่ยนแปลงปริมาณของเอทิลีนไดเอมีน (en) และโพรเพน-1,2-ไดเอมีน (enMe) และพีเอชของ
ปฏิกิริยา โครงสร้าง (en)ZnV₂O₇ ประกอบด้วยชั้นที่เกิดจากสายโซ่พอลิเมอร์เกลียวคู่ของทรงเหลี่ยมสี่
หน้าของ ZnO₃N และทรงพีระมิดฐานสามเหลี่ยมของ ZnO₄N ซึ่งถูกเชื่อมโดยสะพานลิแกนด์ en และ
เชื่อมต่อกับเสาทรงเหลี่ยมสี่หน้าของ VO₄ เกิดเป็นโครงร่างตาข่ายเกลียวไครอลสามมิติ ส่วนโครงสร้าง
(HenMe)₂Zn(V₂O₇)₄ ประกอบขึ้นด้วยชั้นผลสมวาเลนซ์ของ [(V⁴⁺O)(V⁵⁺O₄)₃]₅ เชื่อมต่อกับเสาทรงเหลี่ยม
แปดหน้าของ ZnO₄N₂ เกิดเป็นโครงร่างเปิดสามมิติ สารประกอบทั้งสองชนิดแสดงความคงทนต่อ
ความร้อนที่อุณหภูมิ 283 และ 338 °C ตามลำดับ สำหรับโครงสร้างอื่นๆ ได้แก่ (Hen)₂Cd(VO₃)₄
(en)Zn(VO₃)₂ และ (enMe)₂Zn(VO₃)₂·2H₂O ประกอบด้วยสายโซ่พอลิเมอร์เมตาวานาเดตเชื่อมด้วยทรง
เหลี่ยมแปดหน้าของโลหะเกิดเป็นโครงร่างสายโซ่คู่หนึ่งมิติ ชั้นคู่สองมิติและโครงร่างเปิดสามมิติ

สารประกอบโลหะอัลคาไลไดรวานาเดตแบบชั้น M_xV₃O₈ สามารถเตรียมขึ้นจากการเติมเกลือ
โลหะ อัลคาไลเพิ่มในระบบและใช้อุณหภูมิที่ค่อนข้างต่ำกว่ารายงานวิจัยที่ผ่านมา ได้ผลิตลักษณะที่มาก
และมีความเป็นผลึกที่สูงที่สภาวะเป็นกลางเมื่อ x = 1 และ M = K Rb Cs และที่สภาวะเป็นเบสเมื่อ x =
2 และ M = K โดยที่ Zn(OAc)₂ จะไม่ทำปฏิกิริยาแต่อาจทำหน้าที่เป็นตัวเร่งปฏิกิริยา หรือ HOAc/OAc⁻
ทำหน้าที่เป็นตัวควบคุมพีเอช และ enMe ทำหน้าที่เป็นตัวปรับพีเอชและตัวรีดิวซ์ในการเตรียม
สารประกอบ K₂V₃O₈ และยังพบว่าเมื่อเพิ่มสัดส่วน โมล Zn(OAc)₂ เป็นสองเท่าในระบบ สารประกอบ
แบบชั้น K₂ZnV₂O₇ เกิดร่วมด้วยและหน่วยเซลล์ด้านแกน c มีความยาวเป็นสองเท่าของ K₂(VO)V₂O₇
โดยประมาณ ซึ่งทรงเหลี่ยมสี่หน้าที่บิดเบี้ยวของ ZnO₄ เข้าไปแทนที่ทรงพีระมิดฐานสี่เหลี่ยมของ VO₅
ในชั้นของ [(V⁴⁺O)V⁵⁺O₇]²⁻

สารประกอบพอลิเมอร์ใหม่ {[Zn(Im)₄][V₂O₇]}_n สังเคราะห์ได้ในปริมาณผลผลิตที่สูงจากการ
ใช้อิมิดาโซลเป็นสารออร์แกนิกไดเอมีนแบบวงห้าเหลี่ยมแบนราบ ผลการวิเคราะห์ด้วยเทคนิคดิฟเฟอ-
เรนเชียลสแกนนิ่งแคลอริเมทรี แสดงให้เห็นการเปลี่ยนเฟสแบบย้อนกลับลำดับที่หนึ่ง ซึ่งคายความ-

ร้อนและจุดความร้อนที่อุณหภูมิ 2 และ 4 °C โดยจะไม่ซ้อนทับกันสนิทประมาณ ~2 °C เมื่อเพิ่มและลดอุณหภูมิด้วยอัตราเร็ว 5 °C min⁻¹ เทคนิควิธีทางเอกซเรย์แบบผลึกเดี่ยวแสดงให้เห็นว่าที่อุณหภูมิ -173 (2) °C เป็นเฟสระบบไตรคลินิกหมู่ *P1̄* ที่เป็นระเบียบและที่อุณหภูมิ 20 (2) °C เป็นเฟสระบบไตรคลินิกหมู่ *P1̄* ที่ไม่เป็นระเบียบและแกน *c* มีความยาวเป็นครึ่งหนึ่งที่อุณหภูมิ -173 (2) °C มีการหันเหไปจากรูปแบบที่เป็นระเบียบอยู่เดิมของไอออนลบและการยึดหดแกนพอลิเมอร์ตามแนวแกน *c* ด้วย รวมทั้งโครงสร้างตาข่ายซูปราโมเลกุลควอเตอร์สามมิติเฉพาะในไอออนบวกพบที่มีการจัดเรียงตัวใหม่ นำไปสู่การสังเกตความแตกต่างอย่างเห็นได้ชัดของอันตรกิริยาพันธะไฮโดรเจน C-H...O แบบอ่อนระหว่างไอออนบวกกับไอออนลบ และอันตรกิริยาพันธะไฮโดรเจนของกลุ่มอะโรมาติกที่ประสานกัน อย่างพร้อมเพียงของ *off* N-H... π , *off* และ *ef* C-H... π แบบอ่อนมากระหว่างไอออนบวกด้วยกันเอง ความแตกต่างของอันตรกิริยาเกี่ยวพันกันกับความแตกต่างของอินฟราเรดสเปกตรัมเมื่ออุณหภูมิเปลี่ยนแปลงไป



ACKNOWLEDGEMENTS

I would like to express my sincere gratitude to my supervisors, Assoc. Prof. Dr. Kenneth J. Haller and Prof. Dr. Ian D. Williams for their kindness give my opportunity and experience in Crystallography. I would not have achieved this far and this thesis would not have been completed without all the support, guidance, and help from them.

I would also like to express my sincere gratitude to all members in School of Chemistry who taught and helped me during my study at SUT. I wish to express my special thanks to chairman of the School of Chemistry, Asst. Prof. Dr. Kunwadee Rangriwatananon and thesis examining committees, Assoc. Prof. Dr. Adrian E. Flood, Assoc. Prof. Dr. David J. Harding, and Dr. Weenawan Somphon for their warm hearted support, encouragement, and help. Thanks to Ph.D. Scholarship Program and Thailand Research Fund (3.C.TS/45B.1) for a Research Grant to support my thesis research, and thanks to SUT for a Travel Grant to support my attendance at Pure and Applied Chemistry International Conference 2010, Ubon Ratchathani, Thailand. Thanks to the Asian Crystallographic Association (AsCA), the American Crystallographic Association (ACA), and International Union of Crystallography (IUCr) for a Bursary Student Awards to support my attendance at AsCA'04 (Hong Kong), AsCA'07 (Taiwan), AsCA'10 (Korea), IUCr'08 (Japan), ACA'09 (Canada), and AsCA'10 (Korea).

Finally, I most gratefully acknowledge my family and my friends at SUT, particular Kenneth's group members, and HKUST, for all their support throughout the period of this research.

Samroeng Krachodnok

CONTENTS

	Page
ABSTRACT IN THAI	I
ABSTRACT IN ENGLISH.....	III
ACKNOWLEDGEMENTS	V
CONTENTS	VI
LIST OF TABLES	IX
LIST OF FIGURES	XIII
LIST OF SYMBOLS AND ABBREVIATIONS	XXI
CHAPTER	
I INTRODUCTION	1
1.1 Vanadium Oxide	1
1.2 Main Group Vanadates	3
1.3 Supramolecular Interactions.....	10
1.4 Research Objectives	18
1.5 References	19
II HYDROTHERMAL SYNTHESIS AND PHYSICAL METHODS	
FOR CHARACTERIZING SOLIDS	27
2.1 Hydrothermal Synthesis	27
2.2 Physical Methods for Characterizing Solids.....	36
2.3 Research Procedure	45
2.4 References	48

CONTENTS (Continued)

	Page
III HYDROTHERMAL SYNTHESSES AND STRUCTURAL CHARACTERIZATIONS OF HYBRID ORGANIC-INORGANIC MATERIALS OF DIVALENT METAL VANADATES	51
3.1 Introduction	51
3.2 Experimental	52
3.3 Results and Discussion.....	61
3.4 Conclusions	97
3.5 References	98
IV HYDROTHERMAL SYNTHESSES AND STRUCTURAL CHARACTERIZATIONS OF ALKALI METAL VANADATES	103
4.1 Introduction	103
4.2 Experimental	108
4.3 Results and Discussion.....	111
4.4 Conclusions	127
4.5 References	127
V REVERSIBLE ORDER-DISORDER PHASE TRANSITION IN A NEW POLYMERIC METAVANADATE: {[Zn(Im)₄][VO₃]₂]_n.....	132
5.1 Introduction	132
5.2 Experimental	135
5.3 Results and Discussion.....	140
5.4 Conclusions	165

CONTENTS (Continued)

	Page
5.5 References	166
VI CONCLUSIONS	173
6.1 Conclusions	173
6.2 Suggesting for the Future Work	176
APPENDICES	178
APPENDIX A SUPPORTING INFORMATION CHAPTER III.....	179
APPENDIX B SUPPORTING INFORMATION CHAPTER IV	186
APPENDIX C SUPPORTING INFORMATION CHAPTER V	188
APPENDIX D CONFERENCE PRESENTATIONS.....	195
CURRICULUM VITAE	200

LIST OF TABLES

Table	Page
1.1 Bond Lengths in V–O _n Polyhedra.....	4
3.1 Hydrothermal Synthetic Conditions	56
3.2 X-ray Crystallographic Data of Compound 3a-e	62
3.3 Selected Bond Lengths and Bond Angles (Å, °) for Compound 3a	68
3.4 Selected Bond Lengths and Bond Angles (Å, °) for Compound 3b	73
3.5 Selected Bond Lengths and Bond Angles (Å, °) for Compound 3c	76
3.6 Selected Bond Lengths and Bond Angles (Å, °) for Compound 3d	78
3.7 Selected Bond Lengths and Bond Angles (Å, °) for Compound 3e	84
3.8 Summary the Coordination Geometries and Bond Valence Sums for Compounds 3a-e	88
3.9 Hydrogen Bond Interactions for Compounds 3a-e	89
3.10 Physical and Analytical Data for Compounds 3a , 3d and 3e	90
3.11 IR Spectral Data for Compounds 3a and 3c-e	91
3.12 Decompositions as a Function of Temperature	95
4.1 Published Lists of A ₂ ⁺ B ²⁺ V ₂ O ₇ Compounds in Literature Reviews.....	106
4.2 Preparation Lists of Alkaline Metal Vanadates in Literature Reviews	109
4.3 The Product Yield of A _x V ₃ O ₈ (Based on V ₂ O ₅) as a Function of Temperature.....	112
4.4 Crystal Data and Structure Refinements for CsV ₃ O ₈ and K ₂ ZnV ₂ O ₇	113

LIST OF TABLES (Continued)

Table	Page
4.5 Atomic Coordinates and Equivalent Isotropic Displacement Parameters ($\text{\AA}^2 \times 10^3$) for CsV_3O_8	118
4.6 Comparison of the V–O and A–O bond Distances of MV_3O_8	120
4.7 Atomic Coordinates ($\times 10^4$) and Equivalent Isotropic Displacement Parameters ($\text{\AA}^2 \times 10^3$) for $\text{K}_2\text{ZnV}_2\text{O}_7$	122
4.8 Selected Bond Lengths (\AA) and Angles ($^\circ$) for $\text{K}_2\text{ZnV}_2\text{O}_7$	123
5.1 Crystal Data and Refinement Details for $\{[\text{Zn}(\text{Im})_4][\text{V}_2\text{O}_6]\}_n$	139
5.2 Selected Bond Lengths (\AA) for $\{[\text{Zn}(\text{Im})_4][\text{V}_2\text{O}_6]\}_n$	145
5.3 Selected Bond Angles ($^\circ$) for the Cationic $[\text{Zn}(\text{Im})_4]^{2+}$ Complexes	147
5.4 Selected Bond Angles ($^\circ$) for the Anionic $[\text{V}_2\text{O}_6]^{2-}$ Chains.....	147
5.5 Hydrogen Bond Interactions between Cations and Anions for $\{[\text{Zn}(\text{Im})_4][\text{V}_2\text{O}_6]\}_n$	155
5.6 N–H $\cdots\pi$ and C–H $\cdots\pi$ Hydrogen Bond the Intercation Interactions of $\{[\text{Zn}(\text{Im})_4][\text{V}_2\text{O}_6]\}_n$	156
5.7 Thermochemical Properties of $\{[\text{Zn}(\text{Im})_4][\text{V}_2\text{O}_6]\}_n$	157
5.8 Decompositions as a Function of Temperature.....	159
5.9 Observed Frequencies (cm^{-1}) and Intensities for the $\{\text{VO}_3\}_n^{n-}$ Chain in MVO_3	163
5.10 Observed Frequencies (cm^{-1}) and Intensities for the Imidazole in $[\text{Zn}(\text{Im})_4][\text{X}]_2$	164

LIST OF TABLES (Continued)

Table	Page
A1 Atomic Coordinates ($\times 10^4$) and Equivalent Isotropic Displacement Parameters ($\text{\AA}^2 \times 10^3$) for 3a . $U(\text{eq})$ is Defined as One Third of the Trace of the Orthogonalized U^{ij} Tensor.....	179
A2 Atomic Coordinates ($\times 10^4$) and Equivalent Isotropic Displacement Parameters ($\text{\AA}^2 \times 10^3$) for 3b . $U(\text{eq})$ is Defined as One Third of the Trace of the Orthogonalized U^{ij} Tensor	180
A3 Atomic Coordinates ($\times 10^4$) and Equivalent Isotropic Displacement Parameters ($\text{\AA}^2 \times 10^3$) for 3c . $U(\text{eq})$ is Defined as One Third of the Trace of the Orthogonalized U^{ij} Tensor	181
A4 Atomic Coordinates ($\times 10^4$) and Equivalent Isotropic Displacement Parameters ($\text{\AA}^2 \times 10^3$) for 3d . $U(\text{eq})$ is Defined as One Third of the Trace of the Orthogonalized U^{ij} Tensor	182
A5 Atomic Coordinates ($\times 10^4$) and Equivalent Isotropic Displacement Parameters ($\text{\AA}^2 \times 10^3$) for 3e . $U(\text{eq})$ is Defined as One Third of the Trace of the Orthogonalized U^{ij} Tensor	183
A6 XRD Pattern Searching from PDF Database Library	184
B1 Anisotropic Displacement Parameters ($\text{\AA}^2 \times 10^3$) for CsV_3O_8 . The Anisotropic Displacement Factor Exponent Takes the Form: $-2\pi^2[h^2a^{*2}U^{11} + \dots + 2hka^*b^*U^{12}]$	186
B2 Anisotropic Displacement Parameters ($\text{\AA}^2 \times 10^3$) for $\text{K}_2\text{ZnV}_3\text{O}_8$.	

LIST OF TABLES (Continued)

Table	Page
The Anisotropic Displacement Factor Exponent Takes the Form: $-2\pi^2[h^2a^*2U^{11} + \dots + 2hka^*b^*U^{12}] \dots\dots\dots$	187
C1 Atomic Coordinates ($\times 10^4$) and Equivalent Isotropic Displacement Parameters ($\text{\AA}^2 \times 10^3$) for $\{[\text{Zn}(\text{Im})_4][\text{V}_2\text{O}_6]\}_n$ at $-173\text{ }^\circ\text{C}$. $U(\text{eq})$ is Defined as One Third of the Trac of the Orthogonalized U^{ij} Tensor $\dots\dots\dots$	188
C2 Atomic Coordinates ($\times 10^4$) and Equivalent Isotropic Displacement Parameters ($\text{\AA}^2 \times 10^3$) for $\{[\text{Zn}(\text{Im})_4][\text{V}_2\text{O}_6]\}_n$ at $20\text{ }^\circ\text{C}$. $U(\text{eq})$ is Defined as One Third of the Trace of the Orthogonalized U^{ij} Tensor $\dots\dots\dots$	192

LIST OF FIGURES

Figure	Page
1.1 Metamorphosis of the vanadium coordination polyhedra (coordination number on the vertical axis; oxidation state on the horizontal axis) (Zavalij and Whittingham, 1999).....	2
1.2 Coordination geometries in (V–O _n) polyhedra: (a) [1+4+1]-coordination; (b) [2+2+2]-coordination with two <i>cis</i> vanadyl bonds and two <i>trans</i> bonds in a <i>trans</i> arrangement to each vanadyl bond; (c) [2+3]-coordination with two vanadyl bonds in this <i>cis</i> position (Schindler, Hawthorne, and Baur, 2000).....	3
1.3 Carbonyl···carbonyl interactions.....	11
1.4 Carbonyl–carbonyl antiparallel interactions in (a) the structure of pyridine-3,5-dicarboxylic acid (Krachodnok and Haller, 2005) and (b) the structure of Co(picoline) ₃ ·H ₂ O (Chainok, 2004).....	12
1.5 Hydrogen bond geometry and partial charges. Donor and acceptor atoms in a hydrogen bond (left), and angular dependence in hydrogen bonds (right).....	12
1.6 Structure of hydrogen bonds: symmetric and asymmetric; linear, bent, and bifurcated; equally strong, differently strong (Lutz, 2003).....	13
1.7 O–H···O hydrogen bond interactions in (a) MV ₂ O ₆ ·2H ₂ O (M = Ni and Co) projected parallel to <i>a</i> axis and (b) [H ₂ en] ₅ [V ₆ B ₂₀ O ₅₀ H ₈]·7H ₂ O projected of half-clusters on <i>bc</i> plane (Chatkon, 2001).....	15

LIST OF FIGURES (Continued)

Figure	Page
1.8 Diamond diagram of Fe(TPP)Cl showing (a) the C–H··· π_{phenyl} and (b) C–H··· π_{pyrrole} hydrogen bond interactions (Puntharod, Webster, Asghari, Khiavi, Bambery, Safinejad, Rivadehi, Langford, Haller, and Wood, 2010)	16
1.9 Aromatic–aromatic interaction motifs	17
1.10 Aromatic–aromatic interactions in (a) Co(picoline) ₃ ·H ₂ O (Chainok, 2004) and (b) metal phenanthroline complexes (Russell, Scudder, and Dance, 2001)	17
2.1 Temperature–density diagram of pure water (after Millero, 1982).....	30
2.2 pH dependence of the phases formed when V ₂ O ₅ , TMAOH and LiOH in the molar ratio 1:2:1 are reacted at 185 °C. pH controlled by addition of acetic acid (Chirayil, Zavalij, and Whittingham, 1998)	31
2.3 Morphologies of the compounds formed at different pH levels: (a) TMAV ₃ O ₇ , (b) TMA ₄ [V ₂₂ O ₅₄ (OAc)]·4H ₂ O, (c) Li _x V ₂ O ₄ ·H ₂ O, (d) TMA(V ₂ O ₅) ₂ , (e) TMA(V ₂ O ₅) ₄ , and (f) TMA _{0.17} H _{0.1} V ₂ O ₅ (Chirayil, Zavalij, and Whittingham, 1998).....	32
2.4 Organo-directed synthesis of manganese vanadates with variable stoichiometry and dimensionality (Law and Williams, 2000; Williams, Law, Sung, Wen, and Zhang, 2000)	33
2.5 The Parr design of the Teflon-lined reaction vessel (Parr Instrument Company).	34

LIST OF FIGURES (Continued)

Figure	Page
2.6 Schematic P – T diagram for preparative techniques (Yoshimura and Suchanek, 1997).....	35
2.7 (a) X-ray tube and (b) an X-ray emission spectrum.....	37
2.8 Bragg's law The difference between the path lengths of X-rays reflected (diffracted) from successive planes in the crystal must be an integer multiple of the wavelength for constructive interference to result	39
2.9 The general research procedure	46
3.1 Crystal morphologies of compounds 3a-e	57
3.2 Comparing simulated powder XRD of (a) 3a , (b) 3b , (c) $[\text{enH}_2][\text{V}_2\text{O}_6]$ (Xu, Yang, Wang, Ma, Sun, Xu, and Huang, 1996), and (d) $(\text{en})_2\text{ZnV}_6\text{O}_{14}$ (Zhang, DeBord, O'Connor, Haushalter, Clearfield, and Zubieta, 1996), with experimental powder XRD patterns of 1mmol en at (e) pH 9, (f) pH 11 and (g) pH 13, and with (h) 5 mmol en at pH 9, and (i) substituted NH_4VO_3 for V_2O_5	58
3.3 Comparing of (a) simulated $[\text{H}_2\text{en}]_{0.5}[\text{V}_2\text{O}_5]$ (Riou and Féray, 1995a,b) and $(\text{Hen})_2\text{Mn}(\text{VO}_3)_4$ (Law and Williams, 2000) with (b) simulated and (c) experimental powder XRD patterns of 3c	58
3.4 Comparing of (a) simulated and (b) experimental powder XRD patterns of 3d (space group $P2_1/c$) with (c) simulated $(\text{HenMe})_2\text{Cd}(\text{V}^{4+}\text{V}^{5+}\text{O}_5)_4$ (space group $C2/m$) (Zhang, Shi, Yang, Chen, and Feng, 2000).....	59

LIST OF FIGURES (Continued)

Figure	Page
3.5 Comparing of (a) simulated and (b) experimental powder XRD patterns of 3e	59
3.6 Crystal structures of (a) decavanadate and (b) metavanadate	64
3.7 Polyhedral representations of (a) sheets perpendicular to the <i>a</i> axis and (b) ZnO ₂ N ₄ pillars forming 0-D rectangular channel along the <i>b</i> axis in (en) ₂ ZnV ₆ O ₁₄ (Zhang, DeBord, O'Connor, Haushalter, Clearfield, and Zubietta, 1996)	65
3.8 ORTEP drawing of (a) the coordination environments of the Zn and V atoms and (b) the pyrovanadate unit connected to zinc neighbors in 3a with the atom labeling scheme and 50% thermal ellipsoids	69
3.9 ORTEP view of (a) the helices, type A and B as solid and dashed lines, respectively, and an undulating sheet in 3a , showing (b) the helices connected through μ_2 -O(2) atoms as dashed line, and (c) the packing of the undulating sheets perpendicular to the <i>a</i> axis, the chiral coordination axis, as dashed lines	70
3.10 View of a 3-D chiral network in 3a V(1)O ₄ pillars (polyhedral highlight)interconnecting alternately to the undulating sheets above and below the current layer	71
3.11 The structure of 3b , showing the zinc dimer by edge sharing to its neighbor	74
3.12 The double layered structure of 3b , showing	

LIST OF FIGURES (Continued)

Figure	Page
the double chains as a dashed line.....	74
3.13 The structure of 3c , showing (a) the Cd coordination geometry and (b) 1-D the double chain projected on the <i>ab</i> plane includes the labeling of the atoms with 50% probability displacement ellipsoids. The hydrogen bond interactions are as shown dashed lines..	77
3.14 Polyhedral representation of sheets perpendicular to the <i>b</i> axis in 3d	80
3.15 Perspective diagram showing ZnO ₄ N ₂ pillars forming 0-D rectangular channel along the <i>a</i> axis in 3d	80
3.16 Comparing the relative orientation of square pyramids and tetrahedral on layers with/without mark are represented up and down, respectively	82
3.17 Hydrogen bond interactions in 1-D rectangular channels of 3d	83
3.18 Asymmetric unit of 3e , including the labeling of the atoms with 50% probability displacement ellipsoids	85
3.19 Polyhedral representation of the dimensions of the three nearly perpendicular channels, (a) one bounded by 12-membered [Zn ₄ V ₈ O ₁₂] rings along [001] and (b) two bounded by 12-membered [Zn ₂ V ₁₀ O ₁₂] rings along [110]. The C and H atoms are omitted for clarity.....	86
3.20 Hydrogen bonding interactions showing the $R_4^3(10)$ motif in 3e	87
3.21 Infrared spectra	91
3.22 TGA curve of 3a	94
3.23 TGA curve of 3d	94

LIST OF FIGURES (Continued)

Figure	Page
3.24 TGA curve of 3e	95
3.25 The SEM images of 3d	96
3.26 The XRD patterns of 3d (a) RT, with heated (b) at 350 °C, (c) at 470 °C and (d) at 600 °C.....	96
4.1 Crystal structure of $K_2V_3O_8$ projected onto <i>ab</i> plane, showing (a) $[(V^{4+}O)(V^{5+}_2O_7)]^{2-}$ layer and (b) <i>ac</i> plane with K^+ ions lying between layers, and (c) perspective view of KO_{10} coordination with polyhedral represent, and (d) <i>ORTEP-III</i> represent with bond distances.....	105
4.2 Crystal morphologies of (a) KV_3O_8 , (b) RbV_3O_8 , (c) CsV_3O_8 , and (d) $K_2V_3O_8$ (this work), (e) Xu, He, and Yan (2004), and (f) Shi, Rocha, Trindade (2005).....	114
4.3 The simulated and experimental XRD patterns of MV_3O_8	117
4.4 XRD patterns of $K_2V_3O_8$	118
4.5 Crystal structure of CsV_3O_8 projected onto the <i>bc</i> plane (a) showing the $[V_3O_8]^-$ layers occupied by Cs^+ ions and (b) CsO_8 coordination	121
4.6 Comparing the $[ZnV_2O_7]^{2-}$ layer projected onto (a) the <i>ab</i> plane and (b) the <i>ac</i> plane, and $[(V^{4+}O)V_2O_7]^{2-}$ layer projected onto (c) the <i>ab</i> plane and (d) the <i>ac</i> plane (Chakoumakos, Custelcean, Kamiyama, Oikawa, Sales, and Lumsden, 2007).....	123
4.7 (a) Perspective view of the distorted square prismatic environments of the K atoms and projection views of (b) K(1) and (c) K(2) occupied the	

LIST OF FIGURES (Continued)

Figure	Page
pentagonal channel in $K_2ZnV_2O_7$	124
4.8 FT-IR spectra of alkali metal vanadates	127
5.1 SEM images (a) prism of $\{[Zn(Im)_4][V_2O_6]\}_n$, and (b) needles of $[Zn(\mu-Im)_2]_n$	137
5.2 Comparing of simulated and experimental powder XRD patterns of $\{[Zn(Im)_4][V_2O_6]\}_n$: (a) calc. of $\{[Zn(Im)_4][V_2O_6]\}_n$, (b) calc. $[Zn(\mu-Im)_2]_n$, (c) measured of $\{[Zn(Im)_4][V_2O_6]\}_n$ at pH 9, (d) pH 11, and (e) pH 13	141
5.3 Comparing of the simulated powder XRD patterns of $\{[Zn(Im)_4][V_2O_6]\}_n$	142
5.4 ORTEP drawing of the structures projected on the <i>ac</i> planes (a) at -173 °C, and (b) at 20 °C	143
5.5 A 3-D supramolecular network in $\{[Zn(Im)_4][V_2O_6]\}_n$ projection to the <i>ab</i> plane (a) at -173 °C and (b) at 20 °C. Hydrogen atoms are omitted for clarity	149
5.6 Weak C–H···O hydrogen bond interactions projected to the <i>ac</i> plane at -173 °C (left) and 20 °C (right). Hydrogen atoms are omitted for clarity	150
5.7 A 2-D supramolecular cationic layers forming through weaker N–H··· π and C–H··· π hydrogen bond interactions projected to the <i>bc</i> plane (a) at -173 °C and (b) at 20 °C. The anionic chains are omitted	

LIST OF FIGURES (Continued)

Figure	Page
for clarity.....	151
5.8 A 3-D supramolecular cationic network via weaker C–H... π H–bond interactions projected to the <i>ac</i> plane at –173 °C. The anionic chains are omitted for clarity.....	153
5.9 A 3-D supramolecular cationic network via weaker C–H... π H–bond interactions projected to the <i>ac</i> plane at 20 °C, showing eight-fold aryl embraces. The anionic chains are omitted for clarity.....	154
5.10 DSC curves of {[Zn(Im) ₄][V ₂ O ₆]} _n	158
5.11 DSC curves of {[Zn(Im) ₄][V ₂ O ₆]} _n with a cooling and heating rate of 5 °C min ⁻¹	158
5.12 TGA curve of {[Zn(Im) ₄][V ₂ O ₆]} _n	159
5.13 The infrared spectra of {[Zn(Im) ₄][V ₂ O ₆]} _n (pressed KBr pellet).....	161
C1 The asymmetric unit of {[Zn(Im) ₄][V ₂ O ₆]} _n at –173 (2) °C.....	193
C2 IR spectra of {[Zn(Im) ₄][V ₂ O ₆]} _n (nujol mulls) in the region 3200-2600 cm ⁻¹ at various temperatures.....	194
C3 IR spectra of {[Zn(Im) ₄][V ₂ O ₆]} _n (nujol mulls) in the region 1500-700 cm ⁻¹ at various temperatures.....	194

LIST OF SYMBOLS AND ABBREVIATIONS

Å	angstrom unit (10^{-10} m)
a, b, c	unit cell axial lengths
a, b, c, n, d	glide planes. The row parallel to the translation is designated; it is the side of the net (a, b , or c) or its diagonal (n in a primitive net, d in a centered net).
Anal	analytical
b	bridging atom
Calc	calculation
°C	degree Celsius
cm^{-1}	wavenumber (per centimeter)
CN	coordination number
D	deuterium
1-D	one-dimension(al)
2-D	two-dimension(al)
3-D	three-dimension(al)
D_{calc}	calculated density
en	ethane-1,2-diamine (ethylenediamine), $\text{H}_2\text{NCH}_2\text{CH}_2\text{NH}_2$
enMe	propane-1,2-diamine, $\text{H}_2\text{NCH}_2\text{CH}(\text{NH}_2)\text{CH}_3$
F_o and F_c	measured and calculated the structure factors
F_o^2 and F_c^2	measured and calculated intensities
g	gram

LIST OF SYMBOLS AND ABBREVIATIONS (Continued)

h,k,l	the reflection data
Hen	ethylenediamine monocation, $[\text{H}_2\text{NCH}_2\text{CH}_2\text{NH}_3]^+$
H_2en	ethylenediamine dication, $[\text{H}_3\text{NCH}_2\text{CH}_2\text{NH}_3]^{2+}$
HenMe	propane-1,2-diamine monocation, $[\text{H}_2\text{NCH}_2\text{CH}(\text{NH}_3)\text{CH}_3]^+$
H_2enMe	propane-1,2-diamine dication, $[\text{H}_3\text{NCH}_2\text{CH}(\text{NH}_3)\text{CH}_3]^{2+}$
Hpn	propane-1,3-diamine monocation, $[\text{H}_2\text{NCH}_2\text{CH}_2\text{CH}_2\text{NH}_3]^+$
H_2pn	propane-1,3-diamine dication, $[\text{H}_3\text{NCH}_2\text{CH}_2\text{CH}_2\text{NH}_3]^{2+}$
HOAc	acetic acid, CH_3COOH
Im	imidazole, $\text{C}_3\text{H}_4\text{N}_2$
LT	low temperature
m	mirror planes
m^{-3}	per cubic meter
mg	milligram
mL	milliliter
mmol	millimole
M_r	chemical formula
nm	nanometer
OAc	acetate anion, CH_3COO^-
P, C	lattice symbol. Primitive (P) and centered on one set of faces (C)
pn	propane-1,3-diamine, $\text{H}_2\text{NCH}_2\text{CH}_2\text{CH}_2\text{NH}_2$

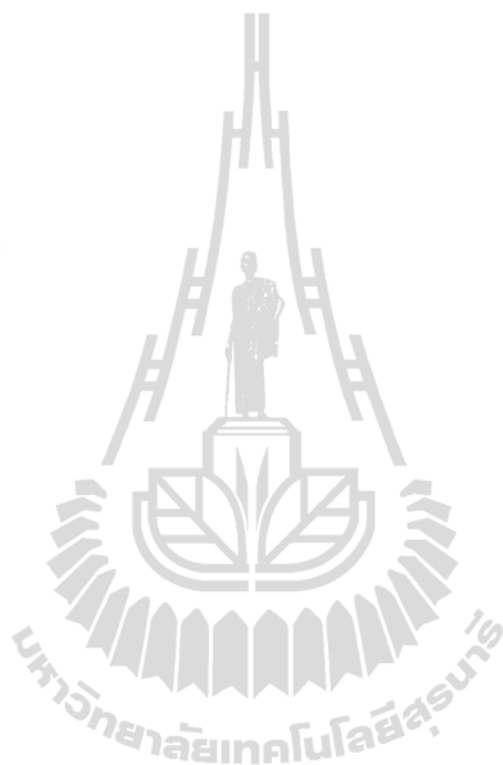
$$R_1 \quad \text{conventional discrepancy index} = R_1 = \frac{\sum_{hkl} \|F_o\| - |F_c|}{\sum_{hkl} \|F_o\|}$$

LIST OF SYMBOLS AND ABBREVIATIONS (Continued)

wR_2	the square root of weighted sum of the squares of the discrepancies,
	$wR_2 = \left[\frac{\sum_{hkl} w(F_o^2 - F_c^2)^2}{\sum_{hkl} wF_o^2} \right]^{1/2}$
RT	room temperature
T_i	onset temperature
T_f	endset temperature
T_m	midpoint temperature
TMAOH	tetramethylammonium hydroxide, $N(CH_3)_4OH$
TMA	tetramethylammonium ion, $[N(CH_3)_4]^+$
t	terminal atom
$U()$	isotropic and anisotropic vibration parameters
ν_s and ν_{as}	vibrational frequency (cm^{-1}) of symmetric and asymmetric stretching modes, respectively
Z	number of formula units or molecules in the unit cell
θ	Bragg angle or scattering angle
$\Delta\rho$	different electron density
δ	vibrational frequency (cm^{-1}) of bending mode
μ	linear absorption coefficient
$\bar{\lambda}$	an average wavelength
α, β, γ	interaxial angles between b and c, a and c, and a and b, respectively (alpha, beta, gamma)

LIST OF SYMBOLS AND ABBREVIATIONS (Continued)

% percentage



CHAPTER I

INTRODUCTION

1.1 Vanadium Oxide

The significant interest in organic-inorganic hybrid materials, particularly polyoxovanadate has increased rapidly as evidenced by numerous papers published (Yan, Luo, Dube, Sefat, Greedan, and Maggard, 2006; Larrea, Mesa, Pizarro, Arriortua, and Rojo, 2007; Lin and Maggard, 2008; Khan, Nome, Deb, MaNeely, and Cage, 2009; Lian, Zhang, Gu, Wang, and Lou, 2009). They not only possess remarkable chemical and structural diversity with fascinating architectures but also have interesting catalytic, electrochemical, magnetic, and medicinal properties. As an example, layered lithium vanadates are used as cathode materials for lithium batteries (Torardi, Miao, Lewittes, and Li, 2002; Huang, Fu, and Qin, 2003). Magnesium vanadates show catalytic activities in the oxidative dehydrogenation of hydrocarbons (Korili, Ruiz, and Delmon, 1996; Bahranowski, Bueno, Corberán, Kooli, Serwicka, Valenzuela, and Wcislo, 1999). Vanadium oxide and its compounds (vanadyl, vanadates and peroxovanadates) are increasingly being recognized to have biological functions such as vanadium enzymes; vanadium–nitrogenase and vanadium–thiolate/thioether related thio-functional ligands (Rehder, 1999). The potential use of their compounds as therapeutic antidiabetic agents has been the subject of a number of recent reviews (Thompson, McNeill, and Orvig, 1999). There has been a continuous upsurge in interest in the chemistry of vanadium peroxides mainly owing to their insulin-mimetic properties (Thompson and Orvig, 2000). The different valence states

(-1 to +5), coordination numbers, and geometries (planar, tetrahedral, tetragonal pyramidal, trigonal or pentagonal bipyramidal, octahedral and capped octahedral, and dodecahedral) available in vanadium chemistry give rise to many different structural types and geometries (Cotton, Wilkinson, Murillo, and Bockmann, 1999). Figure 1.1 shows metamorphosis of the vanadium coordination polyhedra associated with three common oxidation states (Zavalij and Whittingham, 1999), include partially filled and empty d orbitals ($+3(d^2)$, $+4(d^1)$, and $+5(d^0)$).

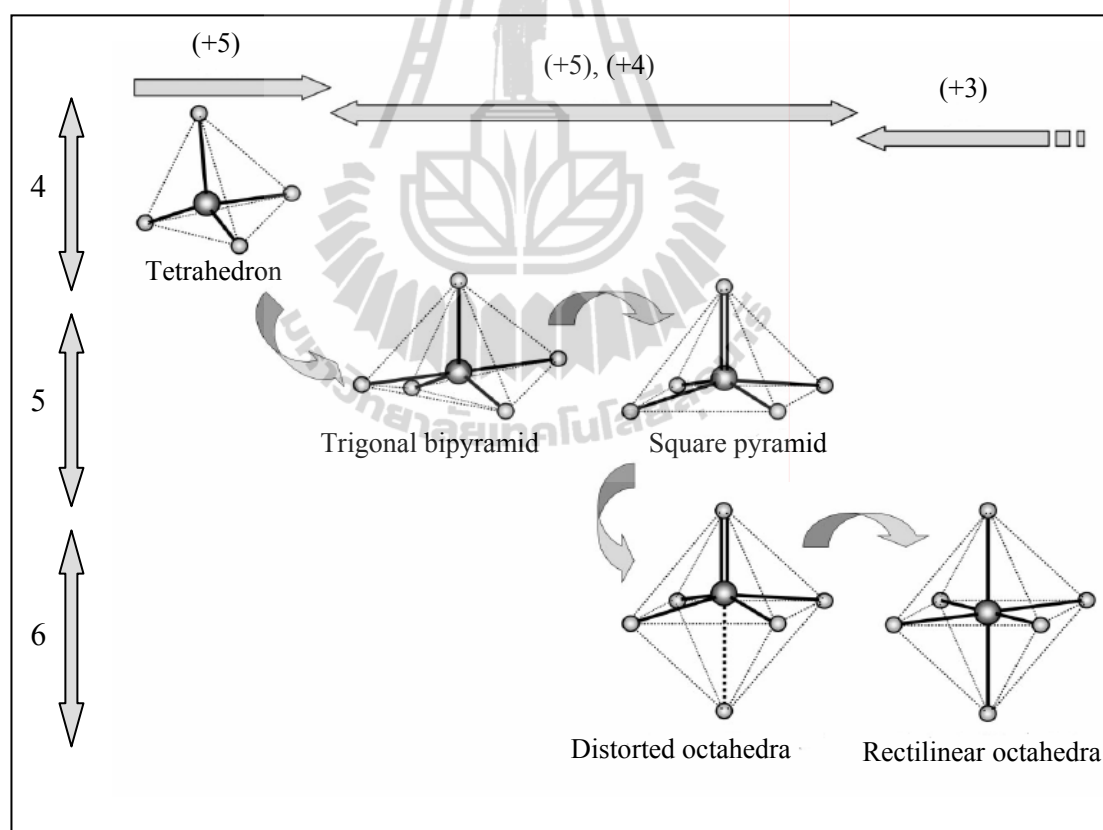


Figure 1.1 Metamorphosis of the vanadium coordination polyhedra (coordination number on the vertical axis; oxidation state on the horizontal axis) (Zavalij and Whittingham, 1999).

Schindler and his group (2000) discussed crystallographic aspect of vanadium oxides summarized the distribution of bond length in ($V^{4+}O_n$) and ($V^{5+}O_n$) ($n = 5, 6$) polyhedra showing distinct populations which can be used to define *vanadyl*, *equatorial*, and *trans* V–O bonds (Figure 1.2 and Table 1.1)

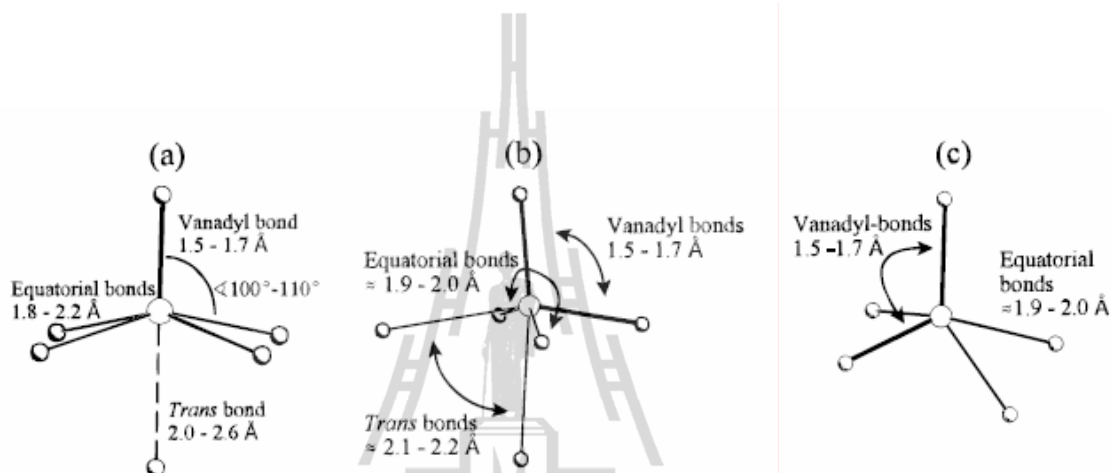


Figure 1.2 Coordination geometries in ($V-O_n$) polyhedra: (a) [1+4+1]-coordination; (b) [2+2+2]-coordination with two *cis* vanadyl bonds and two *trans* bonds in a *trans* arrangement to each vanadyl bond; (c) [2+3]-coordination with two vanadyl bonds in a *cis* position (Schindler, Hawthorne, and Baur, 2000).

Several tetravalent (+4) and pentavalent (+5) vanadium oxides are observed in a large number of compounds such as vanadyl (VO^{2+}), vanadate (VO_4^{3-}), peroxovanadate (HVO_4^{2-}), divanadate or pyrovanadate ($V_2O_7^{4-}$), trivanadate ($V_3O_8^-$), tetravanadate ($V_4O_{12}^{4-}$), decavanadate ($V_{10}O_{28}^{6-}$) anions etc.

1.2 Main Group Vanadates

Main group vanadates are mixed-metal vanadates with *s*-block, alkali metal, and *d*-block, zinc and cadmium (Cotton, Wilkinson, Murillo, and Bockmann, 1999)

represent an important subclass of the family of vanadium oxides, VMO.

Alkali Metal Vanadates when $M = \text{Li, Na, K, Rb, Cs, and Fr}$ all have a single s electron outside a noble gas core. The chemistry of these elements is principally that of M^+ ion. The several structures and applications of alkali metal vanadates have been reported in the literature. For example, the layered lithium vanadates are used as cathode materials for lithium batteries due to the Li^+ ion having the highest electropositive charges with the smallest ionic radii (Torardi, Miao, Lewittes, and Li, 2002; Huang, Fu, and Qin, 2003; Yang, Li, Zhang, and Jin, 2008). The layered dipotassium trivanadate ($\text{K}_2\text{V}_3\text{O}_8$) is a member of the fresnoite-type structure, $\text{M}_2(\text{VO})\text{V}_2\text{O}_7$ ($M = \text{K, Rb, NH}_4$), which are of interest their low-temperature magnetic properties (Galy and Carpy, 1975; Liu and Greedan, 1995; Choi, Zhu, Musfeldt, Rag-

Table 1.1 Bond Lengths in $\text{V}-\text{O}_n$ Polyhedra.

No. and Kind of Polyhedra	Bond ^a	(V-O) ^b
72 octahedra [6], overall mean:	$\text{V}^{3+}-\text{O}_{\text{all}}$	2.01(5)
84 square pyramids [1+4]:	$\text{V}^{4+}-\text{O}_{\text{V}}$	1.59(2)
	$\text{V}^{4+}-\text{O}_{\text{E}}$	1.98(4)
overall mean	$\text{V}^{4+}-\text{O}_{\text{all}}$	1.90(15)
93 octahedra [1+4+1]:	$\text{V}^{4+}-\text{O}_{\text{V}}$	1.60(4)
	$\text{V}^{4+}-\text{O}_{\text{E}}$	2.00(5)
	$\text{V}^{4+}-\text{O}_{\text{T}}$	2.27(12)
overall mean	$\text{V}^{4+}-\text{O}_{\text{all}}$	1.98(2)
34 square pyramids [1+4]:	$\text{V}^{5+}-\text{O}_{\text{V}}$	1.59(3)
	$\text{V}^{5+}-\text{O}_{\text{E}}$	1.89(3)
overall mean	$\text{V}^{5+}-\text{O}_{\text{all}}$	1.83(13)
125 octahedra [1+4+1]:	$\text{V}^{5+}-\text{O}_{\text{V}}$	1.61(3)
	$\text{V}^{5+}-\text{O}_{\text{E}}$	1.92(9)
	$\text{V}^{5+}-\text{O}_{\text{T}}$	2.31(8)
overall mean	$\text{V}^{5+}-\text{O}_{\text{all}}$	1.93(22)
49 polyhedra [2+3]:	$\text{V}^{5+}-\text{O}_{\text{V}}$	1.66(4)
	$\text{V}^{5+}-\text{O}_{\text{E}}$	1.95(8)
overall mean	$\text{V}^{5+}-\text{O}_{\text{all}}$	1.83(16)
66 octahedra [2+2+2]:	$\text{V}^{5+}-\text{O}_{\text{V}}$	1.67(4)
	$\text{V}^{5+}-\text{O}_{\text{E}}$	1.93(6)
	$\text{V}^{5+}-\text{O}_{\text{T}}$	2.20(14)
overall mean	$\text{V}^{5+}-\text{O}_{\text{all}}$	1.93(23)

^aVanadyl bond, $\text{V}-\text{O}_{\text{V}}$: equatorial bond, $\text{V}-\text{O}_{\text{E}}$: *trans* bond, $\text{V}-\text{O}_{\text{T}}$.

^b σ of (V-O) (=x) is $((x_i - (x))^2/n-1$

ghianti, Mandrus, Sales, and Thompson, 2001). Similar to the fresnoite-type structure are melilite-type compounds, e.g. the $K_2MgV_2O_7$ and $M_2CaV_2O_7$ ($M = K, Rb, Cs$) vanadates and the alkali metal–strontium cyclotetравanadates $M_2Sr(VO_3)_4$, ($M = Na, K, Rb, Cs$) which have been used to develop red phosphors for color TV, active media for near-IR and IR lasers, and luminescence screens emitting in the white, blue, green, and red spectral regions, in particular those that improve the performance of light emitting diode lighting devices (Slobodin, Surat, Zubkov, Tyutyunnik, Berger, Kuznetsov, Perelyaeva, Shein, Ivanovskii, Shulgin, Solomonov, Svensson, Forslund, and Sayagués, 2005; Slobodin, Surat, Samigullina, Ishchenko, Shulgin, and Cherepanov, 2010). According to Nakajima and his group (2009) vanadium oxide phosphors, MVO_3 ($M = K, Rb, \text{ and } Cs$), showed broadband emission from 380 to 800 nm and the two latter compounds showed high internal quantum efficiency (79% and 87%, respectively) as white light-emitting devices.

Divalent Metal Vanadates when $M = Zn$ and Cd . These elements have a filled $(n-1)d$ shell plus two ns electrons. While Cu give rise to ions or complexes in which one partly $(n-1)d$ electron or even one partly $(n-1)d$ electron plus one ns electron are lost and oxidation states are I and II, and Ag and Au ions or complexes in which a single s electron outside or one partly $(n-1)d$ electron plus two ns electrons are lost, that is to compounds in oxidation states I and III, no such compound has ever been isolated for Zn and Cd where the oxidation state is only II. However, this group of metals differ markedly from those in alkaline metal earth in nearly all respects expect having II as their only important oxidation state. Thus, while the Zn^{2+} and Mg^{2+} ions are very similar in their 6-coordinate radii (0.88 Å and 0.86 Å, respectively), Zn^{2+} has a relatively polarizable $3d^{10}$ shell whereas the neon core of Mg^{2+} is very “hard.” This special combination of “softness” and a high charge-to-radius ratio appears to be

responsible for the unique role played by zinc in biochemistry. The M^{2+} ions with their d^{10} configurations show no stereochemical preferences arising from ligand field stabilization effects. Therefore, they display a variety of coordination numbers (4, 5, and 6) and geometries (tetrahedral, square pyramidal, trigonal bipyramidal, octahedral) based on the interplay of electrostatic forces, covalency, and the size factors. Because of its size, Cd^{2+} is more often found with a coordination number of 6 than Zn^{2+} . A variety structures and applications of zinc and cadmium vanadates are found in the literature. For example, Zhang and coworkers (1997) documented that the layered zinc double vanadium oxide, $Zn_yV_2O_{5\pm\delta}\cdot nH_2O$ ($y = 0.42$), contains double layered V_2O_5 sheets with zinc ions and water molecules between the layers and showed that this compound is electrochemically active with an initial cell voltage of over 3.5 volts, readily, and reversibly undergoing redox reactions with lithium in non-aqueous cells. Fuentes et al. (1999) reported zinc and cadmium vanadates, $Zn_xV_2O_{5+x}$ ($x = 1, 2, 3$) and $Cd_yV_2O_{5+y}$ ($y = 1, 2$), can be used as cathode materials for lithium-ion batteries. In addition, Zavalij and coworkers (2002) have successfully synthesized four novel layered zinc vanadium oxides, $Zn_3(OH)_2(V_2O_7)\cdot 2H_2O$, $Zn_2(OH)_3(VO_3)$, δ - $Zn_{0.8}V_4O_{10}\cdot 0.6H_2O$ and $TMA_4[Zn_4V_{21}O_{58}]$ (TMA = tetramethyl ammonium cation, $[N(CH_3)_4]^+$) under hydrothermal conditions and found these are at potential interest for fast ion transport and intercalation chemistry, the first compound has a very open crystalline lattice that should lead to high ionic mobility akin to that observed in (β - Al_2O_3). The last two compounds have δ -type vanadium oxide lattices that are readily reducible by lithium ions and show promise as cathode active materials in lithium batteries. Mattos et al. (2002) mentioned zinc-modified β - Al_2O_3 supported vanadium oxides acted as good catalysts for propane oxidative dehydrogenation (ODH) notably

three zinc meta-, pyro-, and ortho-vanadates (ZnV_2O_6 , ZnV_2O_7 , $\text{Zn}_3\text{V}_2\text{O}_8$, respectively) on an alumina-supported surface. Those catalytic activities of Al_2O_3 supported zinc oxides and magnesium metavanadates which showed very low activity in the reaction and no activity with very selective for alkane ODH, respectively.

Mordkovich and co-workers (2003) reported that zinc divanadates, $\text{Zn}_4\text{V}_2\text{O}_9$ and $\text{Zn}_3\text{V}_2\text{O}_8$, are of interest displaying yellow 560 nm luminescence. According to Nakajima and his group (2009) the photoluminescence property of $\text{M}_3\text{V}_2\text{O}_8$ ($\text{M} = \text{Mg}$ and Zn) which showed broadband emission between 410 and 900 nm and high internal quantum efficiency (52%). On the other hand, Wang and his group (2005) noted that the $\text{Zn}_3\text{V}_2\text{O}_8$ also acts as the visible-light-driven-photocatalyst for O_2 evolution in aqueous AgNO_3 solution. In 2008 Liu and Tang studied the electrochemical properties of ZnV_2O_6 at a constant current density of 30 mA g^{-1} in a potential range of 2.0 and 3.6 V. The discharge capacity ($288.7 \text{ mA h g}^{-1}$) showed only 16.7% loss of the initial discharge capacity ($347.4 \text{ mA h g}^{-1}$) after 40 cycles.

Hybrid Main Group Vanadates In order to obtain new materials with novel structure and interesting properties, organic molecules have been employed in the synthesis of VMO compounds. Organic amines including nitrogen donor atoms can serve as the organic components in hybrid organic-inorganic structures. The amine may adopt a variety of roles depending on its structure and charge, the most common roles are as structure directing and templating agents to construct inorganic frameworks, charge compensating cations, and/or space filling entities, such as $[\text{N}(\text{CH}_3)_4]^+$ ions, linked with the layered $[\text{Zn}_4\text{V}_{21}\text{O}_{58}]^{4-}$ anions through hydrogen bonds into a network in $\text{TMA}_4[\text{Zn}_4\text{V}_{21}\text{O}_{58}]$ under hydrothermal conditions (Zavalij, Zhang, and Whittingham, 2002). On the other hand, they may also function as ligands coordinated to vanadium centers of VMO as terminal groups and may act as ligands

bonded to the secondary metal center. In this case, the secondary metal-ligand complex $[M'L_x]^{n+}$ may be present as an isolated, discrete charge-balancing cation as $[Zn(LH_3)]^{2+}$ complex dications in $[Zn^{II}(LH_3)(L)V^{IV}][PF_6]_3$ [$LH_3 = N,N,N$ (-tris(2S)-2-hydroxypropyl-1,4,7-triazacyctono-nane)] (Fallis, Farrugia, Macdonald, and Peacock, 1993); $[Zn(bipy)_3]^{2+}$ complex dications in $[Zn(bipy)_3]_2[V_4O_{12}] \cdot 11H_2O$, a species with an isolated $[V_4O_{12}]^{4-}$ cluster (Zhang, Zapf, Meyer, Haushalter, and Zubieta, 1997); $[Zn(NH_3)_4]^{2+}$ complex dications with the pentagonal pyramidal diperoxovanadium(V), the $[VO(O_2)_2(NH_3)]^-$ anions in $[Zn(NH_3)_4][VO(O_2)_2(NH_3)]_2$ (Chrappová, Schwendt, Dudášová, Tatiersky, and Marek, 2008). These complexes are covalently linked the vanadate species through oxygen terminal or bridging atoms forming a variety of structural dimensionalities. For example, the discrete 0-D hexanuclear clusters were observed in $[\{Zn(bipy)_2\}_2V_4O_{12}]$ and $[\{Zn(phen)_2\}_2V_4O_{12}]$ which first consists of a $[V_4O_{12}]^{4-}$ ring covalently attached to each of two $[Zn(bipy)_2]^{2+}$ moieties through the terminal oxo groups of alternate vanadium sites. While the latter structure exhibits a $[V_4O_{12}]^{4-}$ ring linked through oxo groups of adjacent vanadium sites to two $[Zn(phen)_2]^{2+}$ moieties (Zhang, Zapf, Meyer, Haushalter, and Zubieta, 1997) and in $[\{Cd(phen)_2\}_2V_4O_{12}] \cdot 5H_2O$ consists of a $[V_4O_{12}]^{4-}$ cluster covalently attached to two $[Cd(phen)_2]^{2+}$ fragments, in which the $[V_4O_{12}]^{4-}$ cluster adopts a chair-like configuration (Qi, Wang, Li, Cao, Hu, Wang, Hu, and Jia, 2003). The 2-D layer structures were observed in $[\{Zn(2,2'-bpy)\}_2V_4O_{12}]$ and $[\{Zn(terpy)\}_2V_6O_{17}]$ (2,2'-bpy = 2,2'-bipyridine and terpy = 2,2':6',2''-terpyridine) which the cyclo $[V_4O_{12}]^-$ tetravanadate and metavanadate chains with zinc square pyramid, respectively (Hagman, and Zubieta, 2001); $[Zn(tpytrz)_2V_2O_6]$ (tpytrz = 2,4,6-tri(4-pyridyl)-1,3,5-triazine) composed of the metavanadate chains across with zinc tetrahedra (Rarig and

Zubieta, 2003); $[\text{Zn}(\text{phen})(\text{H}_2\text{O})\text{V}_2\text{O}_6]$ (phen = 1,10-phenanthroline) covalently constructed from cyclic tetramer $[\text{V}_4\text{O}_{12}]^-$ subunits and $[\text{Zn}(\text{phen})(\text{H}_2\text{O})]^{2+}$ fragments (Chen, Gu, Peng, Shi, and Wang, 2004) or in $[(\text{NH}_3(\text{CH}_2)_3\text{NH})\text{Zn}]_2^{3+}[\text{V}_4\text{O}_{13}]^{6-}$ which consists of the corner-sharing of vanadium tetrahedra and zinc tetrahedra which one terminal amine group of ligand is protonated (Natarajan, 2003). The 3-D framework structures, such as in $[(\text{en})_2\text{ZnV}_6\text{O}_{14}]$, the $[\text{V}_6\text{O}_{14}]^{2-}$ layers linked with the zinc octahedral pillars (Zhang, DeBord, O'Connor, Haushalter, Clearfield, and Zubieta, 1996); a novel 3-D network of $[\text{Zn}_2(\text{tp})(4,4'\text{-bpy})\text{V}_2\text{O}_6]$ (tp = terephthalate, 4,4'-bpy = 4,4'-bipyridine) composed of polycatenated tetravanadate-pillared double-layered sheets which constructed from polymeric cationic $[\text{Zn}_2(\text{tp})(4,4'\text{-bpy})]_n^{2n+}$ layers and $[\text{V}_4\text{O}_{12}]^{4-}$ pillars, thus, there are three directional channels of sizes ca. 11.8 x 8.1, 11.8 x 9.2 and 9.2 x 8.1 Å, respectively (Tao, Zhang, Tong, and Chen, 2001); $[\text{Zn}_3(\text{tpytrz})_2(\text{H}_2\text{O})_2\text{V}_6\text{O}_{18}] \cdot 6\text{H}_2\text{O}$ (tpytrz = 2,4,6-tri(4-pyridyl)-1,3,5-triazine) composed of the corner-sharing vanadium tetrahedra, zinc tetrahedra and zinc octahedra with a large channel of 11.6 x 11.3 Å, occupied by the tpytrz ligand (Rarig and Zubieta, 2003); $\text{Zn}(\text{bpp})\text{V}_2\text{O}_6$ (bpp = 1,3-di-4-pyridylpropane) consists of a polymeric metavanadate chains and polymeric left-handed helical zinc complex chains (Qu, Xu, Li, Gao, and Yang, 2007). Finally, in certain cases they may be necessary components of the reaction medium, as in the synthesis of the porous structure of $[\text{Zn}_3(\text{OH})_2\text{V}_2\text{O}_7] \cdot 2\text{H}_2\text{O}$, where the $[\text{TMA}]^+$ monocation is not incorporated into the structure, but is necessary to maintain the pH of the reaction mixture (Zavalij, Zhang, and Whittingham, 1997). Combining this with the hydrothermal technique provides more chance to obtain a large variety number of new VMO materials.

1.3 Supramolecular Interactions

Supramolecular chemistry has been defined by one of its leading proponents, Jean-Marie Lehn, who won the Nobel Prize for his work in the area in 1987, as the “chemistry of molecular assemblies and of the intermolecular bond”. More colloquially this may be expressed as “chemistry beyond the molecule”. Other definitions include phrases such as “the chemistry of the noncovalent bond” (Steed and Atwood, 2000). They play distinctive roles in molecular recognition, guiding molecular association, and in determining molecular and supramolecular phenomena in crystal engineering, structure chemistry and biology (Desiraju and Steiner, 2001). These interactions include ion-dipole interactions, dipole-dipole interactions, hydrogen bonding, and dispersion interactions, are of interest in large areas of experimental and theoretical research as described below.

Ion–Dipole interactions (40-210 kJ mol⁻¹) are the electrostatic attractions which an ion and a nearby polar molecule (dipole) attract each other, an ion-dipole interaction results. The most important example takes place when an ionic compound dissolves in water. The ions become separated because the attractions between the ions and the oppositely charged poles of the H₂O molecules overcome the attractions between the ions themselves. According to Steed (2001) the alkali cations, Li⁺, Na⁺, K⁺, Rb⁺, and Cs⁺, interact with polar macrocyclic crown ether molecules.

Dipole–Dipole interactions (4-40 kJ mol⁻¹) are intermolecular interactions between molecules or groups of atoms having a permanent electric dipole moment. Allen and coworkers (1998) studied these interactions in carbonyl group, the attraction between the positive polarity carbon atom and the negative polarity oxygen atom of adjacent carbonyl groups as shown in Figure 1.3, which are common in organic and biochemical systems, by correlation/MO calculations established that carbonyl–

carbonyl dipole interaction energies can be up to -22 kJ mol^{-1} for the antiparallel geometry with an optimum 3.02 \AA separation between the $>\text{C}(\delta^+)$ of one carbonyl dipole to the oxygen of another are comparable to medium to strong hydrogen bond interactions (*ca* -20 to -30 kJ mol^{-1}) (Jeffrey and Seanger, 1994).

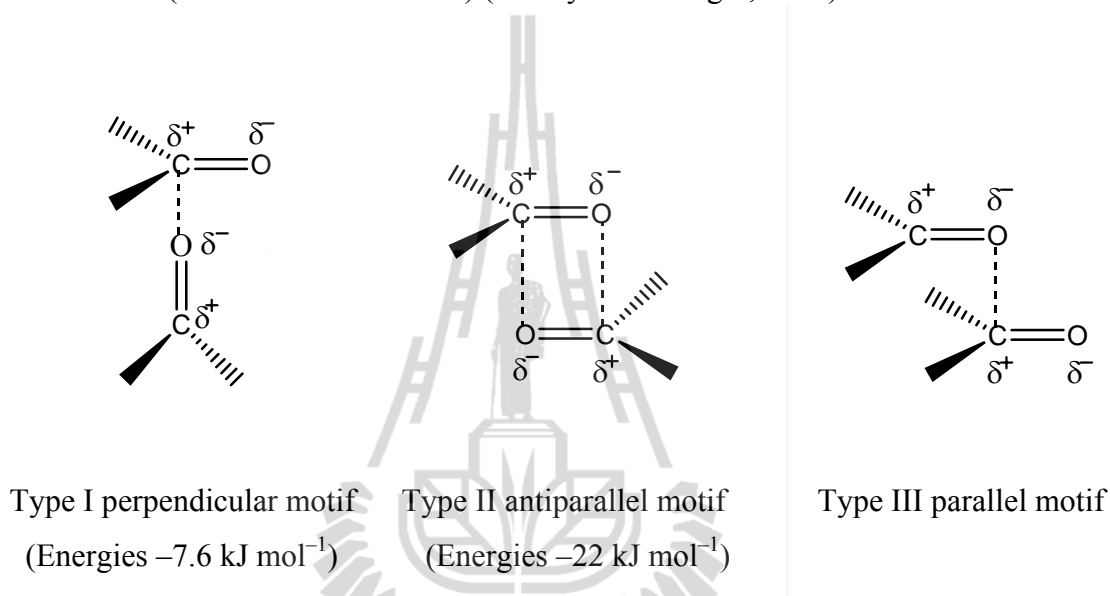


Figure 1.3 Carbonyl \cdots carbonyl interactions.

In 2005 Krachodnok and Haller observed the strong $>\text{C}(\delta^+)\cdots\text{O}(\delta^-)$ carbonyl-carbonyl interlayer interactions in the structure of pyridine-3,5-dicarboxylic acid, which had not been recognized when the previous work was reported (Takusagawa, Hirotsu, and Shimada, 1973), complete the three dimensional assemblage. In addition, Chainok (2004) found these interactions in the molecular structure of $\text{Co}(\text{picoline})_3\cdot\text{H}_2\text{O}$ as illustrated in Figure 1.4.

Hydrogen Bond Interactions ($4\text{-}65 \text{ kJ mol}^{-1}$) may be regarded as a special type of dipole-dipole interaction in which a hydrogen atom attached to negatively charged or negatively polarized atoms with (or without) lone pairs, are described by the formulae $\text{X-H}\cdots\text{Y}$ as shown in Figure 1.5. The atom of the donor (D) that is

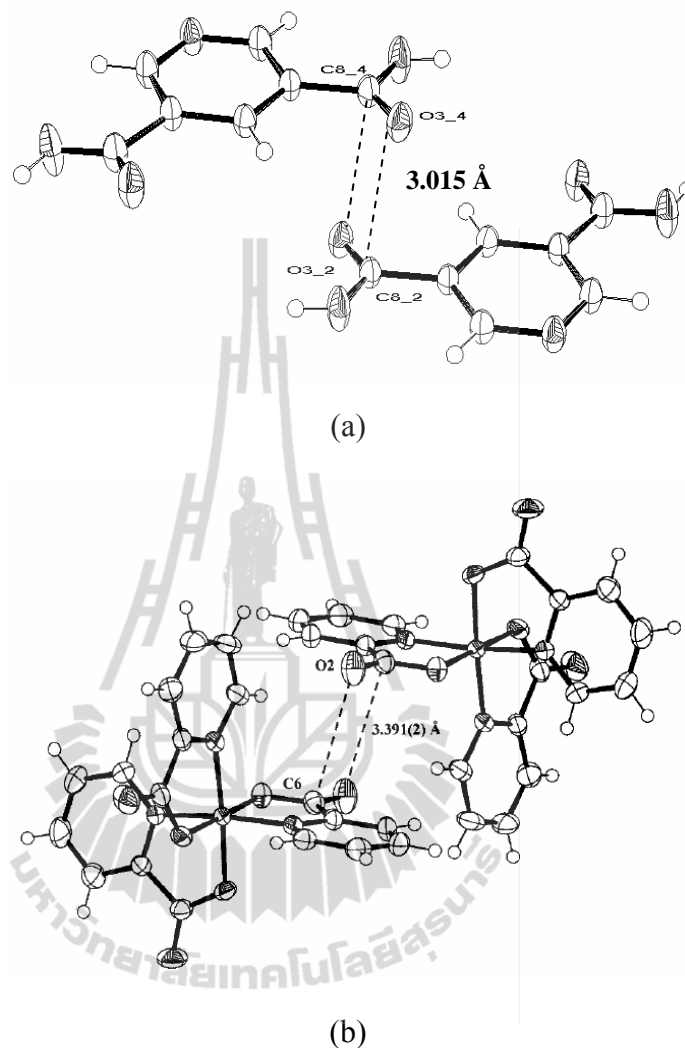


Figure 1.4 Carbonyl–carbonyl antiparallel interactions in (a) the structure of pyridine-3,5-dicarboxylic acid (Krachodnok and Haller, 2005) and (b) the structure of $\text{Co}(\text{picoline})_3 \cdot \text{H}_2\text{O}$ (Chainok, 2004).



Figure 1.5 Hydrogen bond geometry and partial charges. Donor and acceptor atoms in a hydrogen bond (left), and angular dependence in hydrogen bonds (right).

bonded to the acidic hydrogen atom is labeled X, the atoms of the acceptors (A) which are hydrogen-bonded to the acidic H atom are labeled Y. Hydrogen bonds are mainly electrostatic in nature but bonding (covalent) and repulsive orbital-orbital interactions are also important, especially in the case of strong hydrogen bonds. Nature and strength of hydrogen bonds strongly depend on both the hydrogen-bond donors and acceptors involved and the structural arrangement of the hydrogen bonds. Thus, the strength of hydrogen bonds increases with both increasing acceptor capability of the hydrogen bond acceptor groups and increasing donor strength of the hydrogen-bond donors. These interactions are of attention in large areas of experimental (X-ray, neutron, IR, Raman, NMR, NQR, etc.) and theoretical results on X–H(D)⋯bond lengths and angles, XH(D) stretching and bending modes (frequencies, intensities, and half widths), ^1H MAS NMR chemical shifts, and 2D NQR coupling constants reviewed by Lutz (2003) and he also classified the structure of hydrogen bonds as shown in Figure 1.6.

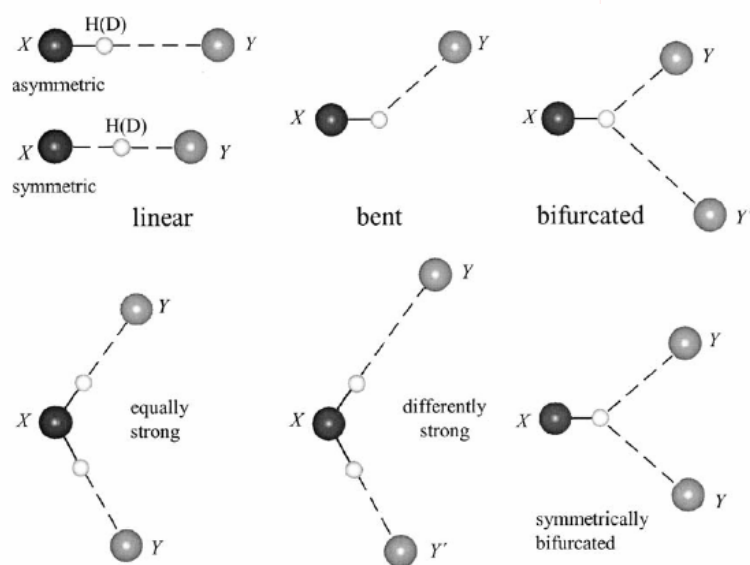
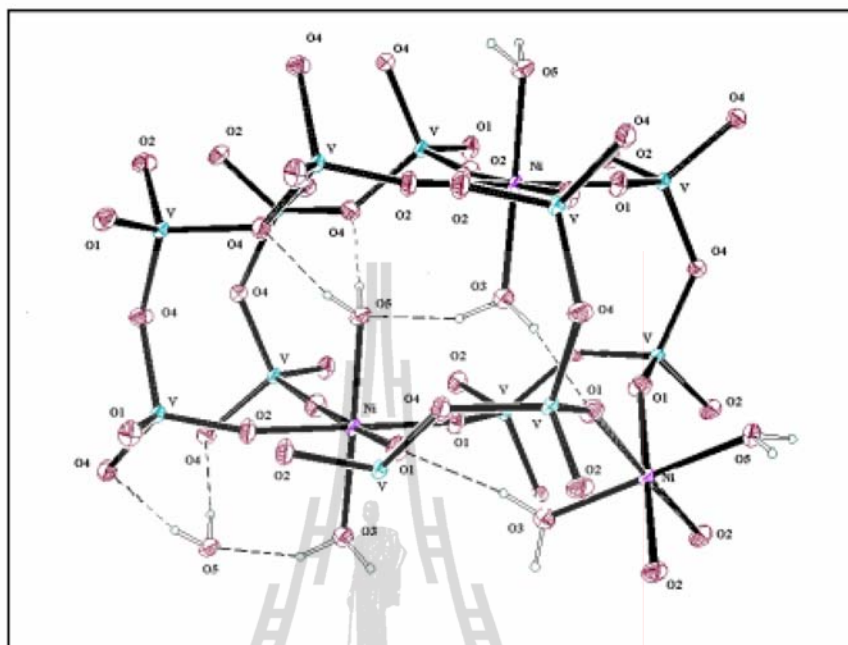


Figure 1.6 Structure of hydrogen bonds: symmetric and asymmetric; linear, bent, and bifurcated; equally strong, differently strong (Lutz, 2003).

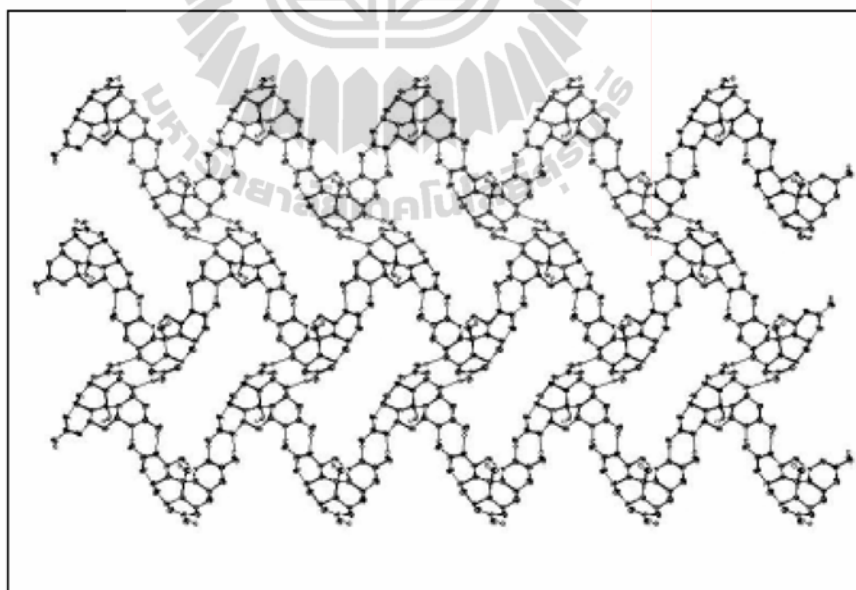
According to our previous research group work, Chatkon (2001) reported two nonequivalent coordination of the waters, one ordered and other disordered, caused by O–H...O hydrogen bond interactions in two microporous structures of $MV_2O_6 \cdot 2H_2O$ ($M = Co$ and Ni) by single crystal X-ray diffraction, infrared spectroscopy and thermal gravimetric analysis and the strength of a porous 3-D supramolecular array of $[H_2en]_5[V_6B_{20}O_{50}H_8] \cdot 7H_2O$ caused from O–H...O hydrogen bond interactions of the raft-like $[B_{10}O_{16}H_4]^{10-}$ polyborate ligands, interconnect between adjacent clusters through the hydroxyl H atoms, and the cations and waters filled in the channel form N/O–H...O hydrogen bond interaction with each other by single crystal X-ray diffraction as shown in Figure 1.7.

Currently, Puntharod et al. (2010) reported their intermolecular noncovalent interactions types above include C–H... π hydrogen bond play an integral role in enabling excitonic enhancement observed in β -hematin (malaria pigment) and other related heme derivatives by DFT calculation, X-ray diffraction, and Raman spectroscopy (Figure 1.8).

Aromatic–Aromatic Interactions ($0-10 \text{ kJ mol}^{-1}$) are noncovalent interactions involving aromatic sections of the molecules and are common and ubiquitous, particularly when acting in concert, rival the robustness of hydrogen bonds. Several studies (Lopes, Lamoureux, Roux, and Mackerell, 2007; Escudero, Frontera, Quiñonero, and Deyà, 2008) suggest the existence of a competition between face-to-face (*ff*) π – π interaction and C–H... π edge-to-face (*ef*) hydrogen bond interaction which is strongly affected by the polarity of the environment and by the possibility of forming hydrogen bonds. The π – π interaction is dominated by dispersion and electrostatic (quadrupole–quadrupole) forces. The *ef* orientation has favorable



(a)



(b)

Figure 1.7 O–H...O hydrogen bond interactions in (a) $MV_2O_6 \cdot 2H_2O$ ($M = Ni$ and Co) projected parallel to *a* axis and (b) $[H_2en]_5[V_6B_{20}O_{50}H_8] \cdot 7H_2O$ projected of half-clusters on *bc* plane (Chatkon, 2001).

electrostatics but weaker dispersion, and it is very close in energy to the parallel displaced (*off*) configuration that has more dispersion but less favorable electrostatics as illustrated in Figure 1.9.

A feature of the supramolecular interactions of phenylated molecules is the widespread occurrence of multiple phenyl embraces, in which individual intermolecular phenyl...phenyl attractive or dispersive interactions operate in concert with significant net attraction. Multiple phenyl embraces are characterized by (a) the participation of two or more phenyl groups from each neighbouring molecules, (b) geometrical concertedness, and (c) strong attraction (Dance and Scudder, 1998; Scudder and Dance, 1998; Lewis and Dance, 2000) as shown in Figure 1.10.

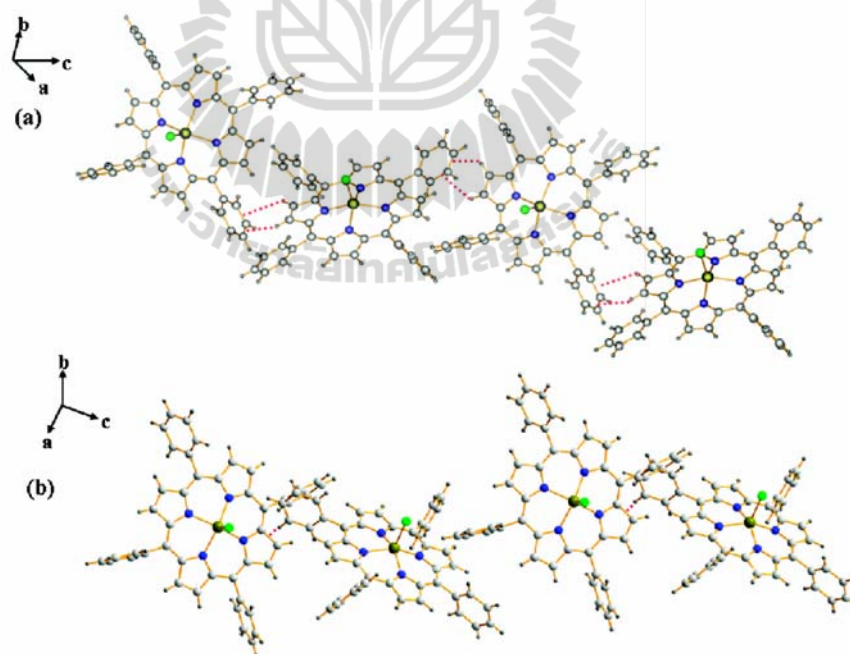


Figure 1.8 Diamond diagram of Fe(TPP)Cl showing (a) the C–H... π_{phenyl} and (b) C–H... π_{pyrrole} hydrogen bond interactions (Puntharod, Webster, Asghari-Khiavi, Bambery, Safinejad, Rivadehi, Langford, Haller, and Wood, 2010).

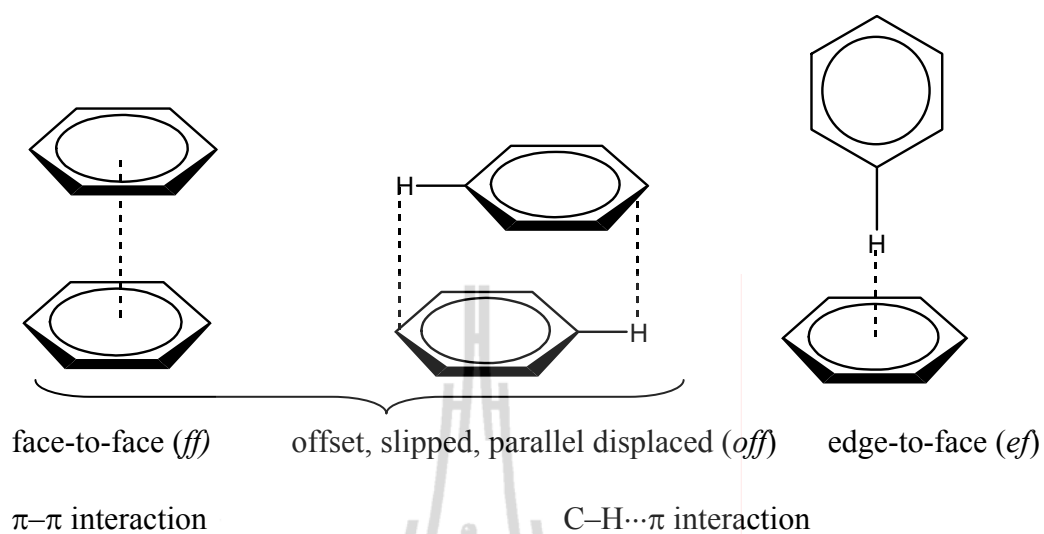
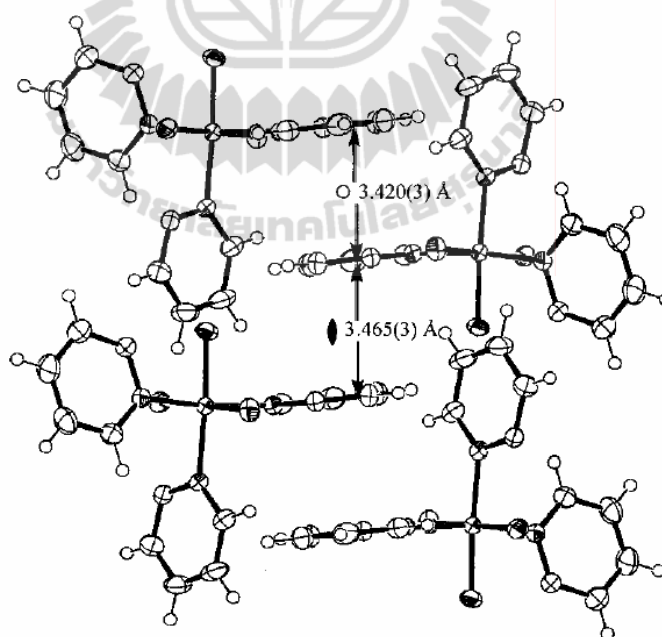


Figure 1.9 Aromatic–aromatic interaction motifs.



(a)

Figure 1.10 Aromatic–aromatic interactions in (a) $\text{Co}(\text{picoline})_3 \cdot \text{H}_2\text{O}$ (Chainok, 2004) and (b) metal phenanthroline complexes (Russell, Scudder, and Dance, 2001).

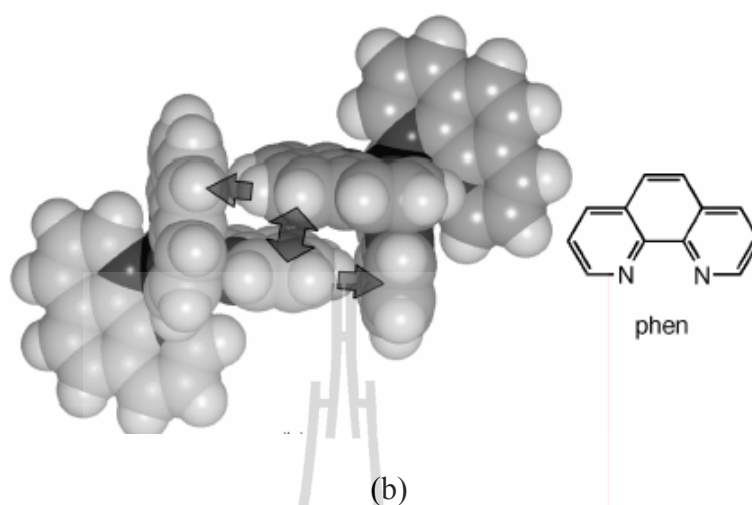


Figure 1.10 (Continued).

1.4 Research Objectives

1. To conduct synthesis under hydrothermal conditions attempting to create new main group vanadates.
2. To characterize crystalline materials created, using single crystal X-ray diffraction to determine 3-D structure.
3. To investigate the physical characterization of compounds as required to support the structure analysis such as phase identification, functional group of chemical bonding, chemical compositions, and the level of inorganic and organic components in materials using powder X-ray diffraction (XRD), Fourier-transform infrared spectroscopy (FT-IR), elemental analyses (CHN), and thermogravimetric analysis (TGA), respectively.

1.5 References

- Allen, F. H., Baalham, C. A., Lommerse, J. P. M, and Raithby, P. R. (1998). Carbonyl–carbonyl interactions can be competitive with hydrogen bond. **Acta Crystallographica Section B**. 54(3): 320-329.
- Bahranowski, K., Bueno, G., Corberán, V. C., Kooli, F., Serwicka, E. M., Valenzuela, R. X., and Wcisło, K. (1999). Oxidative dehydrogenation of propane over calcined vanadate exchanged Mg, Al-layered double hydroxides. **Applied Catalysis A: General**. 185(1): 65-73.
- Chainok, K. (2004). **Synthesis and Structural Studies of Cobalt and Vanadium Oxide Compounds**. Master Thesis, Suaranaree University of Technology, Thailand.
- Chatkon, A. (2001). **Structural Studies of Supramolecular Microporous Materials**. Master Thesis, Suaranaree University of Technology, Thailand.
- Chen, Y., Gu, X., Peng, J., Shi, Z., and Wang, E. (2004). Hydrothermal synthesis and crystal structure of organic–inorganic hybrid vanadate: [Zn(phen)(H₂O)V₂O₆] (phen = 1,10-phenanthroline). **Journal of Molecular Structure**. 692(1-3): 243-247.
- Choi, L., Zhu, Z. T., Musfeldt, J. L., Ragghianti, G., Mandrus, D., Sales, B. C., and Thompson, J. R. (2001). Local symmetry breaking in K₂V₃O₈ as studied by infrared spectroscopy. **Physical Review B**. 65(5): 54101-54106.
- Chrappová, J., Schwendt, P., Dudášová, D., Tatiarsky, J., and Marek, J. (2008). Synthesis, X-ray crystal structure and thermal decomposition of two peroxovanadium complexes with coordinated ammonia molecules: [$\{\text{VO}(\text{O}_2)_2(\text{NH}_3)\}_2\{\mu\text{-Cu}(\text{NH}_3)_4\}$] and $[\text{Zn}(\text{NH}_3)_4][\text{VO}(\text{O}_2)_2(\text{NH}_3)]_2$. **Polyhedron**. 27(2): 641-647.

- Cotton, F. A., Wilkinson, G., Murillo, C. A., and Bockmann, M. (1999). **Advanced Inorganic Chemistry**. 6th edition, John Wiley & Sons, Inc, New York. pp. 715-958.
- Dance, I., and Scudder, M. (1998). Supramolecular motifs: sextuple aryl embraces in crystalline $[M(2,2'\text{-bipy})_3]$ and related complexes. **Journal of the Chemical Society, Dalton Transactions**. (8): 1341-1350.
- Desiraju, G., and Steiner, T. (2001). **The Weak Hydrogen Bond in Structural Chemistry and Biology**. Vol. 9, Oxford University Press/International Union of Crystallography, Oxford. pp. 293-323.
- Escudero, D., Frontera, A., Quiñonero, D., and Deyà, P. M. (2008). Interplay between edge-to-face aromatic and hydrogen-bonding interactions. **The Journal of Physical Chemistry A**. 112(26): 6017-6022 and references cited therein.
- Fallis, I., Farrugia, L. J., Macdonald, N. M., and Peacock, R. D. (1993). $[Zn^{II}(LH_3)(L)V^{IV}][PF_6]_3$ [$LH_3 = N,N',N''$ -Tris(2*S*)-2-hydroxypropyl-1,4,7-triazacyctononane]: A chiral mixed-metal pendant-arm macrocyclic dimer containing non-vanadyl vanadium(IV). **Inorganic Chemistry**. 32(6): 779-780.
- Fuentes, A. F., Treviño, L., Martínez-de la Cruz, A., and Torres-Martínez, L. M. (1999). Electrochemical lithium insertion in some nickel, zinc and cadmium vanadates. **Journal of Power Sources**. 81-82(1-2): 264-267.
- Galy, J., and Carpy, A. (1975). Structure cristalline de $K_2V_3O_8$ ou $K_2(VO)[V_2O_7]$. **Acta Crystallographica Section B**. 31(6): 1794-1795.
- Hagman, P. J., and Zubieta, J. (2001). Hydrothermal syntheses and structural characterizations of organic-inorganic hybrid materials of the M(II)-ligand/vanadium oxide system (M(II) = Cu(II) and Zn(II); Ligand = 2,2'-

- bipyridine and 2,2':6',2''-terpyridine). **Inorganic Chemistry**. 40(12): 2800-2809.
- Huang, F., Fu, Z.-W., and Qin, Q.-Z. (2003). A novel $\text{Li}_2\text{Ag}_{0.5}\text{V}_2\text{O}_5$ composite film cathode for all-solid-state lithium batteries. **Electrochemistry Communications**. 5(2): 262-266.
- Jeffrey, G. A., and Seanger, W. (1991). **Hydrogen Bonding in Biological Systems**. Springer-Verlag, Berlin. pp. 1-42.
- Khan, M. I., Nome, R. C., Deb, S., MaNeely, J. H., and Cage, B. (2009). Inorganic-organic hybrid materials with novel framework structures: synthesis, structure, and magnetic properties of $[\text{Ni}(\text{py})_4]_2\text{V}_{10}\text{O}_{29}$ and $[\text{Ni}(\text{py})_5(\text{H}_2\text{O})_3]\text{V}_4\text{O}_{12}$. **Crystal Growth & Design**. 9(6): 2848-2852.
- Korili, S. A., Ruiz, P., and Delmon, B. (1996). Oxidative dehydrogenation of *n*-pentane on magnesium vanadate catalysts. **Catalysis Today**. 32(1-4): 229-235.
- Krachodnok, S., and Haller, K. J. (2005). Supramolecular structure analysis: detection of a novel carbonyl-carbonyl interaction in the structure of pyridine-3,5-dicarboxylic Acid. In **Proceeding of the 9th Annual National Symposium on Computational Science & Engineering 2005 (ANSCSE 9)**. Mahidol University press, Bangkok. pp. 464-470.
- Larrea, E. S., Mesa, J. L., Pizarro, J. L., Arriortua, M. I., and Rojo, T. (2007). Hydrothermal synthesis and crystal structure of the $\text{Ni}_2(\text{C}_4\text{H}_4\text{N}_2)(\text{V}_4\text{O}_{12})(\text{H}_2\text{O})_2$ and $\text{Ni}_3(\text{C}_4\text{H}_4\text{N}_2)_3(\text{V}_8\text{O}_{23})$ inorganic-organic hybrid compounds. Thermal, spectroscopic and magnetic studies of the hydrated phase. **Journal of Solid State Chemistry**. 180(3): 1149-1157.

- Lewis, G. R., and Dance, I. (2000). Crystal supramolecularity. Multiple phenyl embraces by [PPN]⁺ cations. **Journal of the Chemical Society, Dalton Transactions.** (3): 299-306.
- Lian, Z., Zhang, J., Gu, Y., Wang, T., and Lou, T. (2009). Synthesis and crystal structures of two inorganic-organic hybrid vanadium selenites with layered structures: (H₂DABCO)[(VO₂)(SeO₃)₂].1.25H₂O and (H₂pipe)[(VO)₂(C₂O₄)(SeO₃)₂]. **Journal of Molecular Structure.** 919(1-3): 122-127.
- Lin, H., and Maggard, P. A. (2008). Synthesis and structures of a new series of silver-vanadate hybrid solids and their optical and photocatalytic peoperties. **Inorganic Chemistry.** 47(18): 8044-8052.
- Liu, G., and Greedan, J. E. (1995). Magnetic properties of Fresnoite-type vanadium oxides: M₂V₃O₈ (M = K, Rb, NH₄). **Journal of Solid State Chemistry.** 114(1): 499-505.
- Liu, H., and Tang, D. (2008). Synthesis of ZnV₂O₆ powder and its cathodic performance for lithium secondary battery. **Materials Chemistry and Physics.** 114(2-3): 656-659.
- Lopes, P. E. M., Lamoureux, G., Roux, B., and Mackerell, A. D. (2007). Polarizable empirical force field for aromatic compounds base on the classical drude oscillator. **The Journal of Physical Chemistry B.** 111(11): 2873-2885.
- Lutz, H. D. (2003). Structure and strength of hydrogen bonds in inorganic solids. **Journal of Molecular Structure.** 646(1-3): 227-236.
- Mattos, A. R. J. M., Gil, R. A. S. S., Rocco, M. L. M., and Eon, J.-G. (2002). Zinc-modified, alumina-supported vanadium oxides as catalysts for propane

- oxidative dehydrogenation. **Journal of Molecular Catalysis A: Chemical.** 178(1-2): 229-237.
- Mordkovich, V. Z., Hayashi, H., Haemori, M., Fukumura, T., and Kawasaki, M. (2003). Discovery and optimization of new ZnO-based phosphors using a combinatorial methods. **Advanced Functional Materials.** 13(7): 518-524.
- Nakajima, T., Isobe, M., Tsuchiya, T., Ueda, Y., and Kumagai, T. (2009). A revisit of photoluminescence property for vanadium oxides MVO_3 (M: K, Rb and Cs) and $M_3V_2O_8$ (M: Mg and Zn). **Journal of Luminescence.** 129(12): 1598-1601.
- Natarajan, S. (2003). Hydrothermal synthesis and crystal structure of a two-dimensional zinc vanadate, $[(NH_3(CH_2)_3NH)Zn]_2^{3+}[V_4O_{13}]^{6-}$. **Inorganica Chimica Acta.** 348(1): 233-236.
- Puntharod, R., Webster, G. T., Asghari-Khiavi, M., Bambery, K. R., Safinejad, F., Rivadehi, S., Langford, S. J., Haller, K. J., and Wood, B. R. (2010). Supramolecular interactions playing an integral role in the near-infrared Raman “excitonic” enhancement observed in β -Hematin (malaria pigment) and other related heme derivatives. **The Journal of Physical Chemistry B.** 114(3): 12104-12115.
- Qi, Y., Wang, Y., Li, H., Cao, M., Hu, C., Wang, E., Hu, N., and Jia, H. (2003). Hydrothermal syntheses and crystal structures of bimetallic cluster complexes $[\{Cd(phen)_2\}_2V_4O_{12}] \cdot 5H_2O$ and $[Ni(phen)_3]_2[V_4O_{12}] \cdot 17.5H_2O$. **Journal of Molecular Structure.** 650(1-3): 123-129.
- Qu, X., Xu, L., Li, F., Gao, G., and Yang, Y. (2007). A novel chiral 3-D architecture containing left-handed helical chains constructed from vanadate clusters: $Zn(bpp)V_2O_6$ (bpp = 1,3-di-4-pyridylpropane). **Inorganic Chemistry**

Communications. 10(12): 1404-1408.

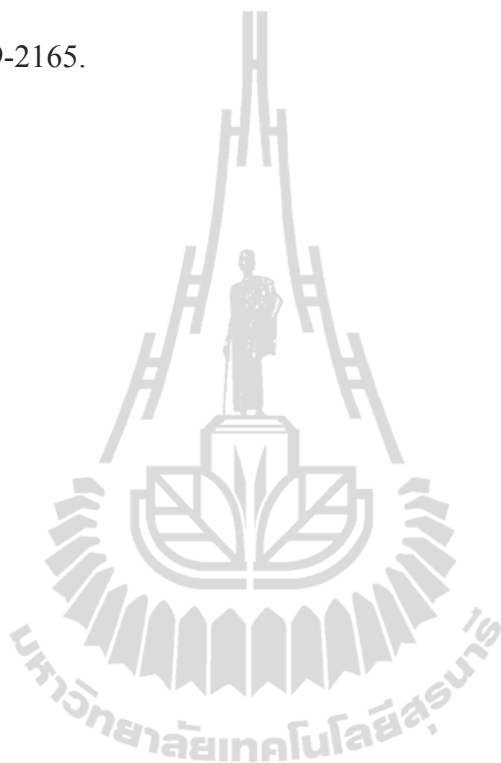
- Rarig, R. S., Zubieta, J. and J. (2003). Solid state coordination chemistry: secondary metal–ligand influences on the structures of vanadium oxides. Hydrothermal syntheses and structures of $[\text{Zn}(\text{tpytrz})_2\text{V}_2\text{O}_6]$, $[\text{Zn}_3(\text{tpytrz})_2(\text{H}_2\text{O})_2\text{V}_6\text{O}_{18}] \cdot 6\text{H}_2\text{O}$ and $[\text{Cu}_3(\text{tpytrz})_2(\text{H}_2\text{O})_2\text{V}_8\text{O}_{23}] \cdot 3\text{H}_2\text{O}$ (tpytrz = 2,4,6-tri(4-pyridyl)-1,3,5-triazine). **Dalton Transactions.** (9): 1861-1868.
- Rehder, D. (1999). The coordination chemistry of vanadium as related to its biological functions. **Coordination Chemistry Reviews.** 182(1): 297-322.
- Russell, V. M., Scudder, M., and Dance, I. (2001). The crystal supramolecularity of metal phenanthroline complexes. **Journal of the Chemical Society, Dalton Transactions.** (6): 789-799.
- Schindler, M., Hawthorne, F. C., and Baur, W. H. (2000). Crystal chemical aspects of vanadium: polyhedral geometries, characteristic bond valences, and polymerization of (VO_n) polyhedra. **Chemistry of Materials.** 12(5): 1248-1259.
- Scudder, M., and Dance, I. (1998). Crystal supramolecular motifs. Ladders, layers and labyrinths of Ph_4P^+ cations engaged in fourfold phenyl embraces. **Journal of the Chemical Society, Dalton Transactions.** (19): 3155-3165.
- Slobodin, B. V., Surat, L. L., Zubkov, V. G., Tyutyunnik, A. P., Berger, I. F., Kuznetsov, M. V., Perelyaeva, L. A., Shein, I. R., Ivanovskii, A. L., Shulgin, B. V., Solomonov, V. I., Svensson, G., Forslund, B., and Sayagués, M. J. (2005). Structural, luminescence and electronic properties of the alkaline metal–strontium cyclotetranavanadates $\text{M}_2\text{Sr}(\text{VO}_3)_4$, (M = Na, K, Rb, Cs). **Physical Reviews B: Condensed Matter and Materials Physics.** 72(15):

155205-155216.

- Slobodin, B. V., Surat, L. L., Samigullina, R. F., Ishchenko, A. V., Shulgin, B. V., and Cherepanov, A. N. (2010). Thermochemical and luminescent properties of the $K_2MgV_2O_7$ and $M_2CaV_2O_7$ ($M = K, Rb, Cs$) vanadates. **Inorganic Materials**. 46(5): 522-528.
- Steed, J. W., and Atwood, J. L. (2000). **Supramolecular Chemistry**. John Wiley & Sons, Ltd, Chichester. pp. 1-33.
- Steed, J. W. (2001). First- and second-sphere coordination chemistry of alkali metal crown ether complexes. **Coordination Chemistry Reviews**. 215(1): 171-221.
- Takusagawa, F., Hirotsu, K., and Shimada, A. (1973). The crystal structure of dinicotinic acid. **Bulletin of Chemical Society of Japan**. 46(8): 2292-2299.
- Tao, J., Zhang, X.-M., Tong, M.-L., and Chen, X.-M. (2001). A novel polycatenated double-layered hybrid organic-inorganic material constructed from $[Zn_2(tp)(4,4'-bpy)]_n^{2n+}$ layers and $[V_4O_{12}]^{4-}$ pillars ($tp = terephthalate$, $4,4'-bpy = 4,4'$ -bipyridine). **Journal of Chemical Society, Dalton Transactions**. (1): 770-771.
- Thompson, K. H., McNeill, J. H., and Orvig, C. (1999). Vanadium compounds as insulin mimics. **Chemical Reviews**. 99(9): 2561-2571.
- Thompson, K. H., and Orvig, C. (2000). Design of vanadium compounds as insulin enhancing agents. **Journal of the Chemical Society, Dalton Transactions**. (17): 2885-2892.
- Torardi, C. C., Miao, C. R., Lewittes, M. E., and Li, Z. (2002). High lithium capacity $M_xV_2O_5A_y \cdot nH_2O$ for rechargeable batteries. **Journal of Solid State Chemistry**. 163(1): 93-99.

- Wang, D., Zou, Z., and Ye, J. (2005). Photocatalytic O₂ evolution with the visible-light-driven photocatalysts M₃V₂O₈ (M = Mg, Zn). **Research on Chemical Intermediates**. 31(4-6): 433-439.
- Yan, B., Luo, J., Dube, P., Sefat, A. S., Greedan, J. E., and Maggard, P. A. (2006). Spin-gap formation and thermal structural studies in reduced hybrid layered vanadates. **Inorganic Chemistry**. 45(13): 5109-5118.
- Yang, H., Li, J., Zhang, X.-G., and Jin, Y.-L. (2008). Synthesis of LiV₃O₈ nanocrystallites as cathode materials for lithium ion batteries. **Journal of Materials Processing Technology**. 207(1-3): 265-270.
- Zavalij, P. Y., Zhang, F., and Whittingham, M. S. (1997). A new zinc pyrovanadate, Zn₃(OH)₂V₂O₇·2H₂O, from X-ray Powder Data. **Acta Crystallographica Section C**. 53(12): 1738-1739.
- Zavalij, P. Y., and Whittingham, M. S. (1999). Structural chemistry of vanadium oxides with open frameworks. **Acta Crystallographica Section B**. 55(5): 627-663.
- Zavalij, P. Y., Zhang, F., and Whittingham, M. S. (2002). The zinc-vanadium-oxygen-water-system: hydrothermal synthesis and characterization. **Solid State Sciences**. 4(5): 591-597.
- Zhang, F., Zavalij, P. Y., and Whittingham, M. S. (1997). Hydrothermal synthesis of iron and zinc double vanadium oxides using the tetramethyl ammonium ion. **Materials Research Bulletin**. 32(6): 701-707.
- Zhang, Y., DeBord, J. R. D., O'Connor, C. J., Haushalter, R. C., Clearfield, A., and Zubieta, J. (1996). Solid state coordination chemistry: hydrothermal synthesis of layered vanadium oxides with interlayer metal coordination complexes. **Angewandte Chemie International Edition in English**. 35(9): 989-991.

Zhang, Y., Zapf, P. J., Meyer, L. M., Haushalter, R. C., and Zubieta, J. (1997). Polyoxoanion coordination chemistry: synthesis and characterization of the heterometallic, hexanuclear clusters $[\{Zn(bipy)_2\}_2V_4O_{12}]$, $[\{Zn(phen)_2\}_2V_4O_{12}] \cdot H_2O$, and $[\{Ni(bipy)_2\}_2Mo_4O_{14}]$. **Inorganic Chemistry**. 36(10): 2159-2165.



CHAPTER II

HYDROTHERMAL SYNTHESIS AND PHYSICAL METHODS FOR CHARACTERIZING SOLIDS

2.1 Hydrothermal Synthesis

From geological origin to a powerful synthetic technique in the laboratory, the hydrothermal method is well-known and used in large areas. Zeolites (Davis and Lobo, 1992), AlPO_4 's analogues (Wilson, Lok, Messina, Cannan, and Flanigen, 1982), and other porous inorganic solid materials, have been successfully synthesized under hydrothermal conditions. Currently, it has been used to prepare a new generation of porous materials, metal-organic frameworks (MOF), and the multifunctional hybrid materials. Williams and co-workers have reported many novel structures of porous metal-tartrates (Thushari, Cha, Sung, Chui, Leung, Yen, and Williams, 2005; Au-Yeung, Sung, Cha, Siu, Chui, and Williams, 2006), inorganic-organic hybrid vanadates (Law and Williams, 2000; Chainok, 2008), under hydrothermal crystallization conditions.

There are several definitions of the *hydrothermal synthesis* in the literatures. Morey and Niggli (1913) defined hydrothermal synthesis as synthesis subjected to the action of water at a temperature, generally near, though often considerably above the critical temperature of water ($\sim 370^\circ\text{C}$) in closed bombs, and therefore, also under the correspondingly high pressures developed by such solutions. Sixty-seven years later, the definition of hydrothermal synthesis has been considerably relaxed. Laudise

(1970) defined hydrothermal growth as growth from aqueous solution at ambient or near-ambient conditions and according to Lobachev (1973), as a group of methods in which crystallization is carried out from superheated aqueous solutions at high pressures. Rabenau (1985) defined hydrothermal synthesis as heterogeneous reactions in aqueous media above 100 °C and 1 bar. According to Byrappa (1992) hydrothermal synthesis involves any heterogeneous reaction in aqueous media carried out above room temperature and at a pressure greater than 1 atm. Roy (1994) remarked that hydrothermal synthesis involves water as a catalyst and occasionally as a component of solid phases in the synthesis at elevated temperature ($> 100\text{ }^{\circ}\text{C}$) and pressure (greater than a few atmospheres).

From the above hydrothermal synthesis can be defined crystallization as any heterogeneous reaction in the presence of aqueous solvents or mineralizer under autogenous pressure and temperature conditions, such that the reaction mixture is heated in hot water or vapor in a closed system, to dissolve and recrystallize materials that are relatively insoluble under ordinary conditions. The increased pressure is achieved by placing the reactants in a sealed reactor and upon heating to $> 100\text{ }^{\circ}\text{C}$ in an oven of solvent vapor as water, the reaction conditions mimic those found in natural processes.

This technique uses water as the solvent. Water is not only a good solvent due to its polarity but also environmentally the safest material and the cheapest of all solvents. It also can act as a mineralizer, or a catalyst under elevated pressure and temperature conditions, due to its viscosity decrease or means that the strong hydrogen bond interactions between its neighbors and with solute become weak or sometime break which allows the ionic species to move to interact or combine with each other,

the desired product will occur. In 1982 Millero studied the behavior of water at high temperatures and pressures are represented by its thermodynamic properties, including its density, viscosity, diffusion, and thermal conductivity. A temperature-density diagram of water with pressure as a parameter, from his work is given in Figure 2.1. The dotted isobars are interpolated, and CP and TP signify the critical point and triple point, respectively. There is evidence that water at 150-200 kbar and 1000 °C has a density of 1.7-1.9 g cm⁻³ and is completely dissociated into H₃O⁺ and OH⁻ (Rabenau, 1985).

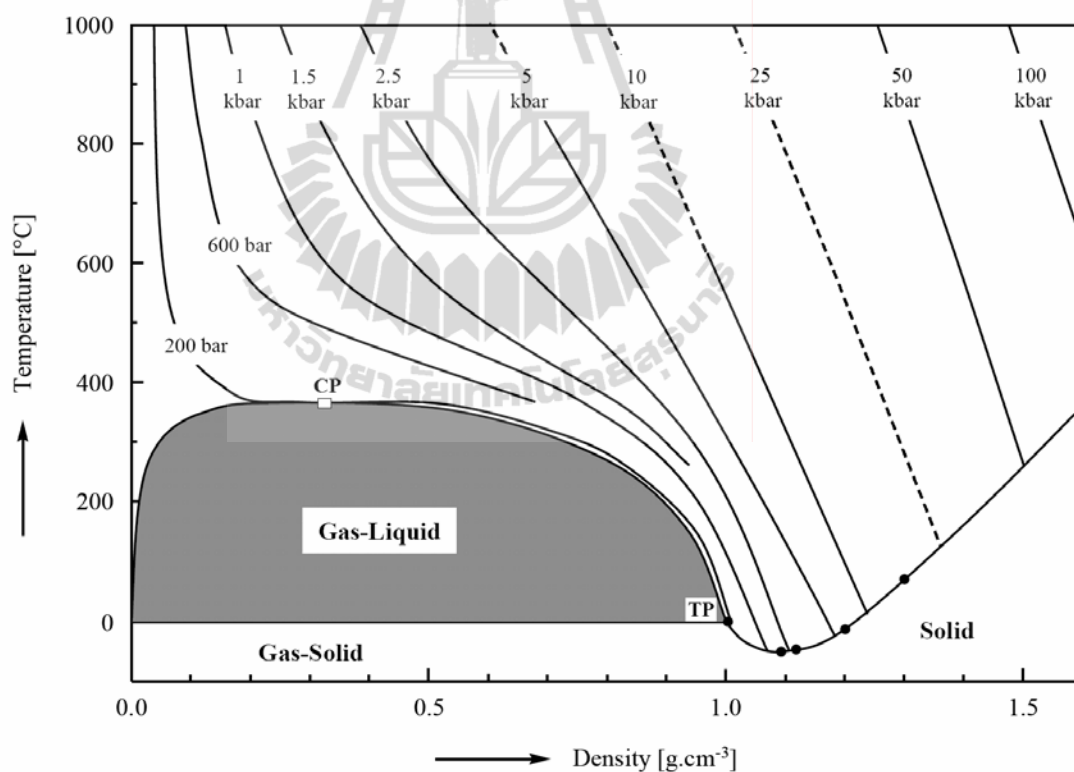


Figure 2.1 Temperature-density diagram of pure water (after Millero, 1982).

Many variables can affect the product formation, for example, Chirayil and co-workers (1998) have successfully synthesized vanadium oxide layers for new cathode materials in Li-ion batteries. They showed the different compounds formed as a

function of the pH of the reaction medium and showed the variety of crystal morphologies of the compounds can be formed, plate to fiber, from high to low pH, respectively, as illustrated in Figures 2.2 and 2.3.

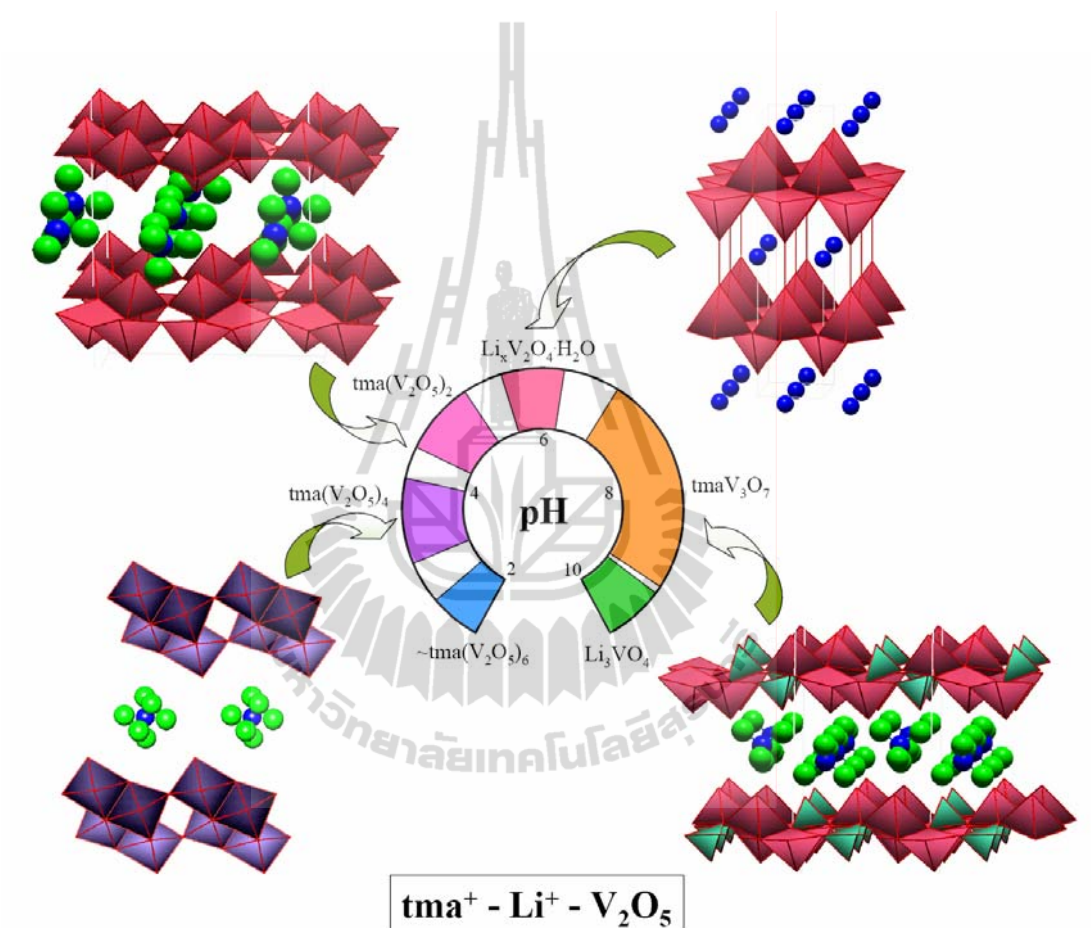


Figure 2.2 pH dependence of the phases formed when V_2O_5 , TMAOH, and LiOH in the molar ratio 1:2:1 are reacted at 185 °C. pH controlled by addition of acetic acid (Chirayil, Zavalij, and Whittingham, 1998).

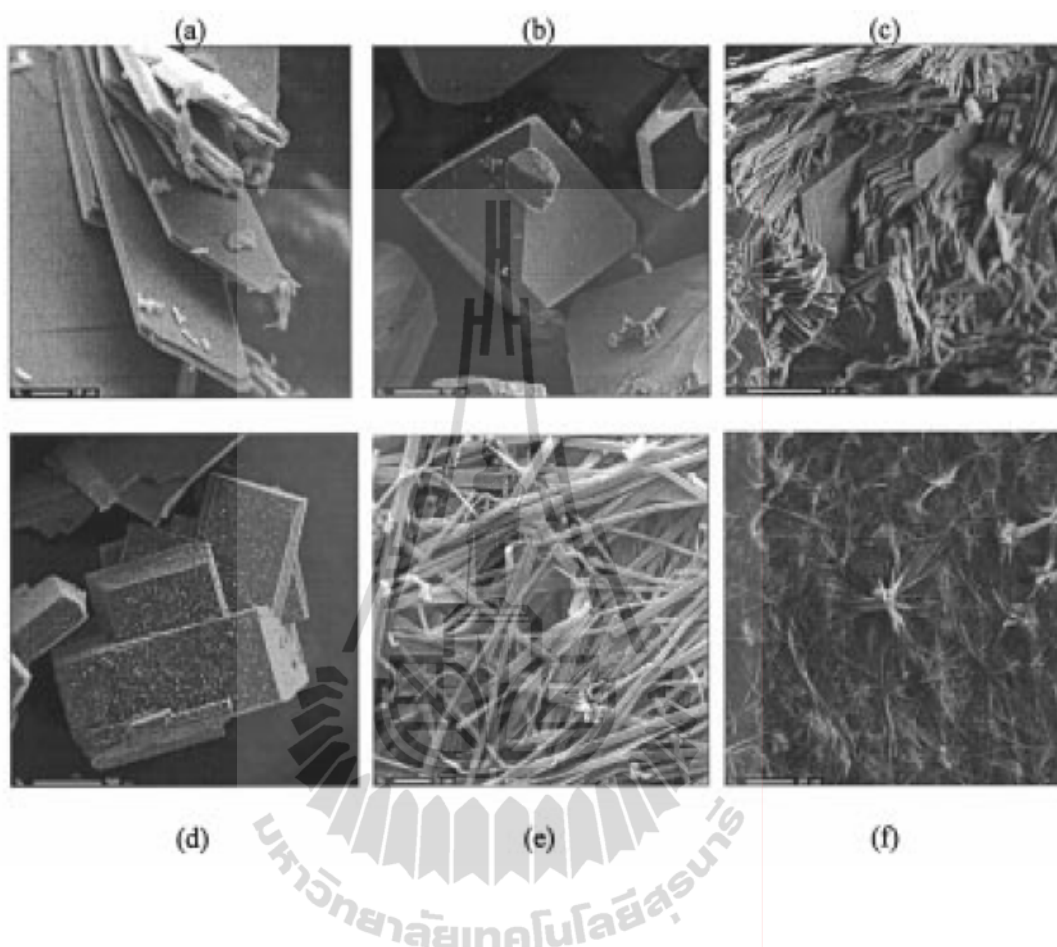


Figure 2.3 Morphologies of the compounds formed at different pH levels: (a) TMAV_3O_7 , (b) $\text{TMA}_4[\text{V}_{22}\text{O}_{54}(\text{OAc})]\cdot 4\text{H}_2\text{O}$, (c) $\text{Li}_x\text{V}_2\text{O}_4\cdot\text{H}_2\text{O}$, (d) $\text{TMA}(\text{V}_2\text{O}_5)_2$, (e) $\text{TMA}(\text{V}_2\text{O}_5)_4$, and (f) $\text{TMA}_{0.17}\text{H}_{0.1}\text{V}_2\text{O}_5$ (Chirayil, Zavalij, and Whittingham, 1998).

In 2000 Law and Williams studied the inorganic-organic hybrid manganese vanadates and found that both reaction pH and temperature played crucial roles in determining the isolated solid phases with those compounds obtained from pH range of 6-8 and even lower temperatures (80 or 110 °C, Figure 2.4). Thus, reaction pH, time, and temperature, the ratio of the reactants, and the ions present in solution which can be adjusted to produce the desired compound.

CHAPTER III

HYDROTHERMAL SYNTHESSES AND STRUCTURAL CHARACTERIZATIONS OF HYBRID ORGANIC-INORGANIC MATERIALS OF DIVALENT METAL VANADATES

3.1 Introduction

Hybrid organic-inorganic materials based on vanadium oxide have attracted considerable interest because of their wide applications in catalysis, optical and magnetic properties (Lin and Maggard, 2008; Williams, Law, Sung, Wen, and Zhang, 2000). Vanadium has a large variety of valency and coordination geometries available, tetrahedral, trigonal bipyramidal, square pyramidal and octahedral coordination environments in various oxidation states (+5, +4, +3). It can be combined with other metals and organic molecules leads to the possibility of designing a variety of structures and properties. The hydrothermal technique provides a means to overcome the differential solubility of inorganic oxides and organic molecules into a single structure at low temperature as found in our previous work. Williams et al. (2000) have successfully synthesized the first examples of 3-D porous divalent manganese vanadate compounds of $[\text{H}_2\text{en}][\text{Mn}_3(\text{V}_2\text{O}_7)_2(\text{H}_2\text{O})_2]$, and $[(\text{Hpn})_2\text{Mn}_3(\text{V}_2\text{O}_7)_2]$ using simple aliphatic diamines, en and pn (propane-1,3-diamine), as templates and show good magnetic properties, and in $[\text{H}_2\text{en}]_2[\text{MnF}(\text{VO}_3)_3]$ utilizing the organic reagent as structure directing agent with reactions addition within the same year, Law and

Williams (2000) progressed more with the same system, for example, 1-D $[(\text{Hen})_2\text{Mn}(\text{VO}_3)_4]$, 2-D $[\text{H}_2\text{en}]_2[\text{Mn}(\text{VO}_3)_6]$ and 3-D at pH about 6-8 and at 110-140 °C.

We continued to explore the divalent metal vanadates under hydrothermal conditions. This work studies, zinc and cadmium as the divalent metal. en and its derivatives are chain aliphatic diamines which can act as a monodentate, bidentate ligand, bridging or chelating ligand, or templating agent depending on their pKa values (en: $\text{p}K_{\text{a}1} = 10.71$ and $\text{p}K_{\text{a}2} = 7.56$; enMe: $\text{p}K_{\text{a}1} = 10.00$ and $\text{p}K_{\text{a}2} = 7.13$).

Herein, we report a new 3-D chiral network and an opened framework structures of divalent zinc vanadate. $(\text{en})\text{Zn}_2\text{V}_2\text{O}_7$ (**3a**) composed of V(V) tetrahedra as pillars linked between the layers formed from polymeric double helix of zinc coordination complexes and zinc vanadate. While $(\text{HenMe})_2\text{ZnV}^{4+}_4\text{V}^{5+}_4\text{O}_{20}$ (**3d**) containing zinc (II) complexes as pillars linked to anionic mixed-valence $\text{V}^{4+}/\text{V}^{5+}$ layers. Others, zinc (II) complexes as cross-linkers of infinite metavanadate chains: 1-D double chains, $(\text{Hen})_2\text{CdV}_4\text{O}_{12}$ (**3c**), 2-D double layers, $(\text{en})\text{ZnV}_2\text{O}_6$ (**3b**), and 3-D opened framework, $(\text{enMe})_2\text{Zn}(\text{VO}_3)_2 \cdot 2\text{H}_2\text{O}$ (**3e**).

3.2 Experimental

3.2.1 Materials, Apparatus, and Syntheses

All chemicals were of reagent grade and used without further purification. Elemental analyses (C, H, and N) were performed by Medac Ltd, Surrey, UK. The powder X-ray diffraction patterns were recorded on a Philips PW 1830 diffractometer equipped with a Cu $K\alpha$ X-ray source ($\bar{\lambda} = 1.54062 \text{ \AA}$) for the angular range $2\theta = 5\text{-}50^\circ$. The infrared spectra were measured on a Perkin Elmer Spectrum One and

Spectrum GX (400-4000 cm^{-1}) infrared spectrophotometer using pressed KBr pellets. The TGA analysis curves were recorded on a TGA Q5000 V2.4 Build 223 instrument a flow of air with a heating rate of 10 $^{\circ}\text{C min}^{-1}$.

3.2.2 Synthesis of Compound $(\text{en})\text{Zn}_2\text{V}_2\text{O}_7$ (**3a**) and $(\text{en})\text{Zn}(\text{VO}_3)_2$ (**3b**)

A mixture of 190 mg $\text{Zn}(\text{OAc})_2 \cdot 2\text{H}_2\text{O}$, 182 mg V_2O_5 , 0.10 mL en, and 2.00 mL H_2O in the approximate mole ratio of 1:1:1:111 was stirred in a 23 mL Teflon-lined cup for 30 minutes, sealed in an autoclave, and heated at 110 $^{\circ}\text{C}$ for 2 days. After the mixture was cooled to room temperature, the two different crystal morphologies of purple crystals (Figure 3.1) were filtered, washed with distilled H_2O , and dried in air at ambient temperature. Compound **3a**, $(\text{en})\text{Zn}_2\text{V}_2\text{O}_7$ (Krachodnok, Haller, and Williams, 2008), as the major product (100 mg, yield: ca 25% based on vanadium pentoxide) and compound **3b** as minor product (16 mg, yield: ca 5% based on vanadium pentoxide) were separated by hand under an optical microscope leaving the residual white powder of ZnO . The initial reaction pH was altered to 11-13 by addition of 0.5-1.0 mmol KOH. The yield of **3a** can be increased to ~69% (140 mg) in pure phase by substituting vanadium base (NH_4VO_3) for the vanadium acid (V_2O_5). Similar experiments with **3b** failed to improve the yield. If the initial reaction pH about 6-9, the orange-red crystals of $[\text{H}_2\text{en}]_3[\text{V}_{10}\text{O}_{28}] \cdot 2\text{H}_2\text{O}$ (Ninlaus, Riou, and Féray, 1996), and the colorless crystals of $[\text{H}_2\text{en}][\text{V}_2\text{O}_6]$ (Khan, Hope, Cevik, Zheng, and Powell, 2000), were isolated, respectively.

3.2.3 Synthesis of Compound $(\text{Hen})_2\text{Cd}(\text{VO}_3)_4$ (**3c**)

The procedure is similar to formation of **3a** and **3b**, using $\text{Cd}(\text{OAc})_2 \cdot 2\text{H}_2\text{O}$ instead of $\text{Zn}(\text{OAc})_2 \cdot 2\text{H}_2\text{O}$ with same mole ratio and heated at 110 $^{\circ}\text{C}$ for 2 days. After the mixture was cooled to room temperature, the dark green powder of $[\text{H}_2\text{en}]_{0.5}[\text{V}_2\text{O}_5]$

(Riou and Féray, 1995a,b; Zhang, Haushalter, and Clearfield, 1996) as a major product and the pale purple crystals of **3c** as a minor product were filtered, washed with distilled H₂O, and dried in air at ambient temperature with the yield of **3c** is 60 mg (ca 5% based on vanadium pentoxide), were separated by hand under an optical microscope leaving the residual dark green powder of [H₂en]_{0.5}[V₂O₅] (Riou and Féray, 1995a,b; Zhang, Haushalter, and Clearfield, 1996).

3.2.4 Synthesis of Compound (HenMe)₂Zn(V₂O₅)₄ (**3d**)

The procedure is similar to formation of **3a** and **3b** except enMe is used instead of en with an initial reaction pH of ~9 and heated at 180 °C or addition enMe 2-3 mmol and heated at 110 °C, the isolation of the pure phase of black crystals of compound **3d** (yield: 184 mg (ca 78%) and 201 mg (ca 85%), respectively, based on vanadium pentoxide). Either compound **3d** or K₂V₃O₈ (Galy and Carpy, 1975; Liu and Greedan, 1995) were formed by increasing the reaction pH to 11 by 1.0 mmol KOH and heated at 110 °C and 180 °C.

3.2.5 Synthesis of Compound (enMe)₂Zn(VO₃)₂·2H₂O (**3e**)

The procedure is similar to formation of **3d** except the amount of enMe was increased to 4-5 mmol with an initial reaction pH of ~11, heated at 110 °C for 2 days, cooled to room temperature, and the colorless solution kept at ambient temperature for two weeks to afford the pure pale brown crystals of compound **3e** (yield: 140 mg (ca 31%) based on vanadium pentoxide).

3.2.6 Powder X-ray Diffraction (XRD)

Figure 3.2 shows powder XRD patterns were recorded for the bulk sample of **3a** and **3b** compared to the simulated patterns of **3a**, **3b**, [H₂en][V₂O₆] (Khan, Hope, Cevik, Zheng, and Powell, 2000) and (en)₂ZnV₆O₁₄ (Zhang, DeBord, O'Connor,

Haushalter, Clearfield, and Zubieta, 1996) which were calculated from the single crystal X-ray structural results as a check that the bulk materials do not contain multiple phases in **3a** when using NH_4VO_3 substituted for V_2O_5 in Figure 3.2(i) and mixed phase **3a** and **3b** in Figure 3.2(f-g). Figures 3.3, 3.4 and 3.5 show powder XRD patterns were recorded for the bulk sample of **3c**, **3d** and **3e** compared to its simulated patterns which were calculated from the single crystal X-ray structural results as a check that the bulk materials do not contain multiple phases, respectively, and with comparable simulated patterns of the isomorphous $(\text{Hen})_2\text{Mn}(\text{VO}_3)_4$ structure (Law and Williams, 2000) with **3c** and the isostructural series between **3d** (space group $P2_1/c$) and $(\text{HenMe})_2\text{Cd}(\text{V}^{4+}\text{V}^{5+}\text{O}_5)_4$, space group $C2/m$ (Zhang, Shi, Yang, Chen, and Feng, 2000) as illustrated in Figures 3.3 and 3.4, respectively.

Table 3.1 Hydrothermal Synthetic Conditions.

Reagents (mmol)			Conditions		Product Colors
V ₂ O ₅	M(OAc) ₂ ·2H ₂ O	Organic Diamine	Initial and Final pH	Temperature and Times	(% Yield Based on V ₂ O ₅)
1	1 (Zn)	en	6-7 and 7	110-140 °C and 2d	Orange-red crystals of [H ₂ en] ₃ [V ₁₀ O ₂₈]·H ₂ O (Ninlaus et al., 1996)
1	1 (Zn)	en	9 and 8	110-140 °C and 2d	Colorless crystals of [H ₂ en][V ₂ O ₆] (Xu et al., 1996) and an uncharacterized green powder
1	1 (Zn)	en	11-13 ^b and 8-9	110 °C and 2d	Two different crystal morphologies of purple crystals (ca 25% for 3a and 5% for 3b) and white powder of ZnO
1 ^a	1 (Zn)	en	11-13 ^b and 8-9	110 °C and 2d	Purple crystal of 3a (ca 69%)
1	1 (Cd)	en	11 ^b and 7	110 °C and 2d	Pale purple crystals of 3c (ca 5%) and dark green powder of [H ₂ en] ₂ [V ₂ O ₅] (Riou and Féray, 1995b)
1	1 (Zn)	(5) en	10 and 10	110 °C and 2d	Black crystals of (en) ₂ ZnV ₆ O ₁₄ (Zhang et al., 1996)
1	1 (Zn)	enMe	9 and 8	180 °C and 2d	Black crystals of 3d (ca 78%)
1	1 (Zn)	enMe	11 ^b and 9	110 °C and 2d	Black crystals of K ₂ V ₃ O ₈ (Galy et al., 1975) (ca 60%) and black powder of 3d (ca 40%) and
1	1 (Zn)	enMe	11 ^b and 9	140 °C and 2d	Black crystals of K ₂ V ₃ O ₈ (ca 80%)
1	1 (Zn)	enMe	11 ^b and 9	180 °C and 2d	Black powder of 3d (ca 50%) and black crystals of K ₂ V ₃ O ₈ (ca 50%)
1	1 (Zn)	(2-3) enMe	10-11 and 8-9	110 °C and 2d	Black crystals of 3d (ca 85%)
1	1 (Zn)	(4-5) enMe	11 ^b and 9	110 °C and 2d	Colorless solution with standing at ambient for two weeks (pale-brown prism, 3e , ca 31%)

^aIncreasing the yield of **3a** by substituting NH₄VO₃ for V₂O₅. ^bAdjusted reaction pH by 0.50-1.0 mmol KOH.

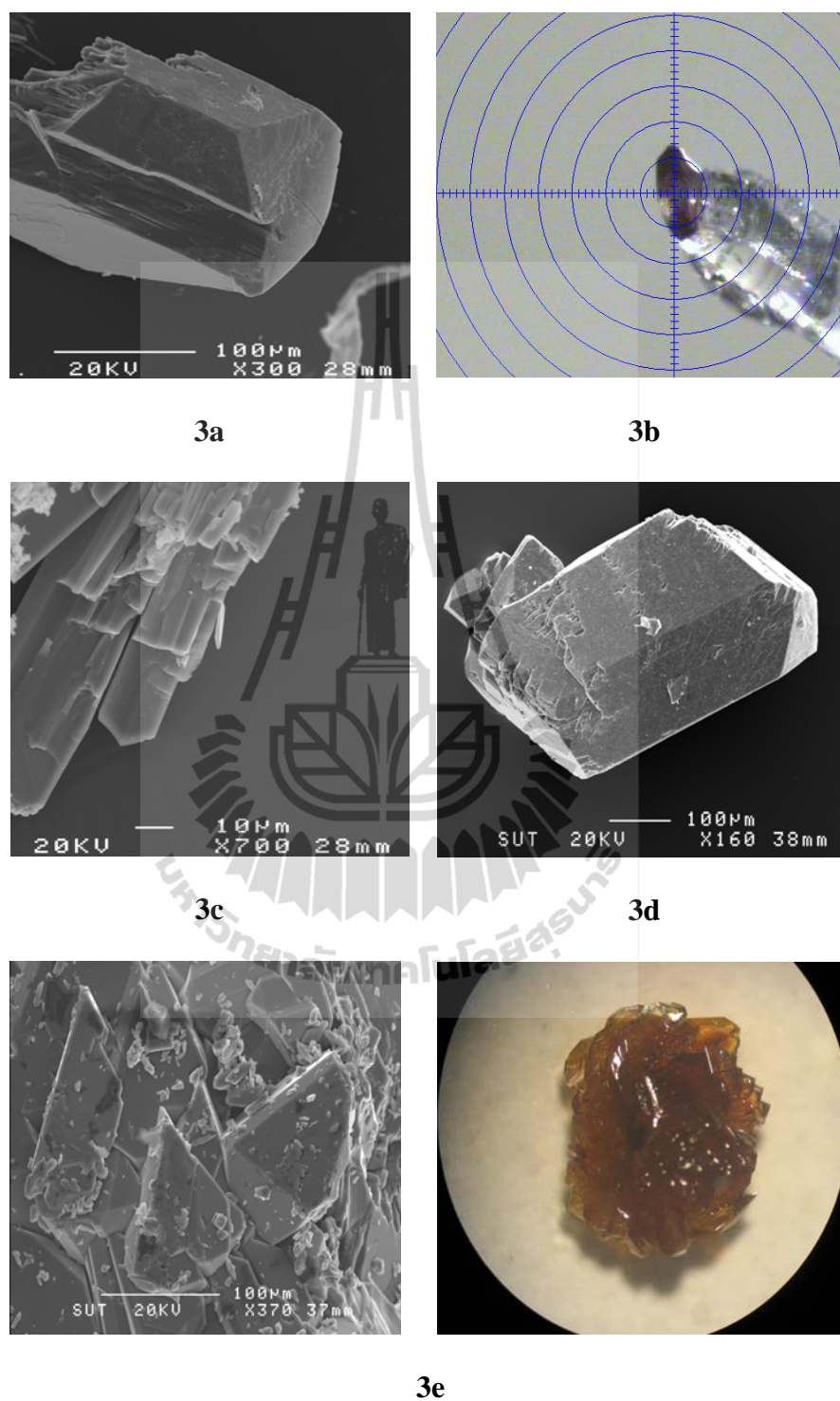


Figure 3.1 Crystal morphologies of compound 3a-e.

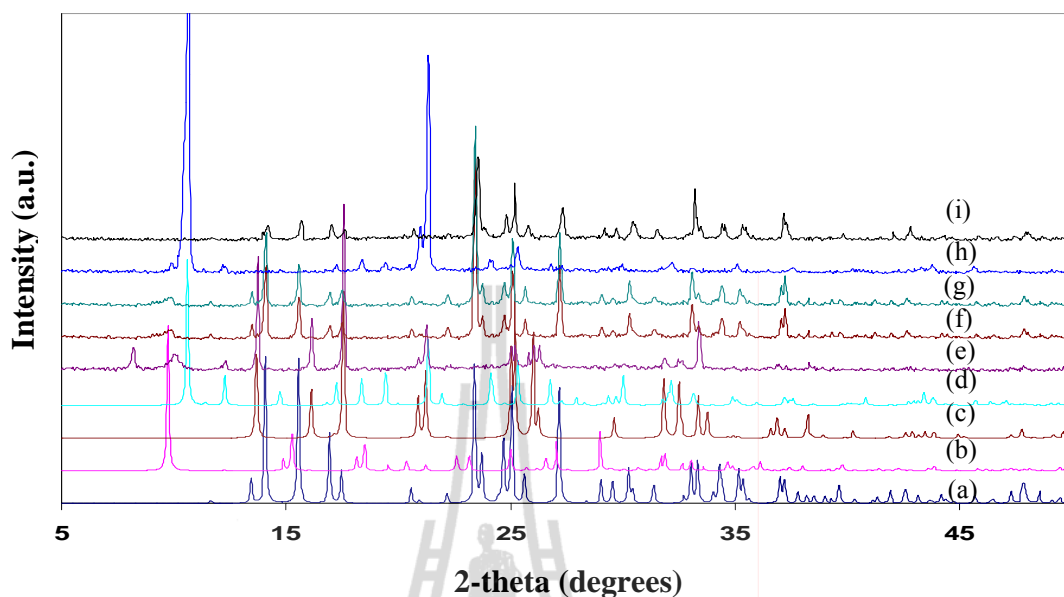


Figure 3.2 Comparing simulated powder XRD patterns of (a) **3a**, (b) **3b**, (c) $[\text{enH}_2][\text{V}_2\text{O}_6]$ (Xu, Yang, Wang, Ma, Sun, Xu, and Huang, 1996), and (d) $(\text{en})_2\text{ZnV}_6\text{O}_{14}$ (Zhang, DeBord, O'Connor, Haushalter, Clearfield, and Zubieta, 1996), with experimental powder XRD patterns of 1 mmol en at (e) pH 9, (f) pH 11 and (g) pH 13, and with (h) 5 mmol en at pH 9, and (i) substituted NH_4VO_3 for V_2O_5 .

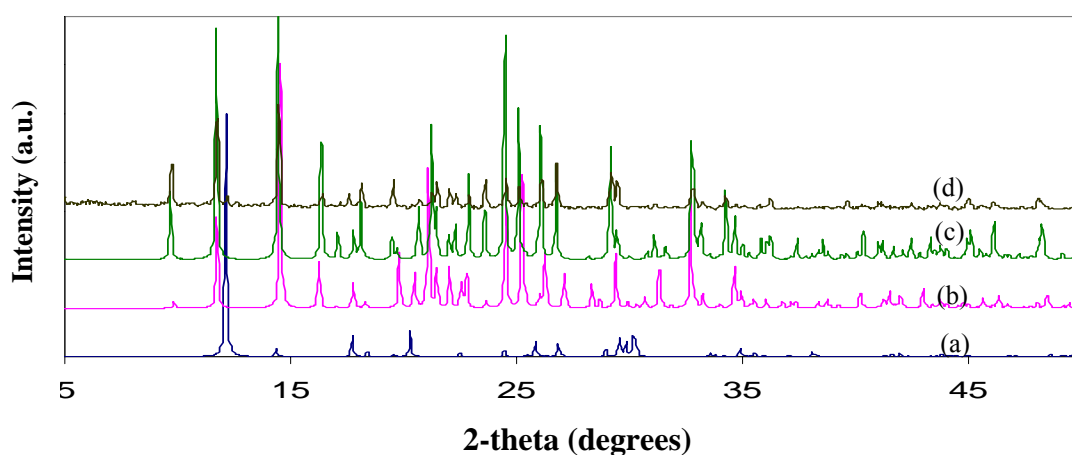


Figure 3.3 Comparing of (a) simulated $[\text{H}_2\text{en}]_{0.5}[\text{V}_2\text{O}_5]$ (Riou and Féray, 1995a,b) and (b) $(\text{Hen})_2\text{Mn}(\text{VO}_3)_4$ (Law and Williams, 2000) with (c) simulated and (d) experimental powder XRD patterns of **3c**.

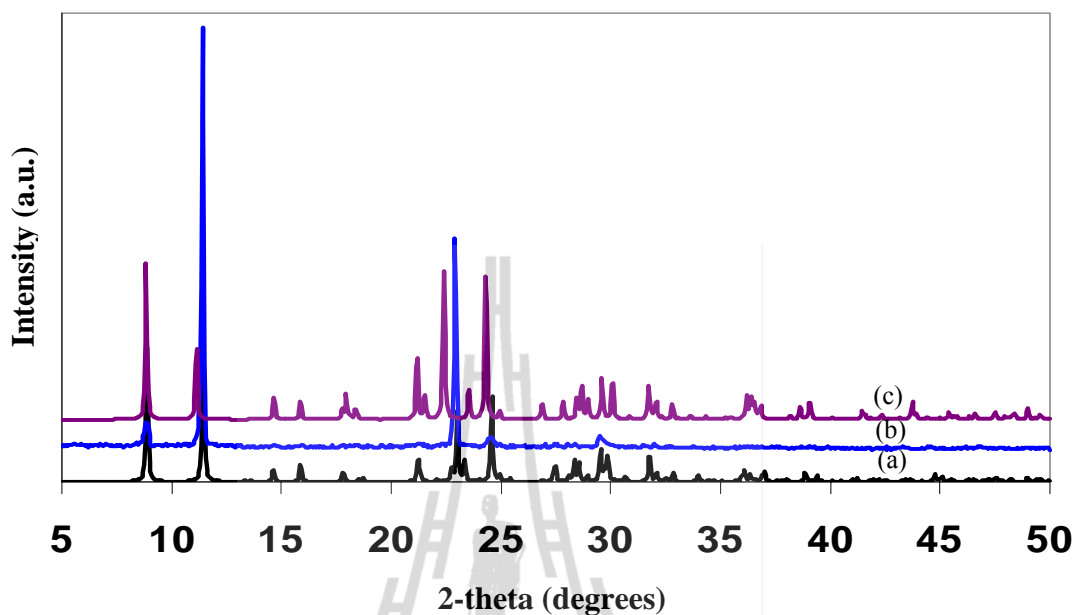


Figure 3.4 Comparing of (a) simulated and (b) experimental XRD patterns of **3d** (space group $P2_1/c$) with (c) simulated $(\text{HenMe})_2\text{Cd}(\text{V}^{4+}\text{V}^{5+}\text{O}_5)_4$ (space group $C2/m$) (Zhang, Shi, Yang, Chen, and Feng, 2000).

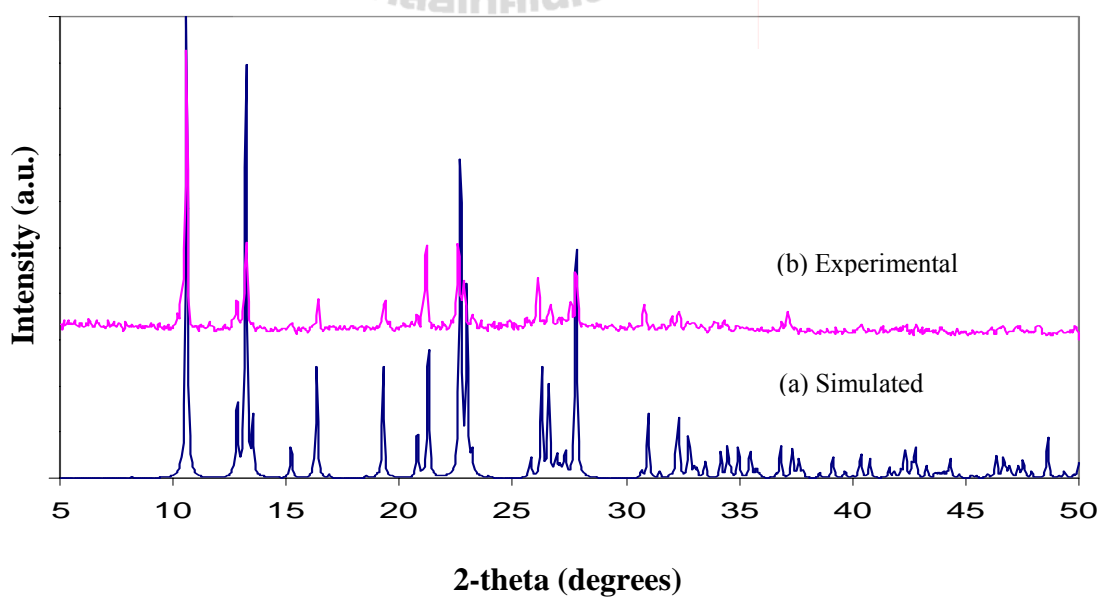


Figure 3.5 Comparing of (a) simulated and (b) experimental powder XRD patterns of **3e**.

3.2.7 X-Ray Crystallography

Suitable single crystals of the five compounds for single-crystal X-ray diffraction were selected and mounted on a thin glass fiber. Intensity data were collected at 25 ± 2 °C for **3a** and **3c** and at -173 ± 2 °C for **3b**, **3d** and **3e** on a Bruker-Nonius SMART APEX CCD diffractometer equipped with a graphite-monochromated Mo $K\alpha$ X-radiation source ($\bar{\lambda} = 0.71073$ Å). Unit cell parameters were determined by standard procedures and the data were processed with the program SAINT (Bruker, 2001a,b) and corrected for absorption and other geometrically related effects with SADABS (Bruker, 1998). Intensity data of compound **3c** was collected at 25 ± 2 °C on an Oxford Diffraction Kappa diffractometer equipped with a Cu $K\alpha$ X-radiation source ($\bar{\lambda} = 1.54184$ Å). The structures were solved by direct methods and refined by full-matrix least-squares refinement on F^2 using SHELXTL-97 (Sheldrick, 2000). Atoms C(2A) and C(2B) of [HenMe]⁺ in **3d** occupy disordered positions, each assigned an occupancy factor of 0.5. The [Hen]⁺ hydrogen atoms on N(1) and N(2) atoms in compound **3c** and the [HenMe]⁺ hydrogen atoms on N(1), C(1), and C(2) atoms in compound **3d** and all enMe hydrogen atoms in compound **3e**, except C6 were located from difference Fourier maps. The other hydrogen atoms were placed in calculated and idealized geometrical positions using geometrical constraints [C–H = 0.970 Å, for **3a**, **3c**, and **3d**; 0.980 Å for **3e**; 0.990 Å for **3b**, N–H = 0.900 Å for **3a** and **3d**; 0.920 Å for **3b** and $U_{\text{iso}}(\text{H}) = 1.2U_{\text{eq}}(\text{C}, \text{N})$]. Experimental X-ray data for **3a-e** are given in Table 3.2. Fractional coordinates and atomic displacement parameters are listed in Tables A1-A5 (Appendix A) and the selected bond lengths and bond angles are given in Tables 3.4-3.7, respectively. The summary of metal coordination geometries and bond valence sums are listed in Table 3.8. The images are illustrated

by *ORTEP-III* (Burnett and Johnson, 1996) and *DAIMOND* version 3.1 (Crystal Impact, 2006).

3.3 Results and Discussion

3.3.1 Hydrothermal Syntheses and Structural Analyses of Compound 3a-e

As progression of an organically templated manganese vanadate compounds in previous work, we have been continued to explore the inorganic-organic hybrid vanadates of V_2O_5 - $M(OAc)_2$ -organic diamines, $M = Zn$ and Cd under hydrothermal conditions as listed in Table 3.1.

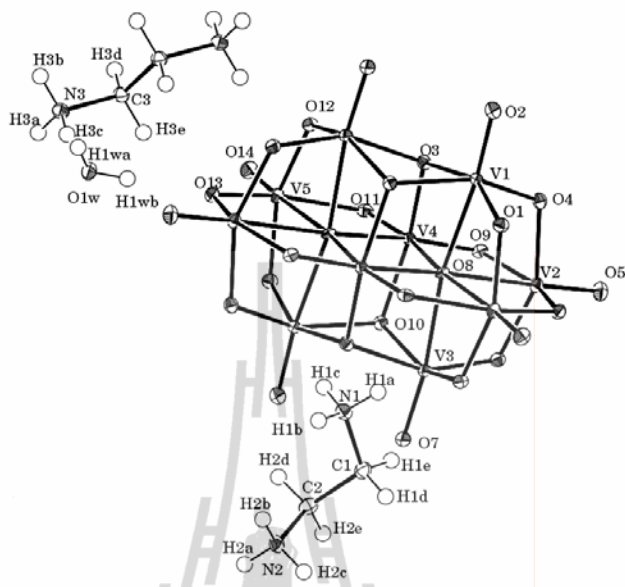
Study of the V_2O_5 - $M(OAc)_2$ -en system in a mole ratio 1:1:1 with the reaction pH ~6-9 and either heated at 110 °C or 140 °C, orange-red crystals, $[H_2en]_3[V_{10}O_{28}] \cdot 2H_2O$ (Ninlaus, Riou, and Féray, 1996), and colorless crystals, $[H_2en][V_2O_6]$ (Khan, Hope, Cevik, Zheng, and Powell, 2000), were isolated, respectively. Their crystal structures are illustrated in Figure 3.6. Increasing the reaction pH to ~11-13 and heating to 110 °C, two purple crystal morphologies of **3a** and **3b** were isolated in low yield. Substituting vanadium base (NH_4VO_3) for the vanadium acid (V_2O_5), the yield of **3a** increases to 69 % in pure phase by elemental analysis as listed in Table 3.10 and powder XRD patterns as shown in Figure 3.2, while the experiments of **3b** failed. Increasing the reaction temperature, the yield of **3a** decreased. In an excess of en, the black crystals, a 3-D mixed-valence metal nanoporous structure of $(en)_2Zn(V^{4+})_4(V^{5+})_2O_{14}$ with a 1-D rectangular channel of 4.90 x 10.27 Å (Zhang, DeBord, O'Connor, Haushalter, Clearfield, and Zubieta, 1996) as illustrated in Figure 3.7, and were formed in pure phase studied by powder XRD pattern as shown in Figure 3.2.

Table 3.2 X-ray Crystallographic Data of Compound **3a-e**.

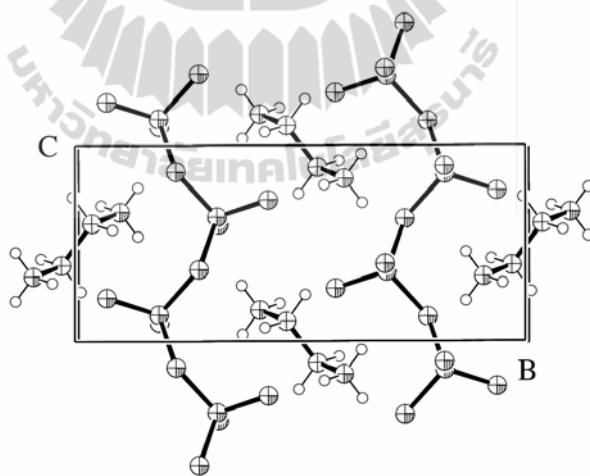
Compound	3a	3b	3c	3d	3e
Crystal data					
Chemical formula	C ₂ H ₈ N ₂ O ₇ V ₂ Zn ₂	C ₂ H ₈ N ₂ O ₆ V ₂ Zn	C ₄ H ₁₈ N ₄ O ₁₂ V ₄ Cd	C ₆ H ₂₂ N ₄ O ₂₀ V ₈ Zn	C ₆ H ₂₄ N ₄ O ₈ V ₂ Zn
M _r	404.72	323.35	630.38	943.17	447.49
Temperature (°C)	25±2	-173±2	25±2	-173±2	-173±2
Crystal system, space group	Monoclinic, <i>P2</i> ₁	Monoclinic, <i>P2</i> ₁ / <i>c</i>	Monoclinic, <i>P2</i> ₁ / <i>n</i>	Monoclinic, <i>P2</i> ₁ / <i>c</i>	Monoclinic, <i>C2</i>
Unit cell dimensions (Å, °)	<i>a</i> = 7.0885(7) <i>b</i> = 8.6040(9) <i>c</i> = 8.1869(8) <i>β</i> = 112.224(2)	<i>a</i> = 5.8422(6) <i>b</i> = 18.1421(18) <i>c</i> = 7.9208(8) <i>β</i> = 97.264(2)	<i>a</i> = 5.771(3) <i>b</i> = 18.171(6) <i>c</i> = 8.428(14) <i>β</i> = 101.43(8)	<i>a</i> = 6.177(3) <i>b</i> = 15.427(6) <i>c</i> = 13.255(5) <i>β</i> = 102.138(6)	<i>a</i> = 10.4919(7) <i>b</i> = 13.8172(7) <i>c</i> = 10.8550(6) <i>β</i> = 91.721(1)
Volume (Å ³)	462.22(8)	832.79(15)	866.2(15)	1234.8(9)	1572.93(16)
<i>Z</i>	2	4	2	2	4
<i>D</i> _{calc} (Mg m ⁻³)	2.908	2.579	2.417	2.537	1.09
Radiation type, wavelength (Å)	Mo, <i>Kα</i> , 0.71073	Mo, <i>Kα</i> , 0.71073	Cu, <i>Kα</i> , 1.54184	Mo, <i>Kα</i> , 0.71073	Mo, <i>Kα</i> , 0.71073
<i>θ</i> _{range} (°)	2.69-28.30	2.25-27.10	4.87-70.36	2.05-27.00	1.88-28.27
<i>μ</i> (mm ⁻¹)	7.103	5.054	27.756	3.931	2.717
Crystal form, color	Prism, Purple	Prism, Purple	Needle, Pale purple	Block, Black	Prism, Pale-brown
Crystal size (mm)	0.04x0.04x0.07	0.05x0.10x0.12	0.02x0.01x0.06	0.04x0.10x0.10	0.20x0.20x0.10
Data collection					
Diffractometer	Bruker-Nonius Smart Apex CCD	Bruker-Nonius Smart Apex CCD	Oxford Diffraction Kappa	Bruker-Nonius Smart Apex CCD	Bruker-Nonius Smart Apex CCD

Table 3.2 (Continued).

Compound	3a	3b	3c	3d	3e
Data collection method	ω scans	ω scans	ω scans	ω scans	ω scans
Absorption correction	Multi-scan	Multi-scan	Multi-scan	Multi-scan	Multi-scan
T_{max}, T_{min}	1.000, 0.759	–	–	–	1.000, 0.895
No. of measured, independent, and observed [$I > 2\sigma(I)$] reflections	4982, 2170, 1949	4713, 1830, 1623	3830, 1569, 1349	6630, 2650, 2149	9263, 3694, 3550
R_{int}	0.0367	0.0221	0.0713	0.0549	0.0231
θ_{max} (°)	28.30	27.10	70.36	27.00	28.27
Completeness to theta	97.8%(theta = 28.30)	99.0%(theta = 27.10)	95.0%(theta = 70.36)	98.5%(theta = 27.00)	97.5%(theta = 28.27)
Range of h, k, l	$-8 \leq h \leq 9,$ $-11 \leq k \leq 11,$ $-10 \leq l \leq 9$	$-7 \leq h \leq 5,$ $-23 \leq k \leq 22,$ $-7 \leq l \leq 10$	$-6 \leq h \leq 7,$ $-22 \leq k \leq 21,$ $-10 \leq l \leq 7$	$-7 \leq h \leq 7,$ $-12 \leq k \leq 19,$ $-16 \leq l \leq 16$	$-13 \leq h \leq 13,$ $-18 \leq k \leq 18,$ $-14 \leq l \leq 14$
Refinement	F^2	F^2	F^2	F^2	F^2
Refinement on	0.0291, 0.0559, 1.007	0.0238, 0.0603, 1.089	0.0648, 0.1866, 1.166	0.0746, 0.1822, 1.144	0.0298, 0.0726, 1.100
$R[F^2 > 2\sigma(F^2)], wR_2(F^2), S$	2170	1623	1569	2149	3550
No. of reflections	136	118	135	205	278
No. of parameters	Geometrically idealized	Geometrically idealized	Geometrically idealized	Geometrically idealized	Geometrically idealized
H-atom treatment	0.000	0.001	0.091	–	–
$(\Delta/\sigma)_{max}$	0.008(18)	–	–	–	0.151(13)
Absolute structure parameter	0.519, -0.591, 0.131	0.731, -0.575, 0.112	1.321, -1.922, 0.262	1.880, -1.372, 0.264	0.882, -0.392, 0.100
$\Delta\rho_{max, min, err}$ (e Å ⁻³)					



(a) $[\text{H}_2\text{en}]_3[\text{V}_{10}\text{O}_{28}] \cdot 2\text{H}_2\text{O}$ at $-173\text{ }^\circ\text{C}$.



(b) $[\text{H}_2\text{en}][\text{V}_2\text{O}_6]$ (Khan, Hope, Cevik, Zheng, and Powell, 2000).

Figure 3.6 Crystal structures of (a) decavanadate and (b) metavanadate.

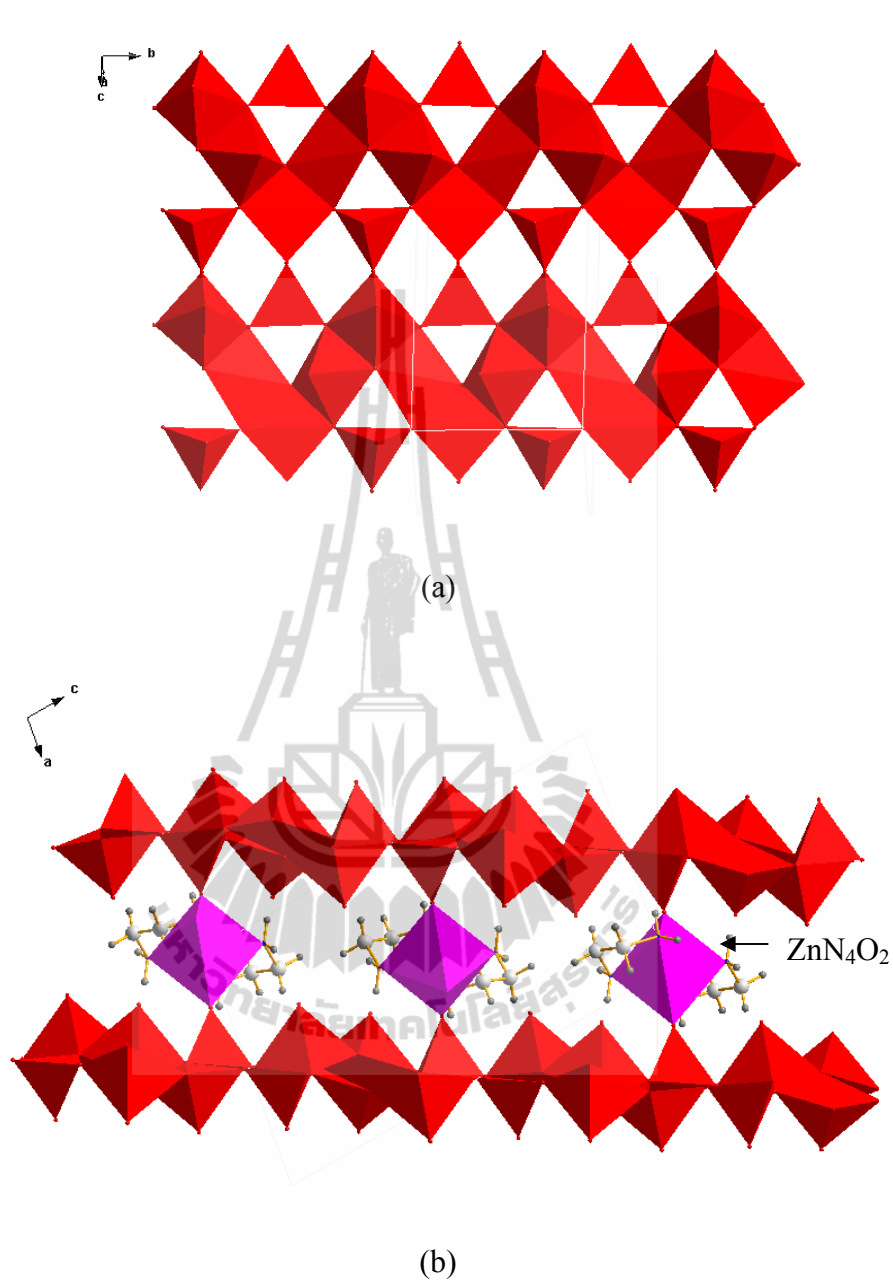


Figure 3.7 Polyhedral representations of (a) sheets perpendicular to the a axis and (b) ZnO_2N_4 pillars forming a 0-D rectangular channel along the b axis in $(en)_2ZnV_6O_{14}$ (Zhang, DeBord, O'Connor, Haushalter, Clearfield, and Zubieta, 1996).

The single crystal X-ray diffraction shows that compound **3a** and **3b** crystallize in the monoclinic system with chiral space group $P2_1$, the Flack absolute structure

parameter of -0.008(18) and with centrosymmetric space group $P2_1/c$, respectively. Both crystal structures are significant different.

3a, (en) $Zn_2V_2O_7$, is a 3-D chiral network. There are two crystallographically distinct V^{5+} atoms and two crystallographically distinct Zn^{2+} atoms in the structure of **3a** (Figure 3.8(a)). Both V^{5+} atoms have distorted tetrahedral geometries, in which the V–O bond lengths are in the range 1.649(5)-1.820(4) Å and the O–V–O bond angles are in the range 108.0(2)-112.3(2)°, with one corner shared with a neighbor forming a common $V_2O_7^{4-}$ dimer unit or pyrovanadate with a V(1)–O(1)–V(2) bond angle of 139.9(2)°. The comparison of the V–O–V bond angles to those pyrovanadate in literature are vary from 180° in (en) $Mn_2(V_2O_7)$ (Cao, Zheng, Fang, and Yang, 2010), to 149.3° in $Zn_2V_2O_7$ (Gopal and Calvo, 1973), to 143.0° in $K_2(VO)V_2O_7$ (Galy and Carpy, 1975), to 140.0° in $Mn_2V_2O_7$ (Gopal and Calvo, 1974), to 136.4° in $[H_2en][Mn_3(V_2O_7)_2(H_2O)_2]$ (Williams, Law, Sung, Wen, and Zhang, 2000) as well as to 136.9° in $K_2ZnV_2O_7$ and to 111.1° in $Ni_2V_2O_7$ (Sauerbrei, Faggiani, and Calvo, 1974). The pyrovanadate unit is also bound to seven separate zinc(II) complexes using one μ_3 -O(4) oxygen and five μ_2 -O(2,3,5,6,7) bridging atoms as shown in Figure 3.8(b). Three of the Zn^{2+} atoms exhibit distorted $Zn(1)O_3N$ tetrahedral geometries ($d[Zn-O]_{(av)} = 1.964$ Å, $d[Zn-N] = 2.014$ Å), and the other four exhibit less common distorted $Zn(2)O_4N$ trigonal bipyramidal geometries ($d[Zn-O]_{(av)} = 2.075$ Å, $d[Zn-N] = 2.015$ Å). The bond lengths and angles are listed in Table 3.3. The en ligand bridges adjacent Zn sites. The most interesting feature of **3a** is the helical structure formed from a –Zn(1)–en–Zn(2)–O(4)– outer strand (Type A helical coil made of seven atom repeating units) and a much tighter –V(2)–O(3)–Zn(2)–O(6)– inner strand (Type B helical coil made up of four atom repeating units) pinched together at the Zn

coordination centers and propagated by the two-fold screw axes parallel to the crystallographic *b*-axis at 0, *y*, ½ (O(6) atom). The approximate diameter and period of the helices are 7.089 and 8.604 Å, respectively (Figure 3.9(a)).

Surprisingly, the en in **3a** acts as a bridging ligand between two same metal sites with different coordination geometries, Zn tetrahedra-en-Zn trigonal bipyramid, and its flexibility is essential to form the observed helix while those previous structures, the en ligand prefers to act as pillars between the same metal sites with the same polyhedra, e.g. Zn tetrahedra-en-Zn tetrahedra in (en)₂Zn₄(SeO₃)₄ (Millange, Serre, Cabourdin, Marrot, and Férey, 2004), and Zn₄SO₄(OH)₆(en)_{0.5}·3H₂O and Zn₄SO₄(OH)₆(en)_{0.5}·18H₂O (Rujiwatra, Mander, Kepert, and Rosseinsky, 2005) or Mn octahedra-en-Mn octahedra in (en)Mn₂(V₂O₇) (Cao, Zheng, Fang, and Yang, 2010). This kind of polymeric helix has been rarely reported compared to those found in literature with similar composition, such as [Ni(en)₃][VO₃]₂ (Liu, Lin, and Lin, 2000) and [Co(en)₃][V₃O₉]·H₂O (Khan, Yohannes, Doedens, Golub, and O'Conner, 2005) which employ an optically active complex of D₃ symmetry, {M(en)₃}, with the en acting as a chelating ligand, and the complex as a chiral template. The neighboring helices are linked through alternation of μ₂-O(2) atom bridges to form an undulating sheet in Figure 3.9(b). Adjacent sheets are further interconnected by alternation of V(1)O₄ tetrahedra to form the 3-D network (Figure 3.10). The strength of the 3-D network is reinforced by N–H···O hydrogen bonding interactions (d[H···O] = 2.064-2.582 Å, ∠[N–H···O] = 135.6-166.1°).

Table 3.3 Selected Bond Lengths and Bond Angles (Å, °) for Compound **3a**.

Zn(1)–O(7) ⁱ	1.955(4)	V(1)–O(5)	1.649(4)
Zn(1)–O(4) ⁱⁱ	1.965(4)	V(1)–O(7)	1.666(3)
Zn(1)–O(2) ⁱⁱⁱ	1.972(3)	V(1)–O(4) ^{iv}	1.766(3)
Zn(1)–N(4)	2.014(4)	V(1)–O(1)	1.767(3)
Zn(2)–O(6)	1.961(3)	V(2)–O(3) ^v	1.649(4)
Zn(2)–O(4)	2.005(3)	V(2)–O(6) ⁱⁱ	1.685(3)
Zn(2)–N(1)	2.015(4)	V(2)–O(2)	1.705(3)
Zn(2)–O(5)	2.138(4)	V(2)–O(1)	1.820(4)
Zn(2)–O(3)	2.196(4)	N(1)–C(2)	1.474(6)
		C(2)–C(3)	1.502(6)
		C(3)–N(4)	1.496(6)
O(7) ⁱ –Zn(1)–O(4) ⁱⁱ	118.84(16)	O(7)–V(1)–O(4) ^{iv}	110.44(17)
O(7) ⁱ –Zn(1)–O(2) ⁱⁱⁱ	97.75(15)	O(5)–V(1)–O(1)	109.62(18)
O(4) ⁱⁱ –Zn(1)–O(2) ⁱⁱⁱ	103.01(14)	O(4) ^{iv} –V(1)–O(1)	109.41(16)
O(7) ⁱ –Zn(1)–N(4)	112.86(16)	O(3) ^v –V(2)–O(6) ⁱⁱ	112.28(17)
O(4) ⁱⁱ –Zn(1)–N(4)	114.56(17)	O(3) ^v –V(2)–O(2)	108.61(18)
O(2) ⁱⁱⁱ –Zn(1)–N(4)	106.96(15)	O(6) ⁱⁱ –V(2)–O(2)	109.94(16)
O(6)–Zn(2)–O(4)	113.25(14)	O(3) ^v –V(2)–O(1)	107.99(18)
O(6)–Zn(2)–N(1)	128.30(15)	O(6) ⁱⁱ –V(2)–O(1)	109.80(18)
O(4)–Zn(2)–N(1)	118.26(15)	O(2)–V(2)–O(1)	108.10(16)
O(6)–Zn(2)–O(5)	90.63(14)	V(1)–O(1)–V(2)	139.9(2)
O(4)–Zn(2)–O(5)	92.38(15)	V(2)–O(2)–Zn(1) ^{vi}	128.08(19)
N(1)–Zn(2)–O(5)	91.44(15)	V(2) ^{vii} –O(3)–Zn(2)	137.2(2)
O(6)–Zn(2)–O(3)	87.54(14)	V(1) ^{viii} –O(4)–Zn(1) ⁱ	121.27(19)
O(4)–Zn(2)–O(3)	83.66(14)	V(1) ^{viii} –O(4)–Zn(2)	122.70(18)
N(1)–Zn(2)–O(3)	93.72(15)	Zn(1) ⁱ –O(4)–Zn(2)	111.42(15)
O(5)–Zn(2)–O(3)	174.56(13)	V(1)–O(5)–Zn(2)	158.5(2)
O(5)–V(1)–O(7)	108.47(19)	V(2) ⁱ –O(6)–Zn(2)	144.0(2)
O(5)–V(1)–O(4) ^{iv}	109.15(18)	V(1)–O(7)–Zn(1) ⁱⁱ	140.5(2)
O(7)–V(1)–O(1)	109.73(18)		

Symmetry code: (i) $-x, y - 1/2, -z + 1$; (ii) $-x, y + 1/2, -z + 1$; (iii) $-x - 1, y - 1/2, -z + 1$; (iv) $-x + 1, y + 1/2, -z + 2$; (v) $x, y + 1, z$; (vi) $-x - 1, y + 1/2, -z + 1$; (vii) $x, y - 1, z$; (viii) $-x + 1, y - 1/2, -z + 2$.

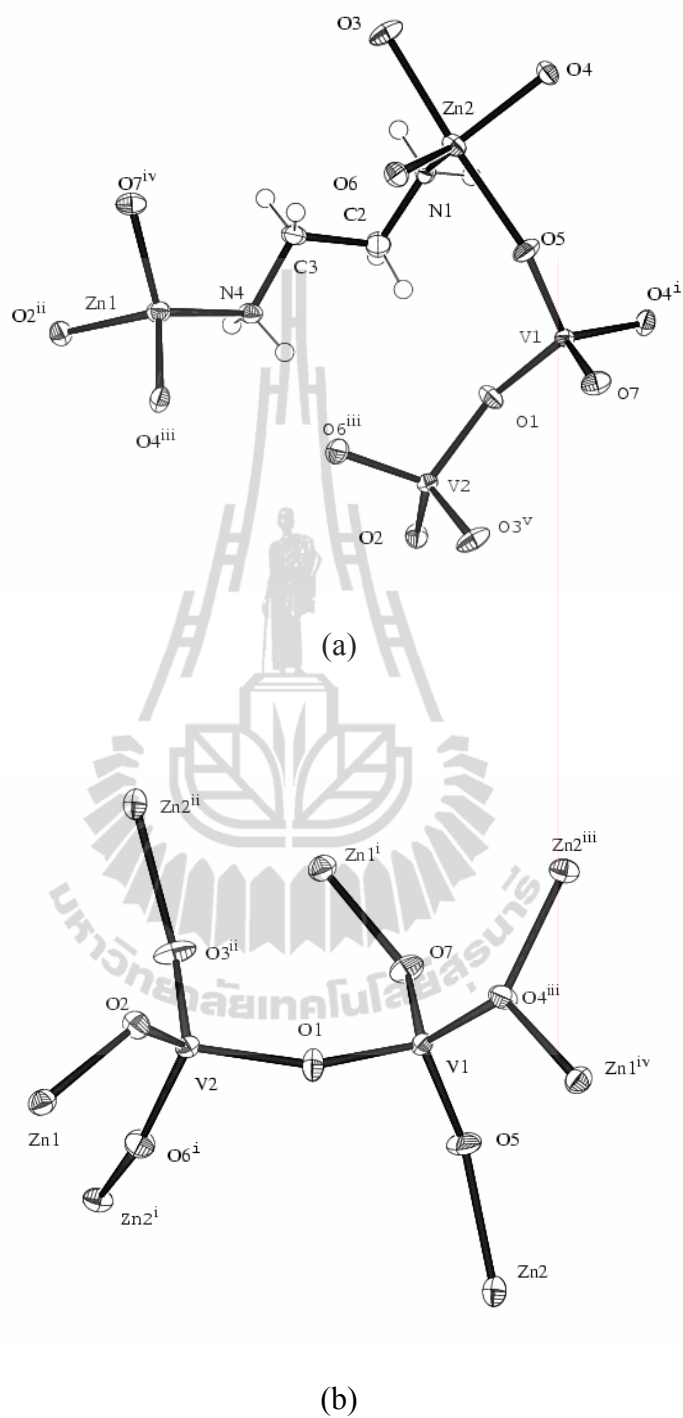


Figure 3.8 ORTEP drawing of (a) the coordination environments of the Zn and V atoms and (b) the pyrovanadate unit connected to zinc neighbors in **3a** with the atom labeling scheme and 50% thermal ellipsoids. Symmetry code: (i) $-x+1, y+1/2, -z+2$; (ii) $-x+1, y-1/2, -z+1$; (iii) $-x, y+1/2, -z+1$; (iv) $-x, y-1/2, -z+1$; (v) $x, y+1, z$.

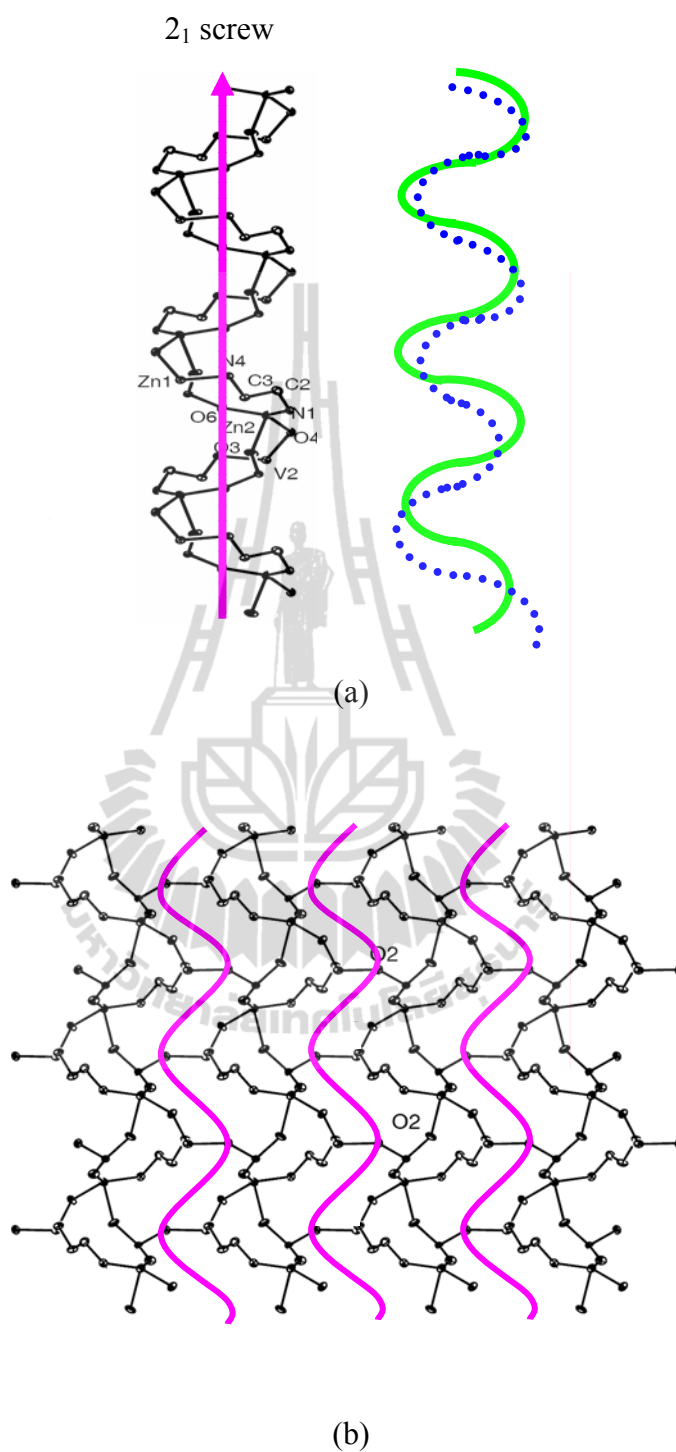


Figure 3.9 ORTEP view of (a) the helices, type A and B as solid and dashed lines, respectively, and an undulating sheet in **3a**, showing (b) the helices connected through μ_2 -O(2) atoms as solid lines, and (c) the packing of the undulating sheets perpendicular to the a axis, the chiral coordination axis, as dashed lines.

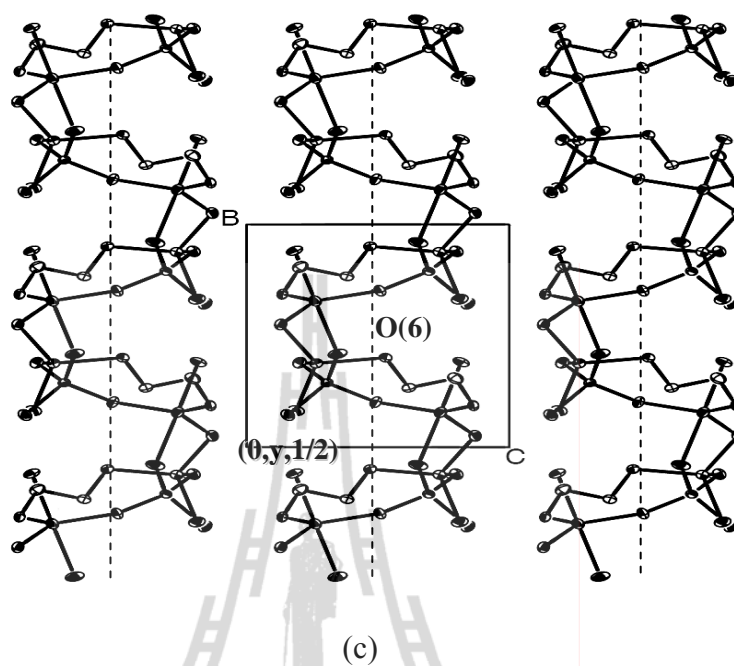


Figure 3.9 (Continued).

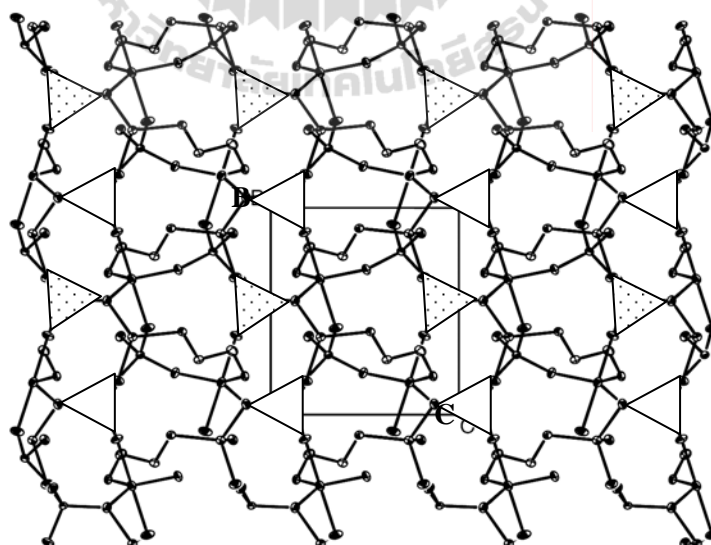


Figure 3.10 View of a 3-D chiral network in **3a** showing $V(1)O_4$ pillars (polyhedral highlight) interconnecting alternately to the undulating sheets above and below the current layer.

3b, (en)ZnV₂O₆, possesses a 2-D double layers. All V⁵⁺ atoms are common distorted tetrahedra coordinated by four O atoms, $d[\text{V}-\text{O}] = 1.612(2)\text{-}1.806(2)$ Å and $\angle[\text{O}-\text{V}-\text{O}] = 106.9(1)\text{-}114.3(1)^\circ$, two corners shared to neighbors forming a 1-D zig-zag polymeric metavanadate chains propagated along the *a* axis in which the bond V–O–V angles are in the range $130.6(1)\text{-}151.4(1)^\circ$ as are listed in Table 3.4. Although these angles are quite varied compared to those observed in the pyrovanadate unit in **3a**, $139.9(2)^\circ$, and discrete polymeric chains in [H₂en][V₂O₆], $132.5(1)^\circ$ (Khan, Hope, Cevik, Zheng, and Powell, 2000), [Co(en)₃][V₃O₉]·H₂O, $132.3(1)^\circ$ (Khan, Yohannes, Doedens, Golub and O’Conner, 2005), and [Ni(en)₃][VO₃]₂, $143.6(6)\text{-}165.9(5)^\circ$ (Liu, Lin and Lin, 2000), but these are smaller than those found the pyrovanadate unit in (en)Mn₂(V₂O₇), 180° (Cao, Zheng, Fang, and Yang, 2010). The Zn²⁺ site is a common distorted ZnO₄N₂ (4+2) octahedra ($d[\text{Zn}-\text{O}]_{(\text{av})} = 2.137$ Å, $d[\text{Zn}-\text{N}] = 2.085$ Å) which is coordinated from two different types of chelating at equatorial positions, a chelating V₂O₇⁴⁻ dimer units (each of repeating second V atoms) of the chains and a chelating en ligand, and the remaining of μ-O(5) and μ₃-O(2) atoms from other two neighbor chains coordinated at axial positions. The trans angle of O(2)–Zn(1)–O(5) of the oxo-group vanadate is $170.7(1)^\circ$ as shown in Figure 3.11. Figure 3.12 shows the chains linked through distorted ZnO₄N₂ octahedra forming 1-D doubly oxovanadate chains. Each Zn²⁺ site shares an edge with the neighbor through two atoms of two chelating divanadate (V₂O₇²⁻) units related by an inversion center forming 2-D double layers with $d[\text{Zn}\cdots\text{Zn}] = 3.206$ Å as observed in (en)CuV₂O₆ (DeBord, Zhang, Zubieta, and O’Connor, 1996). Each layer is held together via hydrogen bonding to generate a 3-D supramolecular framework that is given in Table 3.9.

Table 3.4 Selected Bond Lengths and Bond Angles (Å, °) for Compound **3b**.

Zn(1)–N(2)	2.073(2)	V(1)–O(4) ⁱ	1.8062(18)
Zn(1)–N(1)	2.097(2)	V(2)–O(5)	1.6437(18)
Zn(1)–O(6) ⁱ	2.1128(18)	V(2)–O(6)	1.6595(18)
Zn(1)–O(2)	2.1407(18)	V(2)–O(3)	1.7831(19)
Zn(1)–O(5) ⁱⁱ	2.1455(17)	V(2)–O(4)	1.7899(18)
Zn(1)–O(2) ⁱⁱⁱ	2.1473(17)	C(1)–N(1)	1.472(3)
V(1)–O(1)	1.6121(19)	C(1)–C(2)	1.515(4)
V(1)–O(2)	1.6953(18)	C(2)–N(2)	1.485(3)
V(1)–O(3)	1.7851(18)		
N(2)–Zn(1)–N(1)	84.10(9)	O(2)–V(1)–O(4) ⁱ	108.04(9)
N(2)–Zn(1)–O(6) ⁱ	99.79(8)	O(3)–V(1)–O(4) ⁱ	114.29(8)
N(1)–Zn(1)–O(6) ⁱ	173.66(8)	O(5)–V(2)–O(6)	110.56(10)
N(2)–Zn(1)–O(2)	173.78(8)	O(5)–V(2)–O(3)	111.19(9)
N(1)–Zn(1)–O(2)	89.77(8)	O(6)–V(2)–O(3)	110.65(9)
O(6) ⁱ –Zn(1)–O(2)	86.41(7)	O(5)–V(2)–O(4)	109.24(9)
N(2)–Zn(1)–O(5) ⁱⁱ	92.79(8)	O(6)–V(2)–O(4)	108.19(9)
N(1)–Zn(1)–O(5) ⁱⁱ	89.18(8)	O(3)–V(2)–O(4)	106.88(9)
O(6) ⁱ –Zn(1)–O(5) ⁱⁱ	85.65(7)	V(1)–O(2)–Zn(1)	119.77(9)
O(2)–Zn(1)–O(5) ⁱⁱ	88.22(7)	V(1)–O(2)–Zn(1) ⁱⁱⁱ	137.09(10)
N(2)–Zn(1)–O(2) ⁱⁱⁱ	96.12(8)	Zn(1)–O(2)–Zn(1) ⁱⁱⁱ	96.80(7)
N(1)–Zn(1)–O(2) ⁱⁱⁱ	94.28(8)	V(2)–O(3)–V(1)	151.39(12)
O(6) ⁱ –Zn(1)–O(2) ⁱⁱⁱ	90.29(7)	V(2)–O(4)–V(1) ^{iv}	130.63(11)
O(2)–Zn(1)–O(2) ⁱⁱⁱ	83.20(7)	V(2)–O(5)–Zn(1) ⁱⁱ	137.95(11)
O(5) ⁱ –Zn(1)–O(2) ⁱⁱⁱ	170.72(7)	V(2)–O(6)–Zn(1) ^{iv}	129.79(10)
O(1)–V(1)–O(2)	106.91(9)	N(1)–C(1)–C(2)	109.7(2)
O(1)–V(1)–O(3)	106.85(9)	N(2)–C(2)–C(1)	108.7(2)
O(2)–V(1)–O(3)	112.90(9)	C(1)–N(1)–Zn(1)	107.29(16)
O(1)–V(1)–O(4) ⁱ	107.47(9)	C(2)–N(2)–Zn(1)	107.28(16)

Symmetry code: (i) x+1,y,z; (ii) -x+1,y+1,-z; (iii) -x+2,-y+1,-z+1; (iv) x-1,y,z.

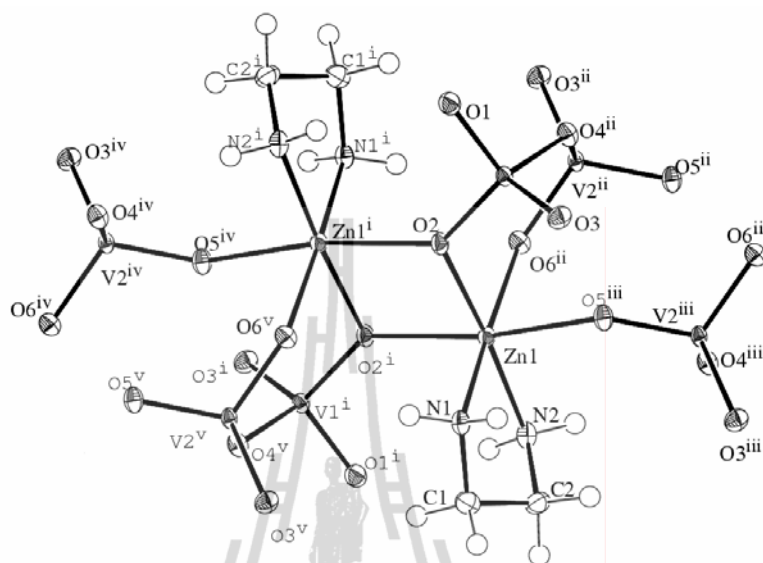


Figure 3.11 The structure of **3b**, showing the zinc dimer by edge sharing to its neighbor.

Symmetry code: (i) $2-x, 1-y, 1-z$; (ii) $1+x, y, z$; (iii) $1-x, 1-y, -z$; (iv) $1+x, y, 1+z$; (v) $1-x, 1-y, 1-z$.

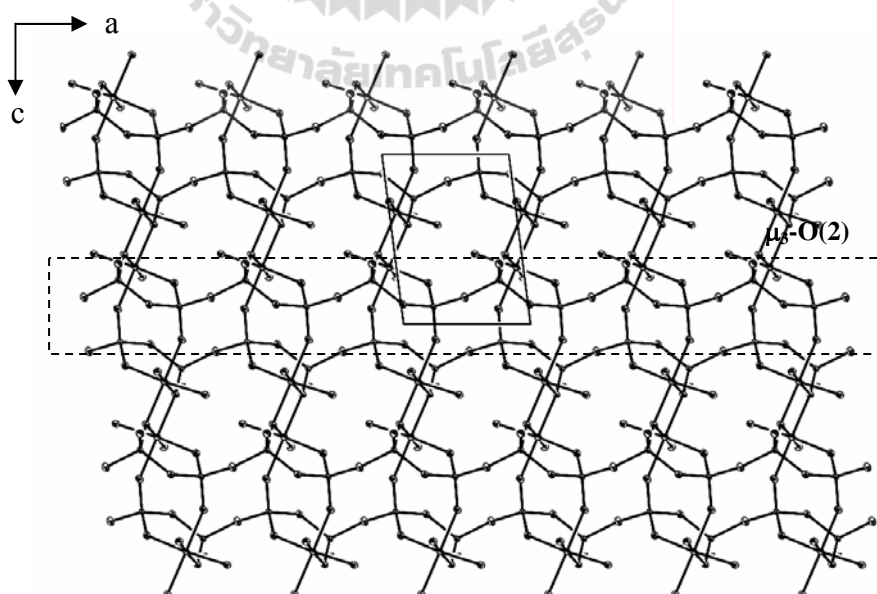


Figure 3.12 The double layered structure of **3b**, showing the double chains as a dashed line. The C and H atoms were omitted for clarity.

Substituting $\text{Cd}(\text{OAc})_2$ for $\text{Zn}(\text{OAc})_2$ in similar conditions to **3a** and **3b**, the pale purple crystals of **3c** were produced in low yield (*ca* 5%) with the dark green powder of $[\text{H}_2\text{en}]_{0.5}[\text{V}_2\text{O}_5]$ (Riou and Féray, 1995a,b) as confirmed by powder XRD patterns in Figure 3.3. The experiment of **3c** failed when the reaction pH and temperatures were varied to improve the yield.

The single X-ray structural analysis reveals that **3c**, $(\text{enH})_2\text{Cd}(\text{VO}_3)_4$, crystallizes in the monoclinic centrosymmetric space group, $P2_1/n$. **3c** is a 1-D double metavanadate chains propagated along the a axis. Each chain is composed of two corner sharing distorted VO_4 tetrahedra, $d[\text{V}-\text{O}] = 1.612(6)-1.820(6)$ Å, $\angle[\text{O}-\text{V}-\text{O}] = 107.3(4)-112.4(3)^\circ$, $\angle[\text{V}-\text{O}-\text{V}] = 129.9(3)-148.4(4)^\circ$, which these are very closed to **3b**. One of the two remaining O atoms of every two V atoms of each chain is linked to the Cd site at the equatorial positions combined with two protonated $[\text{Hen}]^+$ monocations axially coordinated to form a distorted CdO_4N_2 (4+2) octahedron, $d[\text{Zn}-\text{O}_{(\text{av})}] = 2.268$ Å, $d[\text{Zn}-\text{N}] = 2.327$ Å. The *trans* bond N–Cd–N angle is perfect linear, $180.0(1)^\circ$, in contrast to that of **3b**, $170.7(1)^\circ$. Metal complexes in this act as bridges which are located between two chains similar to that observed in $(\text{Hen})_2\text{Mn}(\text{VO}_3)_4$ (Law and Williams, 2000). Each double chain is held together by intramolecular $\text{N}(2)-\text{H}(2\text{C})\cdots\text{O}(1)$ and intermolecular $\text{N}(2)-\text{H}(2\text{A})\cdots\text{O}(4)$ hydrogen bond interactions forming a 2-D supramolecular layer as illustrated in Figure 3.13(b) and listed in Table 3.9.

Replacing enMe for en and using similar conditions to $\text{V}_2\text{O}_5-\text{M}(\text{OAc})_2-\text{en}$, a a mole ratio 1:1:1, an initial reaction pH of 9-11 and after heating at 110-180 °C, two black crystal morphologies of **3d** and $\text{K}_3\text{V}_3\text{O}_8$ (Galy and Carpy, 1975) were obtained. The yield of **3d** (*ca* 85%) has increased by adding 2-3 mmol of enMe and heating at

110 °C. Increasing the amount of enMe to 4-5 mmol, the pale-brown single crystals of **3e** were produced in pure phase which was confirmed by elemental analysis and powder XRD in Table 3.10 and Figures 3.4 and 3.5 for **3d** and **3e**, respectively.

Table 3.5 Selected Bond Lengths and Bond Angles (Å, °) for **3c**.

Cd(1)–N(1) ⁱ	2.268(7)	V(1)–O(5)	1.806(6)
Cd(1)–N(1)	2.268(7)	V(2)–O(6)	1.623(7)
Cd(1)–O(2)	2.324(6)	V(2)–O(2)	1.653(6)
Cd(1)–O(2) ⁱ	2.324(6)	V(2)–O(3) ⁱⁱ	1.796(6)
Cd(1)–O(1)	2.330(6)	V(2)–O(5)	1.820(6)
Cd(1)–O(1) ⁱ	2.330(6)	N(1)–C(1)	1.464(11)
V(1)–O(4)	1.612(6)	N(2)–C(2)	1.485(10)
V(1)–O(1)	1.672(6)	C(1)–C(2)	1.522(11)
V(1)–O(3)	1.767(6)		
N(1) ⁱ –Cd(1)–N(1)	180.000(1)	O(4)–V(1)–O(1)	107.3(4)
N(1) ⁱ –Cd(1)–O(2)	88.6(3)	O(4)–V(1)–O(3)	109.8(3)
N(1)–Cd(1)–O(2)	91.4(3)	O(1)–V(1)–O(3)	109.4(3)
N(1) ⁱ –Cd(1)–O(2) ⁱ	91.4(3)	O(4)–V(1)–O(5)	109.6(3)
N(1)–Cd(1)–O(2) ⁱ	88.6(3)	O(1)–V(1)–O(5)	109.9(3)
O(2)–Cd(1)–O(2) ⁱ	180.0(3)	O(3)–V(1)–O(5)	110.8(3)
N(1) ⁱ –Cd(1)–O(1)	91.9(2)	O(6)–V(2)–O(2)	108.4(3)
N(1)–Cd(1)–O(1)	88.1(2)	O(6)–V(2)–O(3) ⁱⁱ	109.1(3)
O(2)–Cd(1)–O(1)	85.4(2)	O(2)–V(2)–O(3) ⁱⁱ	107.9(3)
O(2) ⁱ –Cd(1)–O(1)	94.6(2)	O(6)–V(2)–O(5)	110.4(3)
N(1) ⁱ –Cd(1)–O(1) ⁱ	88.1(2)	O(2)–V(2)–O(5)	108.5(3)
N(1)–Cd(1)–O(1) ⁱ	91.9(2)	O(3) ⁱⁱ –V(2)–O(5)	112.4(3)
O(2)–Cd(1)–O(1) ⁱ	94.6(2)	V(1)–O(1)–Cd(1)	128.4(3)
O(2) ⁱ –Cd(1)–O(1) ⁱ	85.4(2)	V(2)–O(2)–Cd(1)	139.9(3)
O(1)–Cd(1)–O(1) ⁱ	180.0(3)	V(1)–O(3)–V(2) ⁱⁱⁱ	148.4(4)
		V(1)–O(5)–V(2)	129.8(3)

Symmetry code: (i) $-x, -y, -z+1$; (ii) $x+1, y, z$; (iii) $x-1, y, z$.

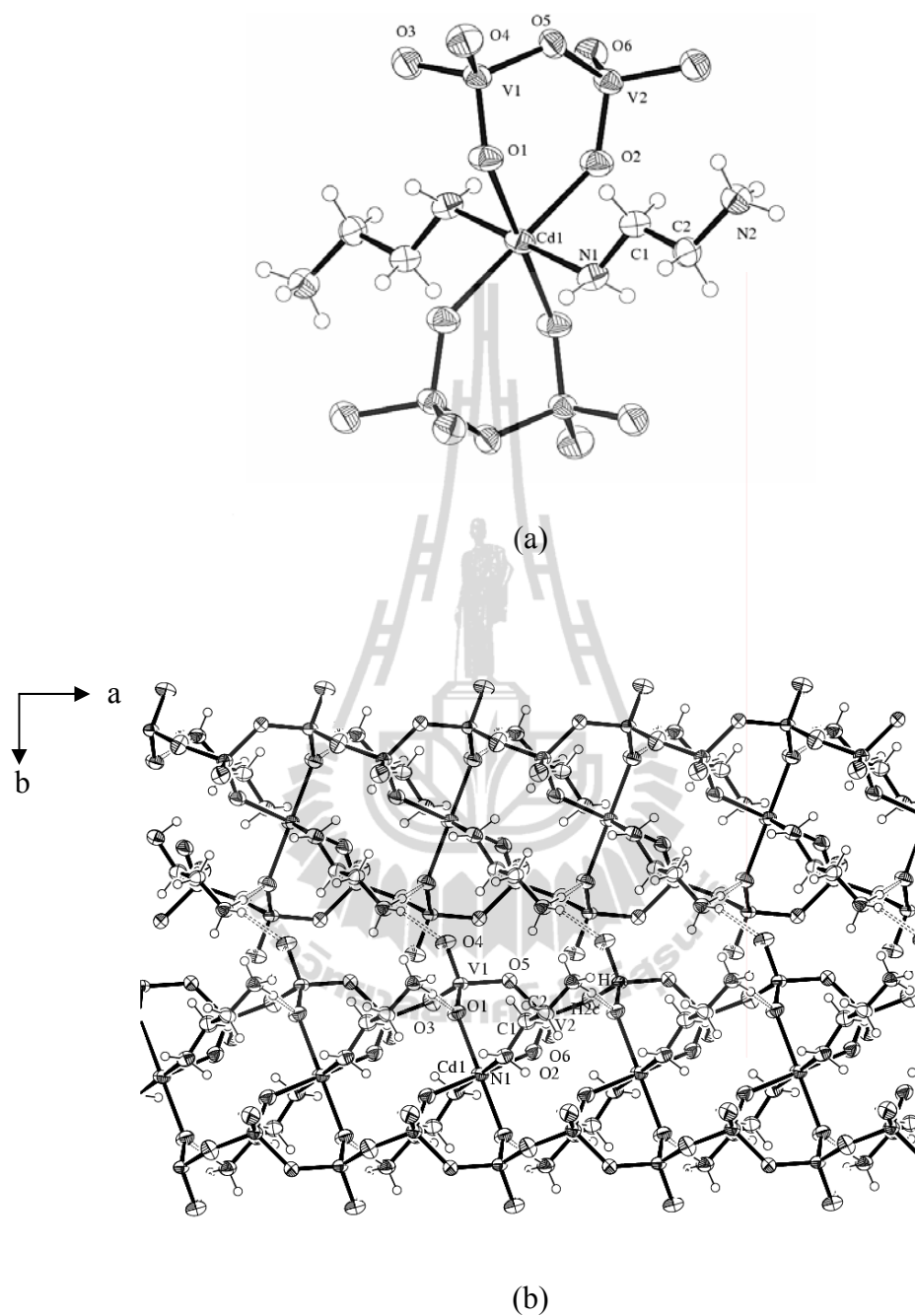


Figure 3.13 The structure of **3c**, showing (a) the Cd coordination geometry and (b) 1-D the double chain projected on the *ab* plane includes the labeling of the atoms with 50% probability displacement ellipsoids. The hydrogen bond interactions are as shown dashed lines.

Table 3.6 Selected Bond Lengths and Bond Angles (\AA , $^\circ$) for **3d**.

Zn(1)–O(10) ⁱ	2.083(6)	V(3)–O(4) ⁱⁱⁱ	1.917(7)
Zn(1)–O(10)	2.083(6)	V(3)–O(6) ⁱⁱⁱ	1.943(7)
Zn(1)–O(1)	2.107(6)	V(3)–O(8)	1.956(7)
Zn(1)–O(1) ⁱ	2.107(6)	V(3)–O(5) ⁱⁱ	2.020(6)
Zn(1)–N(1)	2.141(10)	V(4)–O(10) ^{iv}	1.644(7)
Zn(1)–N(1) ⁱ	2.141(10)	V(4)–O(9)	1.680(7)
V(1)–O(1)	1.666(7)	V(4)–O(4)	1.721(6)
V(1)–O(6)	1.684(7)	V(4)–O(8) ^v	1.817(7)
V(1)–O(7)	1.710(6)	N(1)–C(1)	1.466(14)
V(1)–O(5)	1.827(6)	N(2)–C(2B)	1.47(3)
V(2)–O(2)	1.590(7)	N(2)–C(2A)	1.498(17)
V(2)–O(7)	1.920(7)	C(1)–C(2A)	1.444(19)
V(2)–O(9)	1.938(7)	C(1)–C(2B)	1.55(3)
V(2)–O(5) ⁱⁱ	1.953(6)	C(2A)–C(3)	1.518(18)
V(2)–O(8)	2.019(7)	C(2B)–C(3)	1.58(3)
V(3)–O(3)	1.598(7)	C(2A)–C(2B)	0.97(3)
O(10) ⁱ –Zn(1)–O(10)	180.0(3)	V(4)–O(4)–V(3) ^{vi}	136.1(4)
O(10) ⁱ –Zn(1)–O(1)	94.0(3)	V(1)–O(5)–V(2) ^{vii}	129.5(3)
O(10)–Zn(1)–O(1)	86.0(3)	O(1)–V(1)–O(6)	109.5(3)
O(10)–Zn(1)–O(1) ⁱ	94.0(3)	O(1)–V(1)–O(7)	107.3(3)
O(1)–Zn(1)–O(1) ⁱ	180.000(3)	O(6)–V(1)–O(7)	111.3(3)
O(10) ⁱ –Zn(1)–N(1)	90.5(4)	O(1)–V(1)–O(5)	109.1(3)
O(10)–Zn(1)–N(1)	89.5(4)	O(6)–V(1)–O(5)	111.5(3)
O(1)–Zn(1)–N(1)	86.7(4)	O(7)–V(1)–O(5)	108.0(3)
O(1) ⁱ –Zn(1)–N(1)	93.3(4)	O(2)–V(2)–O(7)	113.7(3)
O(10) ⁱ –Zn(1)–N(1) ⁱ	89.5(4)	O(2)–V(2)–O(9)	101.9(3)
O(1)–Zn(1)–N(1) ⁱ	93.3(4)	O(7)–V(2)–O(9)	86.5(3)
N(1)–Zn(1)–N(1) ⁱ	180.000(4)	O(2)–V(2)–O(5) ⁱⁱ	114.0(3)
O(10) ^{iv} –V(4)–O(9)	110.8(3)	O(7)–V(2)–O(5) ⁱⁱ	131.7(3)
O(10) ^{iv} –V(4)–O(4)	105.8(3)	O(9)–V(2)–O(5) ⁱⁱ	90.6(3)
O(9)–V(4)–O(4)	111.4(3)	O(2)–V(2)–O(8)	101.6(3)
O(10) ^{iv} –V(4)–O(8) ^v	109.5(3)	O(7)–V(2)–O(8)	87.1(3)
O(9)–V(4)–O(8) ^v	112.1(3)	O(9)–V(2)–O(8)	156.2(3)
O(4)–V(4)–O(8) ^v	107.0(3)	O(5) ⁱⁱ –V(2)–O(8)	76.8(3)
V(1)–O(1)–Zn(1)	138.6(4)		

Symmetry code: (i) $-x, -y+2, -z+2$; (ii) $x+1, y, z$; (iii) $x+1, -y+3/2, z+1/2$; (iv) $-x+1, -y+2, -z+2$; (v) $x, -y+3/2, z-1/2$; (vi) $x-1, -y+3/2, z-1/2$; (vii) $x-1, y, z$.

The single crystal X-ray structural analysis shows that **3d**, $\text{Zn}(\text{HenMe})_2\text{V}_8\text{O}_{20}$ or $(\text{HenMe})_2\text{Zn}(\text{V}^{4+}\text{O})_4(\text{V}^{5+}\text{O}_4)_4$, and **3e**, $(\text{enMe})_2\text{Zn}(\text{VO}_3)_2 \cdot 2\text{H}_2\text{O}$, crystallize in the monoclinic centrosymmetric space group, $P2_1/c$ and the chiral space group, $C2$, respectively.

The structure of **3d** is an open 3-D framework structure built up from anionic mixed-valence $\text{V}^{4+}/\text{V}^{5+}$ polyoxovanadate sheets pillared with ZnO_4N_2 octahedra. The sheets are constructed by a combination of equal numbers of V^{5+}O_4 tetrahedra and V^{4+}O_5 square pyramids. While the V^{5+}O_4 tetrahedra are isolated from each other, the V^{4+}O_5 square pyramids exist as edge-sharing pairs linked to the corners of six V^{5+}O_4 tetrahedra to generate 2-D layers perpendicular to the b axis as shown in Figure 3.14. Within a pair of square pyramids, the two apical oxygen atoms are oriented towards opposite sides of the plane of the layer as has been observed in $(\text{HenMe})_2\text{CdV}^{4+}_4\text{V}^{5+}_4\text{O}_{20}$ (Zhang, Shi, Yang, Chen, and Feng, 2000), $[\text{H}_2\text{en}]_{0.5}[(\text{V}^{4+}\text{O})(\text{V}^{5+}\text{O}_4)]$ and $[\text{H}_2\text{pn}]_{0.5}[(\text{V}^{4+}\text{O})(\text{V}^{5+}\text{O}_4)]$ (Riou and Féray, 1995a,b; Zhang, Haushalter, and Clearfield, 1996), and $\text{Cs}[(\text{V}^{4+}\text{O})(\text{V}^{5+}\text{O}_4)]$ (Mumme and Watts, 1971). The layers of these compounds have the same connections of polyhedra but the relative orientations are different.

The oxide layers of this compound show rows of square pyramids units disposed alternately up/down-down/up as in $(\text{HenMe})_2\text{CdV}^{4+}_4\text{V}^{5+}_4\text{O}_{20}$ as can be seen in the left to right progression on Figure 3.16(a). In the other compounds the progression always has the square pyramids pairs arranged down/up. The orientations of the tetrahedra can be examined relative to these progressions of the square pyramids pairs. In the current compound and $(\text{HenMe})_2\text{CdV}^{4+}_4\text{V}^{5+}_4\text{O}_{20}$, the tetrahedral are arranged up-up-down-down, while in $[\text{enH}_2]_{0.5}[(\text{V}^{4+}\text{O})(\text{V}^{5+}\text{O}_4)]$ and $[\text{H}_2\text{pn}]_{0.5}[(\text{V}^{4+}\text{O})(\text{V}^{5+}\text{O}_4)]$ they are up and down alternately, and in $\text{Cs}[(\text{V}^{4+}\text{O})(\text{V}^{5+}\text{O}_4)]$,

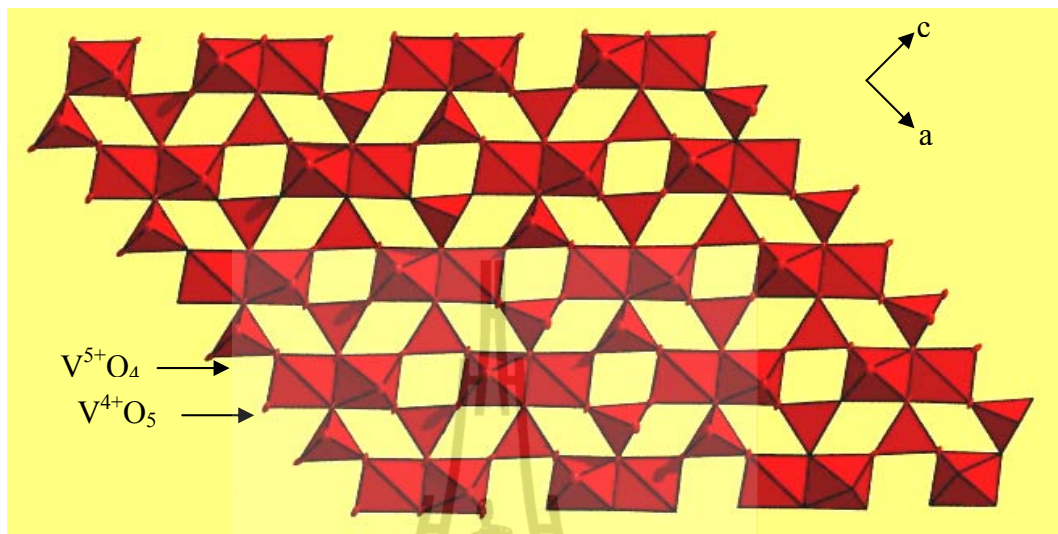


Figure 3.14 Polyhedral representation of sheets perpendicular to the b axis in $3d$.

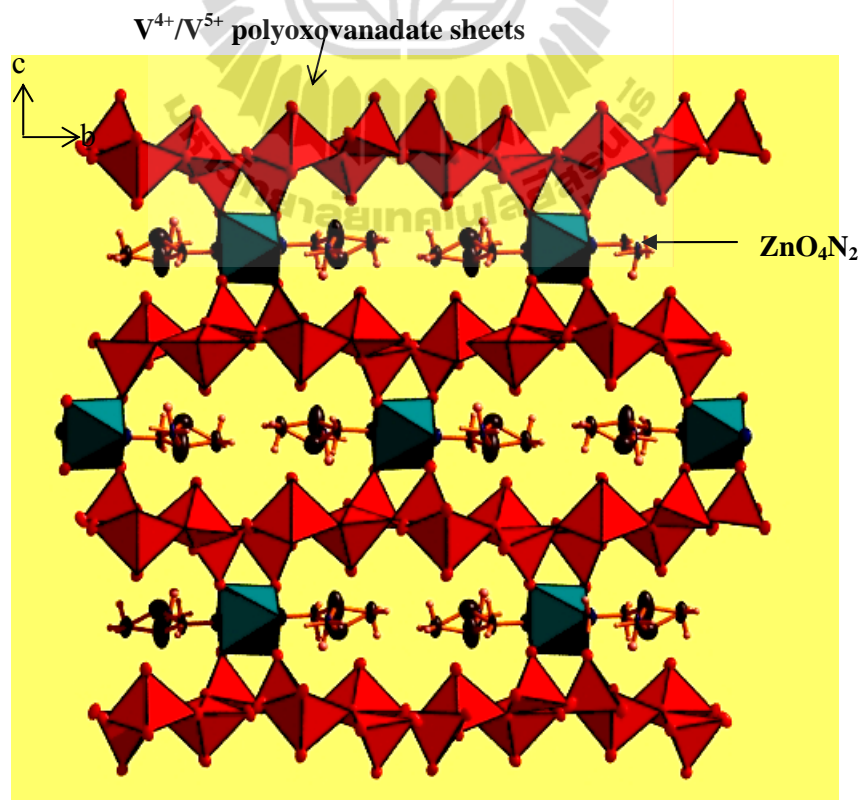
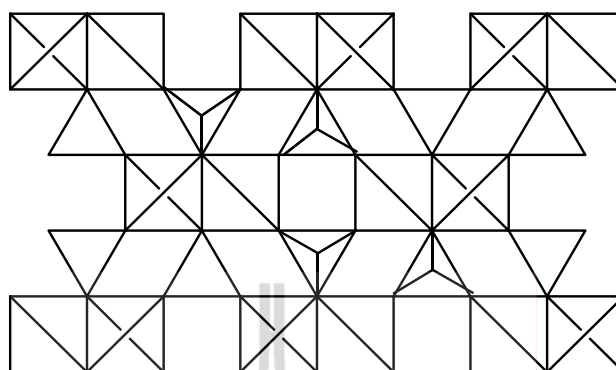


Figure 3.15 Perspective diagram showing ZnO_4N_2 pillars forming 0-D rectangular channels along the a axis in $3d$.

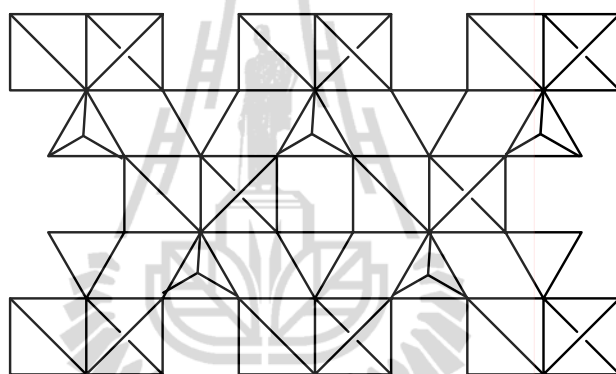
they are alternately all up or all down in any given horizontal progression as shown in Figures 3.16(b) and 3.16(c), respectively. Two out-of-plane oxygen atoms from V^{5+} tetrahedra on each of the two adjacent polyoxovanadate layers are strongly linked to zinc centers with an average distance of 2.095(6) Å to generate a 3-D nanoporous structure with 1-D rectangular channels of 3.97 x 11.65 Å along the *a* axis. The channels are bounded by 10-membered $[Zn_2V_8O_{10}]$ rings, made up of 10 corner-shared polyhedra and filled with a protonated $[HenMe]^+$ ligand (Figure 3.15).

As seen in Table 3.8 below, two V^{5+} atoms realize tetrahedral geometry coordinated with normal bond distances and angles. Two V^{4+} atoms have distorted square pyramidal geometries coordinated with a vanadyl group in the apex at a distance of 1.590(7)-1.598(7) Å, and four oxygen atoms in the base at distances of 1.917(7)-2.029(7) Å. The Zn(1) atom has an octahedral configuration with four equatorial oxygen atoms from the oxo-group of the vanadate layers and two axial nitrogen atoms from $[HenMe]^+$ monocations with distances of 2.095(6) Å and 2.141(10) Å, respectively.

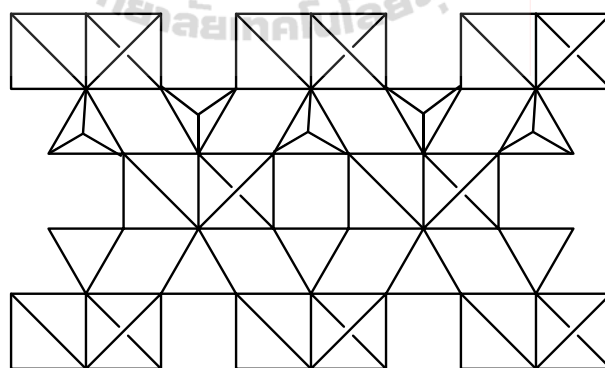
The stability of an open 3-D framework depends on the strength of the interactions within framework. Hydrogen atoms on N(1), N(2), and C(1) atoms of the protonated $HenMe^+$ monodentate ligands hydrogen bond to O(1), O(4), O(7), and O(10) oxygen atoms of $V^{5+}O_4$ tetrahedra and apical O(2) and O(3) oxygen atoms of $V^{4+}O_5$ square pyramids of adjacent vanadium oxide sheets above and below form $H\cdots O$ hydrogen bonds in the range of 2.11-2.62 Å as shown in Figure 3.17 and listed in Table 3.9.



(a) **3d** and $\text{Cd}(\text{HenMe})_2\text{V}^{4+}_4\text{V}^{5+}_4\text{O}_{20}$



(b) $[\text{H}_2\text{en}]_{0.5}[(\text{V}^{4+}\text{O})(\text{V}^{5+}\text{O}_4)]$ and $[\text{H}_2\text{pn}]_{0.5}[(\text{V}^{4+}\text{O})(\text{V}^{5+}\text{O}_4)]$



(c) $\text{Cs}[(\text{V}^{4+}\text{O})(\text{V}^{5+}\text{O}_4)]$

Figure 3.16 Comparing the relative orientation of square pyramids and tetrahedra on layers with/without mark represent up and down, respectively.

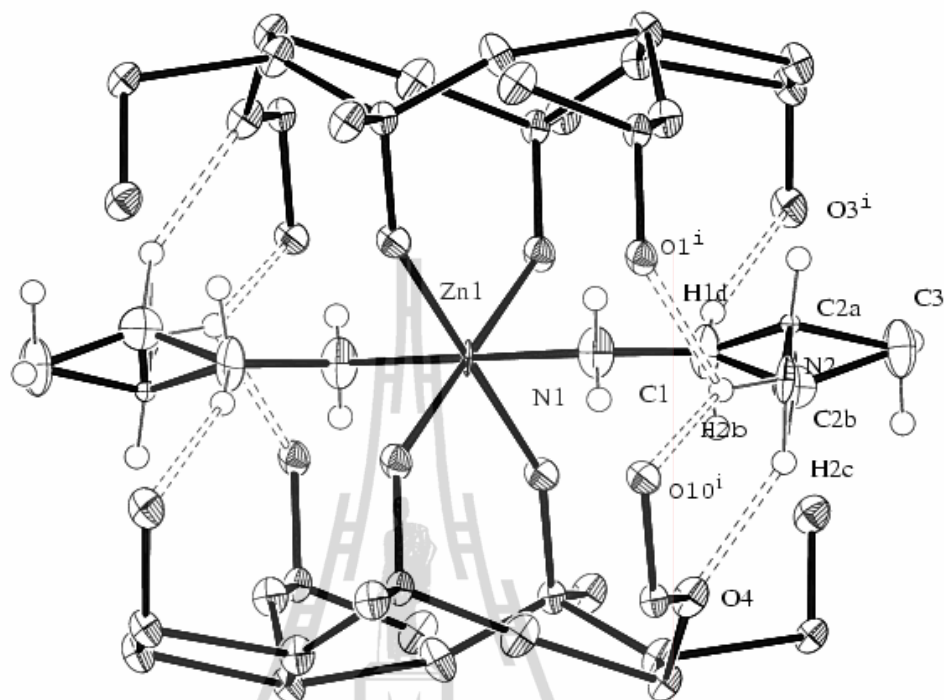


Figure 3.17 Hydrogen bond interactions in 1-D rectangular channels of **3d**. Symmetry codes: (i) $-x+1, -y, -z$.

3e, $(\text{enMe})_2\text{Zn}(\text{VO}_3)_2 \cdot 2\text{H}_2\text{O}$, is an open 3-D framework consists of the polymeric metavanadate chains of corner-sharing VO_4 tetrahedra, two corners of each tetrahedra are shared with neighbors propagating along the c axis, with the chain repeating units are two up and two down while those chains in **3a** and **3c** are repeating are one up and one down. The chains and neighbors are interconnected by ZnO_2N_4 octahedra in the $[110]$ and $[1-10]$ directions generate a 3-D porous framework. The dimensions of the three nearly perpendicular channels, one bounded by 12-membered $[\text{Zn}_4\text{V}_8\text{O}_{12}]$ rings along $[001]$ and two bounded by 12-membered $[\text{Zn}_2\text{V}_{10}\text{O}_{12}]$ rings along $[110]$ and $[1-10]$ are $8.7 \times 8.7 \text{ \AA}$ and $7.4 \times 10.9 \text{ \AA}$, as shown in Figures 3.19(a) and 3.19(b), respectively, occupied by two crystallographic independent water molecules. All vanadium(V) atoms exhibit $\{\text{VO}_4\}$ tetrahedral geometry coordination defined by one terminal oxo-group with bond distances

of 1.615(2)-1.651(3) Å, and three different μ -oxygen bridging atoms from two $\{VO_4\}$ units and one Zn(II) complex with bond distances of 1.635(3)-1.808(3) Å and the O–V–O and V–O–V bond angles are in the range of 105.9(2)-112.9(1)° and 144.9(2)-151.3(2)°, respectively, similar to those observed in **3b-c**. The Zn(II) center embraces a ZnO_2N_4 distorted octahedral geometry, being coordinated by four equatorial nitrogen atoms of two enMe chelate ligands and two axial μ -oxygen bridging atoms from tetrahedral units, which adopt a *trans*-orientation with the O–Zn–O bond angles of 174.1(1)°. The water solvate molecules are hydrogen bonded to the chains through O–H...O hydrogen bond interactions forming a $R_4^3(10)$ motif (graph set notation *R* is ring pattern type with the related the number of donors and acceptors are 4 and 3 and degree of motif are 10) with as illustrated in Figure 3.20. The stability of the framework reinforced by the N–H...O hydrogen bond interactions between the hydrogen atoms of the amine groups on the chelating enMe ligand and the oxygen atoms of the framework as listed in Table. 3.9.

Table 3.7 Selected Bond Lengths and Bond Angles (Å, °) for **3e**.

Zn(1)–N(4)	2.108(3)	V(2)–O(6)	1.787(2)
Zn(1)–N(2)	2.123(3)	N(1)–C(1)	1.482(4)
Zn(1)–N(3)	2.132(3)	N(2)–C(2)	1.475(5)
Zn(1)–N(1)	2.140(3)	N(3)–C(4)	1.480(4)
Zn(1)–O(5)	2.164(3)	N(4)–C(5)	1.480(5)
Zn(1)–O(3)	2.244(2)	C(1)–C(2)	1.518(5)
V(1)–O(1)	1.615(2)	C(1)–C(3)	1.524(5)
V(1)–O(3)	1.652(2)	C(4)–C(6)	1.507(5)
V(1)–O(4)	1.7888(11)	C(4)–C(5)	1.513(5)
V(1)–O(6) ⁱ	1.808(3)	O(1W)–H(1)	0.85(6)
V(2)–O(5)	1.635(3)	O(1W)–H(2)	0.78(8)
V(2)–O(2)	1.651(3)	O(2W)–H(4)	0.82(5)
V(2)–O(7)	1.7819(11)	O(2W)–H(3)	0.71(4)

Symmetry codes: (i) $x+1/2, y+1/2, z$; (ii) $-x+1, y, -z+2$; (iii) $x-1/2, y-1/2, z$; (iv) $-x, y, -z+1$.

Table 3.7 (Continued).

N(4)–Zn(1)–N(2)	177.73(13)	O(3)–V(1)–O(4)	110.45(13)
N(4)–Zn(1)–N(3)	82.06(11)	O(1)–V(1)–O(6) ⁱ	111.39(14)
N(2)–Zn(1)–N(3)	95.77(11)	O(3)–V(1)–O(6) ⁱ	106.22(13)
N(4)–Zn(1)–N(1)	99.97(11)	O(4)–V(1)–O(6) ⁱ	108.47(13)
N(2)–Zn(1)–N(1)	82.20(12)	O(5)–V(2)–O(2)	105.90(16)
N(3)–Zn(1)–N(1)	177.97(12)	O(5)–V(2)–O(7)	110.94(13)
N(4)–Zn(1)–O(5)	91.21(13)	O(2)–V(2)–O(7)	109.05(11)
N(2)–Zn(1)–O(5)	88.23(12)	O(5)–V(2)–O(6)	112.94(13)
N(3)–Zn(1)–O(5)	92.53(12)	O(2)–V(2)–O(6)	107.84(12)
N(1)–Zn(1)–O(5)	87.52(12)	O(7)–V(2)–O(6)	109.98(15)
N(4)–Zn(1)–O(3)	89.27(12)	V(1)–O(3)–Zn(1)	139.82(15)
N(2)–Zn(1)–O(3)	91.51(11)	V(1)–O(4)–V(1) ⁱⁱ	150.3(2)
N(3)–Zn(1)–O(3)	93.36(11)	V(2)–O(5)–Zn(1)	164.6(2)
N(1)–Zn(1)–O(3)	86.59(11)	V(2)–O(6)–V(1) ⁱⁱⁱ	144.86(15)
O(5)–Zn(1)–O(3)	174.09(11)	V(2) ^{iv} –O(7)–V(2)	151.3(2)
O(1)–V(1)–O(3)	110.73(14)	H(1)–O(1W)–H(2)	113(6)
O(1)–V(1)–O(4)	109.53(10)	H(4)–O(2W)–H(3)	109(4)

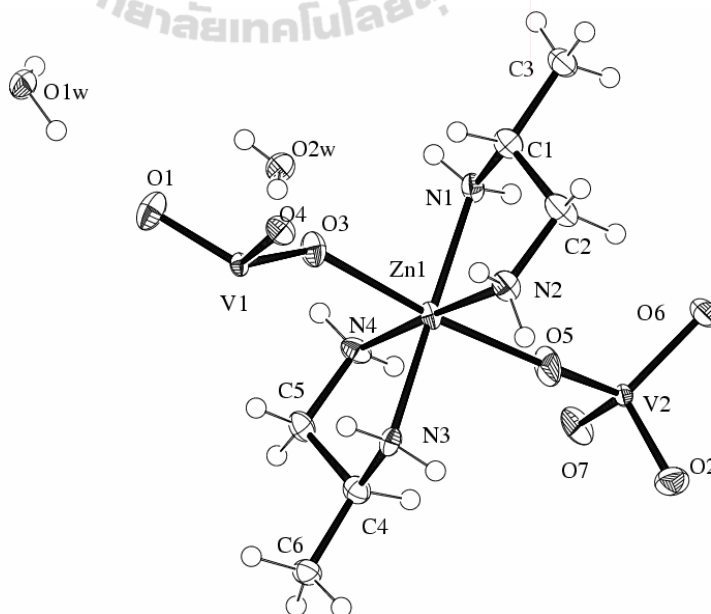


Figure 3.18 Asymmetric unit of **3e**, including the labeling of the atoms with 50% probability displacement ellipsoids.

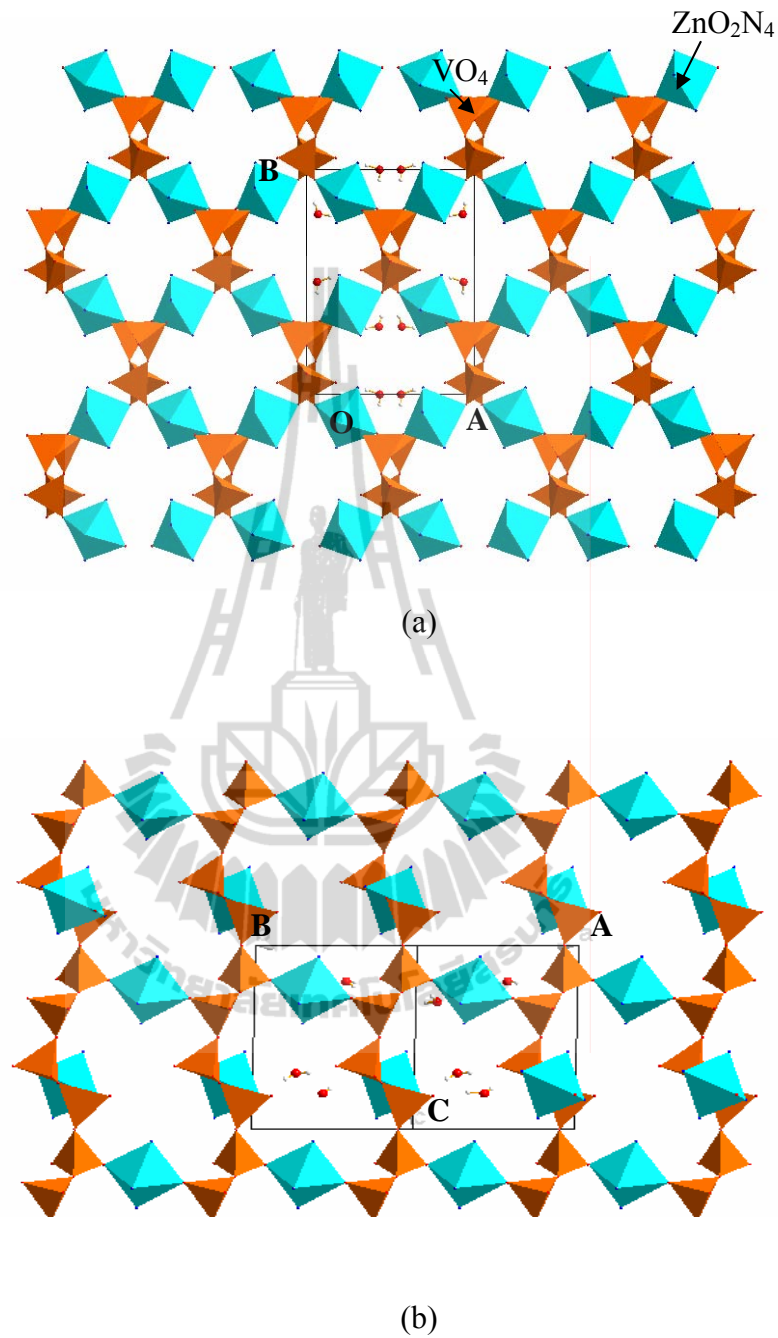


Figure 3.19 Polyhedral representation of the dimensions of the three nearly perpendicular channels, (a) one bounded by 12-membered $[Zn_4V_8O_{12}]$ rings along $[001]$ and (b) two bounded by 12-membered $[Zn_2V_{10}O_{12}]$ rings along $[110]$. The C and H atoms are omitted for clarity.

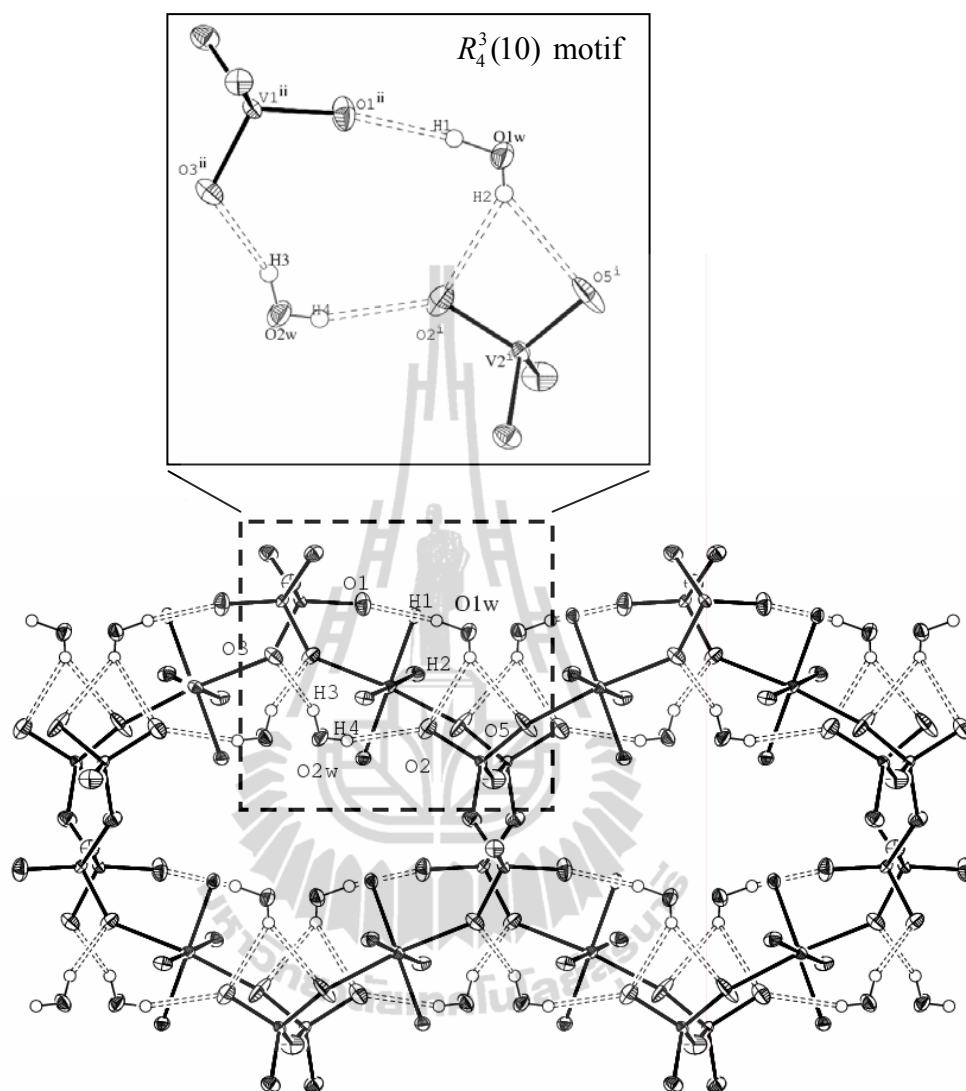


Figure 3.20 Hydrogen bonding interactions showing the $R_4^3(10)$ motif in **3e**.

Reaction pH, temperature or the amount of aliphatic diamines are crucial parameters to form the desired product. The neutral, mono-protonated and di-protonated forms of the aliphatic diamines are dependent on their pK_a values (en: $pK_{a1} = 10.71$ and $pK_{a2} = 7.56$; enMe: $pK_{a1} = 10.00$ and $pK_{a2} = 7.13$). In the V_2O_5 – $M(OAc)_2$ –aliphatic diamines system, compounds **3a**, **3b**, and **3e** are present as en and its derivatives in the neutral form; while compound $[H_2en]_3[V_{10}O_{28}] \cdot 2H_2O$, **3c**, and **3d** are

found in the di- and mono-protonated form. The en and enMe acts as a strong reducing agent for the isolated mixed-valence vanadate compound.

Table 3.8 Summary the Coordination Geometries and Bond Valence Sums for Compounds **3a-e**.

Compound	Metal Centers	Type of Polyhedron	^a Bond Type	Bond Distance (Å)	^b Average of Oxidation State
3a	Zn(1)	Distorted tetrahedra	Zn- μ -N	2.014(4)	1.999
			Zn- μ -O	1.955(4)-1.973(4)	
	Zn(2)	Trigonal bipyramids	Zn- μ -N	2.015(4)	2.028
			Zn- μ -O	1.961(3)-2.196(4)	
	V(1) and V(2)	Distorted tetrahedra	V- μ -O	1.649(4)-1.820(4)	5.160
	3b	Zn(1)	Distorted octahedra	Zn-N	2.073(2)-2.097(2)
V(1) and V(2)		Distorted tetrahedra	V- μ -O	1.612(2)-1.806(2)	5.079
			V- μ_3 -O	1.695(2)	
3c	Cd(1)	Distorted octahedra	Cd-N	2.268(7)	2.142
			Cd- μ^a -O	2.324(6)-2.330(6)	
	V(1) and V(2)	Distorted tetrahedra	V=O _t	1.612(6)-1.623(6)	5.148
			V- μ -O	1.653(7)-1.820(6)	
3d	Zn(1)	Distorted octahedra	Zn-N	2.141(10)	2.118
			Zn- μ -O	2.083(6)-2.107(6)	
	V(1) and V(4)	Distorted tetrahedra	V- μ -O	1.644(7)-1.721(6)	5.096 (5.35) ^c
			V- μ_3 -O	1.817(7)-1.827(6)	
	V(2) and V(3)	Square pyramids	V=O _t	1.590(7)-1.598(7)	4.181 (4.37) ^c
			V- μ -O	1.917(7)-1.943(7)	
V- μ_3 -O	1.953(6)-2.020(6)				
3e	Zn(1)	Distorted octahedra	Zn-N	2.108(3)-2.140(3)	2.038
			Zn- μ -O	2.164(3)-2.244(2)	
	V(1) and V(2)	Distorted tetrahedra	V=O _t	1.615(2)-1.651(3)	5.189
			V- μ -O	1.635(3)-1.808(3)	

^at, μ , and μ_3 are terminal, doubly and triply bridged oxygen atoms, respectively.

^bValence sum calculation (Brown and Altermatt, 1985).

^cThe oxidation state value from Zhang, Shi, Yang, Chen, and Feng (2000).

Table 3.9 Hydrogen Bonding Interactions for Compounds **3a-e**.

	D-H...A	d(D-H) (Å)	d(H...A) (Å)	d(D...A) (Å)	<(DHA) (°)
3a	N(1)-H(1B)...O(2) ⁱ	0.90	2.27	3.057(5)	145
	N(1)-H(1B)...O(7) ⁱⁱ	0.90	2.58	3.285(5)	136
	N(4)-H(4A)...O(6) ⁱⁱⁱ	0.90	2.23	3.084(6)	159
	N(4)-H(4B)...O(5) ^{iv}	0.90	2.53	3.351(5)	152
3b	N(1)-H(1B)...O(6) ⁱ	0.92	2.41	3.233(3)	149
	N(2)-H(4A)...O(1) ⁱⁱ	0.92	2.27	3.059(3)	144
	N(2)-H(4B)...O(1) ⁱⁱⁱ	0.92	2.57	2.993(3)	109
	N(2)-H(4B)...O(4) ^{iv}	0.92	2.43	3.216(3)	144
	C(1)-H(2B)...O(1) ⁱ	0.99	2.67	3.411(3)	132
3c	N(1)-H(1A)...O(6) ⁱ	0.95(2)	2.07	2.956(10)	154
	N(1)-H(1B)...O(2) ⁱⁱ	0.93(8)	2.32	3.222(9)	164
	N(2)-H(2A)...O(4) ⁱⁱⁱ	0.95(2)	2.13	2.982(10)	148
	N(2)-H(2A)...O(6) ^{iv}	0.95(2)	2.35	2.980(10)	124
	N(2)-H(2B)...O(5) ^v	0.94(2)	1.98	2.921(9)	178
	N(2)-H(2C)...O(1) ⁱ	0.98(8)	1.82	3.744(10)	166
3d	C(1)-H(1D)...O(3) ⁱ	0.84	2.53	3.332(13)	159
	N(2)-H(2A)...O(2) ⁱⁱ	0.92	2.20	2.853(11)	127
	N(2)-H(2B)...O(1) ⁱ	0.92	2.28	2.896(11)	124
	N(2)-H(2B)...O(10) ⁱ	0.92	2.13	2.898(10)	140
	N(2)-H(2C)...O(4)	1.00	2.11	3.084(12)	164
3e	O(1W)-H(1)...O(1)	0.89(6)	1.99(6)	2.859(4)	166(5)
	O(1W)-H(2)...O(5) ⁱ	0.70(8)	2.42(9)	3.023(5)	145(8)
	O(1W)-H(2)...O(2) ⁱ	0.70(8)	2.53(8)	3.145(4)	148(8)
	O(2W)-H(4)...O(2) ⁱ	0.71(5)	2.16(5)	2.847(4)	164(5)
	O(2W)-H(3)...O(3)	0.80(2)	2.00(3)	2.770(4)	161(3)
	N(1)-H(1A)...O(1) ⁱⁱ	0.87(2)	2.49(3)	3.296(4)	153(3)
	N(1)-H(1B)...O(2W)	0.81(3)	2.48(4)	3.120(4)	137(4)
	N(2)-H(2A)...O(1) ⁱⁱⁱ	0.88(3)	2.63(3)	3.482(4)	162(3)
	N(2)-H(2B)...O(1W) ^{iv}	0.84(3)	2.37(3)	3.193(5)	166(4)
	N(3)-H(3A)...O(1W) ^{iv}	0.88(3)	2.28(3)	3.080(4)	151(4)
	N(3)-H(3B)...O(6) ^v	0.84(2)	2.30(3)	3.138(4)	174(4)
	N(4)-H(4B)...O(2) ^{vi}	0.84(3)	2.40(3)	3.074(4)	137(4)
	N(4)-H(4A)...O(2W)	0.87(3)	2.36(3)	3.038(4)	136(3)

Symmetry codes: **3a**: (i) $x, y-1, z$; (ii) $-x+1, y-1/2, -z+2$; (iii) $-x, y+1/2, -z+1$; (iv) $x-1, y, z$. **3b**: (i) $-x+1, -y+1, -z+1$; (ii) $-x+2, -y+1, -z+1$; (iii) $-x+2, y+1/2, -z+1/2$; (iv) $x+1, -y+1, z$. **3c**: (i) $x, y, z+1$; (ii) $-x+1, -y, -z+1$; (iii) $x+3/2, -y+1/2, z+1/2$; (iv) $1+x, y, z+1$; (v) $x+1/2, -y+1/2, z+1/2$; (vi) $x+1, y, z$. **3d**: (i) $-x+1, -y+2, -z+2$; (b) $x, -y+3/2, z-1/2$. **3e**: (i) $x+1, y, z$; (ii) $x-1/2, y-1/2, z$; (iii) $-x+1, y, -z+2$; (iv) $x-1, y, z$; (v) $x+1/2, y+1/2, z$; (f) $-x, y, 1-z$.

Table 3.10 Physical and Analytical Data for Compounds **3a**, **3d** and **3e**.

Compound	M _r	Crystal Color	^a D.point (°C)	Elemental Anal. Calc. (Found) (%)				
				C	H	N	^b V	^b Zn
3a : Zn ₂ (en)V ₂ O ₇	404.72	Purple	282.71	5.49 (5.94)	1.90 (1.99)	6.82 (6.92)	1.4	1.0
3d : Zn(HenMe) ₂ (V ⁴⁺ V ⁵⁺ O ₅) ₄	943.17	Black	337.53	7.64 (8.36)	2.35 (2.48)	5.94 (5.52)	7.0	1.0
3e : Zn(enMe) ₂ (VO ₃) ₂ ·2H ₂ O	447.49	Pale- brown	136.92	16.41 (16.20)	5.41 (5.68)	12.52 (12.44)	1.6	1.0

^aD. point is decomposition point. ^bMeasured by EDX.

3.3.2 Infrared spectra

Figure 3.21 shows infrared spectra of **3a**, **3c**, **3d**, and **3e**, particular the frequencies of vanadate and zinc compounds that similar as observed in literature (Frost, Erickson, Weier, and Carmody, 2005; Nakamoto, 1997; Nyquist, Kagel, and Leuqers, 1997). The vibration mode of the terminal $\nu(\text{V}=\text{O}_t)$ symmetric stretch is observed at 985, 947, 926, and 908 cm^{-1} for **3a**; 1001, 967, 958, 945, 923, 914, and 900 cm^{-1} for **3c**; 1020, 986, and 910 cm^{-1} for **3d**; 999, 931, and 902 cm^{-1} for **3e**. The vibration mode of the terminal $\nu(\text{V}=\text{O}_t)$ and bridging V–O–V asymmetric stretches appeared at 837, 779, 735, 701, 666, 637, 538, and 523 cm^{-1} for **3a**; 875, 820, 722, 640, and 556 cm^{-1} for **3c**; 878, 829, 810, 654, and 552 cm^{-1} for **3d**; 838, 820, 644, and 527 cm^{-1} for **3e**. The combination vibration modes of bridging V–O–V symmetric stretches and Zn–O stretches are observed at 480, 440, and 423 cm^{-1} for **3a**; at 475 cm^{-1} for **3c**; 486 and 412 cm^{-1} for **3d**; 494, 453, and 440 cm^{-1} for **3e**. The very strong peak at 3459 cm^{-1} for **3e** is assigned to a $\nu_{\text{as}}(\text{O}-\text{H})$ stretching vibration. Bands in the 3266 and 3193 cm^{-1} for **3a**; 3294 and 3222 cm^{-1} for **3c**; 3329 and 3263 cm^{-1} for **3d**; 3329 and 3283 cm^{-1} for **3e** due to the $\nu_{\text{as}}(\text{N}-\text{H})$ asymmetric stretching. Bands at 3119, and 2951 cm^{-1} for **3a**; 3016 and 2962 cm^{-1} for **3d**; 3176, 2974, 2954, 2939, 2905, and

2880 cm^{-1} for **3e** assigned to combination of $\nu_{\text{as}}(^+\text{N-H})$ and $\nu_{\text{as}}(\text{C-H})$ asymmetric stretches. The peak at 1596 and 1573 cm^{-1} for **3a**; 1625 cm^{-1} for **3c**; 1614 and 1569 cm^{-1} for **3d**; 1630 and 1620 cm^{-1} for **3e** are due to the $\delta(\text{H-O-H})$ and $\delta(\text{H-N-H})$ bending modes.

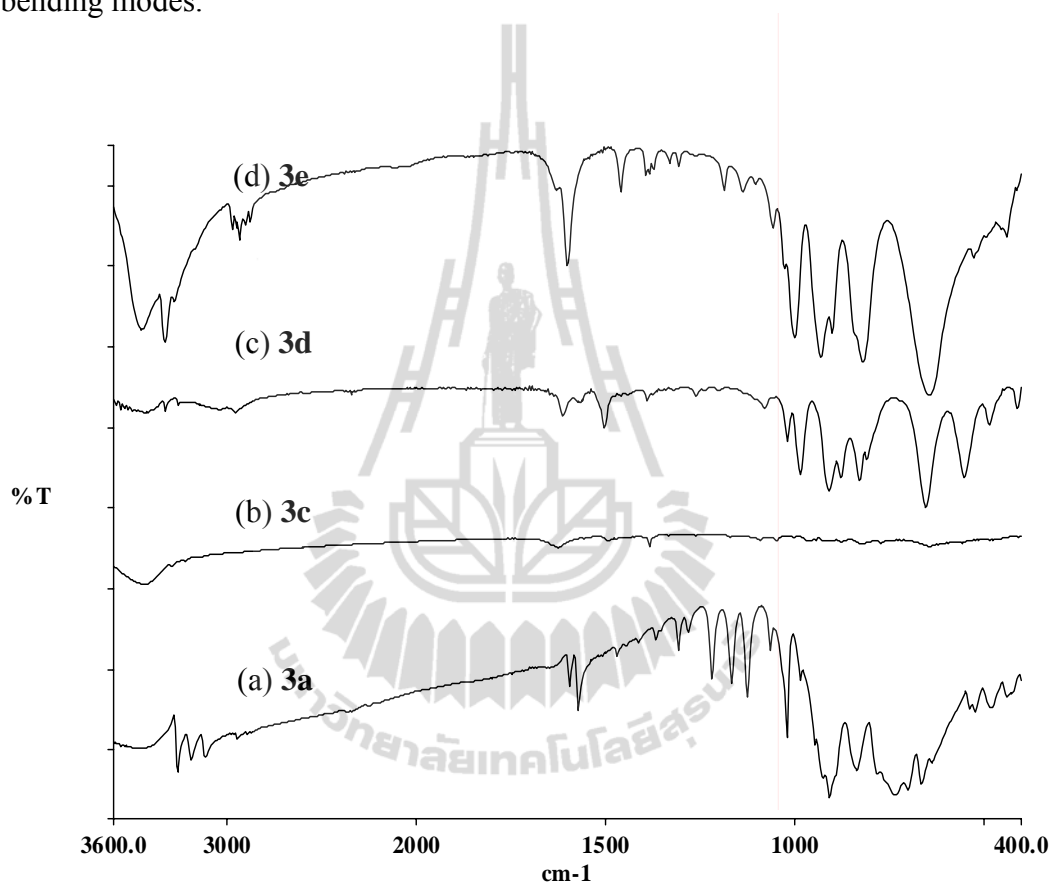


Figure 3.21 Infrared spectra.

Table 3.11 IR Spectral Data for Compounds **3a** and **3c-e**.

^a Assignment	3a	3c	3d	3e
$\nu_{\text{as}}(\text{O-H})$	^b 3447	^b 3438	^b 3446	3459 vs
$\nu_{\text{as}}(\text{N-H})$	3266 m 3193 m	3294 vw 3222 vw	3329 w 3263 w	3329 vs, sp 3263 w
$\nu_{\text{as}}(^+\text{N-H}) + \nu_{\text{as}}(\text{C-H})$	3119 w 2951 vw		3016 vw 2962 vw	3176 sh 2974 w 2954 w 2939 m, sp

Table 3.11 (Continued).

^a Assignment	3a	3c	3d	3e
				2905 w 2880 w
$\delta_{(H-O-H)} + \delta_{(H-N-H)}$	1596 m 1573 m	1625 vw	1614 m 1569 w	1630 vw 1602 vs, sp
$\nu_{s(VO_2)}$	985 vw 947 vw 926 vw 908 m	1001 vw 967 vw 958 vw 945 vw 923 vw 914 vw 900 vw	1020 m, sp 986 vs, sp 910 m	999 vs, sp 931 vs, sp 902 m, sp
$\nu_{as(VO_2)}$	837 m	875 vw 820 vw	878 m 829 m 810 w	838 sh 820 vs
$\nu_{as(V-O-V)}$	779 vw 735 w 701 vw 666 m 637 vw 538 vw 523 vw	722 w 640 vw 556 vw	654 vs, sp 552 vs, sp	644 vs 527 w
$\nu_{s(V-O-V)} + \nu_{(Zn-O)}$	480 m 440 w 423 vw	475 vw	486 m 412 m	494 vw 453 vw 440 m

3.3.3 Thermogravimetric Analysis

Figures 3.22-3.24 show the TGA curves for compounds **3a**, **3d** and **3e**. Total weight loss of 23.626% (calc. 22.752%), 22.625% (calc. 22.859%), and 42.310% (calc. 41.167%) for **3a**, **3d** and **3e** with each is divided into three, two and six stages, respectively. In **3a** and **3d**, first and second weight loss are 15.435% (calc. 14.845%) in the temperature range of 283-385 °C and only first weight loss is 15.910% (calc. 15.926%) in the temperature range of 338-470 °C corresponding to the loss of the bridging en in **3a** and the two monodentated HenMe⁺ ligands in **3d**, respectively. While first weight loss of **3e** about 8.230% (calc. 8.051%) in the temperature range of

83.97-136.92 °C due to the solvate water removal and second to six weigh loss are 32.667% (calc. 33.116%) in the temperature range of over 136.92-861.36 °C corresponded to the loss of the chelating enMe ligands with slightly decrease in weight of 1.982% in the temperature range of 619.44-861.36 °C due to ZnO and V₂O₅ begin to form with the oxidation state of vanadium changing from V⁵⁺ to V⁴⁺, with the residual weight of 58.833%. It is in good agreement with the total calculated weight of two inorganic compounds of 59.103%. The collapsed network and framework in **3a** and **3d** with weight loss of 8.191% (calc. 7.907%) in the temperature range of 385-732 °C and 6.715% (calc. 6.785%) in the temperature range of 470-643 °C due to the loss of the oxygen atoms, followed by a slight increase in weight of 0.742% and 2.808% that could be due to oxidation of sheets from V⁴⁺ to V⁵⁺, respectively. The residual in **3a** and **3d** are assumed to ZnV₂O₅, and Zn_yV₂O₅ (y = 0.01-0.02) with the observed weight remaining about 76.374% (calc. 77.248%), and 77.375% (calc. 77.412% or 77.689% depending on the amount of zinc), respectively. It is clear that the open framework of **3d** has a high thermal stability of 337 °C by the observed crystal surface and confirmed the phase by powder X-ray diffraction at varied temperatures, since the similar coordinate radii of Zn²⁺ (0.88 Å) compare to Mg²⁺ (0.86 Å) and Fe²⁺ (0.92 Å), thus, the residual is the isomorphus phase of Fe_{0.02}V₂O₅ and Mg_{0.01}V₂O₅ (Pattern: 00-049-0805 and Pattern: 01-089-0610, Appendix A) when heated at over 470 °C, as shown in Figures 3.25-3.26. The thermal stability of the network **3a** and the open framework structure of **3e** with the water molecules were removed and stable up to 283 °C and 136 °C, respectively.

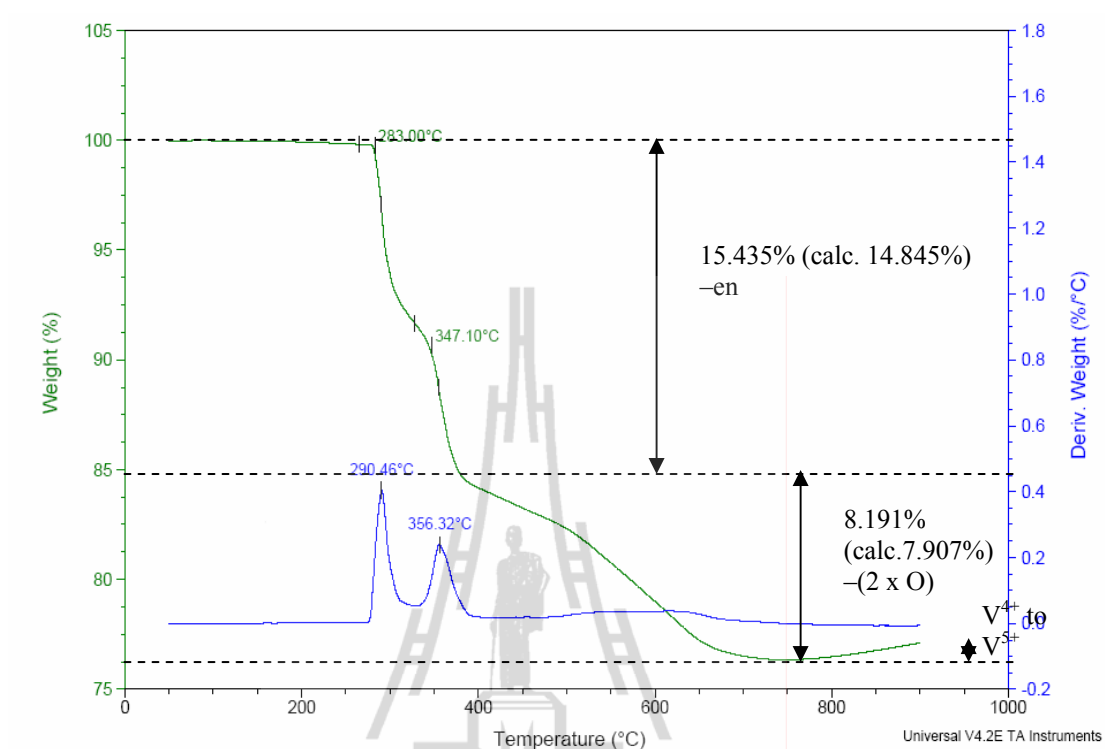


Figure 3.22 TGA curve of 3a.

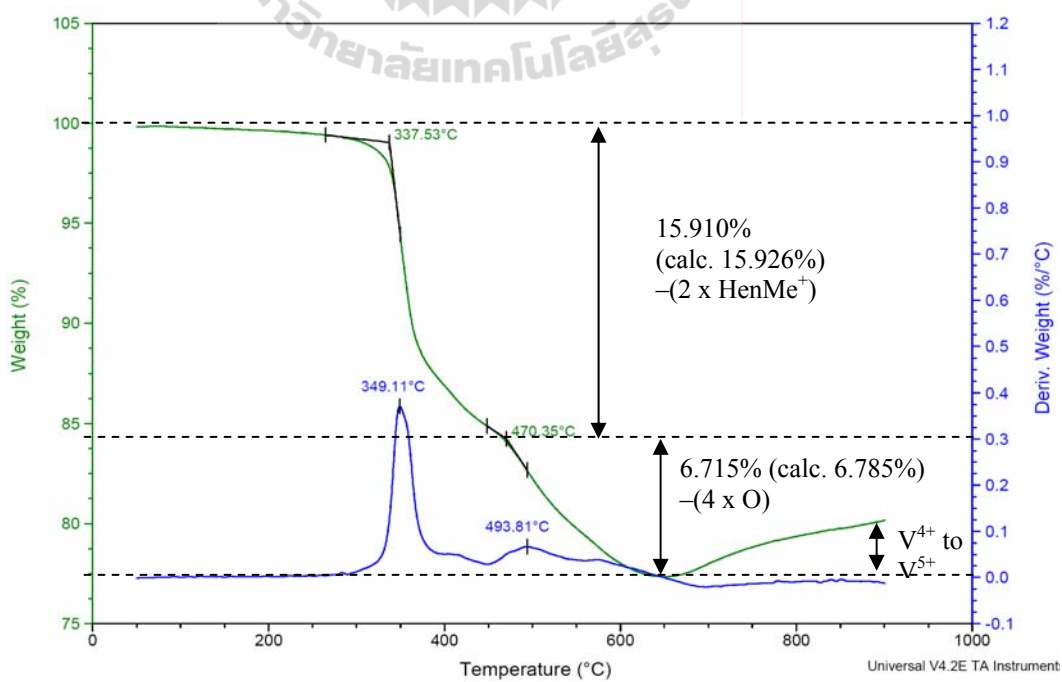


Figure 3.23 TGA curve of 3d.

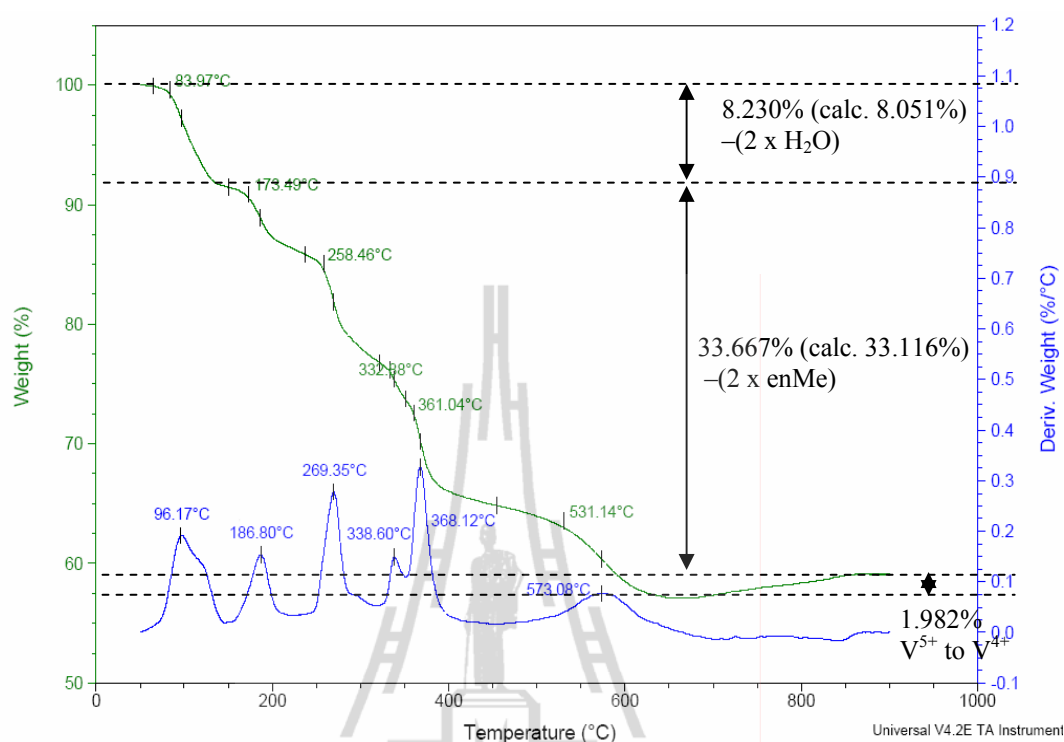


Figure 3.24 TGA curve of **3e**.

Table 3.12 Decompositions as a Function of Temperature.

Comp.	Items	%Weight Loss			Temperature (°C)	Composition
		Calc.	Measure	Error		
3a	Decomposition	14.845	15.435	0.590	282.71-384.85	-en
		7.907	8.191	0.284	384.85-731.70	-(2 x O)
	Residual	77.248	76.374	0.874	>731.70	ZnV ₂ O ₅
			+0.742	>800	V ⁵⁺ to V ⁴⁺	
3d	Decomposition	15.926	15.910	0.016	337.53-470.35	-(2 x HenMe ⁺)
		6.785	6.715	0.070	470.35-642.88	-(4 x O)
	Residual	77.412 77.689	77.375	0.037 0.314	>642.88	4 x Zn _{0.01} V ₂ O ₅ 4 x Zn _{0.02} V ₂ O ₅
			+2.808	642.88-900	V ⁴⁺ to V ⁵⁺	
3e	Decomposition	8.051	8.230	0.187	83.97-136.92	-(2 x H ₂ O)
		33.116	32.667	0.449	136.92-861.36	-(2 x enMe)
	Residual	58.833	59.103	1.143	>861.36	ZnO and V ₂ O ₅
			-1.982	619.44-861.36	V ⁵⁺ to V ⁴⁺	

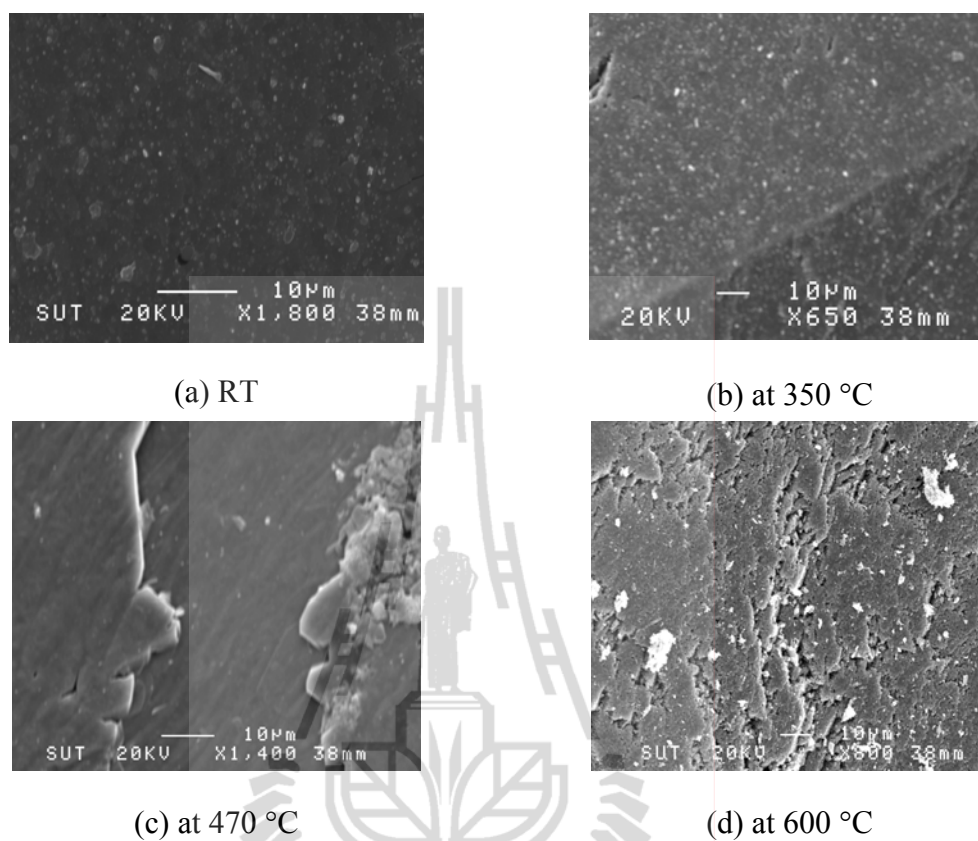


Figure 3.25 The SEM images of 3d.

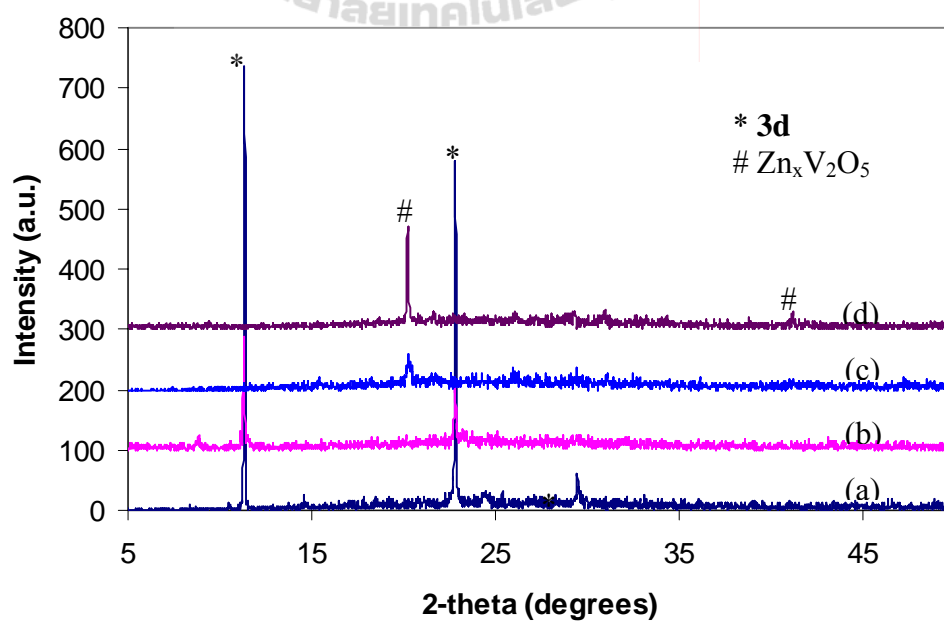


Figure 3.26 The XRD patterns of 3d (a) RT, with heated (b) at 350 °C, (c) at 470 °C and (d) at 600 °C.

3.4 Conclusions

Five new hybrid organic-inorganic vanadate compounds, namely (en)Zn₂V₂O₇ (**3a**), (en)Zn(VO₃)₂ (**3b**), (Hen)₂Cd(VO₃)₄ (**3c**), (HenMe)₂Zn(V₂O₅)₄ (**3d**) and (enMe)₂Zn(VO₃)₂·2H₂O (**3e**), have been synthesized via hydrothermal synthesis. **3a** consists of a V₂O₇⁴⁻ dimer unit or pyrovanadate, while **3b**, **3c** and **3e** are composed of polymeric metavanadate chains and **3d** exhibits a mixed-valence vanadate layer. The dimer unit in **3a** is linked to the different zinc complexes with the flexibility of the bridging ligand essential for formation of the helix, forming a 3-D chiral helical network which contains polymeric helical zinc coordination complex chains, zinc tetrahedra-en-zinc trigonal bipyramid, and the polymeric helical zinc vanadate chains. The polymeric metavanadate chains in **3b**, **3c** and **3e** linked with the metal coordination complexes cross linkers forming 2-D double layers, 1-D double chains, and a 3-D open framework, respectively. The layers of **3b** and chains of **3c** are further hydrogen bonded, N–H···O interactions, to neighbors producing 3-D supramolecular network and 2-D supramolecular layer, respectively. While the O–H···O hydrogen bonding interactions with a $R_4^3(10)$ motif between solvate water molecules and the framework in **3e**. The mixed-valence [(V⁴⁺O)(V⁵⁺O₄)]₅ layers of **3d** are linked together with the pillared zinc coordination complexes forming a 3-D open framework. The successful syntheses of such helical chiral networks or the open framework structures offer a fascinating example of the hybrid organic-inorganic materials.

3.5 References

- Brown, I. D., and Altermatt, D. (1985). Bond-valence parameters obtained from a systematic analysis of the inorganic crystal structure. **Acta Crystallographica Section B**. 41(4): 244-247.
- Burnett, M. N., and Johnson, C. K. (1996). *ORTEP-III: Oak Ridge Thermal Ellipsoid Plot Program for Crystal Structure Illustration*, Report ORNL-6895, Oak Ridge National Laboratory, Oak Ridge, Tennessee.
- Cao, G.-J., Zheng, S.-T., Fang, W.-H., and Yang, G.-Y. (2010). (en)Mn₂(V₂O₇): A 3-D manganese vanadate built by Mn–O layers and two types of pillars of V₂O₇ and en bridges. **Inorganic Chemistry Communications**. 13(7): 834-836.
- Crystal Impact. (2006). *DIAMOND*. Version 3.1. Crystal Impact GbR. Bonn, Germany.
- DeBord, J. R. D., Zhang, Y., Haushalter, R. C., Zubieta, J., and O'Connor, C. J. (1996). One-dimensional vanadium oxide chains containing covalently bound copper coordination complexes: hydrothermal synthesis and characterization of Cu(en)[V₂O₆], Cu(2,2'-bipy)[V₂O₆], and Cu(2,2'-bipy)₂[V₂O₆]. **Journal of Solid State Chemistry**. 122(2): 251-258.
- Frost, R. L., Erickson, K. L., Weier, M. L., and Carmody, O. (2005). Raman and infrared spectroscopy of selected vanadates. **Spectrochimica Acta Part A**. 61(5): 829-834.
- Galy, J., and Carpy, A. (1975). Structure cristalline de K₂V₃O₈ ou K₂(VO)[V₂O₇]. **Acta Crystallographica Section B**. 31(6): 1794-1795.
- Gopal, R., and Calvo, C. (1973). Crystal structure of α-Zn₂V₂O₇. **Canadian Journal of Chemistry**. 51(7): 1004-10119.

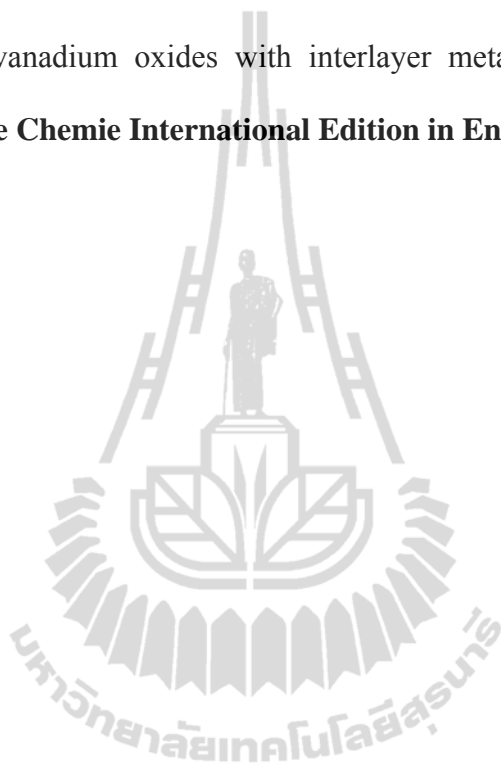
- Gopal, R., and Calvo, C. (1974). Crystal structure of magnesium divanadate. $\text{Mg}_2\text{V}_2\text{O}_7$. **Acta Crystallographica Section B**. 30(10): 2491-2493.
- Khan, M. I., Hope, T., Cevik, S., Zheng, C., and Powell, D. (2000). Organically templated vanadium oxide phases: synthesis and structures of $[\text{H}_3\text{NCH}_2\text{CH}_2\text{NH}_3][\text{V}_2\text{O}_6]$ and $[\text{HN}(\text{CH}_2\text{CH}_2)_3\text{NH}][\text{V}^{\text{V}}\text{P}_2\text{V}^{\text{IV}}_4\text{O}_{14}]\cdot\text{H}_2\text{O}$. **Journal of Cluster Science**. 11(3): 433-447.
- Khan, M. I., Yohannes, E., Doedens, R. J., Golub, V. O., and O'Conner, C. J. (2005). Templated synthesis of a chiral solid: Synthesis and characterization of $[\text{Co}(\text{en})_3][\text{V}_3\text{O}_9]\cdot\text{H}_2\text{O}$, containing a new type of chiral vanadium oxide chain. **Inorganic Chemistry Communication**. 8(9): 841-845.
- Krachodnok, S., Haller, K. J., and Williams, I. D. (2008). Chiral helices in a 3D network of $\text{Zn}_2(\text{en})\text{V}_2\text{O}_7$ (en = Ethylenediamine). **Advanced Materials Research**. 55-57: 669-672.
- Law, T. S.-C., and Williams, I. D. (2000). Organic-directed synthesis of manganese vanadates with variable stoichiometry and dimensionality: 1-D $(\text{Hen})_2\text{Mn}(\text{VO}_3)_4$, 2-D $[(\text{H}_2\text{en})_2][\text{Mn}(\text{VO}_3)_4]$, and 3-D $[(\text{H}_2\text{en})[\text{MnF}(\text{VO}_3)_3]$. **Chemistry of Materials**. 12(1): 2070-2072.
- Lin, H., and Maggard, P. A. (2008). Synthesis and structures of a new series of silver-vanadate hybrid solids and their optical and photocatalytic properties. **Inorganic Chemistry**. 47(18): 8044-8052.
- Liu, G., and Greedan, J. E. (1995). Magnetic properties of Fresnoite-type vanadium oxides: $\text{A}_2\text{V}_3\text{O}_8$ (A = K, Rb, NH_4). **Journal of Solid State Chemistry**. 114(1): 499-505.

- Liu, S.-X., Lin, B.-Z., and Lin, S. (2000). Hydrothermal synthesis and characterization of metavanadate containing spiral chain: $[\text{Ni}(\text{en})_3][\text{VO}_3]_2$. **Inorganica Chimica Acta**. 304(1): 33-37.
- Millange, F., Serre, C., Cabourdin, T., Marrot, J., and Férey, G. (2004). Organically templated zinc selenite: MIL-86 or $(\text{en})_2\text{Zn}_4(\text{SeO}_3)_4$ and MIL-87 or $[\text{H}_2\text{-1,3-dap}]_4[\text{Zn}_4(\text{SeO}_3)_8]$. **Solid State Sciences**. 6(2): 229-233.
- Mumme, W. G., and Watts, J. A. (1971). A refinement of the crystal structure of CsV_2O_5 . **Journal of Solid State Chemistry**. 3(3): 319-322.
- Nakamoto, K. (1997). **Infrared and Raman Spectra of Inorganic and Coordination Compounds**. John Wiley, New York. pp. 1-379.
- Ninlaus, C., Riou, D., and Féray, G. (1996). A new decavanadate dihydrate templated by ethylenediamine. **Acta Crystallographica Section C**. 52(3): 512-514.
- Nyquist, R. A., Kagel, R. O., and Leuqers, M. A. (1997). **Handbook of Infrared and Raman Spectra of Inorganic Compounds and Organic Salts**. Academic press, San Diego. pp. 1-151.
- Pavia, D. L., Lampman, G. M., and Kriz, G. S. (1996). **Introduction to Spectroscopy: A Guide for Students of Organic Chemistry**. 2nd edition, Saunders College Publishing, Washington. pp. 14-95.
- Riou, D., and Féray, G. (1995a). Intercalated vanadyl vanadates: syntheses, crystal structures, and magnetic properties. **Inorganic Chemistry**. 34(26): 6520-6523.
- Riou, D., and Féray, G. (1995b). Intercalated vanadyl vanadate $(\text{V}^{4+}\text{O})[\text{V}^{5+}\text{O}_4]\cdot 0.5[\text{enH}_2]$: hydrothermal synthesis, crystal structure, and structural correlation with V_2O_5 and other vanadyl compounds. **Journal of Solid State Chemistry**. 120(1): 137-145.

- Rujiwatra, A., Mander, G. J., Kepert, C. J., and Rosseinsky, M. J. (2005). Synthesis and characterization of subcell-supper cell related ethylenediamine-pillared zinc hydroxysulfates. **Crystal Growth & Design**. 5(1): 183-189.
- SADABS Version 2.03 (1998), SAINT Version 6.26a (2001a), and SMART Version 5.625 (2001b). Bruker Analytical X-ray Systems Inc., Madison, Wisconsin, USA.
- Sauerbrei, C., Faggiani, E. R., and Calvo, C. (1974). Cobalt vanadate, $\text{Co}_2\text{V}_2\text{O}_7$, and nickel vanadate, $\text{Ni}_2\text{V}_2\text{O}_7$. **Acta Crystallographica Section B**. 30(12): 2907-2909.
- Sheldrick, G.M. (2000). SHELXTL-97, Version 6.10: Structure determination software programs, Bruker Analytical X-ray Systems, Inc., Madison, Wisconsin, U.S.A.
- Shi, Z., Zhang, L., Zhu, G., Yang, G., Jia, H., Ding, H., and Feng, S. (1999). Inorganic/organic hybrid materials: layered vanadium oxides with interlayer metal vanadium complexes. **Chemistry of Materials**. 11(12): 3565-3570.
- Williams, I. D., Law, T. S.-C., Sung, H. H.-Y., Wen, G.-H., and Zhang, X.-X. (2000). Organo-directed synthesis of a 3-D open-framework mixed-metal oxide, $[\text{H}_2\text{en}][\text{Mn}_3(\text{V}_2\text{O}_7)_2(\text{H}_2\text{O})_2]$, incorporating metal trimer building blocks. **Solid State Science**. 2(1): 47-55.
- Zhang, L., Shi, Z., Yang, G., Chen, X., and Feng, S. (2000). Hydrothermal synthesis and crystal structure of a layered vanadium oxide with an interlayer metal coordination complex: $(\text{HenMe})_2\text{CdV}_8\text{O}_{20}$. **Journal of the Chemical Society, Dalton Transactions**. (3): 275-278.
- Zhang, Y., Haushalter, R. C., and Clearfield, A. (1996). Hydrothermal synthesis and structural characterization of layered vanadium oxides incorporating organic

cations: α -, β -[H₂en][V₄O₁₀] and α -, β -[H₂piperazine][V₄O₁₀]. **Inorganic Chemistry**. 35(17): 4950-4956.

Zhang, Y., DeBord, J. R. D., O'Connor, C. J., Haushalter, R. C., Clearfield, A., and Zubieta, J. (1996). Solid state coordination chemistry: hydrothermal synthesis of layered vanadium oxides with interlayer metal coordination complexes. **Angewandte Chemie International Edition in English**. 35(9): 989-991.



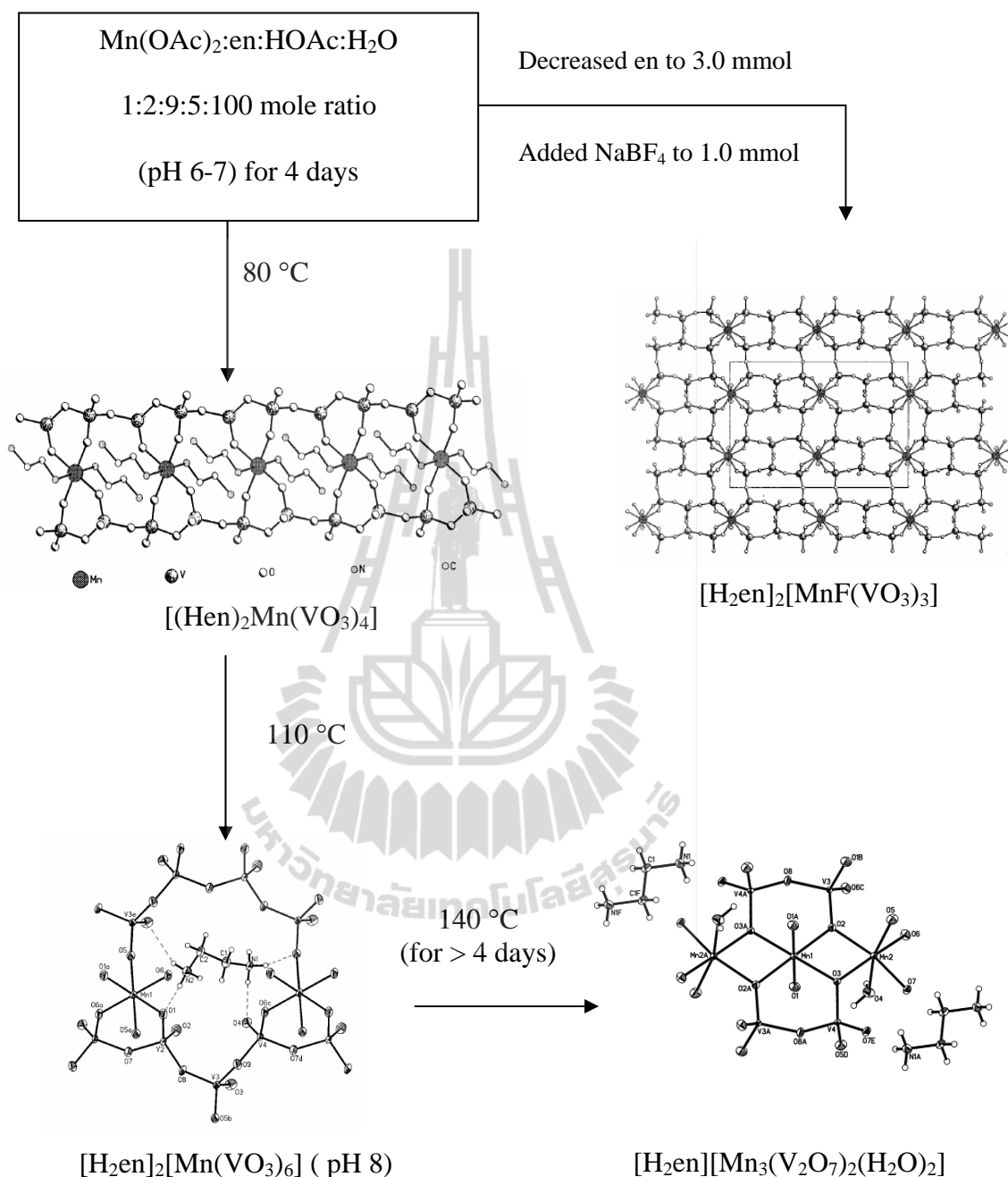


Figure 2.4 Organo-directed synthesis of manganese vanadates with variable stoichiometry and dimensionality (Law and Williams, 2000; Williams, Law, Sung, Wen, and Zhang, 2000).

The hydrothermal method consists of a reaction vessel or Parr reactor which serves to withstand the pressure and to protect the reaction inside and temperature

controlled oven outside. In this work, the Parr 23 mL high pressure reactor was used as the main synthetic apparatus as shown in Figure 2.5. The reactor consists of a stainless steel Parr reactor and a removable Teflon liner. Reactants are weighed or measured, and loaded into the Teflon liner. The vessel is filled with water less than < 60% full. It is then placed inside the stainless steel reactor, sealed, and placed in a temperature controlled oven for heating. After a certain length of time, the reactor is cooled slowly to room temperature and the products are collected for analysis. The typical temperature is constrained below 240 °C as beyond this temperature the Teflon lining of the cups becomes soft and would leak the pressure sealed inside thus possibly being a danger.

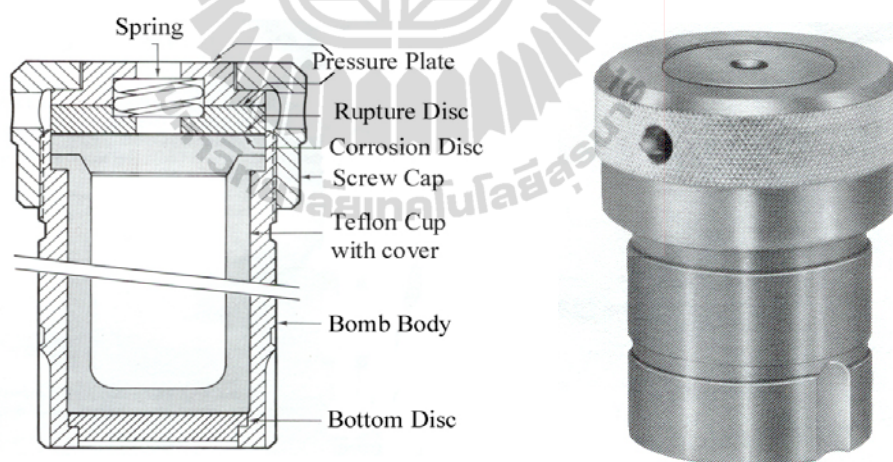


Figure 2.5 The Parr design of the Teflon-lined reaction vessel (Parr Instrument Company).

Some advantages or features of hydrothermal crystallization are summarized below:

1. The hydrothermal method is more environmentally friendly than other synthetic methods, particularly the energy saving low processing temperatures since it enables synthesis at temperatures nearer ambient conditions (Figure 2.6) (Yoshimura and Suchanek, 1997).

2. Lowering the overall cost of the synthesis process, the low reaction temperatures avoid common problems encountered with high-temperature technologies, such as poor stoichiometric control due to volatilization of components, presence of thermally induced defects, formation of undesired phases, and unwanted phase transformations.

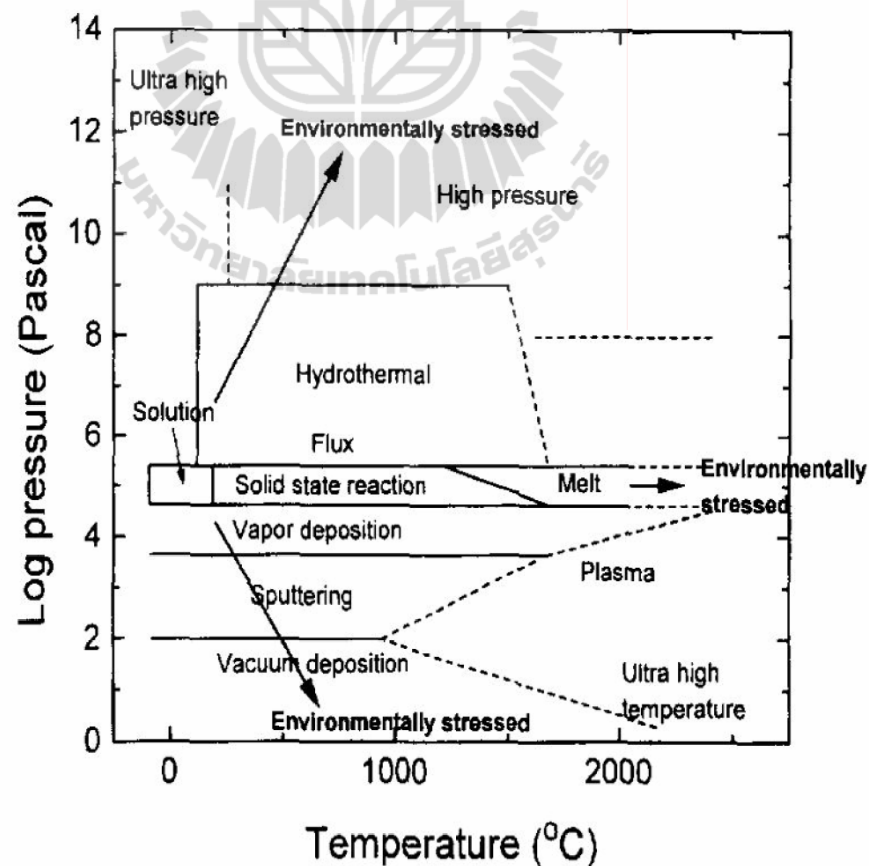


Figure 2.6 Schematic P - T diagram for preparative techniques (Yoshimura and Suchanek, 1997).

2.2 Physical Methods for Characterizing Solids

In order for a solid to be well characterized, one needs to know about the crystal structure, as given by the unit cell, its dimensions and the fractional coordinates of the atoms present in the cell. No single technique is capable of providing a complete characterization of a single crystal. Rather, a variety of techniques are used in combination. There are three main categories of physical technique which may be used to characterize solids: diffraction, microscopic and spectroscopic techniques. In addition, other techniques such as thermal analysis and physical property measurements give valuable information in certain cases (Smart and Moore, 2005; Speight, 2005; West, 1999).

2.2.1 Single Crystal and Powder X-ray Diffraction (XRD)

X-ray diffraction has been used for over a century in two main areas, for the fingerprint characterization of crystalline materials and for determination of their structure. It requires an X-ray source, the sample under investigation, powder or single crystal, and a detector to pick up the diffracted X-rays.

An X-ray source An electrically heated filament, usually tungsten, emits electrons, which are accelerated by a high potential difference (20-50 kV) and allowed to strike a metal target or anode which is water cooled in Figure 2.7(a). The anode emits a continuous spectrum of “white” X-radiation but superimposed on this are sharp, intense X-ray peaks (K_α , K_β) as shown in Figure 2.7(b). The frequencies of the K_α and K_β lines are characteristic of the anode metal; the target metals most commonly used in X-ray crystallographic studies are copper (Cu) and molybdenum (Mo), which have K_α lines at 1.5418 Å and 0.7107 Å, respectively. Normally in X-ray diffraction, monochromatic radiation is required. Usually, the K_α line is selected and the K_β line is

filtered out by using a filter made of a thin metal foil of the element adjacent ($Z-1$) in the Periodic Table, thus, nickel (Ni) effectively filters out the K_β line of the Cu, and niobium (Nb) is used for Mo.

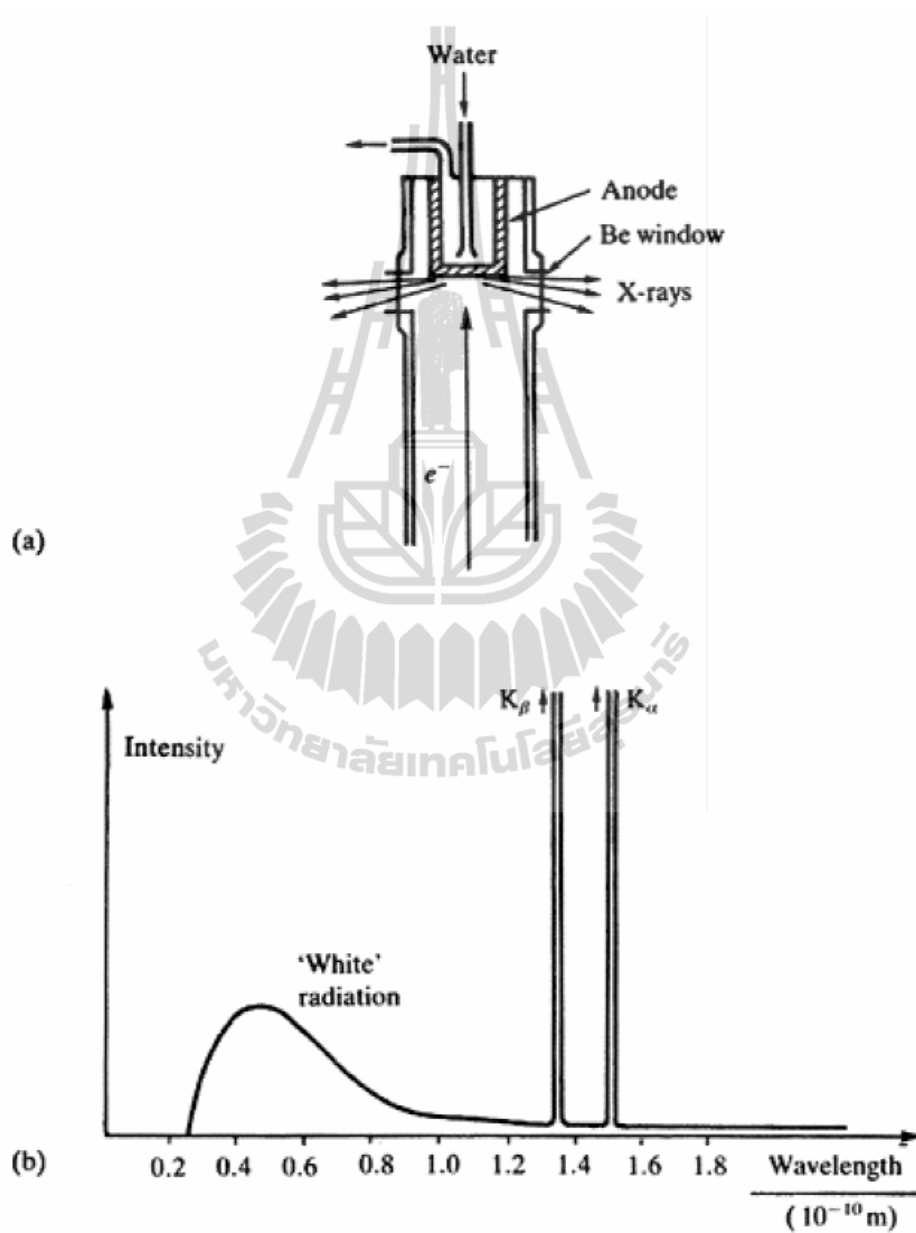


Figure 2.7 (a) an X-ray tube and (b) an X-ray emission spectrum.

Single Crystal X-ray Diffraction From a single crystal, it is possible to measure the position and intensity of the hkl reflections accurately and from this data determine not only the unit cell dimensions and space group, but also the precise atomic positions. In most cases, this can be done with speed and accuracy, and it is one of the powerful structural techniques available to a chemist. The physical principle of diffraction requires the sample to be spatially ordered in order to observe the interference of radiation scattered from different parts of the sample. This condition is fulfilled by crystals, which contain a very large number of unit cells, each built up of several atoms identically arranged within this repetitive structural motif. Unit cells may be very simple and contain only a few atoms (ions), or quite complicated with several identical or different molecules. Generally, the higher the degree of order within the sample, the more accurately can structural details be obtained.

In principle, the radiation is scattered by every atom within the irradiated specimen in all directions. Because the atoms in the crystal are located in the positions which are ordered and repetitive, the radiation scattered from all the atoms of the sample interferes differently in different directions. In every direction the waves scattered from individual atoms combined according to their relative phase. In general, they interfere destructively as they are randomly out of phase and cancel out. Only in certain directions do they interfere in a positive way and produce a ray of radiation with nonzero intensity.

The geometry of this effect is governed by the periodicity of the crystal, the size of the cell and the particular arrangement of the atoms (including symmetry operators). This effect may be represented by rays reflected from a set of parallel planes within the crystal which are populated by atoms. In fact, very often in

crystallography the term ‘reflection’ is used for such an individual diffracted ray of radiation. This is described by Bragg’s law:

$$n\lambda = 2d\sin\theta \quad \text{.....(2.1)}$$

where n is an integer, λ is the wavelength of the radiation, d is the interplanar spacing and θ is the diffraction angle (Figure 2.8).

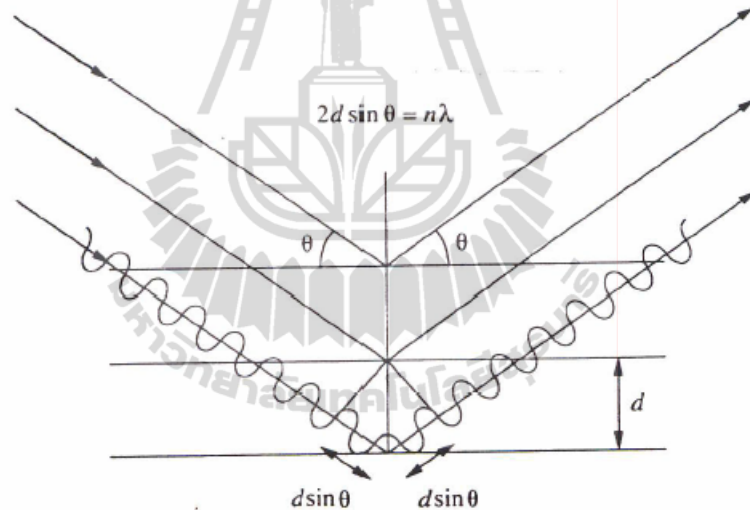


Figure 2.8 Bragg’s law. The difference between the path lengths of X-rays reflected (diffracted) from successive planes in the crystal must be an integer multiple of the wavelength for constructive interference to result.

The intensity of such a reflection depends on the population of the atoms on the corresponding planes. Definition of the orientation of the plane in three-dimensional space requires three numbers, for example three direction cosines relating to the standard axes. In crystallography the plane orientation is defined by three Miller

indices, which are integers indicating which fractions of the unit cell edges are cut by the particular plane. Reflection (h,k,l) passes through the x axis at $1/h$ of its length, the y axis at $1/k$ and the z axis at $1/l$.

In the case of a single crystal, this reciprocal lattice pattern consists of discrete intensity maxima on a three-dimensional periodic lattice related to the unit cell in the crystal. The intensities are measured and converted to structure factors, $F(h,k,l)$. The crystal structure is a model of the three-dimensional electron density, $\rho(x,y,z)$, derived from the structure factors. The general expressions for the three-dimensional Fourier transform pair relating $F(h,k,l)$ with $\rho(x,y,z)$, are as follows:

$$\rho(x,y,z) = \frac{1}{V} \sum_h \sum_k \sum_l \{F(h,k,l) \exp[-2\pi i(hx + ky + lz)]\} \quad \dots\dots(2.2)$$

$$= \frac{1}{V} \sum_h \sum_k \sum_l F(h,k,l) \{ \cos[2\pi(hx + ky + lz)] + i \sin[2\pi(hx + ky + lz)] \} \quad \dots\dots(2.3)$$

where V is the volume of the unit cell, $\rho(x,y,z)$ is the relative electron density at the point (x,y,z) and $F(h,k,l)$ is the structure factor for the particular set of indices h, k, l .

The model is refined using the mathematical linear least squares analysis procedure. The problem is nonlinear, but can be successfully refined by being significantly overdetermined, typically ten or more observations per refined variable. The best fit of the model to the set of measured intensity data is obtained by iterative calculation.

Positional disorder is characterized by alternative positions for an atom or group of atoms when one looks at the various unit cells in the crystal. In any given unit cell (or possibly asymmetric unit), one (and only one) of the potential positions

can be occupied. The current case is a bimodal positional disorder. In modeling such a disorder, the two atoms (or groups of atoms) are assigned site occupancy factors of α and $1-\alpha$. Disorder alters the structure factors such that:

$$F_c^2(h, k, l)_{disorder} = [(1-\alpha)F_c(h, k, l) + \alpha F_c(h', k', l')]^2 \quad \dots\dots(2.4)$$

Progress of refinement is monitored by calculated discrepancy indices. R_I is more commonly quoted, perhaps because it is generally the lower number, however, wR_2 is more relevant to the actual refinement process which minimizes the weighted sum of the squares of the discrepancies between the observed intensities, F_o^2 measured on a diffractometer, and the calculated intensities, F_c^2 , provided by the model.

$$R_I = \frac{\sum_{hkl} \left| |F_o| - |F_c| \right|}{\sum_{hkl} |F_o|} \quad \dots\dots(2.5)$$

$$wR_2 = \left[\frac{\sum_{hkl} w(F_o^2 - F_c^2)^2}{\sum_{hkl} wF_o^2} \right]^{1/2} \quad \dots\dots(2.6)$$

where F_o and F_c are the observed and calculated structure factor amplitudes, respectively.

Powder X-ray Diffraction The principles of this technique are a monochromatic beam of X-rays strikes a finely powdered sample that, ideally, has crystals randomly arranged in every possible orientation. In such a powdered sample, the various lattice planes are also present in every possible orientation. For each of the

set planes, therefore, at least some crystal must be oriented at the Bragg angle, θ , to the incident beam and thus, diffraction occurs for these crystals and planes. The diffracted beams may be detected either by surrounding the sample with a strip of photographic film (Debye-Scherrer and Guinier focusing methods) or by using a movable detector, Geiger counter scintillation counter, connected to a chart recorder or computer (diffractometer) for original or other modern powder X-ray diffraction, respectively. This technique was commonly utilized for the phase identification, purity, and differentiation of polymorphs of sample products. Each crystalline phase has a characteristic powder pattern which can be used as a fingerprint for identification purposes. The two variables in a powder pattern are peak position, i.e. d -spacing, which is more useful and capable of precise measurement, and intensity, which can be measured either qualitatively, needed in using the powder fingerprint method to characterize materials and especially in using the *Powder Diffraction File* to identify unknown, or quantitatively, are necessary in order to solve crystal structures, however, more difficult to measure. The normal practice in using powder patterns for identification purposes is to pay most attention to the d -spacing but, at the same time, check that the intensities are roughly correct.

2.2.2 Electron Microscopy

This is widely used in the characterization of the solids to study structure, morphology, and crystallite size, to examine defects and to determine the distribution of elements. An electron microscope is similar in principle to an optical microscope. The electron beam is produced by heating a tungsten filament, and focused by magnetic fields in a high vacuum (the vacuum prevents interactions of the beam with

any extraneous particles in the atmosphere). The very short wavelength of the electrons allows resolution down to 0.1 nm.

Scanning Electron Microscopy (SEM) In this technique, the electrons form a finely focused beam that are rastered across the surface of the sample. Electrons are reflected by the surface of the sample and emitted secondary electrons are detected to give a map of the surface topography of the samples. It is useful for looking at particle size, crystal morphology, magnetic domains, and surface defects. A wide range of magnification can be used, the best achievable being about 2 nm. The samples may need to be coated with gold or graphite to stop charge building up on the surface.

Energy Dispersive X-ray Analysis (EDAX) As discussed above, an electron beam incident on a metal gives rise to the emission of characteristic X-rays from the metal. In electron microscopy, the elements present in the sample also emit characteristic X-rays. These are separated by a silicon-lithium detector, and each signal collected, amplified and corrected for absorption and other effects, to give both qualitative and quantitative analysis of the elements present (for elements of atomic number greater than 11) in the irradiated particle, a technique known as energy dispersive analysis of the X-rays (**EDAX** or **EDX**).

2.2.3 Thermal Analysis

Thermal analysis methods investigate the properties of solids as a function of a change in temperature. They are useful for investigating phase changes, decomposition, loss of water or oxygen, and for constructing phase diagrams.

Thermogravimetric Analysis (TGA) In this method, the weight of a sample is monitored as a function of time as the temperature is increased at a controlled uniform rate. A testing procedure in which changes in weight of a specimen are

recorded as the specimen is heated in air or in a controlled atmosphere such as nitrogen.

Differential Scanning Calorimetry (DSC) DSC measures the amount of heat released by a sample as the temperature is increased or decreased at a controlled uniform rate, and so can investigate chemical reactions and measure heats of reaction for phase change.

2.2.4 Vibrational Spectroscopy

Spectroscopy was originally the study of the interaction between radiation and matter as a function of wavelength (λ). Historically, spectroscopy referred to the use of visible light dispersed according to its wavelength, e.g. by a prism. Later the concept was expanded greatly to comprise any measurement of a quantity as a function of either wavelength or frequency. Thus, it can also refer to a response to an alternating field or varying frequency (measured in cm^{-1} , wavenumber, ν). A further extension of the scope of the definition added energy (E) as a variable, once the very close relationship $E = h\nu$ for photons was realized (h is the Planck constant). A plot of the response as a function of wavelength or more commonly frequency is referred to as a spectrum.

Fourier Transform Infrared (FTIR) Spectroscopy This is a common technique that is useful for identification to the major functional groups in a compound. The identification of these groups depends upon the amount of infrared radiation absorbed and the particular frequency at which these groups absorbed. The frequencies of many infrared absorption bands are characteristic of the specific types of chemical bonds, and this technique finds its greatest utility for qualitative analysis of organic, inorganic, or coordination compounds, thus, is useful to confirm the identity of a particular compound and as a tool to help determine the structure of a

molecule. Significant for the identification of the source of an absorption band are intensity (weak, medium or strong), shape (broad or sharp), and position (cm^{-1}) in the spectrum.

2.2.5 Other Techniques.

CHN elemental analysis This is useful for determining the elemental compositions such as C, H, and N (more precisely empirical formula) of a sample by combusting the sample under conditions where the resulting combustion products can be quantitatively analyzed.

X-ray Fluorescence (XRF) This is an emission technique which utilizes the characteristic X-ray emission spectra of elements, which are generated by, for instance, bombardment with high-energy electrons. The spectra are used in elemental and chemical analysis.

2.3 Research Procedure

The general research procedure below is used after obtaining a sample product in both single crystal and powder forms under hydrothermal reaction conditions. Sample products are subjected to preliminary examination (under an optical microscopy) which indicates how many phases are obtained and particular physical characteristics, such as crystal morphology, color, shape, and size using an optical microscope model B061 Olympus/Sony CCD color video camera with ExwaveHAD polarizing microscope, and in addition, if heterogeneous or multiple phases need to be separated each by hand.

Next, the solids are measured by XRD with checked the phase identification include crystallinity. The experimental XRD pattern result was compared to the PDF library database or the simulated XRD pattern calculated from the single crystal X-ray structural results from the Cambridge Structural Database (CSD) version 5.27 and Inorganic Crystal Structure Database (ICSD) (Fachinformatiionszentrum Karlsruhe, 2005), generated using the computer program Mercury version 2.3 (The Cambridge Crystallographic Data Centre, 2009). The experimental XRD patterns were measured

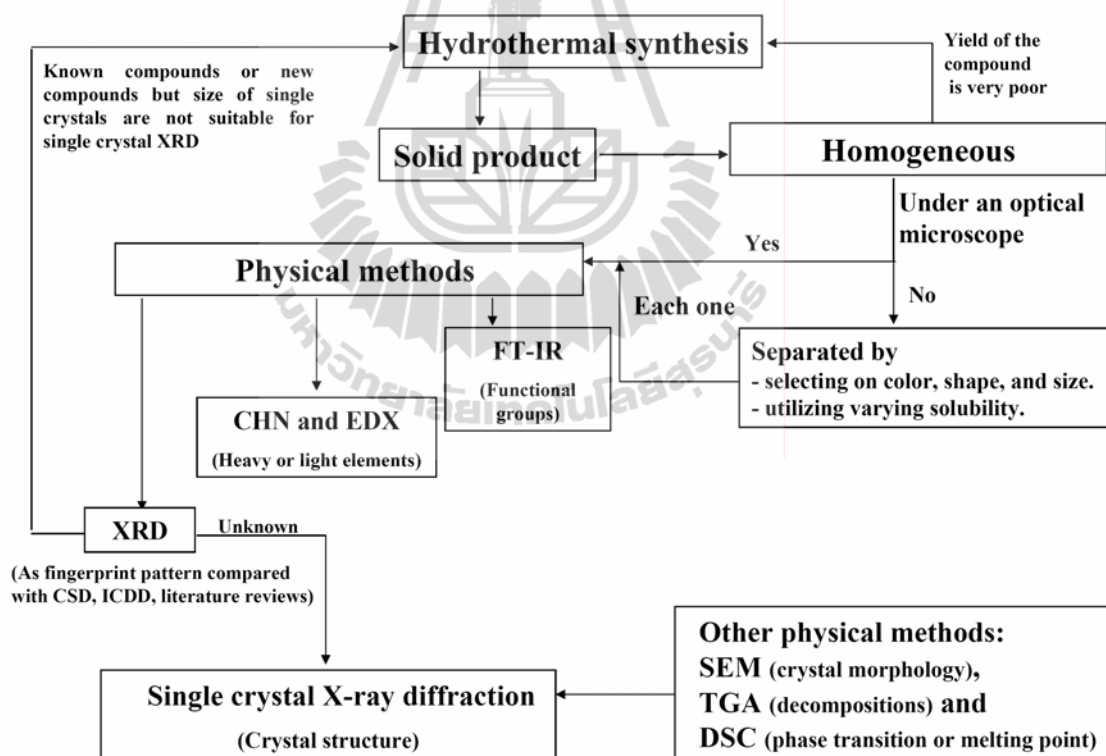


Figure 2.9 The general research procedure.

on a Bruker/Siemens D5005 and a Philips PW 1830 diffractometer equipped with a copper K_{α} -radiation source. As mentioned above no single technique is capable of

providing a complete characterization of a compound. Both the elements and functional groups present in compound are needed for a preliminary check. Heavy element Na and below compositions were measured on a JEOL JSX-3201Z X-ray fluorescence spectrometer and on a JEOL JSM-6400 scanning electron microscope. Light element compositions were determined from MedaC Ltd, Surrey, UK. The infrared spectrum was recorded on Perkin-Elmer Spectrum GX and Perkin-Elmer Spectrum One ($370\text{-}4000\text{ cm}^{-1}$) infrared spectrometers for investigation of functional groups of the compound.

From process above, the compound is confirmed to be a new phase. Next, study the crystal structure, starting by selecting a suitable single crystal and collected data using a Bruker P4-R4 four-circle diffractometer with the computer program XSCAN for cell indexing, data collection or using a Bruker-Nonius D8 diffractometer equipped with Bruker-Nonius Apex CCD detector with computer program SMART (Bruker, 2001b) for unit cell indexing and data collection and SAINT (Bruker, 2001a) for data reduction and corrected for absorption and other geometrically related effects with SADABS (Bruker, 1998). The X-ray structure solution, refinement, and summary tables of the structures were carried out using package SHEXTL version 6.10 (Sheldrick, 1997a,b). The images were illustrated by *ORTEP-III* version 2.02 (Burnett and Johnson, 1996) and *Diamond* version 3.1 (Crystal Impact, 2006).

Other techniques such as thermal analysis are useful to confirm the structure and/or study the phase transition. TGA curve was measured on a TGA 7 Perkin Elmer and a TGA Q5000 V2.4 Build 223 thermogravimetric analyzers. The DSC curve was recorded on DSC 92 Setaram and on a DSC822° Mettler Toledo differential scanning calorimeter equipped with the standard cooling unit and purged with nitrogen gas. Present the crystal morphology or other reason, to get a large image of the crystal

morphology in case some crystal products have very tiny, were photographed on a JEOL JSM-6400 scanning electron microscope.

2.4 References

- Au-Yeung, A. S.-F., Sung, H. H.-Y., Cha, J. A. K., Siu, A. W.-H., Chui, S. S.-Y., and Williams, I. D. (2006). Hydrothermal synthesis of indium tartrates: Structures of the chiral polymer $[\text{In}(\text{L-TAR})^2\text{-H}_2\text{O}]\cdot 0.5\text{H}_2\text{O}$ containing the tartrate trianion, and a microporous hybrid solid $[\text{In}(\text{OH})(\text{D/L-TAR})^2]\cdot 2\text{H}_2\text{O}$. **Inorganic Chemistry Communications**. 9(5): 507-511.
- Brandenburg, K. (2006). *DIAMOND*. Version 3.1. Crystal Impact GbR. Bonn, Germany.
- Burnett, M. N., and Johnson, C. K. (1996). *ORTEP-III: Oak Ridge Thermal Ellipsoid Plot Program for Crystal Structure Illustration*, Report ORNL-6895, Oak Ridge National Laboratory, Oak Ridge, Tennessee.
- Byrappa, K. (1992). **Hydrothermal Growth of Crystal**. Pergamon Press, Oxford. pp. 1.
- Byrappa, K., and Yoshimura, M. (2001). **Handbook of Hydrothermal Technology: a Technology for Crystal Growth and Material Processing**. William Andrew Publishing, Noyes. pp. 1-43.
- Cambride Structural Database. (2006) version 5.27, update May 2006.
- Chainok, K. (2008). **Synthesis and Structural Studies of Hybrid Organic-Inorganic Nanocomposites**. Ph.D. Thesis, Suaranaree University of Technology, Thailand.
- Chirayil, T., Zavalij, P. Y., and Whittingham, M. S. (1998). Hydrothermal synthesis

- of vanadium oxides. **Chemistry of Materials**. 10(10): 2629-2640.
- Davis, M. E., and Lobo, R. F. (1992). Zeolite and molecular sieve synthesis. **Chemistry of Materials**. 4(4): 756-768.
- Laudise, R. A. (1970). **The Growth of Single Crystals**. Prentice-Hall, New York. pp. 1-38.
- Law, T. S.-C., and Williams, I. D. (2000). Organo-directed synthesis of manganese vanadates with variable stoichiometry and dimensionality: 1-D $[(\text{Hen})_2\text{Mn}(\text{VO}_3)_4]$, 2-D $[\text{H}_2\text{en}]_2[\text{Mn}(\text{VO}_3)_6]$, and 3-D $[\text{H}_2\text{en}][\text{MnF}(\text{VO}_3)_3]$. **Chemistry of Materials**. 12(1): 2070-2072.
- Lobachev, A. N. (1973). **Crystallization Processes under Hydrothermal Conditions**. Consultants Bureau, New York. pp. 1-26.
- Millero, F. J. (1982). The effect of pressure on the solubility of minerals in water and seawater. **Geochimica et Cosmochimica Acta**. 46(1): 11-22.
- Morey, G. W., and Niggli, P. (1913). The hydrothermal formation of silicates, a review. **Journal of the American Chemical Society**. 35(9): 1086-1130.
- Rabenau, A. (1985). The role hydrothermal synthesis in preparative chemistry. **Angewandte Chemie International Edition in English**. 24(12): 1026-1040.
- Roy, R. (1994). Acceleration the kinetics of low-temperature inorganic synthesis. **Journal of Solid State Chemistry**. 111(1): 11-17.
- SADABS Version 2.03 (1998), SAINT Version 6.26a (2001a), SMART Version 5.625 (2001b), Bruker Analytical X-ray Systems Inc., Madison, Wisconsin, USA.
- Sheldrick, G. M. (1997a). *SHELX-97 Program for the Solution and Refinement of Crystal Structures*, University of Göttingen, Germany.

- Sheldrick, G. M. (1997b). *SHELXTL*. Version 6.1. Bruker Analytical X-ray Systems Inc., Madison, Wisconsin, USA.
- Smart, L. E., and Moore, E. A. (2005). **Solid State Chemistry: An Introduction**. 3rd edition, CRC press, Boca Raton. pp. 77-118.
- Speight, J. G. (2005). **Lange's Handbook of Chemistry: Section 3 Spectroscopy**. 16th edition, McGraw-Hill, New York. pp. 3-1.
- The Cambridge Crystallographic Data Centre (2009). Mercury version 2.3. The Cambridge Crystallographic Data Centre, Cambridge, United Kingdom.
- Thushari, S., Cha, J. A. K., Sung, H. H.-Y., Chui, S. S.-Y., Leung, A. L.-F., Yen, Y.-F., and Williams, I. D. (2005). Microporous chiral metal coordination polymers: hydrothermal synthesis, channel engineering and stability of lanthanide tartrates. **Chemical Communications**. (44): 5515-5517.
- West, A. R. (1999). **Basic Solid State Chemistry**. 2nd edition, John Wiley & Sons, Chichester. pp. 167-206
- Wilson, S. T., Lok, B. M., Messina, C. A., Cannan, T. R., and Flanigen, E. M. (1982). Aluminophosphate molecular sieves: a new class of microporous crystalline inorganic solids. **Journal of the American Chemical Society**. 104(4): 1146-1147.
- Yoshimura, M., and Suchanek, W. (1997). In situ fabrication of morphology-controlled advanced ceramic materials by Soft Solution Processing. **Solid State Ionics**. 98(3-4): 197-208.

CHAPTER III

HYDROTHERMAL SYNTHESSES AND STRUCTURAL CHARACTERIZATIONS OF HYBRID ORGANIC-INORGANIC MATERIALS OF DIVALENT METAL VANADATES

3.1 Introduction

Hybrid organic-inorganic materials based on vanadium oxide have attracted considerable interest because of their wide applications in catalysis, optical and magnetic properties (Lin and Maggard, 2008; Williams, Law, Sung, Wen, and Zhang, 2000). Vanadium has a large variety of valency and coordination geometries available, tetrahedral, trigonal bipyramidal, square pyramidal and octahedral coordination environments in various oxidation states (+5, +4, +3). It can be combined with other metals and organic molecules leads to the possibility of designing a variety of structures and properties. The hydrothermal technique provides a means to overcome the differential solubility of inorganic oxides and organic molecules into a single structure at low temperature as found in our previous work. Williams et al. (2000) have successfully synthesized the first examples of 3-D porous divalent manganese vanadate compounds of $[\text{H}_2\text{en}][\text{Mn}_3(\text{V}_2\text{O}_7)_2(\text{H}_2\text{O})_2]$, and $[(\text{Hpn})_2\text{Mn}_3(\text{V}_2\text{O}_7)_2]$ using simple aliphatic diamines, en and pn (propane-1,3-diamine), as templates and show good magnetic properties, and in $[\text{H}_2\text{en}]_2[\text{MnF}(\text{VO}_3)_3]$ utilizing the organic reagent as structure directing agent with reactions addition within the same year, Law and

Williams (2000) progressed more with the same system, for example, 1-D $[(\text{Hen})_2\text{Mn}(\text{VO}_3)_4]$, 2-D $[\text{H}_2\text{en}]_2[\text{Mn}(\text{VO}_3)_6]$ and 3-D at pH about 6-8 and at 110-140 °C.

We continued to explore the divalent metal vanadates under hydrothermal conditions. This work studies, zinc and cadmium as the divalent metal. en and its derivatives are chain aliphatic diamines which can act as a monodentate, bidentate ligand, bridging or chelating ligand, or templating agent depending on their pKa values (en: $\text{p}K_{\text{a}1} = 10.71$ and $\text{p}K_{\text{a}2} = 7.56$; enMe: $\text{p}K_{\text{a}1} = 10.00$ and $\text{p}K_{\text{a}2} = 7.13$).

Herein, we report a new 3-D chiral network and an opened framework structures of divalent zinc vanadate. $(\text{en})\text{Zn}_2\text{V}_2\text{O}_7$ (**3a**) composed of V(V) tetrahedra as pillars linked between the layers formed from polymeric double helix of zinc coordination complexes and zinc vanadate. While $(\text{HenMe})_2\text{ZnV}^{4+}_4\text{V}^{5+}_4\text{O}_{20}$ (**3d**) containing zinc (II) complexes as pillars linked to anionic mixed-valence $\text{V}^{4+}/\text{V}^{5+}$ layers. Others, zinc (II) complexes as cross-linkers of infinite metavanadate chains: 1-D double chains, $(\text{Hen})_2\text{CdV}_4\text{O}_{12}$ (**3c**), 2-D double layers, $(\text{en})\text{ZnV}_2\text{O}_6$ (**3b**), and 3-D opened framework, $(\text{enMe})_2\text{Zn}(\text{VO}_3)_2 \cdot 2\text{H}_2\text{O}$ (**3e**).

3.2 Experimental

3.2.1 Materials, Apparatus, and Syntheses

All chemicals were of reagent grade and used without further purification. Elemental analyses (C, H, and N) were performed by Medac Ltd, Surrey, UK. The powder X-ray diffraction patterns were recorded on a Philips PW 1830 diffractometer equipped with a Cu $K\alpha$ X-ray source ($\bar{\lambda} = 1.54062 \text{ \AA}$) for the angular range $2\theta = 5\text{-}50^\circ$. The infrared spectra were measured on a Perkin Elmer Spectrum One and

Spectrum GX (400-4000 cm^{-1}) infrared spectrophotometer using pressed KBr pellets. The TGA analysis curves were recorded on a TGA Q5000 V2.4 Build 223 instrument a flow of air with a heating rate of $10\text{ }^\circ\text{C min}^{-1}$.

3.2.2 Synthesis of Compound $(\text{en})\text{Zn}_2\text{V}_2\text{O}_7$ (**3a**) and $(\text{en})\text{Zn}(\text{VO}_3)_2$ (**3b**)

A mixture of 190 mg $\text{Zn}(\text{OAc})_2 \cdot 2\text{H}_2\text{O}$, 182 mg V_2O_5 , 0.10 mL en, and 2.00 mL H_2O in the approximate mole ratio of 1:1:1:111 was stirred in a 23 mL Teflon-lined cup for 30 minutes, sealed in an autoclave, and heated at $110\text{ }^\circ\text{C}$ for 2 days. After the mixture was cooled to room temperature, the two different crystal morphologies of purple crystals (Figure 3.1) were filtered, washed with distilled H_2O , and dried in air at ambient temperature. Compound **3a**, $(\text{en})\text{Zn}_2\text{V}_2\text{O}_7$ (Krachodnok, Haller, and Williams, 2008), as the major product (100 mg, yield: ca 25% based on vanadium pentoxide) and compound **3b** as minor product (16 mg, yield: ca 5% based on vanadium pentoxide) were separated by hand under an optical microscope leaving the residual white powder of ZnO. The initial reaction pH was altered to 11-13 by addition of 0.5-1.0 mmol KOH. The yield of **3a** can be increased to ~69% (140 mg) in pure phase by substituting vanadium base (NH_4VO_3) for the vanadium acid (V_2O_5). Similar experiments with **3b** failed to improve the yield. If the initial reaction pH about 6-9, the orange-red crystals of $[\text{H}_2\text{en}]_3[\text{V}_{10}\text{O}_{28}] \cdot 2\text{H}_2\text{O}$ (Ninlaus, Riou, and Féray, 1996), and the colorless crystals of $[\text{H}_2\text{en}][\text{V}_2\text{O}_6]$ (Khan, Hope, Cevik, Zheng, and Powell, 2000), were isolated, respectively.

3.2.3 Synthesis of Compound $(\text{Hen})_2\text{Cd}(\text{VO}_3)_4$ (**3c**)

The procedure is similar to formation of **3a** and **3b**, using $\text{Cd}(\text{OAc})_2 \cdot 2\text{H}_2\text{O}$ instead of $\text{Zn}(\text{OAc})_2 \cdot 2\text{H}_2\text{O}$ with same mole ratio and heated at $110\text{ }^\circ\text{C}$ for 2 days. After the mixture was cooled to room temperature, the dark green powder of $[\text{H}_2\text{en}]_{0.5}[\text{V}_2\text{O}_5]$

(Riou and Féray, 1995a,b; Zhang, Haushalter, and Clearfield, 1996) as a major product and the pale purple crystals of **3c** as a minor product were filtered, washed with distilled H₂O, and dried in air at ambient temperature with the yield of **3c** is 60 mg (ca 5% based on vanadium pentoxide), were separated by hand under an optical microscope leaving the residual dark green powder of [H₂en]_{0.5}[V₂O₅] (Riou and Féray, 1995a,b; Zhang, Haushalter, and Clearfield, 1996).

3.2.4 Synthesis of Compound (HenMe)₂Zn(V₂O₅)₄ (**3d**)

The procedure is similar to formation of **3a** and **3b** except enMe is used instead of en with an initial reaction pH of ~9 and heated at 180 °C or addition enMe 2-3 mmol and heated at 110 °C, the isolation of the pure phase of black crystals of compound **3d** (yield: 184 mg (ca 78%) and 201 mg (ca 85%), respectively, based on vanadium pentoxide). Either compound **3d** or K₂V₃O₈ (Galy and Carpy, 1975; Liu and Greedan, 1995) were formed by increasing the reaction pH to 11 by 1.0 mmol KOH and heated at 110 °C and 180 °C.

3.2.5 Synthesis of Compound (enMe)₂Zn(VO₃)₂·2H₂O (**3e**)

The procedure is similar to formation of **3d** except the amount of enMe was increased to 4-5 mmol with an initial reaction pH of ~11, heated at 110 °C for 2 days, cooled to room temperature, and the colorless solution kept at ambient temperature for two weeks to afford the pure pale brown crystals of compound **3e** (yield: 140 mg (ca 31%) based on vanadium pentoxide).

3.2.6 Powder X-ray Diffraction (XRD)

Figure 3.2 shows powder XRD patterns were recorded for the bulk sample of **3a** and **3b** compared to the simulated patterns of **3a**, **3b**, [H₂en][V₂O₆] (Khan, Hope, Cevik, Zheng, and Powell, 2000) and (en)₂ZnV₆O₁₄ (Zhang, DeBord, O'Connor,

Haushalter, Clearfield, and Zubieta, 1996) which were calculated from the single crystal X-ray structural results as a check that the bulk materials do not contain multiple phases in **3a** when using NH_4VO_3 substituted for V_2O_5 in Figure 3.2(i) and mixed phase **3a** and **3b** in Figure 3.2(f-g). Figures 3.3, 3.4 and 3.5 show powder XRD patterns were recorded for the bulk sample of **3c**, **3d** and **3e** compared to its simulated patterns which were calculated from the single crystal X-ray structural results as a check that the bulk materials do not contain multiple phases, respectively, and with comparable simulated patterns of the isomorphous $(\text{Hen})_2\text{Mn}(\text{VO}_3)_4$ structure (Law and Williams, 2000) with **3c** and the isostructural series between **3d** (space group $P2_1/c$) and $(\text{HenMe})_2\text{Cd}(\text{V}^{4+}\text{V}^{5+}\text{O}_5)_4$, space group $C2/m$ (Zhang, Shi, Yang, Chen, and Feng, 2000) as illustrated in Figures 3.3 and 3.4, respectively.

Table 3.1 Hydrothermal Synthetic Conditions.

Reagents (mmol)			Conditions		Product Colors
V ₂ O ₅	M(OAc) ₂ ·2H ₂ O	Organic Diamine	Initial and Final pH	Temperature and Times	(% Yield Based on V ₂ O ₅)
1	1 (Zn)	en	6-7 and 7	110-140 °C and 2d	Orange-red crystals of [H ₂ en] ₃ [V ₁₀ O ₂₈]·H ₂ O (Ninlaus et al., 1996)
1	1 (Zn)	en	9 and 8	110-140 °C and 2d	Colorless crystals of [H ₂ en][V ₂ O ₆] (Xu et al., 1996) and an uncharacterized green powder
1	1 (Zn)	en	11-13 ^b and 8-9	110 °C and 2d	Two different crystal morphologies of purple crystals (ca 25% for 3a and 5% for 3b) and white powder of ZnO
1 ^a	1 (Zn)	en	11-13 ^b and 8-9	110 °C and 2d	Purple crystal of 3a (ca 69%)
1	1 (Cd)	en	11 ^b and 7	110 °C and 2d	Pale purple crystals of 3c (ca 5%) and dark green powder of [H ₂ en] ₂ [V ₂ O ₅] (Riou and Féray, 1995b)
1	1 (Zn)	(5) en	10 and 10	110 °C and 2d	Black crystals of (en) ₂ ZnV ₆ O ₁₄ (Zhang et al., 1996)
1	1 (Zn)	enMe	9 and 8	180 °C and 2d	Black crystals of 3d (ca 78%)
1	1 (Zn)	enMe	11 ^b and 9	110 °C and 2d	Black crystals of K ₂ V ₃ O ₈ (Galy et al., 1975) (ca 60%) and black powder of 3d (ca 40%) and
1	1 (Zn)	enMe	11 ^b and 9	140 °C and 2d	Black crystals of K ₂ V ₃ O ₈ (ca 80%)
1	1 (Zn)	enMe	11 ^b and 9	180 °C and 2d	Black powder of 3d (ca 50%) and black crystals of K ₂ V ₃ O ₈ (ca 50%)
1	1 (Zn)	(2-3) enMe	10-11 and 8-9	110 °C and 2d	Black crystals of 3d (ca 85%)
1	1 (Zn)	(4-5) enMe	11 ^b and 9	110 °C and 2d	Colorless solution with standing at ambient for two weeks (pale-brown prism, 3e , ca 31%)

^aIncreasing the yield of **3a** by substituting NH₄VO₃ for V₂O₅. ^bAdjusted reaction pH by 0.50-1.0 mmol KOH.

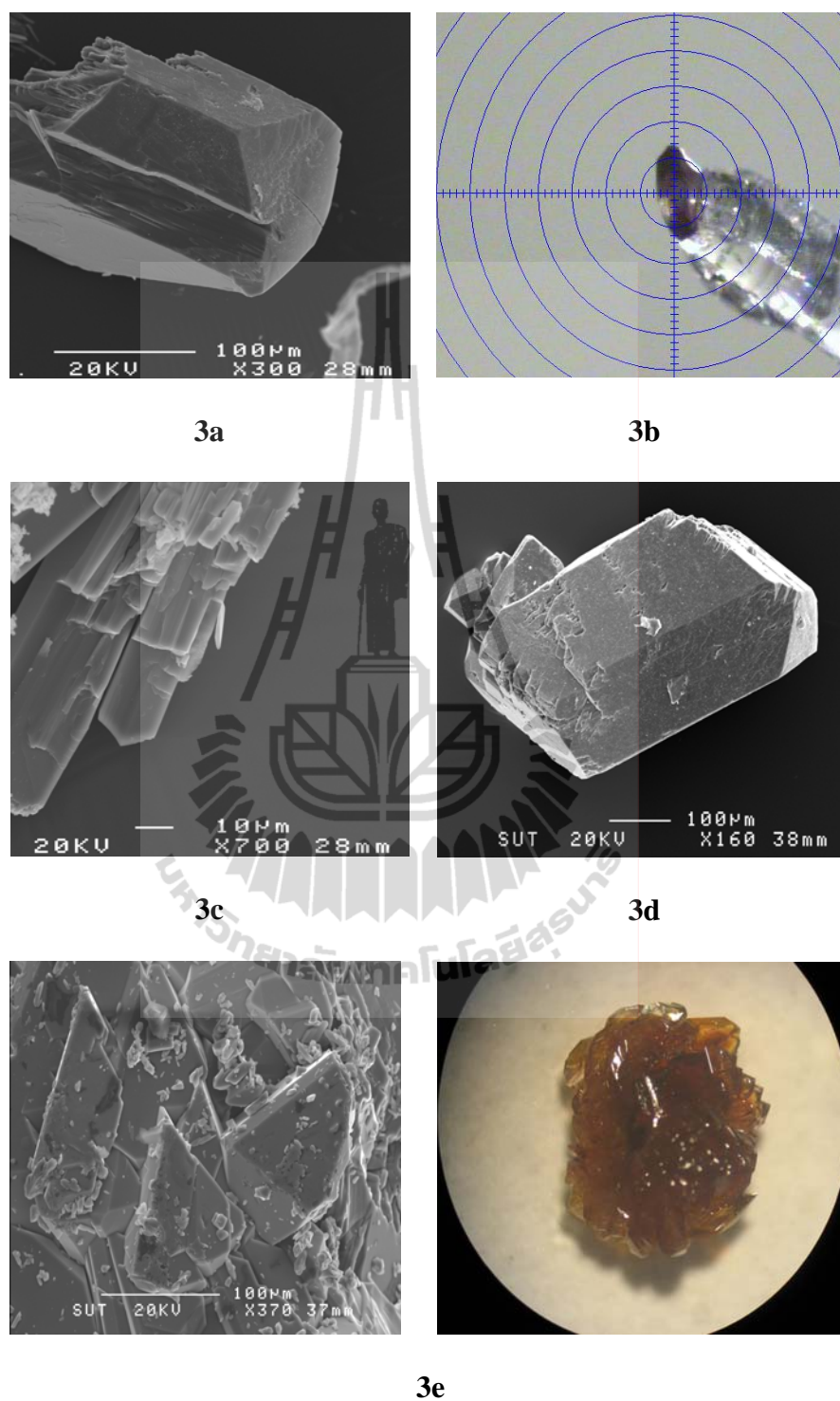


Figure 3.1 Crystal morphologies of compound 3a-e.

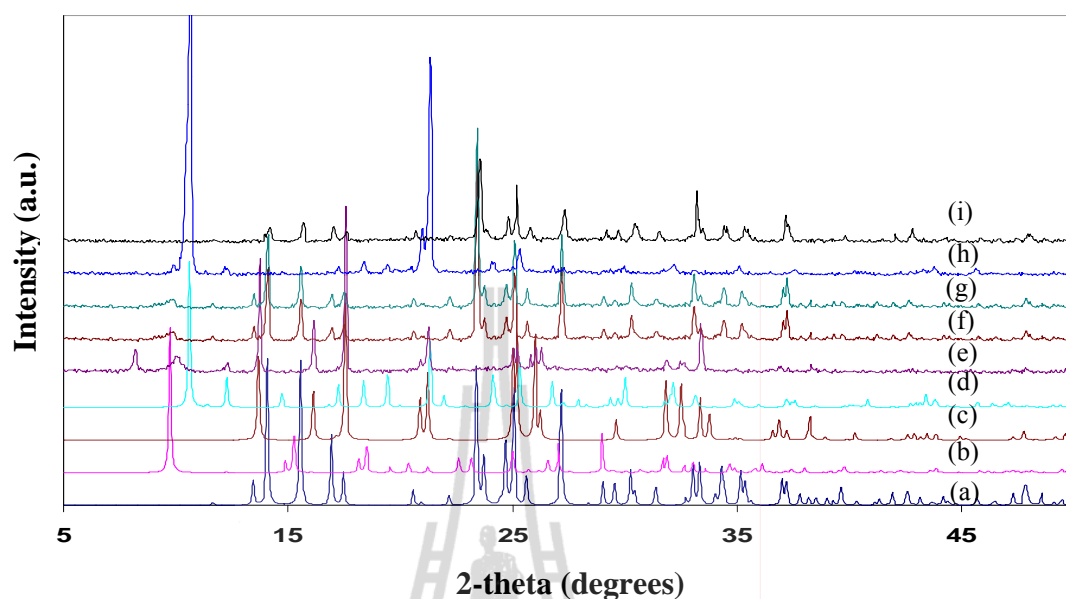


Figure 3.2 Comparing simulated powder XRD patterns of (a) **3a**, (b) **3b**, (c) $[\text{enH}_2][\text{V}_2\text{O}_6]$ (Xu, Yang, Wang, Ma, Sun, Xu, and Huang, 1996), and (d) $(\text{en})_2\text{ZnV}_6\text{O}_{14}$ (Zhang, DeBord, O'Connor, Haushalter, Clearfield, and Zubieta, 1996), with experimental powder XRD patterns of 1 mmol en at (e) pH 9, (f) pH 11 and (g) pH 13, and with (h) 5 mmol en at pH 9, and (i) substituted NH_4VO_3 for V_2O_5 .

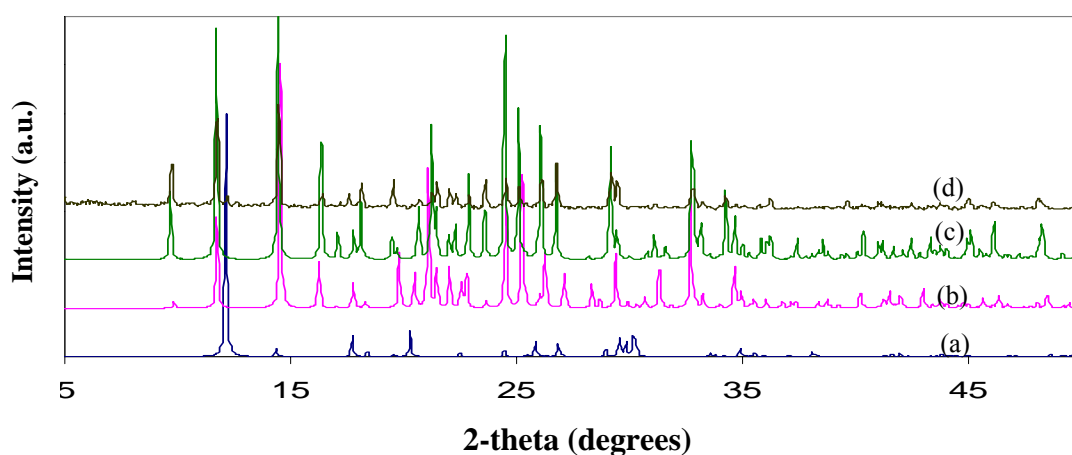


Figure 3.3 Comparing of (a) simulated $[\text{H}_2\text{en}]_{0.5}[\text{V}_2\text{O}_5]$ (Riou and Féray, 1995a,b) and (b) $(\text{Hen})_2\text{Mn}(\text{VO}_3)_4$ (Law and Williams, 2000) with (c) simulated and (d) experimental powder XRD patterns of **3c**.

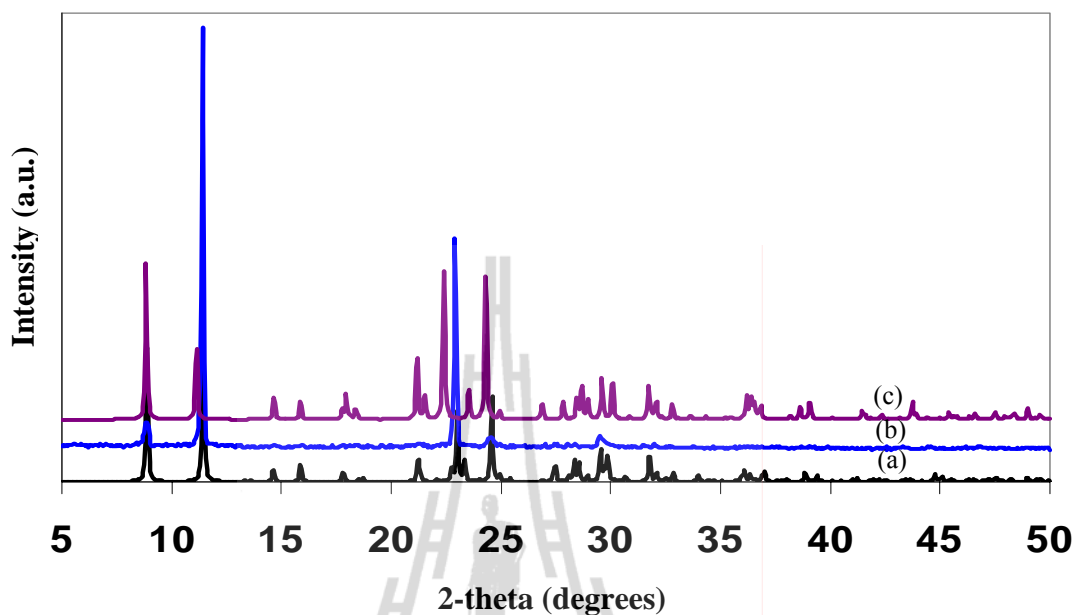


Figure 3.4 Comparing of (a) simulated and (b) experimental XRD patterns of **3d** (space group $P2_1/c$) with (c) simulated $(\text{HenMe})_2\text{Cd}(\text{V}^{4+}\text{V}^{5+}\text{O}_5)_4$ (space group $C2/m$) (Zhang, Shi, Yang, Chen, and Feng, 2000).

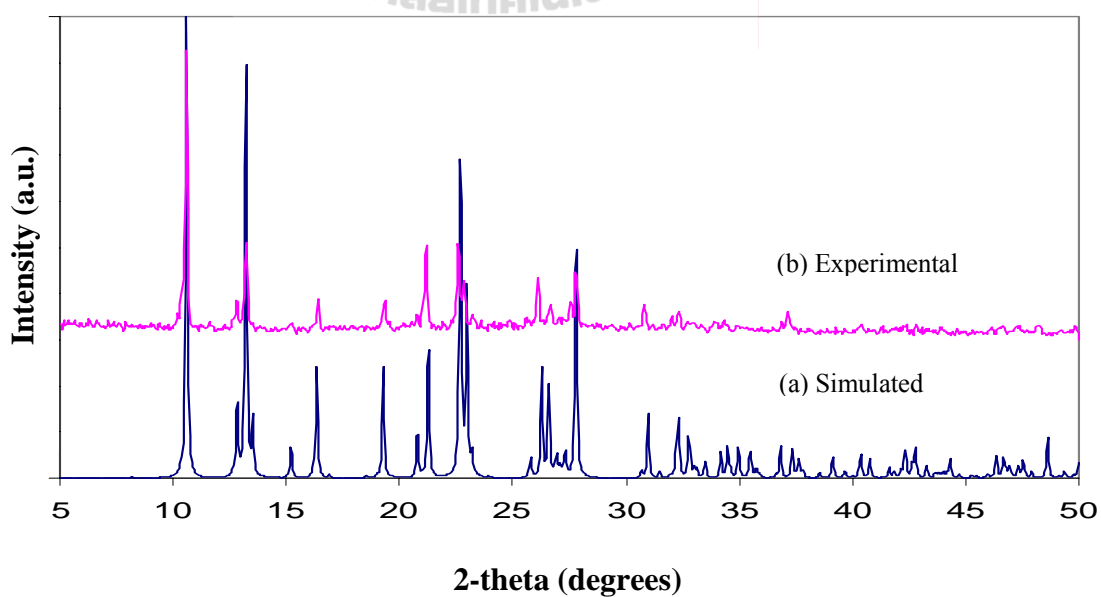


Figure 3.5 Comparing of (a) simulated and (b) experimental powder XRD patterns of **3e**.

3.2.7 X-Ray Crystallography

Suitable single crystals of the five compounds for single-crystal X-ray diffraction were selected and mounted on a thin glass fiber. Intensity data were collected at 25 ± 2 °C for **3a** and **3c** and at -173 ± 2 °C for **3b**, **3d** and **3e** on a Bruker-Nonius SMART APEX CCD diffractometer equipped with a graphite-monochromated Mo $K\alpha$ X-radiation source ($\bar{\lambda} = 0.71073$ Å). Unit cell parameters were determined by standard procedures and the data were processed with the program SAINT (Bruker, 2001a,b) and corrected for absorption and other geometrically related effects with SADABS (Bruker, 1998). Intensity data of compound **3c** was collected at 25 ± 2 °C on an Oxford Diffraction Kappa diffractometer equipped with a Cu $K\alpha$ X-radiation source ($\bar{\lambda} = 1.54184$ Å). The structures were solved by direct methods and refined by full-matrix least-squares refinement on F^2 using SHELXTL-97 (Sheldrick, 2000). Atoms C(2A) and C(2B) of [HenMe]⁺ in **3d** occupy disordered positions, each assigned an occupancy factor of 0.5. The [Hen]⁺ hydrogen atoms on N(1) and N(2) atoms in compound **3c** and the [HenMe]⁺ hydrogen atoms on N(1), C(1), and C(2) atoms in compound **3d** and all enMe hydrogen atoms in compound **3e**, except C6 were located from difference Fourier maps. The other hydrogen atoms were placed in calculated and idealized geometrical positions using geometrical constraints [C–H = 0.970 Å, for **3a**, **3c**, and **3d**; 0.980 Å for **3e**; 0.990 Å for **3b**, N–H = 0.900 Å for **3a** and **3d**; 0.920 Å for **3b** and $U_{\text{iso}}(\text{H}) = 1.2U_{\text{eq}}(\text{C}, \text{N})$]. Experimental X-ray data for **3a-e** are given in Table 3.2. Fractional coordinates and atomic displacement parameters are listed in Tables A1-A5 (Appendix A) and the selected bond lengths and bond angles are given in Tables 3.4-3.7, respectively. The summary of metal coordination geometries and bond valence sums are listed in Table 3.8. The images are illustrated

by *ORTEP-III* (Burnett and Johnson, 1996) and *DAIMOND* version 3.1 (Crystal Impact, 2006).

3.3 Results and Discussion

3.3.1 Hydrothermal Syntheses and Structural Analyses of Compound 3a-e

As progression of an organically templated manganese vanadate compounds in previous work, we have been continued to explore the inorganic-organic hybrid vanadates of V_2O_5 - $M(OAc)_2$ -organic diamines, $M = Zn$ and Cd under hydrothermal conditions as listed in Table 3.1.

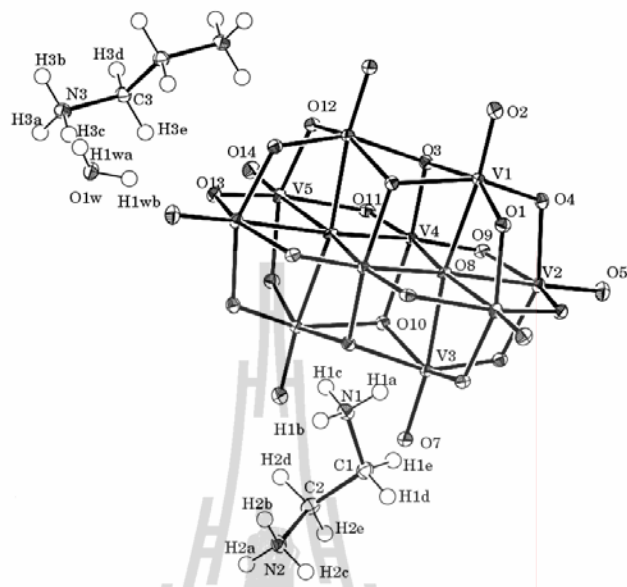
Study of the V_2O_5 - $M(OAc)_2$ -en system in a mole ratio 1:1:1 with the reaction pH ~6-9 and either heated at 110 °C or 140 °C, orange-red crystals, $[H_2en]_3[V_{10}O_{28}] \cdot 2H_2O$ (Ninlaus, Riou, and Féray, 1996), and colorless crystals, $[H_2en][V_2O_6]$ (Khan, Hope, Cevik, Zheng, and Powell, 2000), were isolated, respectively. Their crystal structures are illustrated in Figure 3.6. Increasing the reaction pH to ~11-13 and heating to 110 °C, two purple crystal morphologies of **3a** and **3b** were isolated in low yield. Substituting vanadium base (NH_4VO_3) for the vanadium acid (V_2O_5), the yield of **3a** increases to 69 % in pure phase by elemental analysis as listed in Table 3.10 and powder XRD patterns as shown in Figure 3.2, while the experiments of **3b** failed. Increasing the reaction temperature, the yield of **3a** decreased. In an excess of en, the black crystals, a 3-D mixed-valence metal nanoporous structure of $(en)_2Zn(V^{4+})_4(V^{5+})_2O_{14}$ with a 1-D rectangular channel of 4.90 x 10.27 Å (Zhang, DeBord, O'Connor, Haushalter, Clearfield, and Zubieta, 1996) as illustrated in Figure 3.7, and were formed in pure phase studied by powder XRD pattern as shown in Figure 3.2.

Table 3.2 X-ray Crystallographic Data of Compound **3a-e**.

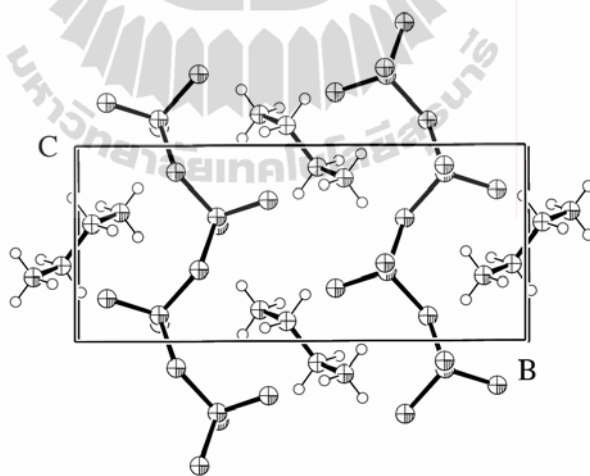
Compound	3a	3b	3c	3d	3e
Crystal data					
Chemical formula	C ₂ H ₈ N ₂ O ₇ V ₂ Zn ₂	C ₂ H ₈ N ₂ O ₆ V ₂ Zn	C ₄ H ₁₈ N ₄ O ₁₂ V ₄ Cd	C ₆ H ₂₂ N ₄ O ₂₀ V ₈ Zn	C ₆ H ₂₄ N ₄ O ₈ V ₂ Zn
M _r	404.72	323.35	630.38	943.17	447.49
Temperature (°C)	25±2	-173±2	25±2	-173±2	-173±2
Crystal system, space group	Monoclinic, <i>P2</i> ₁	Monoclinic, <i>P2</i> ₁ / <i>c</i>	Monoclinic, <i>P2</i> ₁ / <i>n</i>	Monoclinic, <i>P2</i> ₁ / <i>c</i>	Monoclinic, <i>C2</i>
Unit cell dimensions (Å, °)	<i>a</i> = 7.0885(7) <i>b</i> = 8.6040(9) <i>c</i> = 8.1869(8) <i>β</i> = 112.224(2)	<i>a</i> = 5.8422(6) <i>b</i> = 18.1421(18) <i>c</i> = 7.9208(8) <i>β</i> = 97.264(2)	<i>a</i> = 5.771(3) <i>b</i> = 18.171(6) <i>c</i> = 8.428(14) <i>β</i> = 101.43(8)	<i>a</i> = 6.177(3) <i>b</i> = 15.427(6) <i>c</i> = 13.255(5) <i>β</i> = 102.138(6)	<i>a</i> = 10.4919(7) <i>b</i> = 13.8172(7) <i>c</i> = 10.8550(6) <i>β</i> = 91.721(1)
Volume (Å ³)	462.22(8)	832.79(15)	866.2(15)	1234.8(9)	1572.93(16)
<i>Z</i>	2	4	2	2	4
<i>D</i> _{calc} (Mg m ⁻³)	2.908	2.579	2.417	2.537	1.09
Radiation type, wavelength (Å)	Mo, <i>Kα</i> , 0.71073	Mo, <i>Kα</i> , 0.71073	Cu, <i>Kα</i> , 1.54184	Mo, <i>Kα</i> , 0.71073	Mo, <i>Kα</i> , 0.71073
<i>θ</i> _{range} (°)	2.69-28.30	2.25-27.10	4.87-70.36	2.05-27.00	1.88-28.27
<i>μ</i> (mm ⁻¹)	7.103	5.054	27.756	3.931	2.717
Crystal form, color	Prism, Purple	Prism, Purple	Needle, Pale purple	Block, Black	Prism, Pale-brown
Crystal size (mm)	0.04x0.04x0.07	0.05x0.10x0.12	0.02x0.01x0.06	0.04x0.10x0.10	0.20x0.20x0.10
Data collection					
Diffractometer	Bruker-Nonius Smart Apex CCD	Bruker-Nonius Smart Apex CCD	Oxford Diffraction Kappa	Bruker-Nonius Smart Apex CCD	Bruker-Nonius Smart Apex CCD

Table 3.2 (Continued).

Compound	3a	3b	3c	3d	3e
Data collection method	ω scans	ω scans	ω scans	ω scans	ω scans
Absorption correction	Multi-scan	Multi-scan	Multi-scan	Multi-scan	Multi-scan
T_{max}, T_{min}	1.000, 0.759	–	–	–	1.000, 0.895
No. of measured, independent, and observed [$I > 2\sigma(I)$] reflections	4982, 2170, 1949	4713, 1830, 1623	3830, 1569, 1349	6630, 2650, 2149	9263, 3694, 3550
R_{int}	0.0367	0.0221	0.0713	0.0549	0.0231
θ_{max} (°)	28.30	27.10	70.36	27.00	28.27
Completeness to theta	97.8%(theta = 28.30)	99.0%(theta = 27.10)	95.0%(theta = 70.36)	98.5%(theta = 27.00)	97.5%(theta = 28.27)
Range of h, k, l	$-8 \leq h \leq 9,$ $-11 \leq k \leq 11,$ $-10 \leq l \leq 9$	$-7 \leq h \leq 5,$ $-23 \leq k \leq 22,$ $-7 \leq l \leq 10$	$-6 \leq h \leq 7,$ $-22 \leq k \leq 21,$ $-10 \leq l \leq 7$	$-7 \leq h \leq 7,$ $-12 \leq k \leq 19,$ $-16 \leq l \leq 16$	$-13 \leq h \leq 13,$ $-18 \leq k \leq 18,$ $-14 \leq l \leq 14$
Refinement	F^2	F^2	F^2	F^2	F^2
Refinement on	0.0291, 0.0559, 1.007	0.0238, 0.0603, 1.089	0.0648, 0.1866, 1.166	0.0746, 0.1822, 1.144	0.0298, 0.0726, 1.100
$R[F^2 > 2\sigma(F^2)], wR_2(F^2), S$	2170	1623	1569	2149	3550
No. of reflections	136	118	135	205	278
No. of parameters	Geometrically idealized	Geometrically idealized	Geometrically idealized	Geometrically idealized	Geometrically idealized
H-atom treatment	0.000	0.001	0.091	–	–
$(\Delta/\sigma)_{max}$	0.008(18)	–	–	–	0.151(13)
Absolute structure parameter	0.519, -0.591, 0.131	0.731, -0.575, 0.112	1.321, -1.922, 0.262	1.880, -1.372, 0.264	0.882, -0.392, 0.100
$\Delta\rho_{max, min, err}$ (e Å ⁻³)					



(a) $[\text{H}_2\text{en}]_3[\text{V}_{10}\text{O}_{28}] \cdot 2\text{H}_2\text{O}$ at $-173\text{ }^\circ\text{C}$.



(b) $[\text{H}_2\text{en}][\text{V}_2\text{O}_6]$ (Khan, Hope, Cevik, Zheng, and Powell, 2000).

Figure 3.6 Crystal structures of (a) decavanadate and (b) metavanadate.

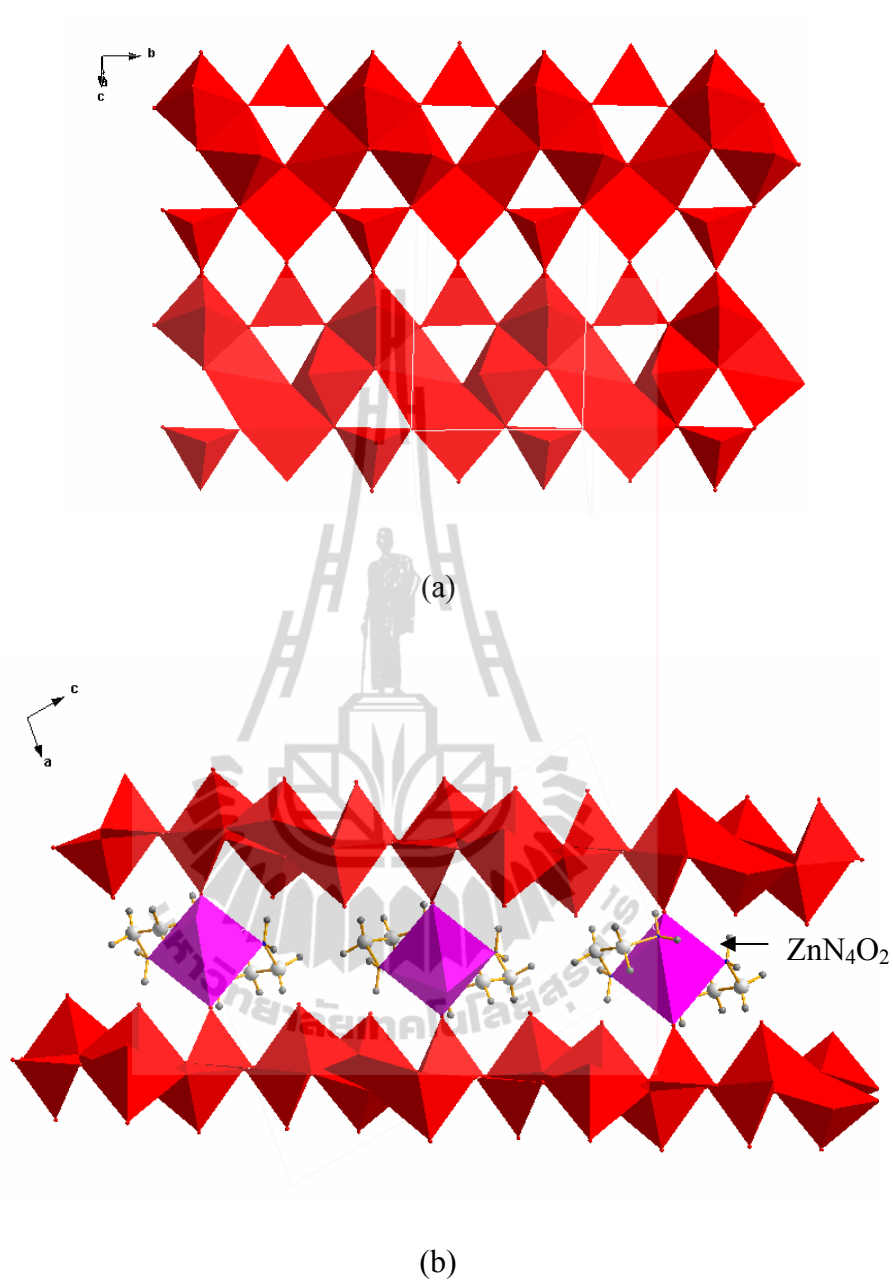


Figure 3.7 Polyhedral representations of (a) sheets perpendicular to the a axis and (b) ZnO_2N_4 pillars forming a 0-D rectangular channel along the b axis in $(en)_2ZnV_6O_{14}$ (Zhang, DeBord, O'Connor, Haushalter, Clearfield, and Zubieta, 1996).

The single crystal X-ray diffraction shows that compound **3a** and **3b** crystallize in the monoclinic system with chiral space group $P2_1$, the Flack absolute structure

parameter of -0.008(18) and with centrosymmetric space group $P2_1/c$, respectively. Both crystal structures are significant different.

3a, (en) $Zn_2V_2O_7$, is a 3-D chiral network. There are two crystallographically distinct V^{5+} atoms and two crystallographically distinct Zn^{2+} atoms in the structure of **3a** (Figure 3.8(a)). Both V^{5+} atoms have distorted tetrahedral geometries, in which the V–O bond lengths are in the range 1.649(5)-1.820(4) Å and the O–V–O bond angles are in the range 108.0(2)-112.3(2)°, with one corner shared with a neighbor forming a common $V_2O_7^{4-}$ dimer unit or pyrovanadate with a V(1)–O(1)–V(2) bond angle of 139.9(2)°. The comparison of the V–O–V bond angles to those pyrovanadate in literature are vary from 180° in (en) $Mn_2(V_2O_7)$ (Cao, Zheng, Fang, and Yang, 2010), to 149.3° in $Zn_2V_2O_7$ (Gopal and Calvo, 1973), to 143.0° in $K_2(VO)V_2O_7$ (Galy and Carpy, 1975), to 140.0° in $Mn_2V_2O_7$ (Gopal and Calvo, 1974), to 136.4° in $[H_2en][Mn_3(V_2O_7)_2(H_2O)_2]$ (Williams, Law, Sung, Wen, and Zhang, 2000) as well as to 136.9° in $K_2ZnV_2O_7$ and to 111.1° in $Ni_2V_2O_7$ (Sauerbrei, Faggiani, and Calvo, 1974). The pyrovanadate unit is also bound to seven separate zinc(II) complexes using one μ_3 -O(4) oxygen and five μ_2 -O(2,3,5,6,7) bridging atoms as shown in Figure 3.8(b). Three of the Zn^{2+} atoms exhibit distorted $Zn(1)O_3N$ tetrahedral geometries ($d[Zn-O]_{(av)} = 1.964$ Å, $d[Zn-N] = 2.014$ Å), and the other four exhibit less common distorted $Zn(2)O_4N$ trigonal bipyramidal geometries ($d[Zn-O]_{(av)} = 2.075$ Å, $d[Zn-N] = 2.015$ Å). The bond lengths and angles are listed in Table 3.3. The en ligand bridges adjacent Zn sites. The most interesting feature of **3a** is the helical structure formed from a –Zn(1)–en–Zn(2)–O(4)– outer strand (Type A helical coil made of seven atom repeating units) and a much tighter –V(2)–O(3)–Zn(2)–O(6)– inner strand (Type B helical coil made up of four atom repeating units) pinched together at the Zn

coordination centers and propagated by the two-fold screw axes parallel to the crystallographic *b*-axis at 0, *y*, ½ (O(6) atom). The approximate diameter and period of the helices are 7.089 and 8.604 Å, respectively (Figure 3.9(a)).

Surprisingly, the en in **3a** acts as a bridging ligand between two same metal sites with different coordination geometries, Zn tetrahedra-en-Zn trigonal bipyramid, and its flexibility is essential to form the observed helix while those previous structures, the en ligand prefers to act as pillars between the same metal sites with the same polyhedra, e.g. Zn tetrahedra-en-Zn tetrahedra in (en)₂Zn₄(SeO₃)₄ (Millange, Serre, Cabourdin, Marrot, and Férey, 2004), and Zn₄SO₄(OH)₆(en)_{0.5}·3H₂O and Zn₄SO₄(OH)₆(en)_{0.5}·18H₂O (Rujiwatra, Mander, Kepert, and Rosseinsky, 2005) or Mn octahedra-en-Mn octahedra in (en)Mn₂(V₂O₇) (Cao, Zheng, Fang, and Yang, 2010). This kind of polymeric helix has been rarely reported compared to those found in literature with similar composition, such as [Ni(en)₃][VO₃]₂ (Liu, Lin, and Lin, 2000) and [Co(en)₃][V₃O₉]·H₂O (Khan, Yohannes, Doedens, Golub, and O'Conner, 2005) which employ an optically active complex of D₃ symmetry, {M(en)₃}, with the en acting as a chelating ligand, and the complex as a chiral template. The neighboring helices are linked through alternation of μ₂-O(2) atom bridges to form an undulating sheet in Figure 3.9(b). Adjacent sheets are further interconnected by alternation of V(1)O₄ tetrahedra to form the 3-D network (Figure 3.10). The strength of the 3-D network is reinforced by N–H···O hydrogen bonding interactions (d[H···O] = 2.064-2.582 Å, ∠[N–H···O] = 135.6-166.1°).

Table 3.3 Selected Bond Lengths and Bond Angles (Å, °) for Compound **3a**.

Zn(1)–O(7) ⁱ	1.955(4)	V(1)–O(5)	1.649(4)
Zn(1)–O(4) ⁱⁱ	1.965(4)	V(1)–O(7)	1.666(3)
Zn(1)–O(2) ⁱⁱⁱ	1.972(3)	V(1)–O(4) ^{iv}	1.766(3)
Zn(1)–N(4)	2.014(4)	V(1)–O(1)	1.767(3)
Zn(2)–O(6)	1.961(3)	V(2)–O(3) ^v	1.649(4)
Zn(2)–O(4)	2.005(3)	V(2)–O(6) ⁱⁱ	1.685(3)
Zn(2)–N(1)	2.015(4)	V(2)–O(2)	1.705(3)
Zn(2)–O(5)	2.138(4)	V(2)–O(1)	1.820(4)
Zn(2)–O(3)	2.196(4)	N(1)–C(2)	1.474(6)
		C(2)–C(3)	1.502(6)
		C(3)–N(4)	1.496(6)
O(7) ⁱ –Zn(1)–O(4) ⁱⁱ	118.84(16)	O(7)–V(1)–O(4) ^{iv}	110.44(17)
O(7) ⁱ –Zn(1)–O(2) ⁱⁱⁱ	97.75(15)	O(5)–V(1)–O(1)	109.62(18)
O(4) ⁱⁱ –Zn(1)–O(2) ⁱⁱⁱ	103.01(14)	O(4) ^{iv} –V(1)–O(1)	109.41(16)
O(7) ⁱ –Zn(1)–N(4)	112.86(16)	O(3) ^v –V(2)–O(6) ⁱⁱ	112.28(17)
O(4) ⁱⁱ –Zn(1)–N(4)	114.56(17)	O(3) ^v –V(2)–O(2)	108.61(18)
O(2) ⁱⁱⁱ –Zn(1)–N(4)	106.96(15)	O(6) ⁱⁱ –V(2)–O(2)	109.94(16)
O(6)–Zn(2)–O(4)	113.25(14)	O(3) ^v –V(2)–O(1)	107.99(18)
O(6)–Zn(2)–N(1)	128.30(15)	O(6) ⁱⁱ –V(2)–O(1)	109.80(18)
O(4)–Zn(2)–N(1)	118.26(15)	O(2)–V(2)–O(1)	108.10(16)
O(6)–Zn(2)–O(5)	90.63(14)	V(1)–O(1)–V(2)	139.9(2)
O(4)–Zn(2)–O(5)	92.38(15)	V(2)–O(2)–Zn(1) ^{vi}	128.08(19)
N(1)–Zn(2)–O(5)	91.44(15)	V(2) ^{vii} –O(3)–Zn(2)	137.2(2)
O(6)–Zn(2)–O(3)	87.54(14)	V(1) ^{viii} –O(4)–Zn(1) ⁱ	121.27(19)
O(4)–Zn(2)–O(3)	83.66(14)	V(1) ^{viii} –O(4)–Zn(2)	122.70(18)
N(1)–Zn(2)–O(3)	93.72(15)	Zn(1) ⁱ –O(4)–Zn(2)	111.42(15)
O(5)–Zn(2)–O(3)	174.56(13)	V(1)–O(5)–Zn(2)	158.5(2)
O(5)–V(1)–O(7)	108.47(19)	V(2) ⁱ –O(6)–Zn(2)	144.0(2)
O(5)–V(1)–O(4) ^{iv}	109.15(18)	V(1)–O(7)–Zn(1) ⁱⁱ	140.5(2)
O(7)–V(1)–O(1)	109.73(18)		

Symmetry code: (i) $-x, y - 1/2, -z + 1$; (ii) $-x, y + 1/2, -z + 1$; (iii) $-x - 1, y - 1/2, -z + 1$; (iv) $-x + 1, y + 1/2, -z + 2$; (v) $x, y + 1, z$; (vi) $-x - 1, y + 1/2, -z + 1$; (vii) $x, y - 1, z$; (viii) $-x + 1, y - 1/2, -z + 2$.

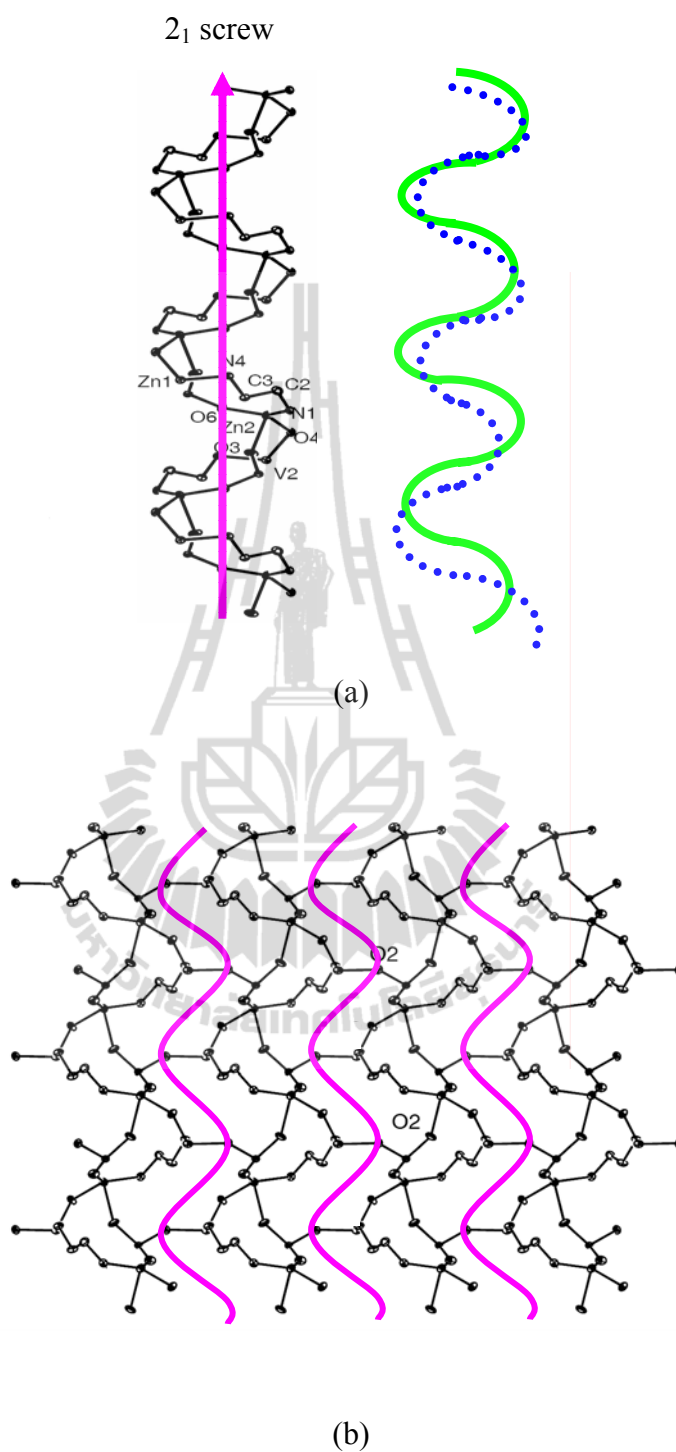


Figure 3.9 ORTEP view of (a) the helices, type A and B as solid and dashed lines, respectively, and an undulating sheet in **3a**, showing (b) the helices connected through μ_2 -O(2) atoms as solid lines, and (c) the packing of the undulating sheets perpendicular to the a axis, the chiral coordination axis, as dashed lines.

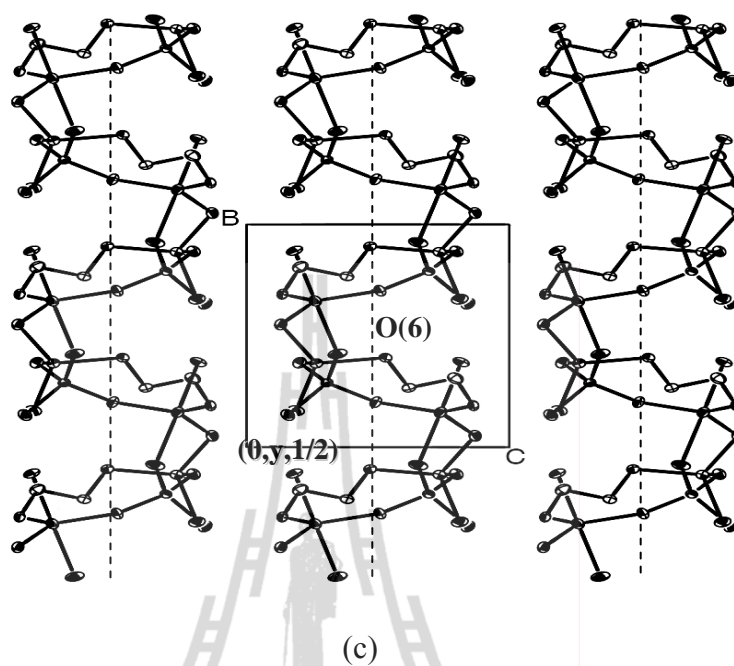


Figure 3.9 (Continued).

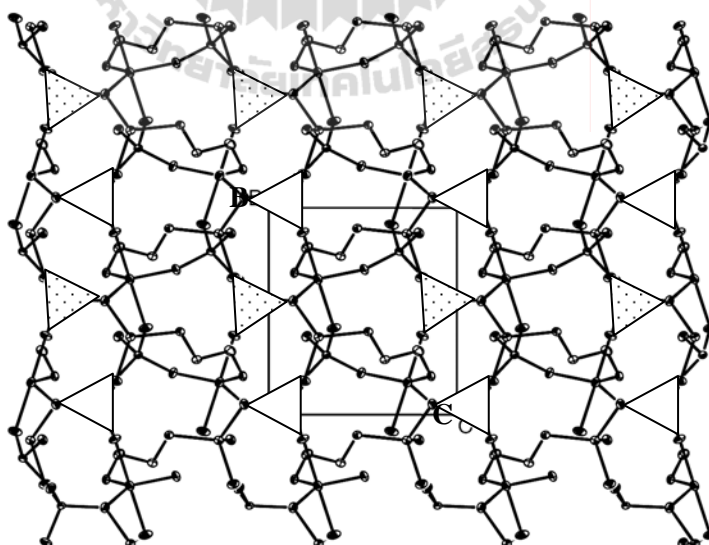


Figure 3.10 View of a 3-D chiral network in **3a** showing $V(1)O_4$ pillars (polyhedral highlight) interconnecting alternately to the undulating sheets above and below the current layer.

3b, (en)ZnV₂O₆, possesses a 2-D double layers. All V⁵⁺ atoms are common distorted tetrahedra coordinated by four O atoms, $d[\text{V}-\text{O}] = 1.612(2)\text{-}1.806(2)$ Å and $\angle[\text{O}-\text{V}-\text{O}] = 106.9(1)\text{-}114.3(1)^\circ$, two corners shared to neighbors forming a 1-D zig-zag polymeric metavanadate chains propagated along the *a* axis in which the bond V–O–V angles are in the range $130.6(1)\text{-}151.4(1)^\circ$ as are listed in Table 3.4. Although these angles are quite varied compared to those observed in the pyrovanadate unit in **3a**, $139.9(2)^\circ$, and discrete polymeric chains in [H₂en][V₂O₆], $132.5(1)^\circ$ (Khan, Hope, Cevik, Zheng, and Powell, 2000), [Co(en)₃][V₃O₉]·H₂O, $132.3(1)^\circ$ (Khan, Yohannes, Doedens, Golub and O’Conner, 2005), and [Ni(en)₃][VO₃]₂, $143.6(6)\text{-}165.9(5)^\circ$ (Liu, Lin and Lin, 2000), but these are smaller than those found the pyrovanadate unit in (en)Mn₂(V₂O₇), 180° (Cao, Zheng, Fang, and Yang, 2010). The Zn²⁺ site is a common distorted ZnO₄N₂ (4+2) octahedra ($d[\text{Zn}-\text{O}]_{(\text{av})} = 2.137$ Å, $d[\text{Zn}-\text{N}] = 2.085$ Å) which is coordinated from two different types of chelating at equatorial positions, a chelating V₂O₇⁴⁻ dimer units (each of repeating second V atoms) of the chains and a chelating en ligand, and the remaining of μ-O(5) and μ₃-O(2) atoms from other two neighbor chains coordinated at axial positions. The trans angle of O(2)–Zn(1)–O(5) of the oxo-group vanadate is $170.7(1)^\circ$ as shown in Figure 3.11. Figure 3.12 shows the chains linked through distorted ZnO₄N₂ octahedra forming 1-D doubly oxovanadate chains. Each Zn²⁺ site shares an edge with the neighbor through two atoms of two chelating divanadate (V₂O₇²⁻) units related by an inversion center forming 2-D double layers with $d[\text{Zn}\cdots\text{Zn}] = 3.206$ Å as observed in (en)CuV₂O₆ (DeBord, Zhang, Zubieta, and O’Connor, 1996). Each layer is held together via hydrogen bonding to generate a 3-D supramolecular framework that is given in Table 3.9.

Table 3.4 Selected Bond Lengths and Bond Angles (Å, °) for Compound **3b**.

Zn(1)–N(2)	2.073(2)	V(1)–O(4) ⁱ	1.8062(18)
Zn(1)–N(1)	2.097(2)	V(2)–O(5)	1.6437(18)
Zn(1)–O(6) ⁱ	2.1128(18)	V(2)–O(6)	1.6595(18)
Zn(1)–O(2)	2.1407(18)	V(2)–O(3)	1.7831(19)
Zn(1)–O(5) ⁱⁱ	2.1455(17)	V(2)–O(4)	1.7899(18)
Zn(1)–O(2) ⁱⁱⁱ	2.1473(17)	C(1)–N(1)	1.472(3)
V(1)–O(1)	1.6121(19)	C(1)–C(2)	1.515(4)
V(1)–O(2)	1.6953(18)	C(2)–N(2)	1.485(3)
V(1)–O(3)	1.7851(18)		
N(2)–Zn(1)–N(1)	84.10(9)	O(2)–V(1)–O(4) ⁱ	108.04(9)
N(2)–Zn(1)–O(6) ⁱ	99.79(8)	O(3)–V(1)–O(4) ⁱ	114.29(8)
N(1)–Zn(1)–O(6) ⁱ	173.66(8)	O(5)–V(2)–O(6)	110.56(10)
N(2)–Zn(1)–O(2)	173.78(8)	O(5)–V(2)–O(3)	111.19(9)
N(1)–Zn(1)–O(2)	89.77(8)	O(6)–V(2)–O(3)	110.65(9)
O(6) ⁱ –Zn(1)–O(2)	86.41(7)	O(5)–V(2)–O(4)	109.24(9)
N(2)–Zn(1)–O(5) ⁱⁱ	92.79(8)	O(6)–V(2)–O(4)	108.19(9)
N(1)–Zn(1)–O(5) ⁱⁱ	89.18(8)	O(3)–V(2)–O(4)	106.88(9)
O(6) ⁱ –Zn(1)–O(5) ⁱⁱ	85.65(7)	V(1)–O(2)–Zn(1)	119.77(9)
O(2)–Zn(1)–O(5) ⁱⁱ	88.22(7)	V(1)–O(2)–Zn(1) ⁱⁱⁱ	137.09(10)
N(2)–Zn(1)–O(2) ⁱⁱⁱ	96.12(8)	Zn(1)–O(2)–Zn(1) ⁱⁱⁱ	96.80(7)
N(1)–Zn(1)–O(2) ⁱⁱⁱ	94.28(8)	V(2)–O(3)–V(1)	151.39(12)
O(6) ⁱ –Zn(1)–O(2) ⁱⁱⁱ	90.29(7)	V(2)–O(4)–V(1) ^{iv}	130.63(11)
O(2)–Zn(1)–O(2) ⁱⁱⁱ	83.20(7)	V(2)–O(5)–Zn(1) ⁱⁱ	137.95(11)
O(5) ⁱ –Zn(1)–O(2) ⁱⁱⁱ	170.72(7)	V(2)–O(6)–Zn(1) ^{iv}	129.79(10)
O(1)–V(1)–O(2)	106.91(9)	N(1)–C(1)–C(2)	109.7(2)
O(1)–V(1)–O(3)	106.85(9)	N(2)–C(2)–C(1)	108.7(2)
O(2)–V(1)–O(3)	112.90(9)	C(1)–N(1)–Zn(1)	107.29(16)
O(1)–V(1)–O(4) ⁱ	107.47(9)	C(2)–N(2)–Zn(1)	107.28(16)

Symmetry code: (i) x+1,y,z; (ii) -x+1,y+1,-z; (iii) -x+2,-y+1,-z+1; (iv) x-1,y,z.

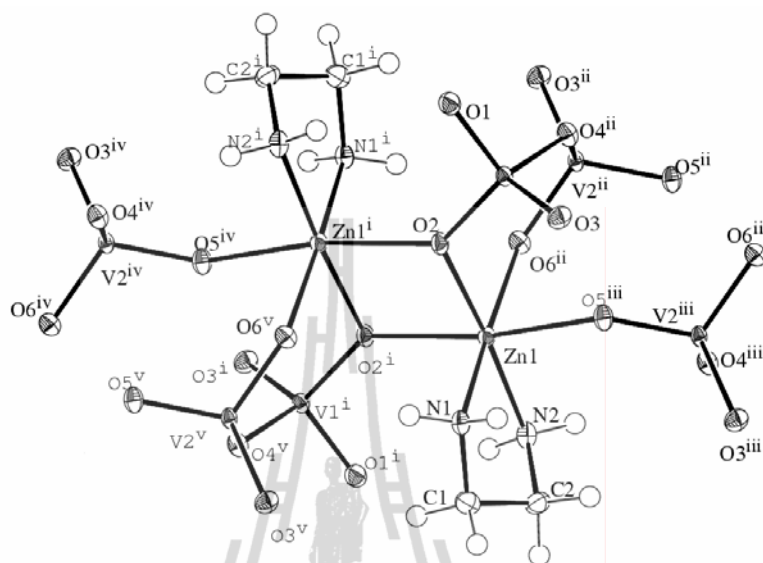


Figure 3.11 The structure of **3b**, showing the zinc dimer by edge sharing to its neighbor.

Symmetry code: (i) $2-x, 1-y, 1-z$; (ii) $1+x, y, z$; (iii) $1-x, 1-y, -z$; (iv) $1+x, y, 1+z$; (v) $1-x, 1-y, 1-z$.

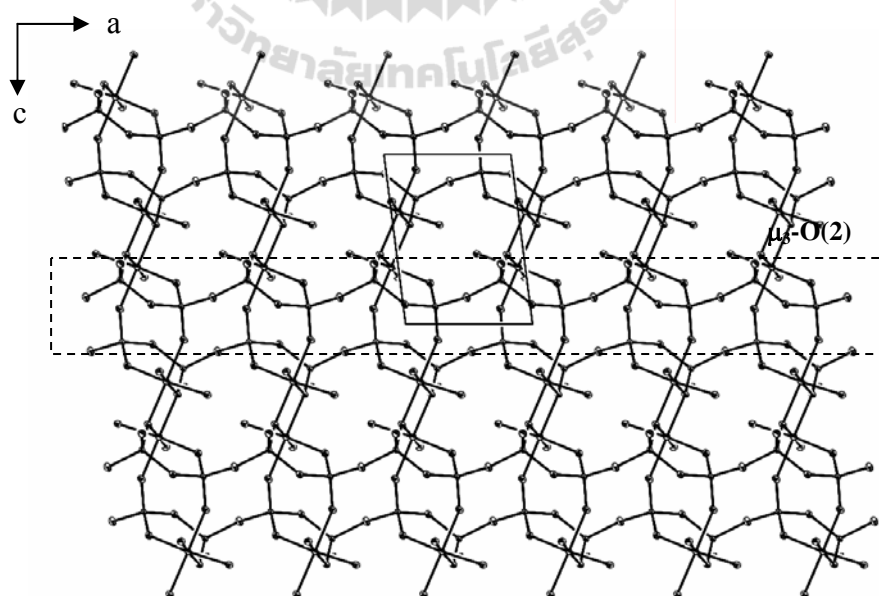


Figure 3.12 The double layered structure of **3b**, showing the double chains as a dashed

line. The C and H atoms were omitted for clarity.

Substituting $\text{Cd}(\text{OAc})_2$ for $\text{Zn}(\text{OAc})_2$ in similar conditions to **3a** and **3b**, the pale purple crystals of **3c** were produced in low yield (*ca* 5%) with the dark green powder of $[\text{H}_2\text{en}]_{0.5}[\text{V}_2\text{O}_5]$ (Riou and Féray, 1995a,b) as confirmed by powder XRD patterns in Figure 3.3. The experiment of **3c** failed when the reaction pH and temperatures were varied to improve the yield.

The single X-ray structural analysis reveals that **3c**, $(\text{enH})_2\text{Cd}(\text{VO}_3)_4$, crystallizes in the monoclinic centrosymmetric space group, $P2_1/n$. **3c** is a 1-D double metavanadate chains propagated along the *a* axis. Each chain is composed of two corner sharing distorted VO_4 tetrahedra, $d[\text{V}-\text{O}] = 1.612(6)-1.820(6)$ Å, $\angle[\text{O}-\text{V}-\text{O}] = 107.3(4)-112.4(3)^\circ$, $\angle[\text{V}-\text{O}-\text{V}] = 129.9(3)-148.4(4)^\circ$, which these are very closed to **3b**. One of the two remaining O atoms of every two V atoms of each chain is linked to the Cd site at the equatorial positions combined with two protonated $[\text{Hen}]^+$ monocations axially coordinated to form a distorted CdO_4N_2 (4+2) octahedron, $d[\text{Zn}-\text{O}_{(\text{av})}] = 2.268$ Å, $d[\text{Zn}-\text{N}] = 2.327$ Å. The *trans* bond N–Cd–N angle is perfect linear, $180.0(1)^\circ$, in contrast to that of **3b**, $170.7(1)^\circ$. Metal complexes in this act as bridges which are located between two chains similar to that observed in $(\text{Hen})_2\text{Mn}(\text{VO}_3)_4$ (Law and Williams, 2000). Each double chain is held together by intramolecular $\text{N}(2)-\text{H}(2\text{C})\cdots\text{O}(1)$ and intermolecular $\text{N}(2)-\text{H}(2\text{A})\cdots\text{O}(4)$ hydrogen bond interactions forming a 2-D supramolecular layer as illustrated in Figure 3.13(b) and listed in Table 3.9.

Replacing enMe for en and using similar conditions to $\text{V}_2\text{O}_5-\text{M}(\text{OAc})_2-\text{en}$, a a mole ratio 1:1:1, an initial reaction pH of 9-11 and after heating at 110-180 °C, two black crystal morphologies of **3d** and $\text{K}_3\text{V}_3\text{O}_8$ (Galy and Carpy, 1975) were obtained. The yield of **3d** (*ca* 85%) has increased by adding 2-3 mmol of enMe and heating at

110 °C. Increasing the amount of enMe to 4-5 mmol, the pale-brown single crystals of **3e** were produced in pure phase which was confirmed by elemental analysis and powder XRD in Table 3.10 and Figures 3.4 and 3.5 for **3d** and **3e**, respectively.

Table 3.5 Selected Bond Lengths and Bond Angles (Å, °) for **3c**.

Cd(1)–N(1) ⁱ	2.268(7)	V(1)–O(5)	1.806(6)
Cd(1)–N(1)	2.268(7)	V(2)–O(6)	1.623(7)
Cd(1)–O(2)	2.324(6)	V(2)–O(2)	1.653(6)
Cd(1)–O(2) ⁱ	2.324(6)	V(2)–O(3) ⁱⁱ	1.796(6)
Cd(1)–O(1)	2.330(6)	V(2)–O(5)	1.820(6)
Cd(1)–O(1) ⁱ	2.330(6)	N(1)–C(1)	1.464(11)
V(1)–O(4)	1.612(6)	N(2)–C(2)	1.485(10)
V(1)–O(1)	1.672(6)	C(1)–C(2)	1.522(11)
V(1)–O(3)	1.767(6)		
N(1) ⁱ –Cd(1)–N(1)	180.000(1)	O(4)–V(1)–O(1)	107.3(4)
N(1) ⁱ –Cd(1)–O(2)	88.6(3)	O(4)–V(1)–O(3)	109.8(3)
N(1)–Cd(1)–O(2)	91.4(3)	O(1)–V(1)–O(3)	109.4(3)
N(1) ⁱ –Cd(1)–O(2) ⁱ	91.4(3)	O(4)–V(1)–O(5)	109.6(3)
N(1)–Cd(1)–O(2) ⁱ	88.6(3)	O(1)–V(1)–O(5)	109.9(3)
O(2)–Cd(1)–O(2) ⁱ	180.0(3)	O(3)–V(1)–O(5)	110.8(3)
N(1) ⁱ –Cd(1)–O(1)	91.9(2)	O(6)–V(2)–O(2)	108.4(3)
N(1)–Cd(1)–O(1)	88.1(2)	O(6)–V(2)–O(3) ⁱⁱ	109.1(3)
O(2)–Cd(1)–O(1)	85.4(2)	O(2)–V(2)–O(3) ⁱⁱ	107.9(3)
O(2) ⁱ –Cd(1)–O(1)	94.6(2)	O(6)–V(2)–O(5)	110.4(3)
N(1) ⁱ –Cd(1)–O(1) ⁱ	88.1(2)	O(2)–V(2)–O(5)	108.5(3)
N(1)–Cd(1)–O(1) ⁱ	91.9(2)	O(3) ⁱⁱ –V(2)–O(5)	112.4(3)
O(2)–Cd(1)–O(1) ⁱ	94.6(2)	V(1)–O(1)–Cd(1)	128.4(3)
O(2) ⁱ –Cd(1)–O(1) ⁱ	85.4(2)	V(2)–O(2)–Cd(1)	139.9(3)
O(1)–Cd(1)–O(1) ⁱ	180.0(3)	V(1)–O(3)–V(2) ⁱⁱⁱ	148.4(4)
		V(1)–O(5)–V(2)	129.8(3)

Symmetry code: (i) $-x, -y, -z+1$; (ii) $x+1, y, z$; (iii) $x-1, y, z$.

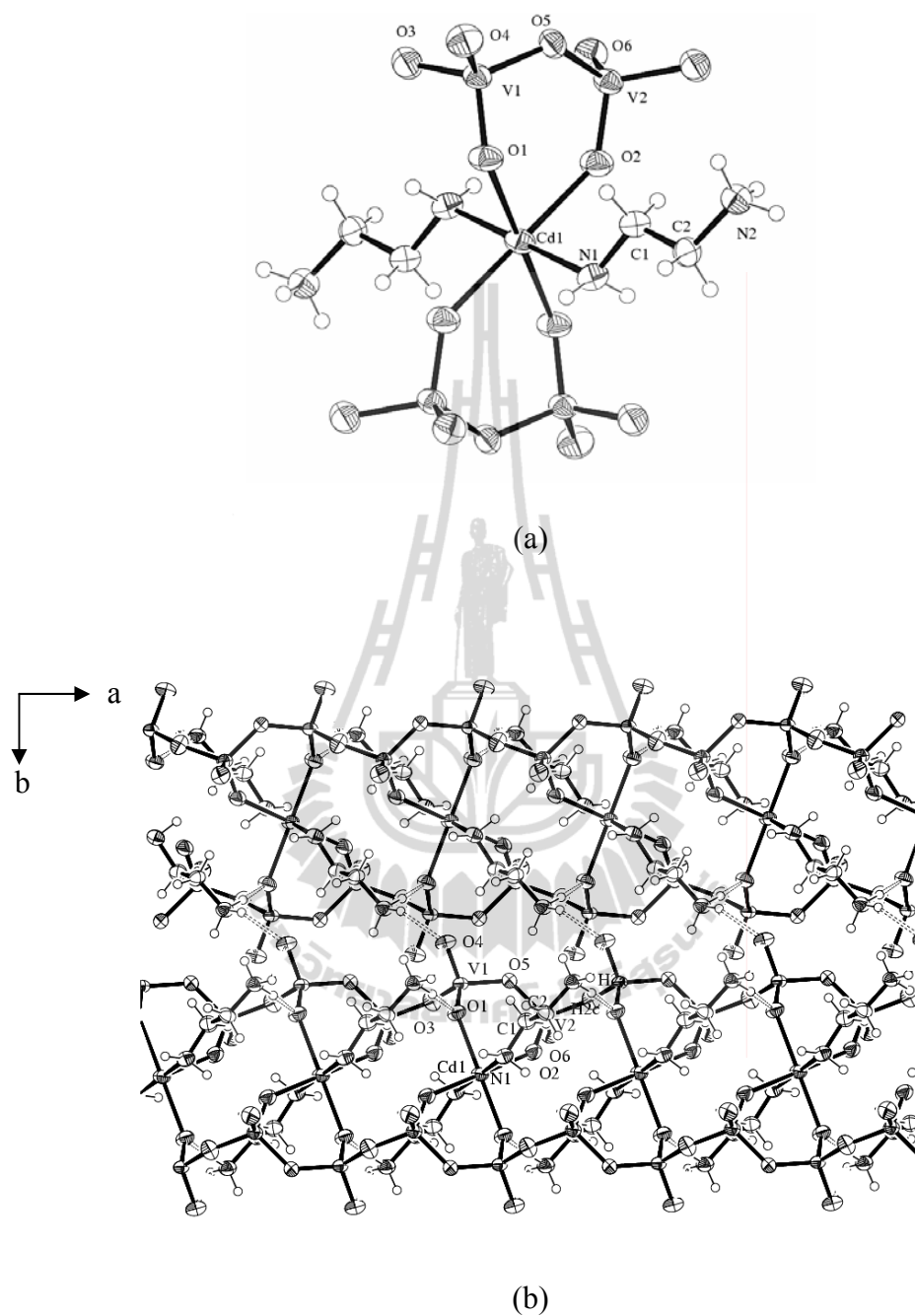


Figure 3.13 The structure of **3c**, showing (a) the Cd coordination geometry and (b) 1-D the double chain projected on the *ab* plane includes the labeling of the atoms with 50% probability displacement ellipsoids. The hydrogen bond interactions are as shown dashed lines.

Table 3.6 Selected Bond Lengths and Bond Angles (\AA , $^\circ$) for **3d**.

Zn(1)–O(10) ⁱ	2.083(6)	V(3)–O(4) ⁱⁱⁱ	1.917(7)
Zn(1)–O(10)	2.083(6)	V(3)–O(6) ⁱⁱⁱ	1.943(7)
Zn(1)–O(1)	2.107(6)	V(3)–O(8)	1.956(7)
Zn(1)–O(1) ⁱ	2.107(6)	V(3)–O(5) ⁱⁱ	2.020(6)
Zn(1)–N(1)	2.141(10)	V(4)–O(10) ^{iv}	1.644(7)
Zn(1)–N(1) ⁱ	2.141(10)	V(4)–O(9)	1.680(7)
V(1)–O(1)	1.666(7)	V(4)–O(4)	1.721(6)
V(1)–O(6)	1.684(7)	V(4)–O(8) ^v	1.817(7)
V(1)–O(7)	1.710(6)	N(1)–C(1)	1.466(14)
V(1)–O(5)	1.827(6)	N(2)–C(2B)	1.47(3)
V(2)–O(2)	1.590(7)	N(2)–C(2A)	1.498(17)
V(2)–O(7)	1.920(7)	C(1)–C(2A)	1.444(19)
V(2)–O(9)	1.938(7)	C(1)–C(2B)	1.55(3)
V(2)–O(5) ⁱⁱ	1.953(6)	C(2A)–C(3)	1.518(18)
V(2)–O(8)	2.019(7)	C(2B)–C(3)	1.58(3)
V(3)–O(3)	1.598(7)	C(2A)–C(2B)	0.97(3)
O(10) ⁱ –Zn(1)–O(10)	180.0(3)	V(4)–O(4)–V(3) ^{vi}	136.1(4)
O(10) ⁱ –Zn(1)–O(1)	94.0(3)	V(1)–O(5)–V(2) ^{vii}	129.5(3)
O(10)–Zn(1)–O(1)	86.0(3)	O(1)–V(1)–O(6)	109.5(3)
O(10)–Zn(1)–O(1) ⁱ	94.0(3)	O(1)–V(1)–O(7)	107.3(3)
O(1)–Zn(1)–O(1) ⁱ	180.000(3)	O(6)–V(1)–O(7)	111.3(3)
O(10) ⁱ –Zn(1)–N(1)	90.5(4)	O(1)–V(1)–O(5)	109.1(3)
O(10)–Zn(1)–N(1)	89.5(4)	O(6)–V(1)–O(5)	111.5(3)
O(1)–Zn(1)–N(1)	86.7(4)	O(7)–V(1)–O(5)	108.0(3)
O(1) ⁱ –Zn(1)–N(1)	93.3(4)	O(2)–V(2)–O(7)	113.7(3)
O(10) ⁱ –Zn(1)–N(1) ⁱ	89.5(4)	O(2)–V(2)–O(9)	101.9(3)
O(1)–Zn(1)–N(1) ⁱ	93.3(4)	O(7)–V(2)–O(9)	86.5(3)
N(1)–Zn(1)–N(1) ⁱ	180.000(4)	O(2)–V(2)–O(5) ⁱⁱ	114.0(3)
O(10) ^{iv} –V(4)–O(9)	110.8(3)	O(7)–V(2)–O(5) ⁱⁱ	131.7(3)
O(10) ^{iv} –V(4)–O(4)	105.8(3)	O(9)–V(2)–O(5) ⁱⁱ	90.6(3)
O(9)–V(4)–O(4)	111.4(3)	O(2)–V(2)–O(8)	101.6(3)
O(10) ^{iv} –V(4)–O(8) ^v	109.5(3)	O(7)–V(2)–O(8)	87.1(3)
O(9)–V(4)–O(8) ^v	112.1(3)	O(9)–V(2)–O(8)	156.2(3)
O(4)–V(4)–O(8) ^v	107.0(3)	O(5) ⁱⁱ –V(2)–O(8)	76.8(3)
V(1)–O(1)–Zn(1)	138.6(4)		

Symmetry code: (i) $-x, -y+2, -z+2$; (ii) $x+1, y, z$; (iii) $x+1, -y+3/2, z+1/2$; (iv) $-x+1, -y+2, -z+2$; (v) $x, -y+3/2, z-1/2$; (vi) $x-1, -y+3/2, z-1/2$; (vii) $x-1, y, z$.

The single crystal X-ray structural analysis shows that **3d**, $\text{Zn}(\text{HenMe})_2\text{V}_8\text{O}_{20}$ or $(\text{HenMe})_2\text{Zn}(\text{V}^{4+}\text{O})_4(\text{V}^{5+}\text{O}_4)_4$, and **3e**, $(\text{enMe})_2\text{Zn}(\text{VO}_3)_2 \cdot 2\text{H}_2\text{O}$, crystallize in the monoclinic centrosymmetric space group, $P2_1/c$ and the chiral space group, $C2$, respectively.

The structure of **3d** is an open 3-D framework structure built up from anionic mixed-valence $\text{V}^{4+}/\text{V}^{5+}$ polyoxovanadate sheets pillared with ZnO_4N_2 octahedra. The sheets are constructed by a combination of equal numbers of V^{5+}O_4 tetrahedra and V^{4+}O_5 square pyramids. While the V^{5+}O_4 tetrahedra are isolated from each other, the V^{4+}O_5 square pyramids exist as edge-sharing pairs linked to the corners of six V^{5+}O_4 tetrahedra to generate 2-D layers perpendicular to the b axis as shown in Figure 3.14. Within a pair of square pyramids, the two apical oxygen atoms are oriented towards opposite sides of the plane of the layer as has been observed in $(\text{HenMe})_2\text{CdV}^{4+}_4\text{V}^{5+}_4\text{O}_{20}$ (Zhang, Shi, Yang, Chen, and Feng, 2000), $[\text{H}_2\text{en}]_{0.5}[(\text{V}^{4+}\text{O})(\text{V}^{5+}\text{O}_4)]$ and $[\text{H}_2\text{pn}]_{0.5}[(\text{V}^{4+}\text{O})(\text{V}^{5+}\text{O}_4)]$ (Riou and Féray, 1995a,b; Zhang, Haushalter, and Clearfield, 1996), and $\text{Cs}[(\text{V}^{4+}\text{O})(\text{V}^{5+}\text{O}_4)]$ (Mumme and Watts, 1971). The layers of these compounds have the same connections of polyhedra but the relative orientations are different.

The oxide layers of this compound show rows of square pyramids units disposed alternately up/down-down/up as in $(\text{HenMe})_2\text{CdV}^{4+}_4\text{V}^{5+}_4\text{O}_{20}$ as can be seen in the left to right progression on Figure 3.16(a). In the other compounds the progression always has the square pyramids pairs arranged down/up. The orientations of the tetrahedra can be examined relative to these progressions of the square pyramids pairs. In the current compound and $(\text{HenMe})_2\text{CdV}^{4+}_4\text{V}^{5+}_4\text{O}_{20}$, the tetrahedral are arranged up-up-down-down, while in $[\text{enH}_2]_{0.5}[(\text{V}^{4+}\text{O})(\text{V}^{5+}\text{O}_4)]$ and $[\text{H}_2\text{pn}]_{0.5}[(\text{V}^{4+}\text{O})(\text{V}^{5+}\text{O}_4)]$ they are up and down alternately, and in $\text{Cs}[(\text{V}^{4+}\text{O})(\text{V}^{5+}\text{O}_4)]$,

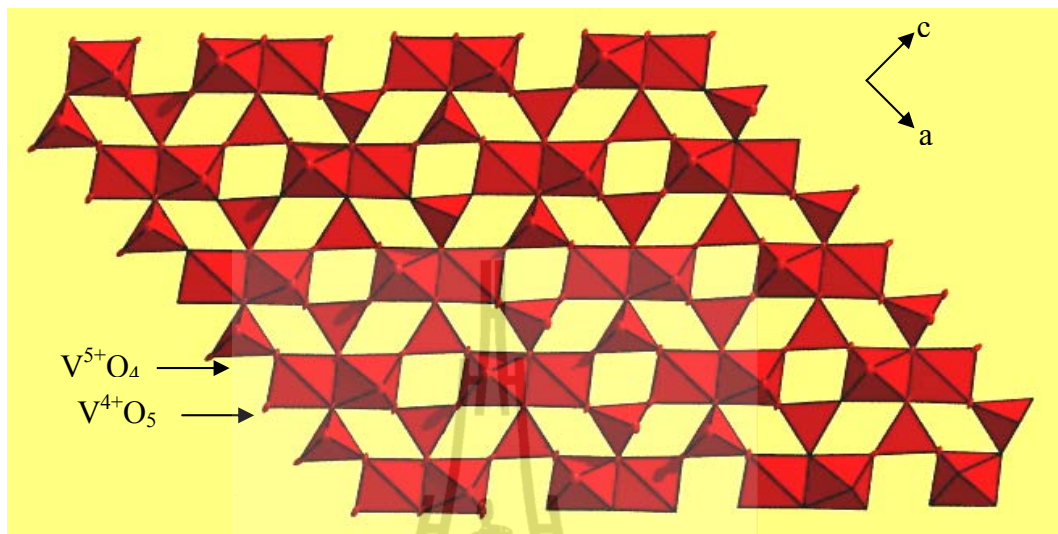


Figure 3.14 Polyhedral representation of sheets perpendicular to the b axis in $3d$.

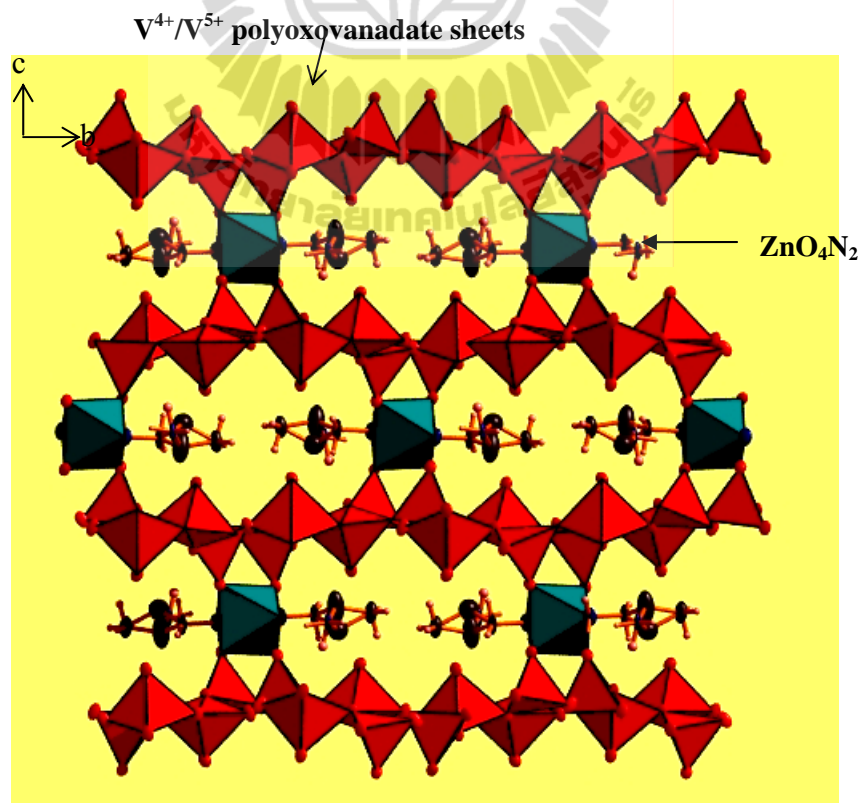
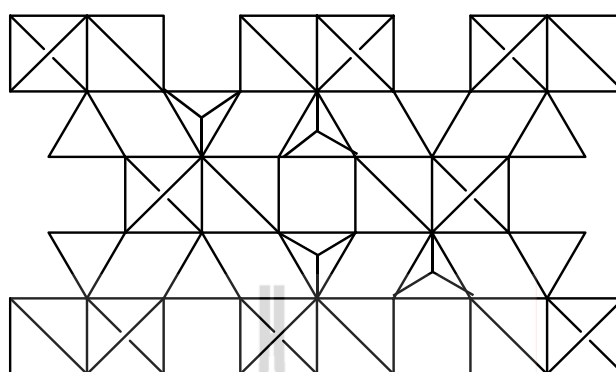


Figure 3.15 Perspective diagram showing ZnO_4N_2 pillars forming 0-D rectangular channels along the a axis in $3d$.

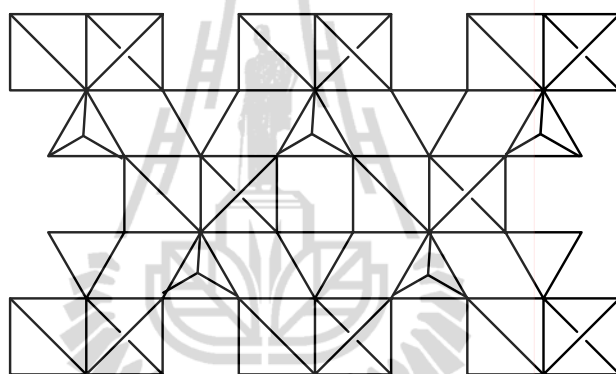
they are alternately all up or all down in any given horizontal progression as shown in Figures 3.16(b) and 3.16(c), respectively. Two out-of-plane oxygen atoms from V^{5+} tetrahedra on each of the two adjacent polyoxovanadate layers are strongly linked to zinc centers with an average distance of 2.095(6) Å to generate a 3-D nanoporous structure with 1-D rectangular channels of 3.97 x 11.65 Å along the *a* axis. The channels are bounded by 10-membered $[Zn_2V_8O_{10}]$ rings, made up of 10 corner-shared polyhedra and filled with a protonated $[HenMe]^+$ ligand (Figure 3.15).

As seen in Table 3.8 below, two V^{5+} atoms realize tetrahedral geometry coordinated with normal bond distances and angles. Two V^{4+} atoms have distorted square pyramidal geometries coordinated with a vanadyl group in the apex at a distance of 1.590(7)-1.598(7) Å, and four oxygen atoms in the base at distances of 1.917(7)-2.029(7) Å. The Zn(1) atom has an octahedral configuration with four equatorial oxygen atoms from the oxo-group of the vanadate layers and two axial nitrogen atoms from $[HenMe]^+$ monocations with distances of 2.095(6) Å and 2.141(10) Å, respectively.

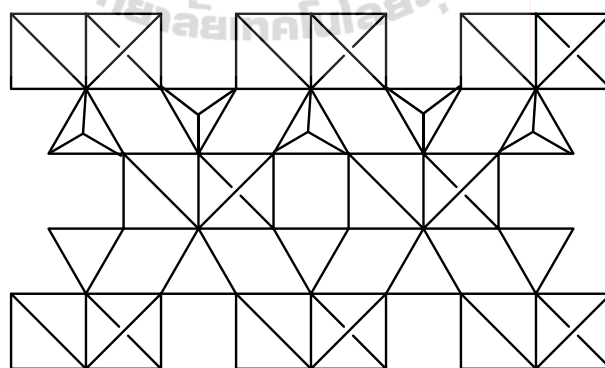
The stability of an open 3-D framework depends on the strength of the interactions within framework. Hydrogen atoms on N(1), N(2), and C(1) atoms of the protonated $HenMe^+$ monodentate ligands hydrogen bond to O(1), O(4), O(7), and O(10) oxygen atoms of $V^{5+}O_4$ tetrahedra and apical O(2) and O(3) oxygen atoms of $V^{4+}O_5$ square pyramids of adjacent vanadium oxide sheets above and below form $H\cdots O$ hydrogen bonds in the range of 2.11-2.62 Å as shown in Figure 3.17 and listed in Table 3.9.



(a) **3d** and $\text{Cd}(\text{HenMe})_2\text{V}^{4+}_4\text{V}^{5+}_4\text{O}_{20}$



(b) $[\text{H}_2\text{en}]_{0.5}[(\text{V}^{4+}\text{O})(\text{V}^{5+}\text{O}_4)]$ and $[\text{H}_2\text{pn}]_{0.5}[(\text{V}^{4+}\text{O})(\text{V}^{5+}\text{O}_4)]$



(c) $\text{Cs}[(\text{V}^{4+}\text{O})(\text{V}^{5+}\text{O}_4)]$

Figure 3.16 Comparing the relative orientation of square pyramids and tetrahedra on layers with/without mark represent up and down, respectively.

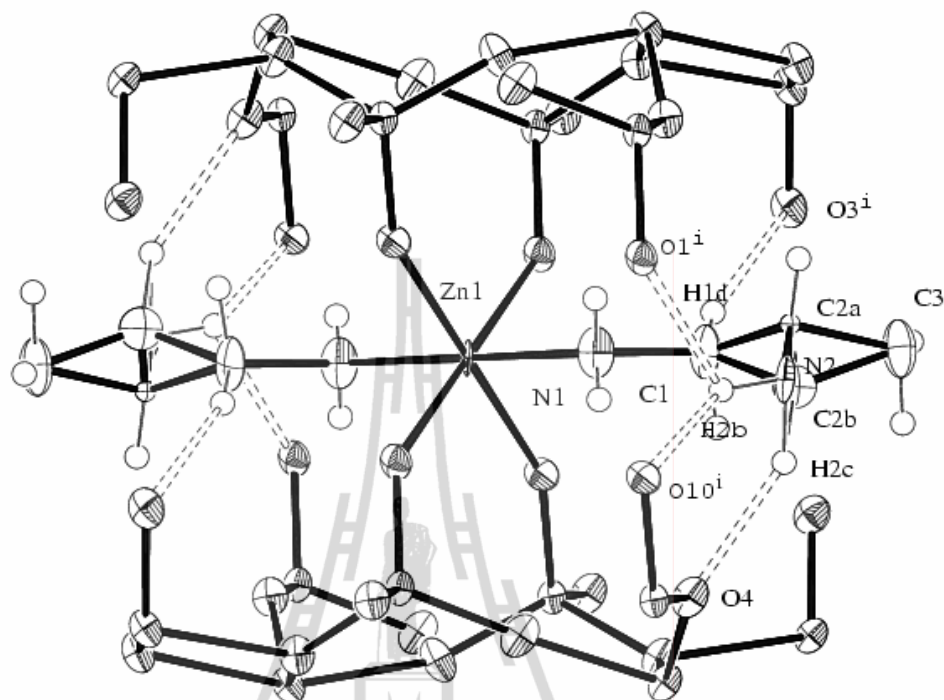


Figure 3.17 Hydrogen bond interactions in 1-D rectangular channels of **3d**. Symmetry codes: (i) $-x+1, -y, -z$.

3e, $(\text{enMe})_2\text{Zn}(\text{VO}_3)_2 \cdot 2\text{H}_2\text{O}$, is an open 3-D framework consists of the polymeric metavanadate chains of corner-sharing VO_4 tetrahedra, two corners of each tetrahedra are shared with neighbors propagating along the c axis, with the chain repeating units are two up and two down while those chains in **3a** and **3c** are repeating are one up and one down. The chains and neighbors are interconnected by ZnO_2N_4 octahedra in the $[110]$ and $[1-10]$ directions generate a 3-D porous framework. The dimensions of the three nearly perpendicular channels, one bounded by 12-membered $[\text{Zn}_4\text{V}_8\text{O}_{12}]$ rings along $[001]$ and two bounded by 12-membered $[\text{Zn}_2\text{V}_{10}\text{O}_{12}]$ rings along $[110]$ and $[1-10]$ are $8.7 \times 8.7 \text{ \AA}$ and $7.4 \times 10.9 \text{ \AA}$, as shown in Figures 3.19(a) and 3.19(b), respectively, occupied by two crystallographic independent water molecules. All vanadium(V) atoms exhibit $\{\text{VO}_4\}$ tetrahedral geometry coordination defined by one terminal oxo-group with bond distances

of 1.615(2)-1.651(3) Å, and three different μ -oxygen bridging atoms from two $\{VO_4\}$ units and one Zn(II) complex with bond distances of 1.635(3)-1.808(3) Å and the O–V–O and V–O–V bond angles are in the range of 105.9(2)-112.9(1)° and 144.9(2)-151.3(2)°, respectively, similar to those observed in **3b-c**. The Zn(II) center embraces a ZnO_2N_4 distorted octahedral geometry, being coordinated by four equatorial nitrogen atoms of two enMe chelate ligands and two axial μ -oxygen bridging atoms from tetrahedral units, which adopt a *trans*-orientation with the O–Zn–O bond angles of 174.1(1)°. The water solvate molecules are hydrogen bonded to the chains through O–H \cdots O hydrogen bond interactions forming a $R_4^3(10)$ motif (graph set notation *R* is ring pattern type with the related the number of donors and acceptors are 4 and 3 and degree of motif are 10) with as illustrated in Figure 3.20. The stability of the framework reinforced by the N–H \cdots O hydrogen bond interactions between the hydrogen atoms of the amine groups on the chelating enMe ligand and the oxygen atoms of the framework as listed in Table. 3.9.

Table 3.7 Selected Bond Lengths and Bond Angles (Å, °) for **3e**.

Zn(1)–N(4)	2.108(3)	V(2)–O(6)	1.787(2)
Zn(1)–N(2)	2.123(3)	N(1)–C(1)	1.482(4)
Zn(1)–N(3)	2.132(3)	N(2)–C(2)	1.475(5)
Zn(1)–N(1)	2.140(3)	N(3)–C(4)	1.480(4)
Zn(1)–O(5)	2.164(3)	N(4)–C(5)	1.480(5)
Zn(1)–O(3)	2.244(2)	C(1)–C(2)	1.518(5)
V(1)–O(1)	1.615(2)	C(1)–C(3)	1.524(5)
V(1)–O(3)	1.652(2)	C(4)–C(6)	1.507(5)
V(1)–O(4)	1.7888(11)	C(4)–C(5)	1.513(5)
V(1)–O(6) ⁱ	1.808(3)	O(1W)–H(1)	0.85(6)
V(2)–O(5)	1.635(3)	O(1W)–H(2)	0.78(8)
V(2)–O(2)	1.651(3)	O(2W)–H(4)	0.82(5)
V(2)–O(7)	1.7819(11)	O(2W)–H(3)	0.71(4)

Symmetry codes: (i) $x+1/2, y+1/2, z$; (ii) $-x+1, y, -z+2$; (iii) $x-1/2, y-1/2, z$; (iv) $-x, y, -z+1$.

Table 3.7 (Continued).

N(4)–Zn(1)–N(2)	177.73(13)	O(3)–V(1)–O(4)	110.45(13)
N(4)–Zn(1)–N(3)	82.06(11)	O(1)–V(1)–O(6) ⁱ	111.39(14)
N(2)–Zn(1)–N(3)	95.77(11)	O(3)–V(1)–O(6) ⁱ	106.22(13)
N(4)–Zn(1)–N(1)	99.97(11)	O(4)–V(1)–O(6) ⁱ	108.47(13)
N(2)–Zn(1)–N(1)	82.20(12)	O(5)–V(2)–O(2)	105.90(16)
N(3)–Zn(1)–N(1)	177.97(12)	O(5)–V(2)–O(7)	110.94(13)
N(4)–Zn(1)–O(5)	91.21(13)	O(2)–V(2)–O(7)	109.05(11)
N(2)–Zn(1)–O(5)	88.23(12)	O(5)–V(2)–O(6)	112.94(13)
N(3)–Zn(1)–O(5)	92.53(12)	O(2)–V(2)–O(6)	107.84(12)
N(1)–Zn(1)–O(5)	87.52(12)	O(7)–V(2)–O(6)	109.98(15)
N(4)–Zn(1)–O(3)	89.27(12)	V(1)–O(3)–Zn(1)	139.82(15)
N(2)–Zn(1)–O(3)	91.51(11)	V(1)–O(4)–V(1) ⁱⁱ	150.3(2)
N(3)–Zn(1)–O(3)	93.36(11)	V(2)–O(5)–Zn(1)	164.6(2)
N(1)–Zn(1)–O(3)	86.59(11)	V(2)–O(6)–V(1) ⁱⁱⁱ	144.86(15)
O(5)–Zn(1)–O(3)	174.09(11)	V(2) ^{iv} –O(7)–V(2)	151.3(2)
O(1)–V(1)–O(3)	110.73(14)	H(1)–O(1W)–H(2)	113(6)
O(1)–V(1)–O(4)	109.53(10)	H(4)–O(2W)–H(3)	109(4)

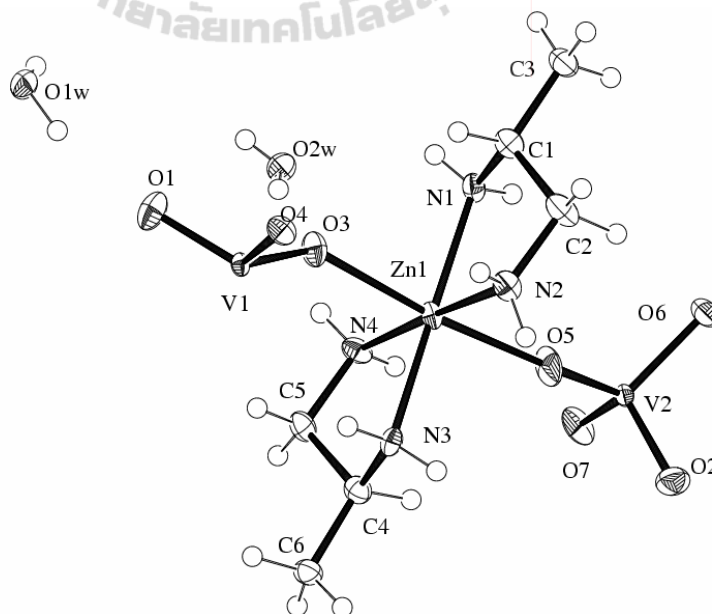


Figure 3.18 Asymmetric unit of **3e**, including the labeling of the atoms with 50% probability displacement ellipsoids.

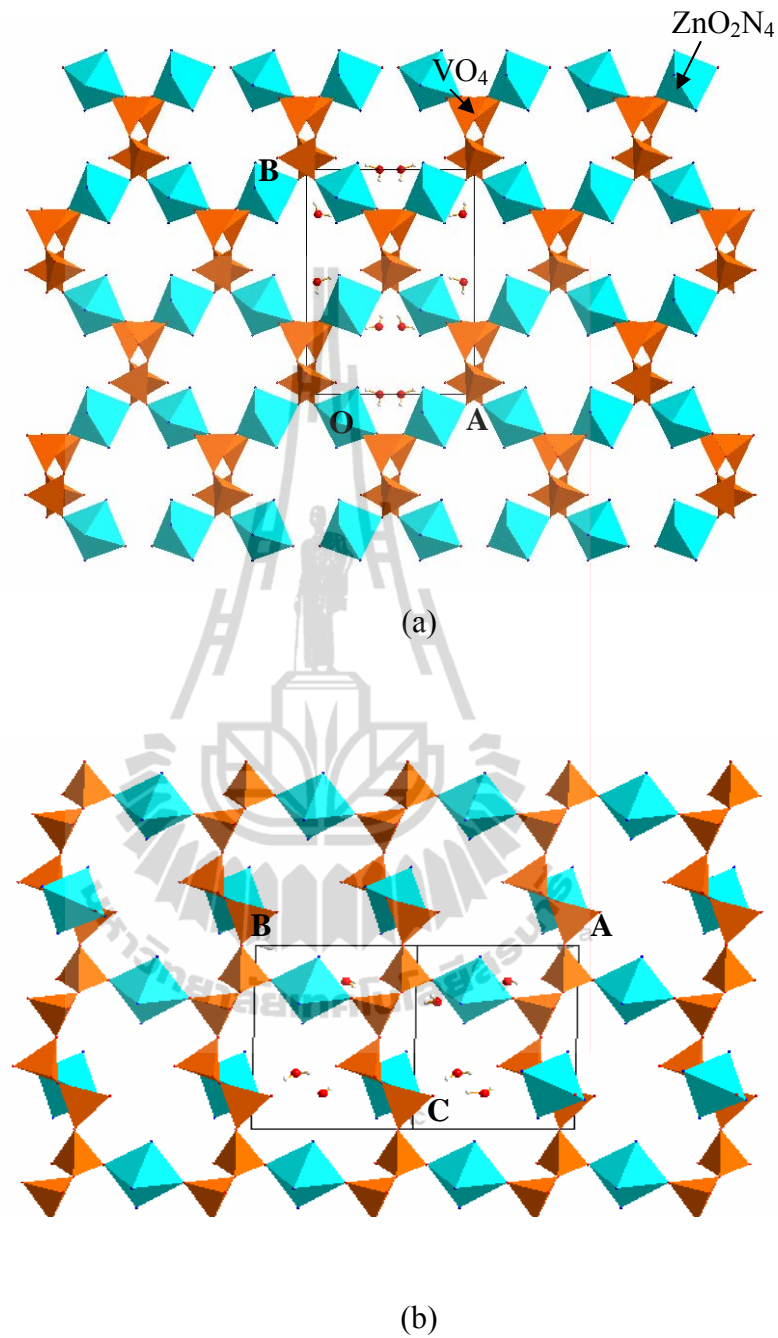


Figure 3.19 Polyhedral representation of the dimensions of the three nearly perpendicular channels, (a) one bounded by 12-membered $[\text{Zn}_4\text{V}_8\text{O}_{12}]$ rings along $[001]$ and (b) two bounded by 12-membered $[\text{Zn}_2\text{V}_{10}\text{O}_{12}]$ rings along $[110]$. The C and H atoms are omitted for clarity.

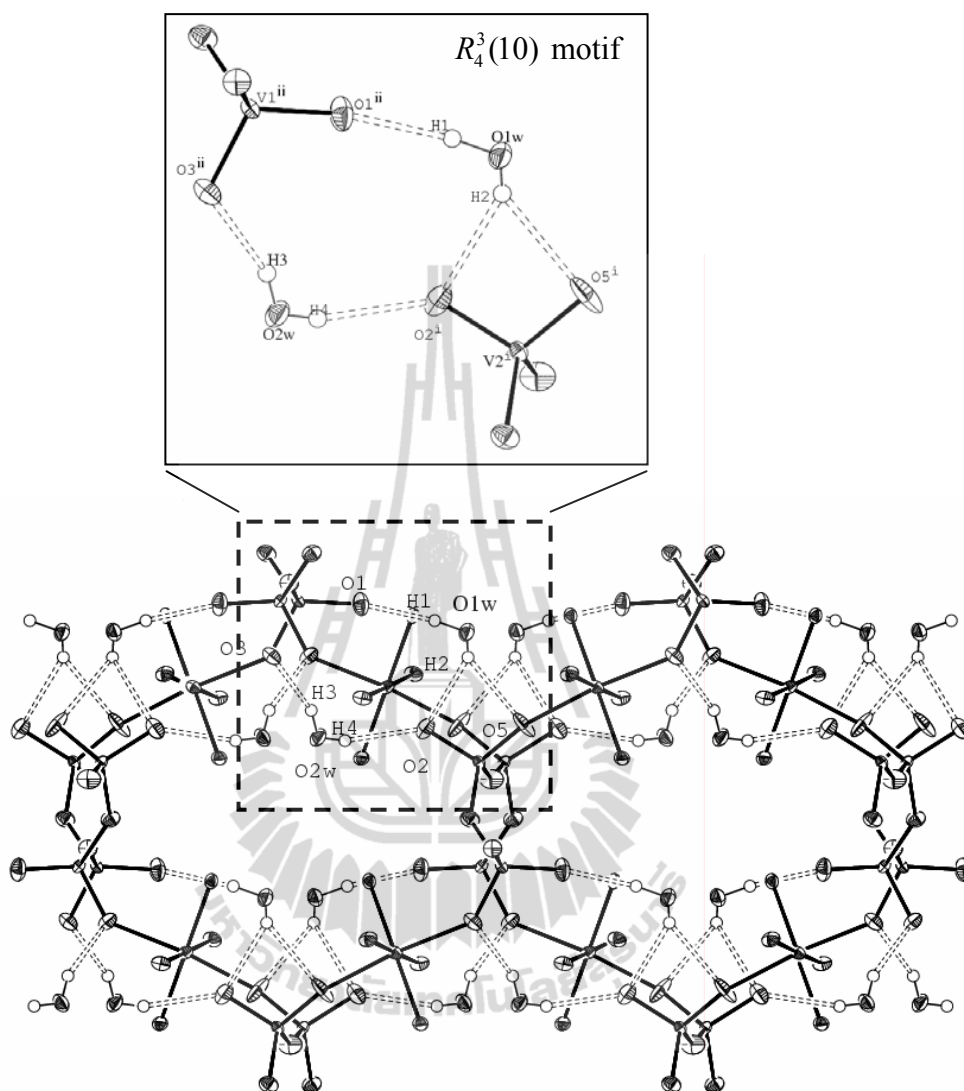


Figure 3.20 Hydrogen bonding interactions showing the $R_4^3(10)$ motif in **3e**.

Reaction pH, temperature or the amount of aliphatic diamines are crucial parameters to form the desired product. The neutral, mono-protonated and di-protonated forms of the aliphatic diamines are dependent on their pK_a values (en: $pK_{a1} = 10.71$ and $pK_{a2} = 7.56$; enMe: $pK_{a1} = 10.00$ and $pK_{a2} = 7.13$). In the V_2O_5 – $M(OAc)_2$ –aliphatic diamines system, compounds **3a**, **3b**, and **3e** are present as en and its derivatives in the neutral form; while compound $[H_2en]_3[V_{10}O_{28}] \cdot 2H_2O$, **3c**, and **3d** are

found in the di- and mono-protonated form. The en and enMe acts as a strong reducing agent for the isolated mixed-valence vanadate compound.

Table 3.8 Summary the Coordination Geometries and Bond Valence Sums for Compounds **3a-e**.

Compound	Metal Centers	Type of Polyhedron	^a Bond Type	Bond Distance (Å)	^b Average of Oxidation State
3a	Zn(1)	Distorted tetrahedra	Zn- μ -N	2.014(4)	1.999
			Zn- μ -O	1.955(4)-1.973(4)	
	Zn(2)	Trigonal bipyramids	Zn- μ -N	2.015(4)	2.028
			Zn- μ -O	1.961(3)-2.196(4)	
	V(1) and V(2)	Distorted tetrahedra	V- μ -O	1.649(4)-1.820(4)	5.160
	3b	Zn(1)	Distorted octahedra	Zn-N	2.073(2)-2.097(2)
V(1) and V(2)		Distorted tetrahedra	V- μ -O	1.612(2)-1.806(2)	5.079
			V- μ_3 -O	1.695(2)	
3c	Cd(1)	Distorted octahedra	Cd-N	2.268(7)	2.142
			Cd- μ^a -O	2.324(6)-2.330(6)	
	V(1) and V(2)	Distorted tetrahedra	V=O _t	1.612(6)-1.623(6)	5.148
			V- μ -O	1.653(7)-1.820(6)	
3d	Zn(1)	Distorted octahedra	Zn-N	2.141(10)	2.118
			Zn- μ -O	2.083(6)-2.107(6)	
	V(1) and V(4)	Distorted tetrahedra	V- μ -O	1.644(7)-1.721(6)	5.096 (5.35) ^c
			V- μ_3 -O	1.817(7)-1.827(6)	
	V(2) and V(3)	Square pyramids	V=O _t	1.590(7)-1.598(7)	4.181 (4.37) ^c
			V- μ -O	1.917(7)-1.943(7)	
V- μ_3 -O	1.953(6)-2.020(6)				
3e	Zn(1)	Distorted octahedra	Zn-N	2.108(3)-2.140(3)	2.038
			Zn- μ -O	2.164(3)-2.244(2)	
	V(1) and V(2)	Distorted tetrahedra	V=O _t	1.615(2)-1.651(3)	5.189
			V- μ -O	1.635(3)-1.808(3)	

^at, μ , and μ_3 are terminal, doubly and triply bridged oxygen atoms, respectively.

^bValence sum calculation (Brown and Altermatt, 1985).

^cThe oxidation state value from Zhang, Shi, Yang, Chen, and Feng (2000).

Table 3.9 Hydrogen Bonding Interactions for Compounds **3a-e**.

	D-H...A	d(D-H) (Å)	d(H...A) (Å)	d(D...A) (Å)	<(DHA) (°)
3a	N(1)-H(1B)...O(2) ⁱ	0.90	2.27	3.057(5)	145
	N(1)-H(1B)...O(7) ⁱⁱ	0.90	2.58	3.285(5)	136
	N(4)-H(4A)...O(6) ⁱⁱⁱ	0.90	2.23	3.084(6)	159
	N(4)-H(4B)...O(5) ^{iv}	0.90	2.53	3.351(5)	152
3b	N(1)-H(1B)...O(6) ⁱ	0.92	2.41	3.233(3)	149
	N(2)-H(4A)...O(1) ⁱⁱ	0.92	2.27	3.059(3)	144
	N(2)-H(4B)...O(1) ⁱⁱⁱ	0.92	2.57	2.993(3)	109
	N(2)-H(4B)...O(4) ^{iv}	0.92	2.43	3.216(3)	144
	C(1)-H(2B)...O(1) ⁱ	0.99	2.67	3.411(3)	132
3c	N(1)-H(1A)...O(6) ⁱ	0.95(2)	2.07	2.956(10)	154
	N(1)-H(1B)...O(2) ⁱⁱ	0.93(8)	2.32	3.222(9)	164
	N(2)-H(2A)...O(4) ⁱⁱⁱ	0.95(2)	2.13	2.982(10)	148
	N(2)-H(2A)...O(6) ^{iv}	0.95(2)	2.35	2.980(10)	124
	N(2)-H(2B)...O(5) ^v	0.94(2)	1.98	2.921(9)	178
	N(2)-H(2C)...O(1) ⁱ	0.98(8)	1.82	3.744(10)	166
3d	C(1)-H(1D)...O(3) ⁱ	0.84	2.53	3.332(13)	159
	N(2)-H(2A)...O(2) ⁱⁱ	0.92	2.20	2.853(11)	127
	N(2)-H(2B)...O(1) ⁱ	0.92	2.28	2.896(11)	124
	N(2)-H(2B)...O(10) ⁱ	0.92	2.13	2.898(10)	140
	N(2)-H(2C)...O(4)	1.00	2.11	3.084(12)	164
3e	O(1W)-H(1)...O(1)	0.89(6)	1.99(6)	2.859(4)	166(5)
	O(1W)-H(2)...O(5) ⁱ	0.70(8)	2.42(9)	3.023(5)	145(8)
	O(1W)-H(2)...O(2) ⁱ	0.70(8)	2.53(8)	3.145(4)	148(8)
	O(2W)-H(4)...O(2) ⁱ	0.71(5)	2.16(5)	2.847(4)	164(5)
	O(2W)-H(3)...O(3)	0.80(2)	2.00(3)	2.770(4)	161(3)
	N(1)-H(1A)...O(1) ⁱⁱ	0.87(2)	2.49(3)	3.296(4)	153(3)
	N(1)-H(1B)...O(2W)	0.81(3)	2.48(4)	3.120(4)	137(4)
	N(2)-H(2A)...O(1) ⁱⁱⁱ	0.88(3)	2.63(3)	3.482(4)	162(3)
	N(2)-H(2B)...O(1W) ^{iv}	0.84(3)	2.37(3)	3.193(5)	166(4)
	N(3)-H(3A)...O(1W) ^{iv}	0.88(3)	2.28(3)	3.080(4)	151(4)
	N(3)-H(3B)...O(6) ^v	0.84(2)	2.30(3)	3.138(4)	174(4)
	N(4)-H(4B)...O(2) ^{vi}	0.84(3)	2.40(3)	3.074(4)	137(4)
	N(4)-H(4A)...O(2W)	0.87(3)	2.36(3)	3.038(4)	136(3)

Symmetry codes: **3a**: (i) $x, y-1, z$; (ii) $-x+1, y-1/2, -z+2$; (iii) $-x, y+1/2, -z+1$; (iv) $x-1, y, z$. **3b**: (i) $-x+1, -y+1, -z+1$; (ii) $-x+2, -y+1, -z+1$; (iii) $-x+2, y+1/2, -z+1/2$; (iv) $x+1, -y+1, z$. **3c**: (i) $x, y, z+1$; (ii) $-x+1, -y, -z+1$; (iii) $x+3/2, -y+1/2, z+1/2$; (iv) $1+x, y, z+1$; (v) $x+1/2, -y+1/2, z+1/2$; (vi) $x+1, y, z$. **3d**: (i) $-x+1, -y+2, -z+2$; (b) $x, -y+3/2, z-1/2$. **3e**: (i) $x+1, y, z$; (ii) $x-1/2, y-1/2, z$; (iii) $-x+1, y, -z+2$; (iv) $x-1, y, z$; (v) $x+1/2, y+1/2, z$; (f) $-x, y, 1-z$.

Table 3.10 Physical and Analytical Data for Compounds **3a**, **3d** and **3e**.

Compound	M _r	Crystal Color	^a D.point (°C)	Elemental Anal. Calc. (Found) (%)				
				C	H	N	^b V	^b Zn
3a : Zn ₂ (en)V ₂ O ₇	404.72	Purple	282.71	5.49 (5.94)	1.90 (1.99)	6.82 (6.92)	1.4	1.0
3d : Zn(HenMe) ₂ (V ⁴⁺ V ⁵⁺ O ₅) ₄	943.17	Black	337.53	7.64 (8.36)	2.35 (2.48)	5.94 (5.52)	7.0	1.0
3e : Zn(enMe) ₂ (VO ₃) ₂ ·2H ₂ O	447.49	Pale- brown	136.92	16.41 (16.20)	5.41 (5.68)	12.52 (12.44)	1.6	1.0

^aD. point is decomposition point. ^bMeasured by EDX.

3.3.2 Infrared spectra

Figure 3.21 shows infrared spectra of **3a**, **3c**, **3d**, and **3e**, particular the frequencies of vanadate and zinc compounds that similar as observed in literature (Frost, Erickson, Weier, and Carmody, 2005; Nakamoto, 1997; Nyquist, Kagel, and Leuqers, 1997). The vibration mode of the terminal $\nu(\text{V}=\text{O}_t)$ symmetric stretch is observed at 985, 947, 926, and 908 cm^{-1} for **3a**; 1001, 967, 958, 945, 923, 914, and 900 cm^{-1} for **3c**; 1020, 986, and 910 cm^{-1} for **3d**; 999, 931, and 902 cm^{-1} for **3e**. The vibration mode of the terminal $\nu(\text{V}=\text{O}_t)$ and bridging V–O–V asymmetric stretches appeared at 837, 779, 735, 701, 666, 637, 538, and 523 cm^{-1} for **3a**; 875, 820, 722, 640, and 556 cm^{-1} for **3c**; 878, 829, 810, 654, and 552 cm^{-1} for **3d**; 838, 820, 644, and 527 cm^{-1} for **3e**. The combination vibration modes of bridging V–O–V symmetric stretches and Zn–O stretches are observed at 480, 440, and 423 cm^{-1} for **3a**; at 475 cm^{-1} for **3c**; 486 and 412 cm^{-1} for **3d**; 494, 453, and 440 cm^{-1} for **3e**. The very strong peak at 3459 cm^{-1} for **3e** is assigned to a $\nu_{\text{as}}(\text{O}-\text{H})$ stretching vibration. Bands in the 3266 and 3193 cm^{-1} for **3a**; 3294 and 3222 cm^{-1} for **3c**; 3329 and 3263 cm^{-1} for **3d**; 3329 and 3283 cm^{-1} for **3e** due to the $\nu_{\text{as}}(\text{N}-\text{H})$ asymmetric stretching. Bands at 3119, and 2951 cm^{-1} for **3a**; 3016 and 2962 cm^{-1} for **3d**; 3176, 2974, 2954, 2939, 2905, and

2880 cm^{-1} for **3e** assigned to combination of $\nu_{\text{as}}(^+\text{N-H})$ and $\nu_{\text{as}}(\text{C-H})$ asymmetric stretches. The peak at 1596 and 1573 cm^{-1} for **3a**; 1625 cm^{-1} for **3c**; 1614 and 1569 cm^{-1} for **3d**; 1630 and 1620 cm^{-1} for **3e** are due to the $\delta(\text{H-O-H})$ and $\delta(\text{H-N-H})$ bending modes.

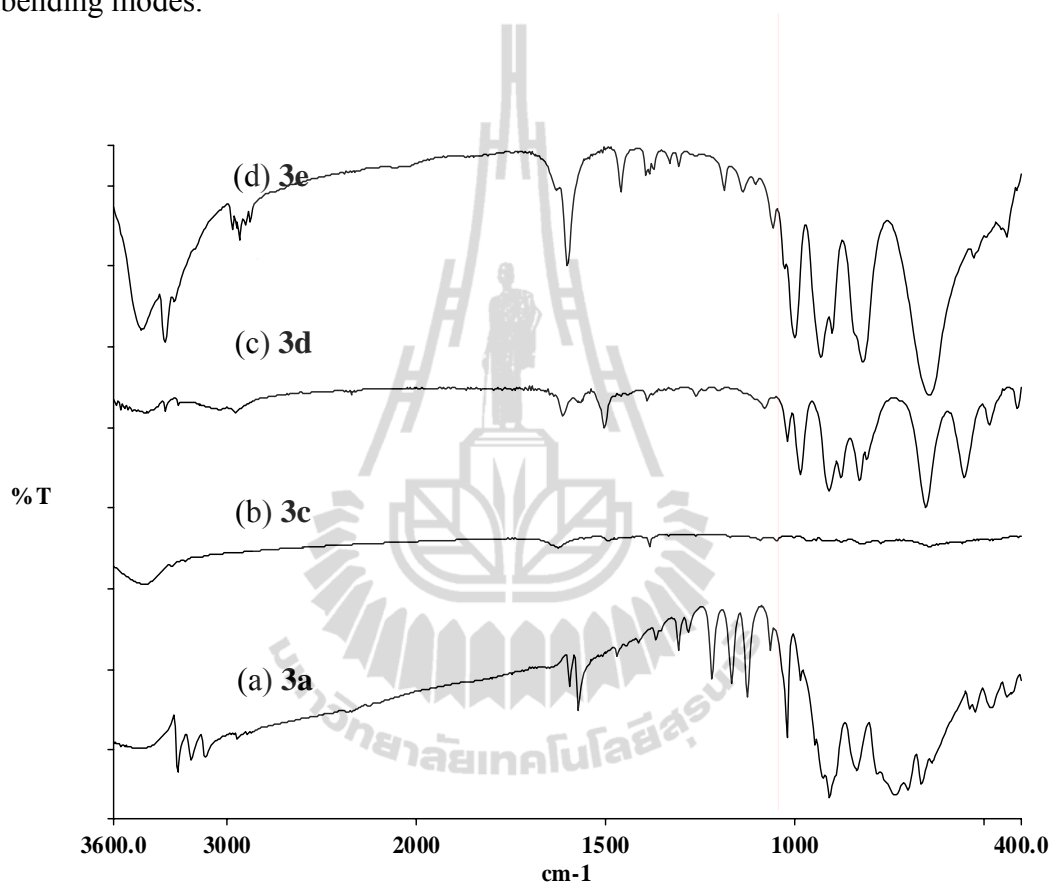


Figure 3.21 Infrared spectra.

Table 3.11 IR Spectral Data for Compounds **3a** and **3c-e**.

^a Assignment	3a	3c	3d	3e
$\nu_{\text{as}}(\text{O-H})$	^b 3447	^b 3438	^b 3446	3459 vs
$\nu_{\text{as}}(\text{N-H})$	3266 m 3193 m	3294 vw 3222 vw	3329 w 3263 w	3329 vs, sp 3263 w
$\nu_{\text{as}}(^+\text{N-H}) + \nu_{\text{as}}(\text{C-H})$	3119 w 2951 vw		3016 vw 2962 vw	3176 sh 2974 w 2954 w 2939 m, sp

Table 3.11 (Continued).

^a Assignment	3a	3c	3d	3e
				2905 w 2880 w
$\delta_{(H-O-H)} + \delta_{(H-N-H)}$	1596 m 1573 m	1625 vw	1614 m 1569 w	1630 vw 1602 vs, sp
$\nu_{s(VO_2)}$	985 vw 947 vw 926 vw 908 m	1001 vw 967 vw 958 vw 945 vw 923 vw 914 vw 900 vw	1020 m, sp 986 vs, sp 910 m	999 vs, sp 931 vs, sp 902 m, sp
$\nu_{as(VO_2)}$	837 m	875 vw 820 vw	878 m 829 m 810 w	838 sh 820 vs
$\nu_{as(V-O-V)}$	779 vw 735 w 701 vw 666 m 637 vw 538 vw 523 vw	722 w 640 vw 556 vw	654 vs, sp 552 vs, sp	644 vs 527 w
$\nu_{s(V-O-V)} + \nu_{(Zn-O)}$	480 m 440 w 423 vw	475 vw	486 m 412 m	494 vw 453 vw 440 m

3.3.3 Thermogravimetric Analysis

Figures 3.22-3.24 show the TGA curves for compounds **3a**, **3d** and **3e**. Total weight loss of 23.626% (calc. 22.752%), 22.625% (calc. 22.859%), and 42.310% (calc. 41.167%) for **3a**, **3d** and **3e** with each is divided into three, two and six stages, respectively. In **3a** and **3d**, first and second weight loss are 15.435% (calc. 14.845%) in the temperature range of 283-385 °C and only first weight loss is 15.910% (calc. 15.926%) in the temperature range of 338-470 °C corresponding to the loss of the bridging en in **3a** and the two monodentated HenMe⁺ ligands in **3d**, respectively. While first weight loss of **3e** about 8.230% (calc. 8.051%) in the temperature range of

83.97-136.92 °C due to the solvate water removal and second to six weigh loss are 32.667% (calc. 33.116%) in the temperature range of over 136.92-861.36 °C corresponded to the loss of the chelating enMe ligands with slightly decrease in weight of 1.982% in the temperature range of 619.44-861.36 °C due to ZnO and V₂O₅ begin to form with the oxidation state of vanadium changing from V⁵⁺ to V⁴⁺, with the residual weight of 58.833%. It is in good agreement with the total calculated weight of two inorganic compounds of 59.103%. The collapsed network and framework in **3a** and **3d** with weight loss of 8.191% (calc. 7.907%) in the temperature range of 385-732 °C and 6.715% (calc. 6.785%) in the temperature range of 470-643 °C due to the loss of the oxygen atoms, followed by a slight increase in weight of 0.742% and 2.808% that could be due to oxidation of sheets from V⁴⁺ to V⁵⁺, respectively. The residual in **3a** and **3d** are assumed to ZnV₂O₅, and Zn_yV₂O₅ (y = 0.01-0.02) with the observed weight remaining about 76.374% (calc. 77.248%), and 77.375% (calc. 77.412% or 77.689% depending on the amount of zinc), respectively. It is clear that the open framework of **3d** has a high thermal stability of 337 °C by the observed crystal surface and confirmed the phase by powder X-ray diffraction at varied temperatures, since the similar coordinate radii of Zn²⁺ (0.88 Å) compare to Mg²⁺ (0.86 Å) and Fe²⁺ (0.92 Å), thus, the residual is the isomorphus phase of Fe_{0.02}V₂O₅ and Mg_{0.01}V₂O₅ (Pattern: 00-049-0805 and Pattern: 01-089-0610, Appendix A) when heated at over 470 °C, as shown in Figures 3.25-3.26. The thermal stability of the network **3a** and the open framework structure of **3e** with the water molecules were removed and stable up to 283 °C and 136 °C, respectively.

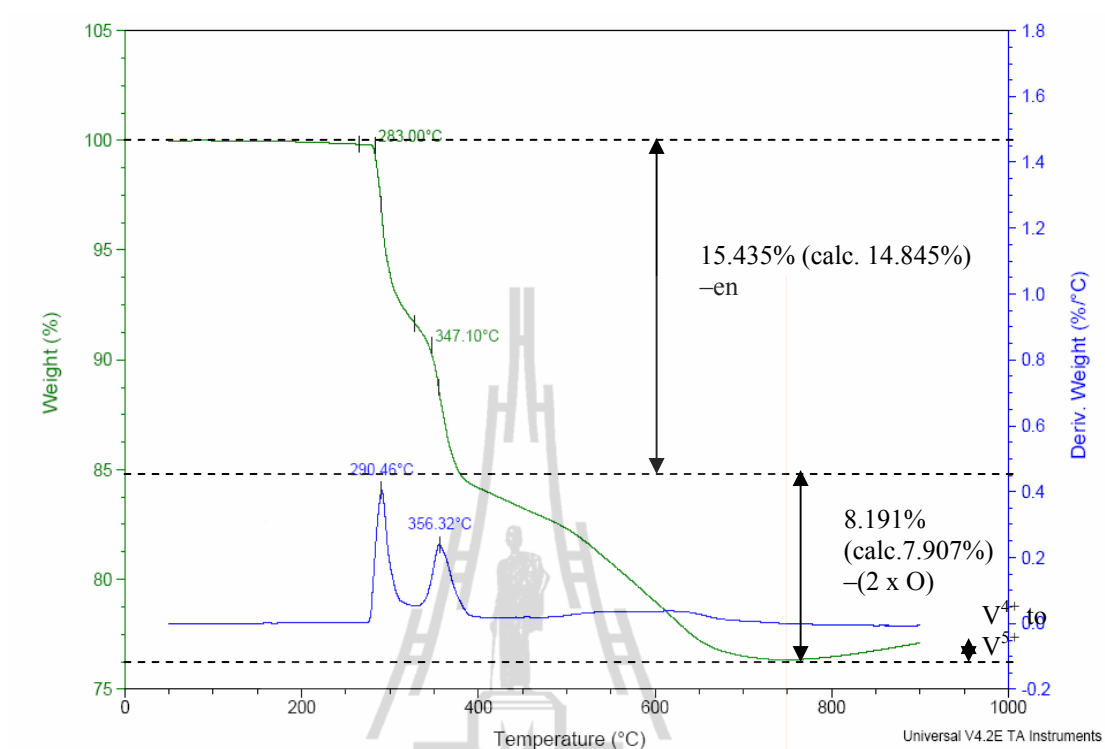


Figure 3.22 TGA curve of 3a.

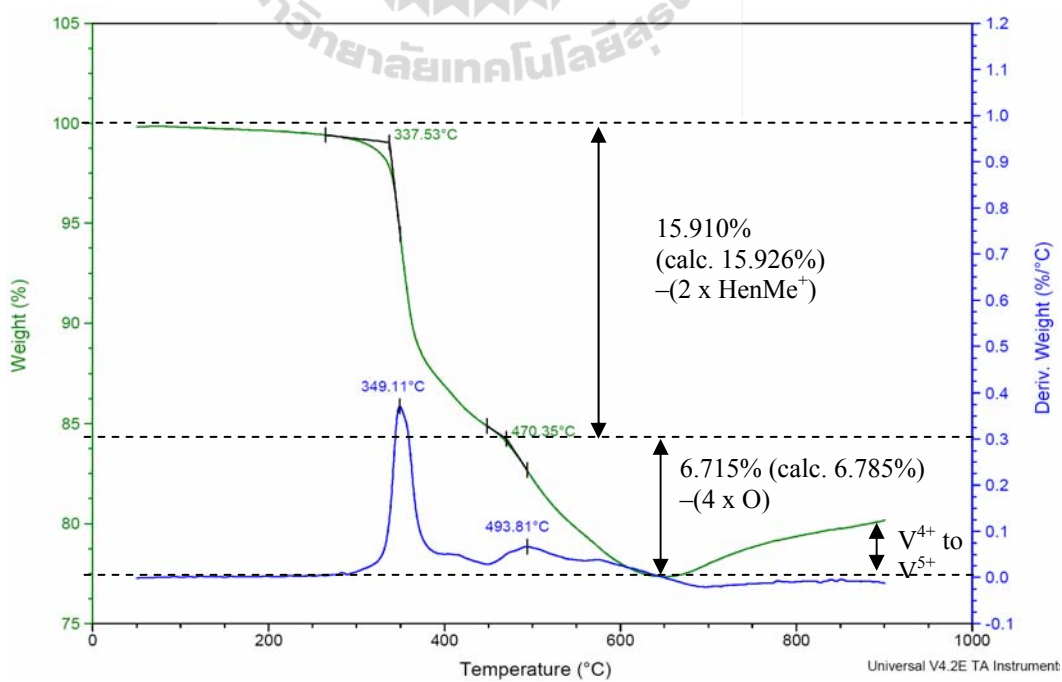


Figure 3.23 TGA curve of 3d.

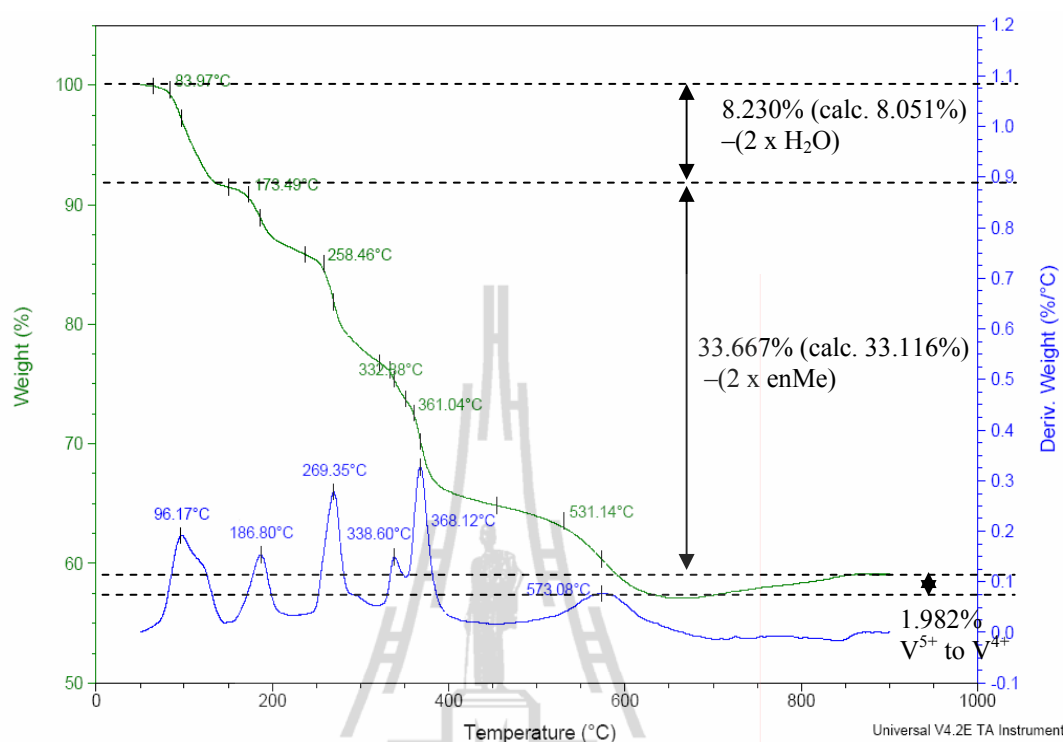


Figure 3.24 TGA curve of **3e**.

Table 3.12 Decompositions as a Function of Temperature.

Comp.	Items	%Weight Loss			Temperature (°C)	Composition
		Calc.	Measure	Error		
3a	Decomposition	14.845	15.435	0.590	282.71-384.85	-en
		7.907	8.191	0.284	384.85-731.70	-(2 x O)
	Residual	77.248	76.374	0.874	>731.70	ZnV ₂ O ₅
			+0.742		>800	V ⁵⁺ to V ⁴⁺
3d	Decomposition	15.926	15.910	0.016	337.53-470.35	-(2 x HenMe ⁺)
		6.785	6.715	0.070	470.35-642.88	-(4 x O)
	Residual	77.412	77.375	0.037	>642.88	4 x Zn _{0.01} V ₂ O ₅
		77.689		0.314		4 x Zn _{0.02} V ₂ O ₅
		+2.808		642.88-900	V ⁴⁺ to V ⁵⁺	
3e	Decomposition	8.051	8.230	0.187	83.97-136.92	-(2 x H ₂ O)
		33.116	32.667	0.449	136.92-861.36	-(2 x enMe)
	Residual	58.833	59.103	1.143	>861.36	ZnO and V ₂ O ₅
			-1.982		619.44-861.36	V ⁵⁺ to V ⁴⁺

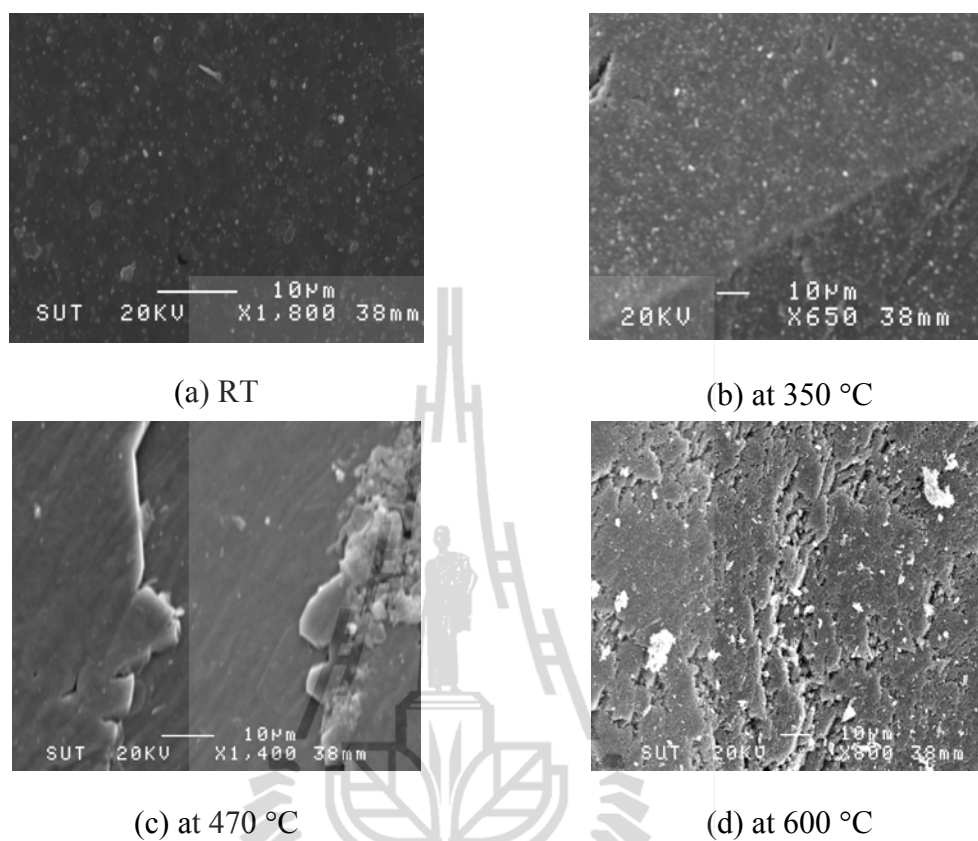


Figure 3.25 The SEM images of 3d.

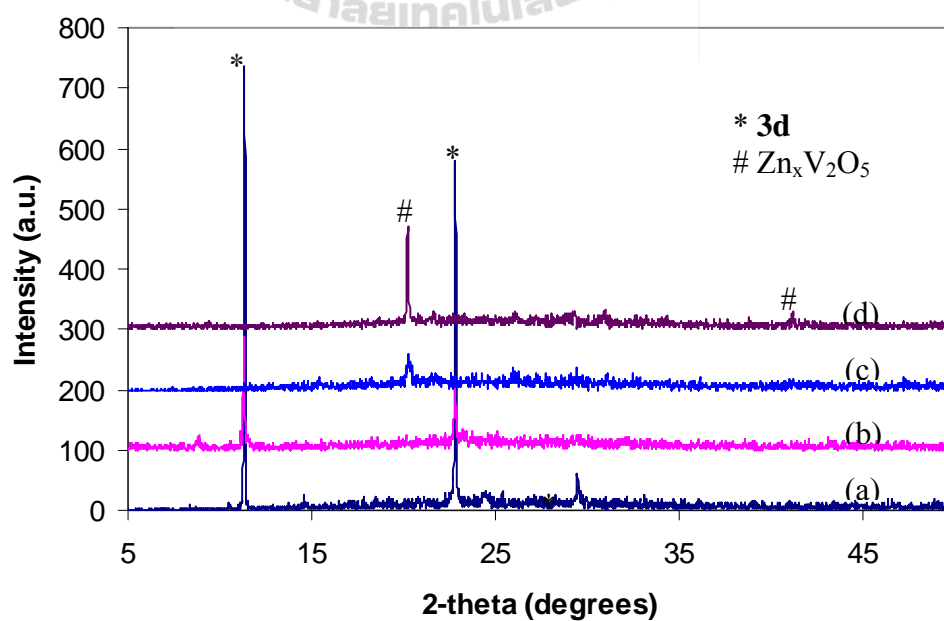


Figure 3.26 The XRD patterns of 3d (a) RT, with heated (b) at 350 °C, (c) at 470 °C and (d) at 600 °C.

3.4 Conclusions

Five new hybrid organic-inorganic vanadate compounds, namely (en)Zn₂V₂O₇ (**3a**), (en)Zn(VO₃)₂ (**3b**), (Hen)₂Cd(VO₃)₄ (**3c**), (HenMe)₂Zn(V₂O₅)₄ (**3d**) and (enMe)₂Zn(VO₃)₂·2H₂O (**3e**), have been synthesized via hydrothermal synthesis. **3a** consists of a V₂O₇⁴⁻ dimer unit or pyrovanadate, while **3b**, **3c** and **3e** are composed of polymeric metavanadate chains and **3d** exhibits a mixed-valence vanadate layer. The dimer unit in **3a** is linked to the different zinc complexes with the flexibility of the bridging ligand essential for formation of the helix, forming a 3-D chiral helical network which contains polymeric helical zinc coordination complex chains, zinc tetrahedra-en-zinc trigonal bipyramid, and the polymeric helical zinc vanadate chains. The polymeric metavanadate chains in **3b**, **3c** and **3e** linked with the metal coordination complexes cross linkers forming 2-D double layers, 1-D double chains, and a 3-D open framework, respectively. The layers of **3b** and chains of **3c** are further hydrogen bonded, N–H···O interactions, to neighbors producing 3-D supramolecular network and 2-D supramolecular layer, respectively. While the O–H···O hydrogen bonding interactions with a $R_4^3(10)$ motif between solvate water molecules and the framework in **3e**. The mixed-valence [(V⁴⁺O)(V⁵⁺O₄)]₅ layers of **3d** are linked together with the pillared zinc coordination complexes forming a 3-D open framework. The successful syntheses of such helical chiral networks or the open framework structures offer a fascinating example of the hybrid organic-inorganic materials.

3.5 References

- Brown, I. D., and Altermatt, D. (1985). Bond-valence parameters obtained from a systematic analysis of the inorganic crystal structure. **Acta Crystallographica Section B**. 41(4): 244-247.
- Burnett, M. N., and Johnson, C. K. (1996). *ORTEP-III: Oak Ridge Thermal Ellipsoid Plot Program for Crystal Structure Illustration*, Report ORNL-6895, Oak Ridge National Laboratory, Oak Ridge, Tennessee.
- Cao, G.-J., Zheng, S.-T., Fang, W.-H., and Yang, G.-Y. (2010). (en)Mn₂(V₂O₇): A 3-D manganese vanadate built by Mn–O layers and two types of pillars of V₂O₇ and en bridges. **Inorganic Chemistry Communications**. 13(7): 834-836.
- Crystal Impact. (2006). *DIAMOND*. Version 3.1. Crystal Impact GbR. Bonn, Germany.
- DeBord, J. R. D., Zhang, Y., Haushalter, R. C., Zubieta, J., and O'Connor, C. J. (1996). One-dimensional vanadium oxide chains containing covalently bound copper coordination complexes: hydrothermal synthesis and characterization of Cu(en)[V₂O₆], Cu(2,2'-bipy)[V₂O₆], and Cu(2,2'-bipy)₂[V₂O₆]. **Journal of Solid State Chemistry**. 122(2): 251-258.
- Frost, R. L., Erickson, K. L., Weier, M. L., and Carmody, O. (2005). Raman and infrared spectroscopy of selected vanadates. **Spectrochimica Acta Part A**. 61(5): 829-834.
- Galy, J., and Carpy, A. (1975). Structure cristalline de K₂V₃O₈ ou K₂(VO)[V₂O₇]. **Acta Crystallographica Section B**. 31(6): 1794-1795.
- Gopal, R., and Calvo, C. (1973). Crystal structure of α-Zn₂V₂O₇. **Canadian Journal of Chemistry**. 51(7): 1004-10119.

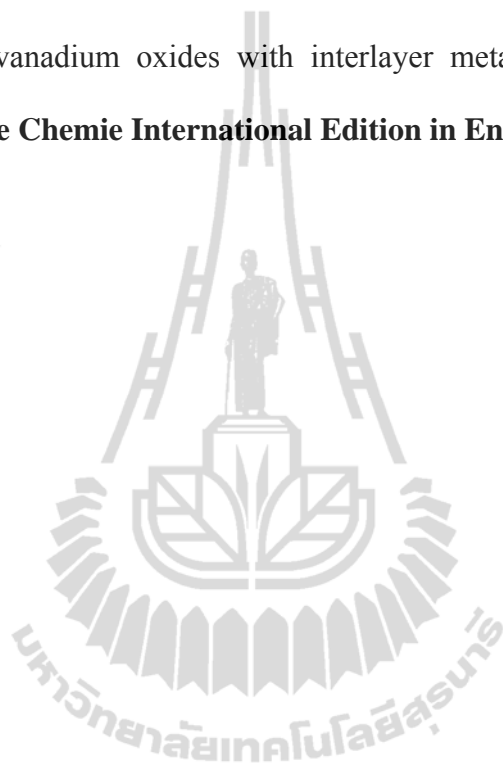
- Gopal, R., and Calvo, C. (1974). Crystal structure of magnesium divanadate. $\text{Mg}_2\text{V}_2\text{O}_7$. **Acta Crystallographica Section B**. 30(10): 2491-2493.
- Khan, M. I., Hope, T., Cevik, S., Zheng, C., and Powell, D. (2000). Organically templated vanadium oxide phases: synthesis and structures of $[\text{H}_3\text{NCH}_2\text{CH}_2\text{NH}_3][\text{V}_2\text{O}_6]$ and $[\text{HN}(\text{CH}_2\text{CH}_2)_3\text{NH}][\text{V}^{\text{V}}\text{P}_2\text{V}^{\text{IV}}_4\text{O}_{14}]\cdot\text{H}_2\text{O}$. **Journal of Cluster Science**. 11(3): 433-447.
- Khan, M. I., Yohannes, E., Doedens, R. J., Golub, V. O., and O'Conner, C. J. (2005). Templated synthesis of a chiral solid: Synthesis and characterization of $[\text{Co}(\text{en})_3][\text{V}_3\text{O}_9]\cdot\text{H}_2\text{O}$, containing a new type of chiral vanadium oxide chain. **Inorganic Chemistry Communication**. 8(9): 841-845.
- Krachodnok, S., Haller, K. J., and Williams, I. D. (2008). Chiral helices in a 3D network of $\text{Zn}_2(\text{en})\text{V}_2\text{O}_7$ (en = Ethylenediamine). **Advanced Materials Research**. 55-57: 669-672.
- Law, T. S.-C., and Williams, I. D. (2000). Organic-directed synthesis of manganese vanadates with variable stoichiometry and dimensionality: 1-D $(\text{Hen})_2\text{Mn}(\text{VO}_3)_4$, 2-D $[(\text{H}_2\text{en})_2][\text{Mn}(\text{VO}_3)_4]$, and 3-D $[(\text{H}_2\text{en})[\text{MnF}(\text{VO}_3)_3]$. **Chemistry of Materials**. 12(1): 2070-2072.
- Lin, H., and Maggard, P. A. (2008). Synthesis and structures of a new series of silver-vanadate hybrid solids and their optical and photocatalytic properties. **Inorganic Chemistry**. 47(18): 8044-8052.
- Liu, G., and Greedan, J. E. (1995). Magnetic properties of Fresnoite-type vanadium oxides: $\text{A}_2\text{V}_3\text{O}_8$ (A = K, Rb, NH_4). **Journal of Solid State Chemistry**. 114(1): 499-505.

- Liu, S.-X., Lin, B.-Z., and Lin, S. (2000). Hydrothermal synthesis and characterization of metavanadate containing spiral chain: $[\text{Ni}(\text{en})_3][\text{VO}_3]_2$. **Inorganica Chimica Acta**. 304(1): 33-37.
- Millange, F., Serre, C., Cabourdin, T., Marrot, J., and Férey, G. (2004). Organically templated zinc selenite: MIL-86 or $(\text{en})_2\text{Zn}_4(\text{SeO}_3)_4$ and MIL-87 or $[\text{H}_2\text{-1,3-dap}]_4[\text{Zn}_4(\text{SeO}_3)_8]$. **Solid State Sciences**. 6(2): 229-233.
- Mumme, W. G., and Watts, J. A. (1971). A refinement of the crystal structure of CsV_2O_5 . **Journal of Solid State Chemistry**. 3(3): 319-322.
- Nakamoto, K. (1997). **Infrared and Raman Spectra of Inorganic and Coordination Compounds**. John Wiley, New York. pp. 1-379.
- Ninlaus, C., Riou, D., and Féray, G. (1996). A new decavanadate dihydrate templated by ethylenediamine. **Acta Crystallographica Section C**. 52(3): 512-514.
- Nyquist, R. A., Kagel, R. O., and Leuqers, M. A. (1997). **Handbook of Infrared and Raman Spectra of Inorganic Compounds and Organic Salts**. Academic press, San Diego. pp. 1-151.
- Pavia, D. L., Lampman, G. M., and Kriz, G. S. (1996). **Introduction to Spectroscopy: A Guide for Students of Organic Chemistry**. 2nd edition, Saunders College Publishing, Washington. pp. 14-95.
- Riou, D., and Féray, G. (1995a). Intercalated vanadyl vanadates: syntheses, crystal structures, and magnetic properties. **Inorganic Chemistry**. 34(26): 6520-6523.
- Riou, D., and Féray, G. (1995b). Intercalated vanadyl vanadate $(\text{V}^{4+}\text{O})[\text{V}^{5+}\text{O}_4]\cdot 0.5[\text{enH}_2]$: hydrothermal synthesis, crystal structure, and structural correlation with V_2O_5 and other vanadyl compounds. **Journal of Solid State Chemistry**. 120(1): 137-145.

- Rujiwatra, A., Mander, G. J., Kepert, C. J., and Rosseinsky, M. J. (2005). Synthesis and characterization of subcell-supper cell related ethylenediamine-pillared zinc hydroxysulfates. **Crystal Growth & Design**. 5(1): 183-189.
- SADABS Version 2.03 (1998), SAINT Version 6.26a (2001a), and SMART Version 5.625 (2001b). Bruker Analytical X-ray Systems Inc., Madison, Wisconsin, USA.
- Sauerbrey, C., Faggiani, E. R., and Calvo, C. (1974). Cobalt vanadate, $\text{Co}_2\text{V}_2\text{O}_7$, and nickel vanadate, $\text{Ni}_2\text{V}_2\text{O}_7$. **Acta Crystallographica Section B**. 30(12): 2907-2909.
- Sheldrick, G.M. (2000). SHELXTL-97, Version 6.10: Structure determination software programs, Bruker Analytical X-ray Systems, Inc., Madison, Wisconsin, U.S.A.
- Shi, Z., Zhang, L., Zhu, G., Yang, G., Jia, H., Ding, H., and Feng, S. (1999). Inorganic/organic hybrid materials: layered vanadium oxides with interlayer metal vanadium complexes. **Chemistry of Materials**. 11(12): 3565-3570.
- Williams, I. D., Law, T. S.-C., Sung, H. H.-Y., Wen, G.-H., and Zhang, X.-X. (2000). Organo-directed synthesis of a 3-D open-framework mixed-metal oxide, $[\text{H}_2\text{en}][\text{Mn}_3(\text{V}_2\text{O}_7)_2(\text{H}_2\text{O})_2]$, incorporating metal trimer building blocks. **Solid State Science**. 2(1): 47-55.
- Zhang, L., Shi, Z., Yang, G., Chen, X., and Feng, S. (2000). Hydrothermal synthesis and crystal structure of a layered vanadium oxide with an interlayer metal coordination complex: $(\text{HenMe})_2\text{CdV}_8\text{O}_{20}$. **Journal of the Chemical Society, Dalton Transactions**. (3): 275-278.
- Zhang, Y., Haushalter, R. C., and Clearfield, A. (1996). Hydrothermal synthesis and structural characterization of layered vanadium oxides incorporating organic

cations: α -, β -[H₂en][V₄O₁₀] and α -, β -[H₂piperazine][V₄O₁₀]. **Inorganic Chemistry**. 35(17): 4950-4956.

Zhang, Y., DeBord, J. R. D., O'Connor, C. J., Haushalter, R. C., Clearfield, A., and Zubieta, J. (1996). Solid state coordination chemistry: hydrothermal synthesis of layered vanadium oxides with interlayer metal coordination complexes. **Angewandte Chemie International Edition in English**. 35(9): 989-991.



CHAPTER IV

HYDROTHERMAL SYNTHESSES AND STRUCTURAL CHARACTERIZATIONS OF ALKALI METAL VANADATES

4.1 Introduction

The layered main group trivanadates ($M_xV_3O_8$) are of great current interest due to potential applications in Li-ion batteries (Li, Pang, Jiang, Guo, and Zhang, 2006; Yang, Li, Zhang, and Jin, 2008) and low-temperature magnetic devices (Liu and Greedan, 1995), and also for their complex structural chemistry, associated with the different valence states (+3, +4, +5), coordination numbers, and geometries (tetrahedral, trigonal bipyramidal, square pyramidal and octahedral) available in vanadium chemistry, that allow layers to be built up from different polyhedral connections and orientations. As a result, several different varieties of layered types have been reported (Galy and Carpy, 1979; Riou and Férey, 1995; Zhang, Haushalter, and Clearfield, 1996).

Monopotassium trivanadate (KV_3O_8 or $K(VO)_2VO_6$) is a member of the MV_3O_8 ($M = K, Rb, Cs$) family (Evans and Block, 1966; Oka, Yao, and Yamamoto, 1997). Dipotassium trivanadate ($K_2V_3O_8$) is a member of the fresnoite-type structure, $M_2(VO)V_2O_7$ ($M = K, Rb, NH_4$) which are of interest due to their low-temperature magnetic properties (Galy and Carpy, 1975; Liu and Greedan, 1995; Choi, Musfeldt, Ragghianti, Mandrus, Sales, and Thompson, 2001). This layered vanadates family

crystallizes in the polar tetragonal space group $P4bm$ and contains mixed-valence $[(V^{4+}O)V^{5+}_2O_7]^{2-}$ layers composed of equal numbers of two building units; the V_2O_7 units lying on $2.mm$ symmetry sites at $1/2,0,z$ and $0,1/2,z$ (each V is approximately trigonal pyramidal), and the square pyramidal VO_5 units lying on 4 sites at $0,0,z$ and $1/2,1/2,z$. The building units combine by corner-sharing basal O atoms such that all V=O groups of the plane (and of the crystal) are oriented in the same direction parallel to the c axis. Basal μ_2 -O connections form a 2-D network of pentagonal motifs in Figure 4.1(a); two sides from two square pyramidal units connected by one trigonal pyramid from the end of a V_2O_7 unit and the 2 related trigonal pyramid from the side of a second V_2O_7 unit. The potassium coordination environment consists of the pentagonal μ_2 -O atoms of one layer and the five associated apical vanadyl O atoms of the adjacent layer giving a pentagonal antiprismatic KO_{10} coordination environment as illustrated in Figure 4.1(b). Figures 4.1(c) and 4.1(d) are drawn perpendicular to the c axis and b axis, respectively (and thus, to the pentagonal channels occupied by the K^+ ions).

Other layered vanadates, namely the melilite-type structure, are of interest in luminescent (Zubkov, Tyutyunnik, Tarakina, Berger, Surat, Slobodin, Svensson, Forslund, Shulgin, Pustovarov, Ishchenko, and Cherepanov, 2009; Slobodin, Surat, Samigullina, Ishchenko, Shulgin, and Cherepanov, 2010) which has the general formula $A_2^+B^{2+}C_2O_7$ (A = alkali metal; B = divalent metal or similar charge, and C = pyrogroups), that are closely related to the fresnoite-type structure, composed of corner-sharing BO_4 tetrahedra and C_2O_7 pyrogroups (one corner shares of two CO_4 tetrahedra). The difference between both structure types is that the B^{2+} dication site forms a distorted tetrahedra which can be replaced with square pyramids of the fresnoite-type structure and the V=O group of each V_2O_7 pyrogroups are oriented in

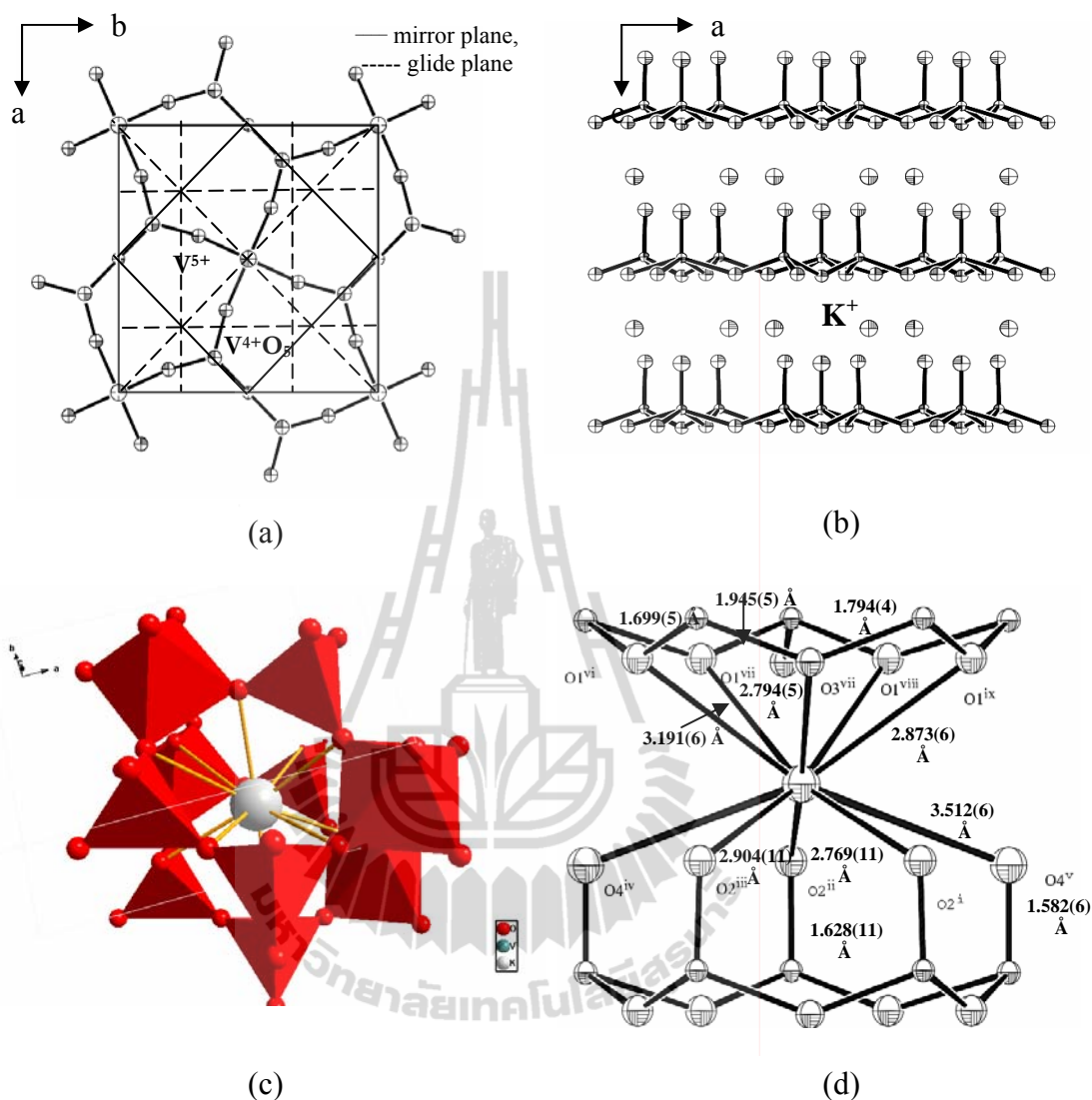


Figure 4.1 Crystal structure of $K_2V_3O_8$ projected onto ab plane, showing (a) $[(V^{4+}O)(V^{5+}_2O_7)]^{2-}$ layer and (b) ac plane with K^+ ions lying between layers, and (c) perspective view of KO_{10} coordination with polyhedral represent, and (d) ORTEP-III represent with bond distances. Symmetry code: (i) $x,y,z-1$; (ii) $-y+1,x,z-1$; (iii) $-x+1,-y,z-1$; (iv) $x+1,y,z-1$; (v) $x+1/2,-y+1/2,z-1$; (vi) $2-x,-y,z$; (vii) $-y+1/2,x,z$; (viii) $x+1/2,y+1/2,z$; (ix) $-y+1/2,-x+1/2,z$ (Galy and Carpy, 1975).

opposite directions. There are two related space groups, $P-42_1m$ and $P4_2/mnm$, in which each $B^{2+}C_2O_7$ layer has the same polyhedral orientation and the A^+ monocation lying between the layers formed is square antiprismatic, whereas two $B^{2+}C_2O_7$ layered types related with the mirror plane and two crystallographically independent A^+ forming a distorted square prism, respectively. If the B^{2+} dication site is an alkaline earth metal, the compounds crystallize in the monoclinic space group $P2_1/n$ in which BO_6 octahedra share the corners with pyrovanadates forming 2-D sheets of hexagonal motifs (Zubkov, Tyutyunnik, Tarakina, Berger, Surat, Slobodin, Svensson, Forslund, Shulgin, Pustovarov, Ishchenko, and Cherepanov, 2009). There are a few reported existences with the pyrovanadates as are listed in Table 4.1.

Table 4.1 Published Lists of $A_2^+B^{2+}V_2O_7$ Compounds in Literature Reviews.

Compounds	Crystal System, Space Group	a (Å)	b (Å)	c (Å)	References
$(NH_4)_2(VO)V_2O_7$	Tetragonal,	8.932	8.932	5.593	Ren et al. (2007).
$K_2(VO)V_2O_7$	$P4bm$ (Z = 2)	8.870(5)	8.870(5)	5.215(2)	Galy and Carpy (1975).
		8.8954(1)	8.8954(1)	5.2472(1)	Chakoumakos et al. (2007).
$Rb_2(VO)V_2O_7$		8.9229(18)	8.9229(18)	5.5014(11)	Withers et al. (2004).
$Na_2ZnV_2O_7$	Tetragonal, $P-42_1m$ (Z = 2)	8.2711(4)	8.2711(4)	5.1132(2)	Tyutyunnik et al. (2005).
$K_2MnV_2O_7$		8.609(3)	8.609(3)	5.538(4)	Yahia et al. (2007).
$K_2MgV_2O_7$	Tetragonal, $P4_2/mnm$	8.38(2)	8.38(2)	11.36(2)	Murashova et al. (1988).
$Rb_2MnV_2O_7$	(Z = 4)	8.577(6)	8.577(6)	11.809(6)	Yahia et al. (2007).
$KRbMnV_2O_7$		8.530(6)	8.530(6)	11.466(5)	Yahia et al. (2007).
$Rb_2CaV_2O_7$	Monoclinic, $P2_1/n$ (Z = 4)	13.8780(1)	5.96394(5)	10.3376(1)	Zubkov et al. (2009)
$Cs_2CaV_2O_7$		14.0713(2)	6.0934(1)	10.5944(1)	Slobodin et al. (2010).
					$\beta = 104.60(1)^\circ$

The various synthetic conditions including reaction temperature and pH, and chemical sources affect to control the structure types of compounds and intrinsically inside crystal structure. Most those trivanadates have been prepared at high temperature by ceramic routes as shown in Table 4.2 with difficulty to control the mixed-valence vanadium compounds such as in the synthesis of $K_2(V^{4+}O)V^{5+}_2O_7$. Galy and Carpy (1975) obtained the single crystal product from solid state reaction of $K_2O-V_2O_5-VO_2$ system. Twenty years later, the same compound was produced from the solid state reaction of KVO_3 , V_2O_3 , and V_2O_5 in a sealed tube at 550 °C (Liu and Greedan, 1995). Last, its single crystals were prepared by cooling of VO_2 in molten KVO_3 flux in a platinum crucible sealed inside a silica container (Choi, Zhu, Musfeldt, Ragghianti, Mandrus, Sales, and Thompson, 2001). In addition, the mixed-cation pyrovanadate, $K_2ZnV_2O_7$, was made by heating a 1:1:1 molar mixture of K_2CO_3 , ZnO and V_2O_5 at 550 °C overnight. It was reground and heated again at 550 °C for 2 days (McMurdie, Morris, Evans, Paretzkin, Wong-Ng, and Zhang, 1986).

From above, their methods are complicated and expensive, and have difficulties in controlling the homogeneity, particle size, and morphology of the product (Xu, He, Wang, and Yan, 2004). Hydro(solvo)thermal synthesis is a simple and inexpensive alternative technique which has many advantages over the earlier methods. From its many features as describe in Chapter II, Oka and his group (1997) have been synthesized good single crystals of KV_3O_8 from hydrothermal reactions of V_2O_5 powder with alkali metal nitrate, chloride, and sulfate solution in low yield at 250 °C, although this compound can be obtained by acidification of the corresponding metavanadate solutions at near ambient temperatures of about 60-80 °C but the quality of single crystals are not good enough (Evans and Block, 1966).

Xu and coworkers (2004) have successfully prepared $K_2V_3O_8$ nanorods under solvothermal condition employing ethanol as a solvent and a reducing agent in low yield at 200 °C. Whereas Shi and his group (2005) obtained tubular-windows on sheet-like $K_2V_3O_8$ single crystals in pure phase under hydrothermal conditions of 1.0KVO₃:2.1KOH :2.0apidic acid:123H₂O at 180 °C for 2 days. Apidic acid (HOOC(CH₂)₄COOH) acts as a mild reductant, a buffer and a morphological directing agent. Therefore, $K_2V_3O_8$ was obtained in lower yield (Choi, Zhu, Musfeldt, Raghianti, Mandrus, Sales, and Thompson, 2001), and reaction temperature at 180 °C (Shi, Rocha, Lopes, and Trindade, 2005) under hydro(solvo)thermal condotions.

In this work, we report high yield with high crystalline of $M_xV_3O_8$, under hydrothermal reaction conditions at various reaction temperatures and enMe acts to adjust the reaction pH and a reducing agent for $x = 2$. Zn(OAc)₂ acts not only as a catalyst in the formation of $M_xV_3O_8$ but also acts as an inhibitor by donating Zn²⁺ ions which replace VO²⁺ ions to form the $K_2ZnV_2O_7$ compound.

4.2 Experimental

4.2.1 Chemicals and Instruments

All reagents were used without further purification. All syntheses were carried out in PTFE-lined stainless steel reactors under autogenous pressure. The 23 mL reaction vessels were filled to approximately 40% volume capacity. Powder X-ray diffraction patterns were recorded on a Philips PW 1830 diffractometer equipped with a Cu $K\alpha$ X-ray source ($\lambda = 1.54062 \text{ \AA}$) in the angular range 2-theta = 5-50°, with a step size of 0.05° and a counting time of 3 s per step. XRD pattern analyses were carried out by the Traces program version 3. Infrared spectra of the samples

Table 4.2 Preparation Lists of Alkali Metal Vanadates in Literature Reviews.

Compound	Sources	Synthetic Method	Temperature and Time	Crystal Morphology	% Yield	References
MV ₃ O ₈ (M = K, Rb, Cs)	(1) KVO ₃ in acidification	Slow evaporation	60-80 °C	Single crystal (the quality is not good)	-	Evans and Block (1966) Oka et al. (1997)
	(2) V ₂ O ₅ +alkali metal nitrate, chloride, and sulfate	Hydrothermal synthesis	250 °C and 2 days	Single crystal	Low	
K ₂ V ₃ O ₈	(1) K ₂ O+V ₂ O ₅ +VO ₂	Solid state reaction	-	Single crystal	-	Galy and Carpy (1975)
	(2) 8KVO ₃ +V ₂ O ₃ +V ₂ O ₅	Solid state reaction	550 °C and a day	Single crystal	-	Liu and Greedan (1995)
	(3) VO ₂ + KVO ₃	Cooling VO ₂ in a molten KVO ₃ flux	-	Single crystal	Low	Choi et al. (2001)
	(4) 4KOH+3V ₂ O ₅ +EtOH(excess)	Solvothermal synthesis	200 °C and 2 days	Nanorod	Low	Xu et al. (2004)
	(5) KVO ₃ +2.1KOH+2apidic acid+123H ₂ O	Hydrothermal synthesis	180 °C and 2 days	Sheet-like crystal (tubular-window)	High	Shi et al. (2005)
K ₂ ZnV ₂ O ₇	(1) K ₂ CO ₃ +ZnO+V ₂ O ₅	Solid state reaction	550 °C, overnight, then reground and heated again at 550 °C for 2 days	Powder	-	Mcmuride et al. (1986)

were recorded using pressed KBr pellets on a Perkin-Elmer Spectrum GX in the range of 650-1100 cm^{-1} (5 scans, resolution 1 cm^{-1}).

4.2.2 Synthesis of Monopotassium (or Rubidium or Cesium) Trivanadates, MV_3O_8

A mixture of V_2O_5 (181 mg), $Zn(OAc)_2 \cdot 2H_2O$ (220 mg), KOH (56 mg) or RbCl (121 mg) or CsCl (168 mg), and water (2.0 mL), mole ratio 1:1:1:111 was heated at 110 °C, 160 °C and 200 °C for 2 days. The initial and final reaction pH was ~7 without adjustment. Orange plates of AV_3O_8 were isolated with the product yield as function of temperature (Table 4.3). Selected FT-IR bands (cm^{-1}): KV_3O_8 , 990 (w), 959 (s) and 737 (br); RbV_3O_8 , 1005 (m), 967 (s, sh) and 780 (sh), and 737 (br); CsV_3O_8 , 1000 (m), 963 (s), 783 (sh), and 741 (br).

4.2.3 Synthesis of Dipotassium Trivanadate, $K_2V_3O_8$

A mixture of V_2O_5 (181 mg), $Zn(OAc)_2 \cdot 2H_2O$ (220 mg), KOH (56 mg), and water (2.0 mL), mole ratio 1:1:1:111 was heated at 110 °C for 2 days. The initial reaction pH was adjusted to ~11 with enMe. The final reaction pH was ~9. Black plates of $K_2V_3O_8$ (yield ~60%, based on vanadium) were obtained as the major product with a small amount of black powder, $(HenMe)_2ZnV_8O_{20}$ (Krachodnok, Haller and Williams, 2007), as a minor product. The highest product yield (yield ~80%) was obtained by increasing reaction temperature to 140 °C. The yield decreased with increasing reaction temperature above 140 °C (yield ~40% at 200 °C). Selected FT-IR bands (cm^{-1}): 991 (m), 941 (w), 925 (vw), 817 (br) and 740 (br).

4.2.4 Synthesis of Dipotassium Zinc Pyrovanadate, $K_2ZnV_2O_7$

The procedure is similar to compound $K_2V_3O_8$ except an excess of $Zn(OAc)_2 \cdot 2H_2O$ (2.0 mmol) which is heated at 110 °C for 2 days, obtained ~60% yield (based on vanadium) of black plates, $K_2V_3O_8$, ~35% yield of black blocks, $Zn(HenMe)_2V_8O_{20}$, and ~5% yield of colorless needles, $K_2ZnV_2O_7$. Selected FT-IR bands

(cm^{-1}): 936 (br), 896 (br), 851 (br) and 691 (br).

4.2.5 X-ray Crystallography

Single crystals of CsV_3O_8 and $\text{K}_2\text{ZnV}_2\text{O}_7$ are suitable for single-crystal X-ray diffraction with size $0.02 \times 0.5 \times 0.5$ and $0.04 \times 0.04 \times 0.10$ mm, respectively, were selected. Preliminary unit cell parameters and crystal orientation were determined by standard procedures (Bruker, 2001). Structure analysis carried out using data collected on a Bruker-Nonius Smart Apex CCD diffractometer equipped with a graphite-monochromated Mo $K\alpha$ X-radiation source ($\bar{\lambda} = 0.71073 \text{ \AA}$) at $-173 \pm 2 \text{ }^\circ\text{C}$. The data were processed with the program SAINT (Bruker, 2001a) and corrected for absorption and other geometrically related effects with SADABS (Bruker, 1998). The structures were solved by direct methods and refined by full-matrix least-squares refinement on F^2 using SHELXTL-97 (Sheldrick, 2000). Experimental X-ray data for CsV_3O_8 and $\text{K}_2\text{ZnV}_2\text{O}_7$ are given in Table 4.4. Atomic coordinates and equivalent isotropic displacement parameters for CsV_3O_8 and $\text{K}_2\text{ZnV}_2\text{O}_7$ are listed in Tables 4.5, 4.7, respectively. Anisotropic displacement parameters for CsV_3O_8 and $\text{K}_2\text{ZnV}_2\text{O}_7$ are listed in Tables B1 and B2 (Appendix B), respectively.

4.3 Results and Discussion

4.3.1 Hydrothermal Syntheses

Hydrothermal synthesis is a promising, simple and inexpensive technique which has been many advantages over the synthetic methods described above. In addition, using water as an environmentally friendly solvent leads to less air pollution. Both reaction pH and temperatures play crucial roles in determining the isolated solid product (Law and Williams, 2000). In addition, the nature of organic sources and solvent can be affected to reduce the oxidation state of the transition metal and/or to control the size and

morphology of the crystal products (Shi, Rocha, Lopes, and Trindade, 2005; Xu, He, Wang, and Yan, 2004). Four $M_xV_3O_8$ compounds have been successfully synthesized from hydrothermal reactions of V_2O_5 and $Zn(OAc)_2 \cdot 2H_2O$ with alkali metal sources (KOH, RbCl, CsCl) in mole ratio of 1:1:1 within 2 days. With $x = 1$ and $M = K, Rb, Cs$, the orange plates were formed in neutral media at 110 °C without an organic source, whereas where $x = 2$ and $M = K$, the black plates were isolated pure phase in a basic media at 140 °C, using an organic base (enMe) to adjust pH and acts as a reducing agent. The crystal morphology of $K_2V_3O_8$ is similar that of to Shi's group (2005), except the length of crystal plates in this work are shorter (product size of 0.15 x 0.15 x 0.30 mm).

According to no well-aligned tubular-windows inside crystals compared to previous work (Shi, Rocha, Lopes, and Trindade, 2005) due to using an organic diamine instead of the aliphatic dicarboxylic acid (apidic acid) that enMe acts as reductant than morphological directing agent or template for the formation of the $K_2V_3O_8$ plates. Both hydrothermal reactions gave large plates due to acetic acid/acetate in this work similar to apidic acid/apidate in Shi's group work (2005) acts as a buffer. Compared to the nanorods obtained under solvothermal reaction employing ethanol as a solvent as well as a reducing

Table 4.3 The Product Yield of $M_xV_3O_8$ (Based on V_2O_5) as a Function of Temperature.

Compounds	Reaction Temperature		
	110 °C	160 °C	200 °C
KV_3O_8	66%	87%	90%
RbV_3O_8	86%	88%	90%
CsV_3O_8	91%	94%	100%
$K_2V_3O_8$	60%	80% ^a	50% ^b
$K_2ZnV_2O_7$	5%		

^aObtaining $K_2V_3O_8$ at 140 °C and ^bat 180 °C

Table 4.4 Crystal Data and Structure Refinements for CsV₃O₈ and K₂ZnV₂O₇.

Compound	CsV ₃ O ₈	K ₂ ZnV ₂ O ₇
Crystal data		
Chemical formula	CsO ₈ V ₃	KO _{3.50} VZn _{0.50}
M _r	413.73	178.72
Temperature (°C)	-173±2	-173±2
Crystal system, space group	Monoclinic, <i>P2₁/m</i>	Tetragonal, <i>P4₂/mmm</i>
Unit cell dimensions (Å, °)	<i>a</i> = 4.990(3) Å α = 90° <i>b</i> = 8.524(5) Å β = 95.453(10)° <i>c</i> = 8.171(5) Å γ = 90°	<i>a</i> = 8.3478(16) Å α = 90° <i>b</i> = 8.3478(16) Å β = 90° <i>c</i> = 11.297(3) Å γ = 90°
Volume (Å ³)	346.0(4)	787.2(3)
Z	2	4
<i>D</i> _{calc} (Mg m ⁻³)	3.971	1.508
Radiation type, wavelength (Å)	Mo, <i>K</i> α , 0.71073	Mo, <i>K</i> α , 0.71073
θ _{range} (°)	2.50-24.90°	3.03-28.27°
μ (mm ⁻¹)	9.156	3.198
Crystal form, color	Prism, orange	Needle, colorless
Crystal size (mm)	0.20x0.20x0.30	0.01 x 0.01 x 0.30
Data collection		
Diffractometer	Bruker-Nonius Smart Apex CCD	Bruker-Nonius Smart Apex CCD
Data collection method	ω scans	ω scans
Absorption correction	Multi-scan	Multi-scan
No. of measured, independent, and observed [<i>I</i> > 2 σ (<i>I</i>)] reflections	1290, 614, 516	4518, 542, 499
<i>R</i> _{int}	0.0490	0.0501
θ _{max} (°)	24.90°	28.27°
Completeness to theta	95.8 % (theta = 24.90°)	97.3 % (theta = 28.27°)
Range of <i>h</i> , <i>k</i> , <i>l</i>	-3 ≤ <i>h</i> ≤ 5, -10 ≤ <i>k</i> ≤ 5, -9 ≤ <i>l</i> ≤ 9	9 ≤ <i>h</i> ≤ 10, -10 ≤ <i>k</i> ≤ 9, -14 ≤ <i>l</i> ≤ 14
Refinement		
Refinement on	<i>F</i> ²	<i>F</i> ²
R [<i>F</i> ² > 2 σ (<i>F</i> ²)], wR ₂ (<i>F</i> ²), <i>S</i>	0.0439, 0.0987, 0.985	0.0331, 0.0701, 1.189
No. of reflections	516	499
(Δ/σ) _{max}	65	37
Extinction coefficient	0.000	0.001
$\Delta\rho$ _{max, min, err} (e Å ⁻³)	-	0.0002(7)
	2.547, -1.145, 0.323	1.094, -0.451, 0.138

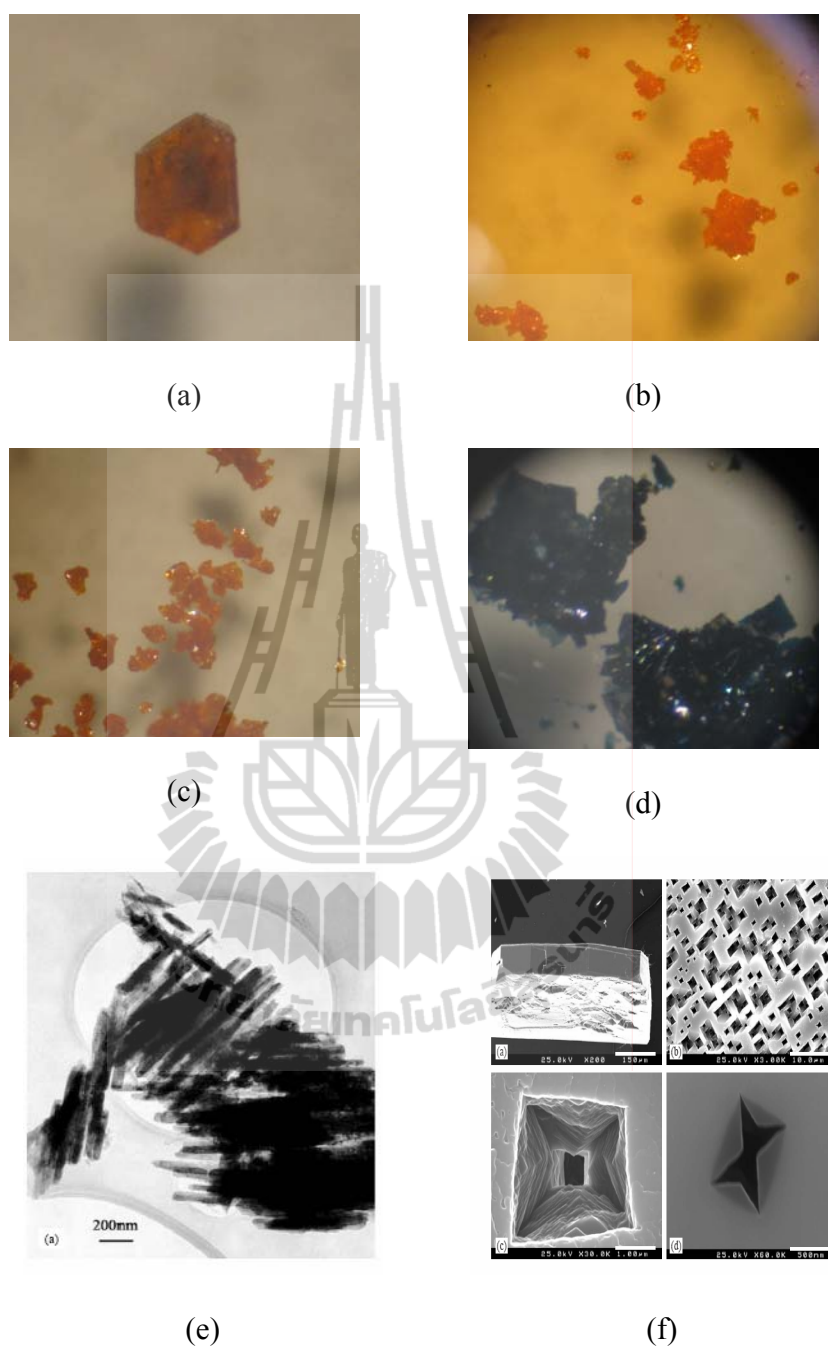


Figure 4.2 Crystal morphologies of (a) KV_3O_8 , (b) RbV_3O_8 , (c) CsV_3O_8 , and (d) $K_2V_3O_8$ (this work), (e) Xu, He, and Yan (2004), and (f) Shi, Rocha, and Trindade (2005).

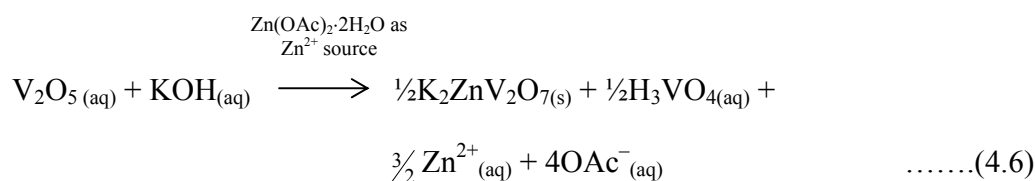
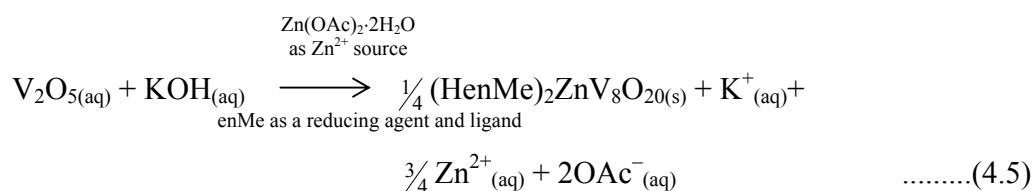
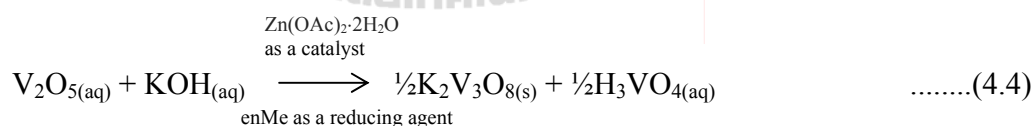
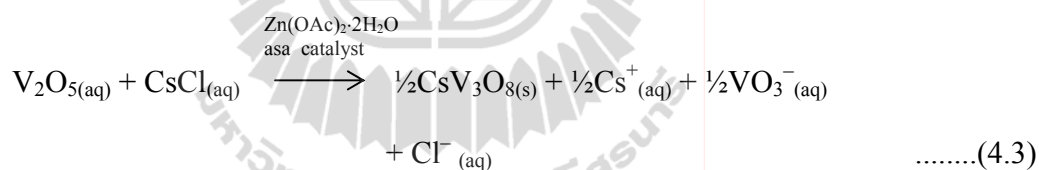
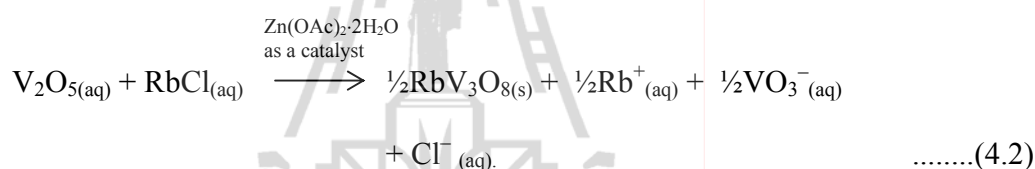
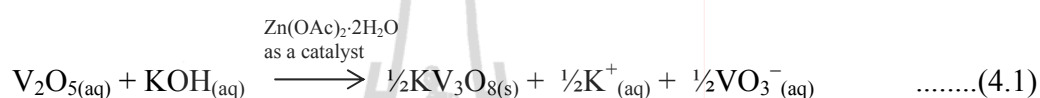
agent (Xu, He, Wang, and Yan, 2004). Even through an organic reactants and solvent are crucial factors, vanadium oxide sources seem to have no effect to the size and morphology of product, including acidity, V_2O_5 (Xu, He, Wang, and Yan, 2004; this work) and basicity, KVO_3 (Shi, Rocha, Lopes, and Trindade, 2005). Zinc acetate acts as a good catalyst in the formation of $K_2V_3O_8$ with high yield while its yield is decreased due to Zn^{2+} ions acting as an inhibitor to vanadyl VO^{2+} ions, the isolated products included $K_2ZnV_2O_7$ with increasing the amount of $Zn(OAc)_2 \cdot 2H_2O$. However, the yield of $K_2ZnV_2O_7$ product is low and poorly crystalline as listed in Table 4.4.

4.3.2 X-ray Diffraction

Figures 4.3-4.4 show the experimental XRD patterns of all compounds recorded by the bulk sampling compared to the simulated XRD patterns that were calculated from the single crystal X-ray structural results from Oka and coworkers (1997), pure phase and highly crystalline with increasing reaction temperature. The XRD patterns of MV_3O_8 (Figure 4.3) show the highest crystalline phase MV_3O_8 at 200 °C, actually the crystalline product is formed at 110 °C and 160 °C. With an increase in reaction temperature, crystallinity was enhanced as shown by the increasing intensity and sharpening of the XRD peaks (Yang, Li, Zhang, and Jin, 2008). Only a few diffraction peaks were observed which indicated that poorly crystalline RbV_3O_8 and CsV_3O_8 with high yield of 86% and 91%, respectively, at 110 °C. Due to unreacted zinc acetate possibly acting as a catalyst (Zhao, Zhang, and Wang, 2004), thus, the reaction temperature to obtain the MV_3O_8 compounds from this work is significantly lower at 140 °C compared to Oka and coworkers (1997). The XRD patterns of $K_2V_3O_8$ (Figure 4.4) show the high crystalline phase $K_2V_3O_8$ at 140 °C (~80% yield) that is the optimum reaction temperature which is significantly lower by 40 °C and 60 °C compared to the hydrothermal reaction in slightly acidic solution (pH 4.5-6) (Shi, Rocha, Lopes, and Trindade, 2005) and solvothermal

reaction (Xu, He, Wang, and Yan, 2004), respectively, because of unreacted zinc acetate acting as a catalyst that mentioned above. Lower or higher reaction temperatures than at 140 °C, black crystals, the 3-D nanoporous structure of $(\text{HenMe})_2\text{ZnV}_8\text{O}_{20}$ (Krachodnok, Haller, and Williams, 2007), were also present.

Thus, a new route for hydrothermal preparation of $\text{M}_x\text{V}_3\text{O}_8$ was proposed as follow



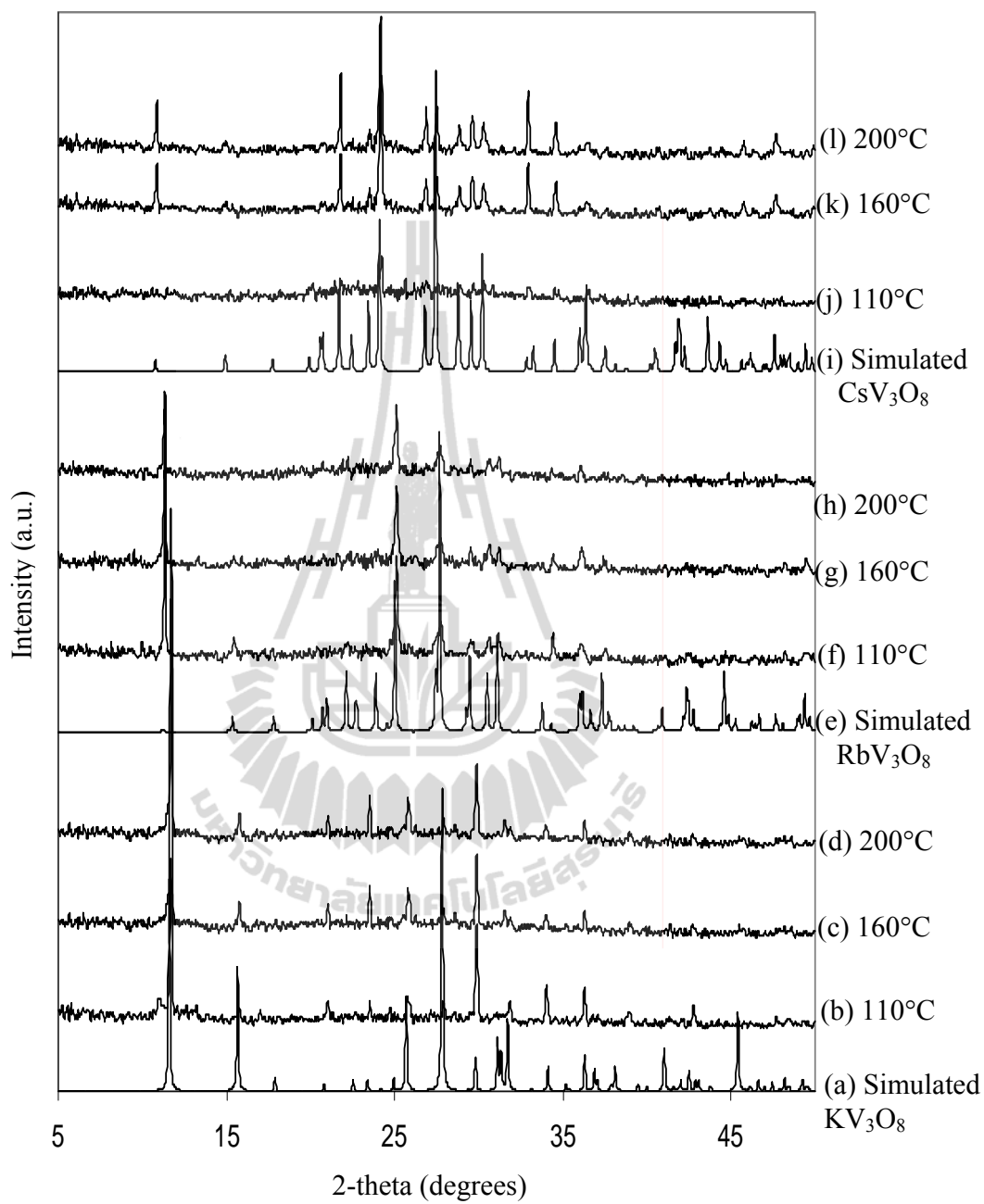


Figure 4.3 The simulated and experimental XRD patterns of MV_3O_8 .

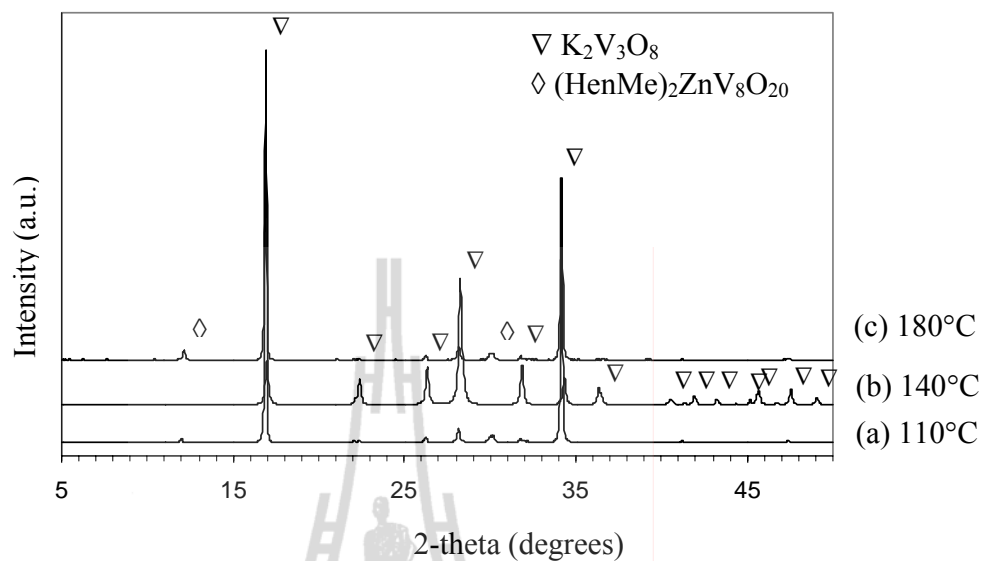


Figure 4.4 XRD patterns of $K_2V_3O_8$.

Table 4.5 Atomic Coordinates and Equivalent Isotropic Displacement Parameters ($\text{\AA}^2 \times 10^3$) for CsV_3O_8 .

Atoms	Multiplicity and Wyckoff letter	Site	x	y	z	U_{eq}
Cs(1)	2e	<i>m</i>	0.93953(14)	$\frac{1}{4}$	1.05699(10)	14.1(3)
V(1)	2e	<i>m</i>	0.9109(4)	$\frac{1}{4}$	0.5683(3)	9.7(9)
V(2)	4f	1	0.4305(3)	0.05676(17)	0.6767(2)	10.4(6)
O(1)	2e	<i>m</i>	1.1171(16)	$\frac{1}{4}$	0.4301(11)	11(3)
O(2)	2e	<i>m</i>	0.5825(16)	$\frac{1}{4}$	0.7435(11)	11(3)
O(3)	4f	1	0.6858(11)	0.0862(7)	0.5040(8)	12.1(15)
O(4)	4f	1	0.5538(12)	-0.0580(7)	0.8198(8)	15.0(16)
O(5)	4f	1	1.1072(11)	0.0996(7)	0.7214(8)	10.3(14)

^a U_{eq} is defined as one third of the trace of the orthogonalized U^{ij} tensor.

4.3.3 The Crystal Structure of CsV₃O₈

The single crystal X-ray diffraction reveals that the cesium trivanadate crystallizes in the isostructural KV₃O₈ monoclinic space group $P2_1/m$ as reported by Oka and coworkers (1997). The structure contains [V₃O₈]_nⁿ⁻ layers and the Cs⁺ ions are between layers with the layers stacked along the *c* axis and layer spacing of 3.201 Å (selected the distance between O atoms from the apex of VO₅ square pyramids of the layer and neighbors) is very close to that previous work, 3.255 Å, and larger spacing compared to other monovalent cations, 3.009 Å for M = Rb, and 2.903 Å for M = K. This is due to their ionic radii, 1.74 Å for Cs⁺, 1.61 for Rb⁺ and 1.51 Å for K⁺.

The layer is composed of corner-sharing VO₆ octahedra and V₂O₈ units. The V₂O₈ units themselves contain two edge-sharing VO₅ square pyramids with the apical oxygen atoms oriented toward opposite sides of the square pyramidal layer which shows rows of square pyramidal units disposed alternately up/down as illustrated in Figure 4.5. The bond distances and angles are similar to previous work as listed in Table 4.5. The coordination number is 8 for Rb⁺ and Cs⁺, respectively, and is 6 for K⁺ due to the ionic radius, 1.51 Å, being the smallest in the same group.

4.3.4 The Crystal Structures of K₂ZnV₂O₇

Single crystal X-ray diffraction reveals that crystallizes in the tetragonal space group $P4_2/mnm$. Its cell parameters are close to K₂MgV₂O₇ (Murashova, Velikodnyi, and Trunov, 1988). The *c* cell constant is doubly that of K₂V₃O₈, space group $P4bm$, explained by the existence of the mirror plane perpendicular to the [001] direction between two [BV₂O₇]²⁻ layers (B = Mg) (Yahia, Guadin, and Darriet, 2007). The structure contains a [ZnV₂O₇]²⁻ layer with K⁺ positioned between the layers. The layer consisting of equal numbers of two building units; the tetrahedral ZnO₄ units lying on -4 sites at $0, \frac{1}{2}, z$ and $\frac{1}{2}, 0, z$ where $z = \frac{1}{4}$ and $\frac{3}{4}$ and the V₂O₇ units lying on $2.mm$ symmetry

Table 4.6 Comparison of the V–O and M–O Bond Distances of MV_3O_8 .

^a Bond type	^b KV_3O_8	^b RbV_3O_8	^b CsV_3O_8	CsV_3O_8 (this work)
V(1)–O				
V(1)=O(1) ⁱⁱⁱ	1.602(3)	1.620(7)	1.608(6)	1.599(9)
V(1)– μ -O(2) ⁱ	2.267(3)	2.265(7)	2.288(5)	2.276(9)
V(1)– μ -O(3) ^{i,ii}	1.837(2)	1.836(5)	1.838(4)	1.837(6)
V(1)– μ -O(5) ^{iii,iv}	1.972(2)	1.973(5)	1.972(4)	1.984(6)
V(1)–O				
V(1)=O(1) ⁱⁱⁱ	1.602(3)	1.620(7)	1.608(6)	1.599(9)
V(1)– μ -O(2) ⁱ	2.267(3)	2.265(7)	2.288(5)	2.276(9)
V(1)– μ -O(3) ^{i,ii}	1.837(2)	1.836(5)	1.838(4)	1.837(6)
V(1)– μ -O(5) ^{iii,iv}	1.972(2)	1.973(5)	1.972(4)	1.984(6)
V(2)–O				
V(2)– μ -O(2) ⁱ	1.877(1)	1.873(3)	1.873(3)	1.873(4)
V(2)– μ -O(3) ⁱ	1.944(2)	1.950(5)	1.997(4)	2.005(6)
V(2)– μ -O(3) ^v	1.955(2)	2.009(5)	1.961(4)	1.959(7)
V(2)=O(4) ^v	1.599(2)	1.609(6)	1.594(5)	1.602(7)
V(2)– μ -O(5) ⁱ	1.735(2)	1.733(4)	1.732(4)	1.727(6)
M–O				
M–O(2) ^{vi}	2.718(3)	2.849(7)	2.989(6)	2.978(9)
M–O(1) ⁱⁱⁱ	2.811(3)	2.914(8)	3.082(6)	3.093(9)
M–O(4) ^{iii,iv}	2.837(2)	2.963(5)	3.118(4)	3.098(6)
M–O(5) ^{vii,viii}	2.970(2)	3.072(5)	3.226(4)	3.209(6)
M–O(4) ^{i,ii}	3.182(2)	3.151(5)	3.216(4)	3.197(6)

^aSymmetry code: (i) x,y,z ; (ii) $x,1/2-y,z$; (iii) $x+1,y,z$; (iv) $1+x,1/2-y,z$; (v) $1-x,-y,1-z$; (vi) $x,y,z-1$; (vii) $x+1,y,z-1$; (viii) $x+1,1/2-y,z-1$.

^bCrystal data from Oka, Yao, and Yamamoto (1997).

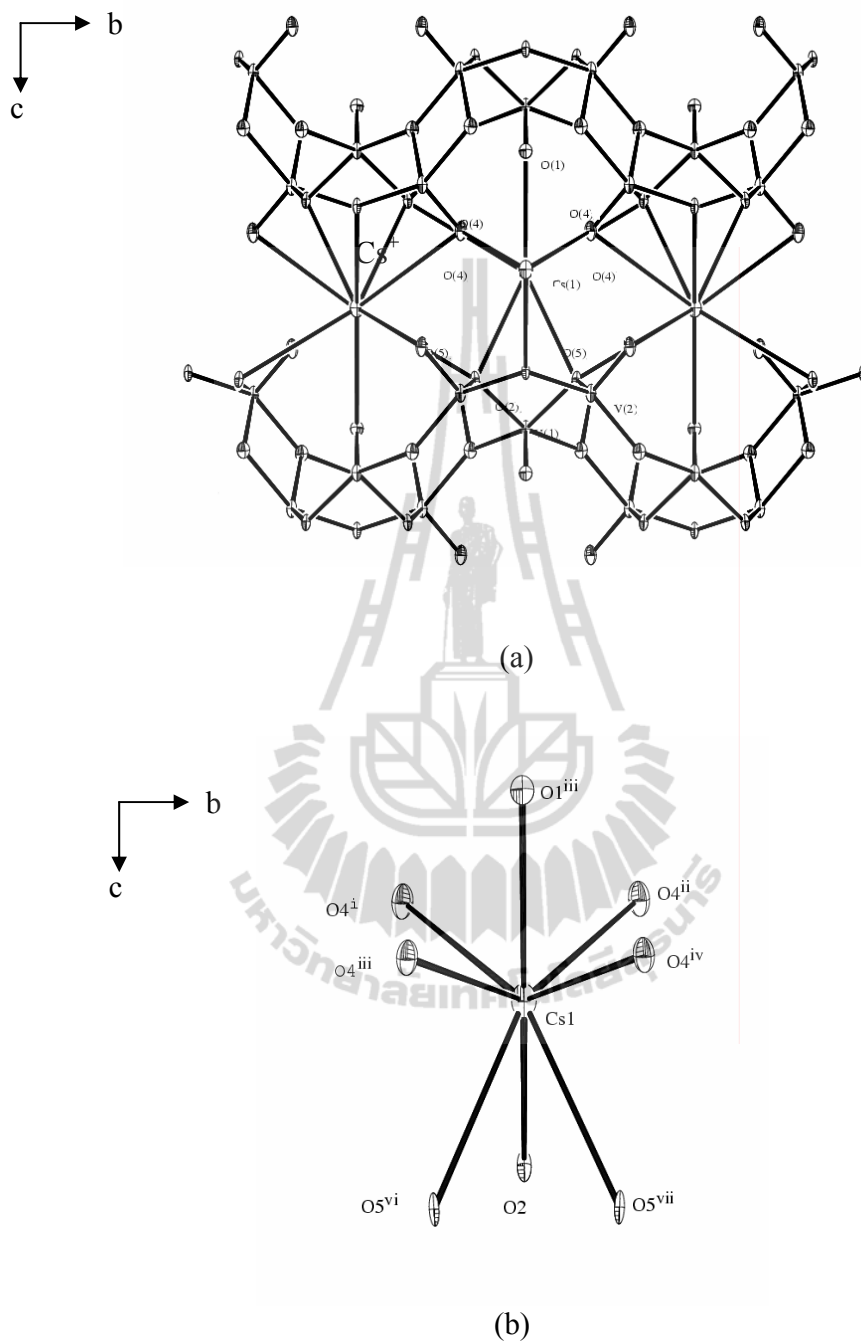


Figure 4.5 Crystal structure of CsV_3O_8 projected onto the bc plane (a) showing the $[\text{V}_3\text{O}_8]^-$ layers occupied by Cs^+ ions and (b) CsO_8 coordination.

sites at $0,0,z$; $1/2,1/2,z+1/2$; $1/2,1/2,-z+1/2$ and $0,0,-z$. The building units combined by corner-sharing all tetrahedral ZnO_4 units and all basal O atoms of the V_2O_7 units form pentagonal

motifs similar that observed in $K_2V_3O_8$ (Figure 4.6) except the V=O groups of pyrovanadate units are oriented in the opposite direction while those units are oriented the same direction in $K_2V_3O_8$. The interlayer space is 3.230 Å and similar to that observed in $K_2MgV_2O_7$ (Murashova, Velikodnyi, and Trunov, 1988), but is larger than $K_2(VO)V_2O_7$, 3.055 Å (Chakoumakos, Custelcean, Kamiyama, Oikawa, Sales, and Lumsden, 2007), and is smaller than $Rb_2MnV_2O_7$ and $KRbMnV_2O_7$, 3.477 and 3.444 Å, respectively (Yahia, Guadin and Darriet, 2007). The bond distances and angles are listed in Table 4.8. The Zn–O bonds are shorter than 2σ of $[Zn-O]_{av} = 2.090$ Å (Bürgi and Dunitz, 1994). The O–Zn–O angles of $114.25(13)^\circ$ show smallest deviation from normal tetrahedral geometry, 109° , compared to the O–B–O angles, $121.05(7)$, $117.4(2)^\circ$, $115.63(19)^\circ$ and $115(1)^\circ$, in $K_2MnV_2O_7$, $Rb_2MnV_2O_7$, $KRbMnV_2O_7$, and $K_2MnV_2O_7$, respectively. The V–O bond distances and the O–V–O angles are in normal the range similar to that observed in $Na_2ZnV_2O_7$ (Tyutyunnik, Zubkov, Surat, Slobodin, and Svensson, 2005), $Rb_2MnV_2O_7$ and $KRbMnV_2O_7$ (Yahia, Guadin, and Darriet, 2007).

Table 4.7 Atomic Coordinates ($\times 10^4$) and Equivalent Isotropic Displacement Parameters ($\text{Å}^2 \times 10^3$) for $K_2ZnV_2O_7$.

Atoms	Multiplicity and Wyckoff letter	Site Symmetry Symbol	x	y	z	$^a U_{eq}$
K(1)	4f	<i>m.2m</i>	–1806(1)	1806(1)	$1/2$	15(1)
K(2)	4g	<i>m.2m</i>	8535(1)	1465(1)	0	10(1)
Zn(1)	4d	–4..	$1/2$	0	$1/4$	7(1)
V(1)	8j	..m	1423(1)	1423(1)	2883(1)	6(1)
O(1)	4e	2.mm	0	0	3471(4)	10(1)
O(2)	8j	..m	1395(3)	1395(3)	1429(3)	11(1)
O(3)	16k	1	3253(2)	906(3)	3440(2)	9(1)

^a U_{eq} is defined as one third of the trace of the orthogonalized U^{ij} tensor.

Table 4.8 Selected Bond Lengths (Å) and Angles (°) for $K_2ZnV_2O_7$.

2 x K(1)–O(1) ⁱⁱⁱ	2.744(3)	4 x Zn(1)–O(3) ^{x,ix,xvii}	1.956(2)
2 x K(1)–O(2) ^{i,ii}	2.668(3)	V(1)–O(1)	1.8063(18)
4 x K(1)–O(3) ^{iii,iv,v,vi}	3.113(2)	V(1)–O(2)	1.643(3)
4 x K(2)–O(2) ^{xii,xiii,xiv,xv}	2.883(3)	2 x V(1)–O(3) ^{vi}	1.707(2)
4 x K(2)–O(3) ^{viii,ix,x,xi}	2.825(2)		
O(3) ^{xvii} –Zn(1)–O(3) ⁿ	107.13(6)	O(2)–V(1)–O(3) ^{vi}	112.15(10)
O(3) ^{xviii} –Zn(1)–O(3)	107.13(6)	O(2)–V(1)–O(3)	112.15(10)
O(3) ^{xv} –Zn(1)–O(3)	114.25(13)	O(3) ^{vi} –V(1)–O(3)	108.50(15)
O(3) ^{xviii} –Zn(1)–O(3) ^x	114.25(13)	O(2)–V(1)–O(1)	110.41(17)
O(3) ^{xv} –Zn(1)–O(3) ^x	107.13(6)	O(3) ^{vi} –V(1)–O(1)	106.67(11)
O(3)–Zn(1)–O(3) ^x	107.13(6)	O(3)–V(1)–O(1)	106.67(11)

Symmetry code:

(i) $y^{-1/2}, -x^{+1/2}, z^{+1/2}$; (ii) $y^{-1/2}, -x^{+1/2}, -z^{+1/2}$; (iii) $-x, -y, -z+1$; (iv) $-x, -y, z$; (v) $y, x, -z+1$; (vi) y, x, z ;
 (vii) $x, y, -z+1$; (viii) $y^{+1/2}, -x^{+1/2}, z^{-1/2}$; (ix) $x^{+1/2}, -y^{+1/2}, -z^{+1/2}$; (x) $y^{+1/2}, -x^{+1/2}, -z^{+1/2}$; (xi) $x^{+1/2}, -y^{+1/2}, z^{-1/2}$;
 (xii) $-x+1, -y, -z$; (xiii) $x+1, y, z$; (xiv) $-x+1, -y, z$; (xv) $x+1, y, -z$; (xvi) $-x+2, -y, -z$;
 (xvii) $-y^{+1/2}, x^{-1/2}, -z^{+1/2}$.

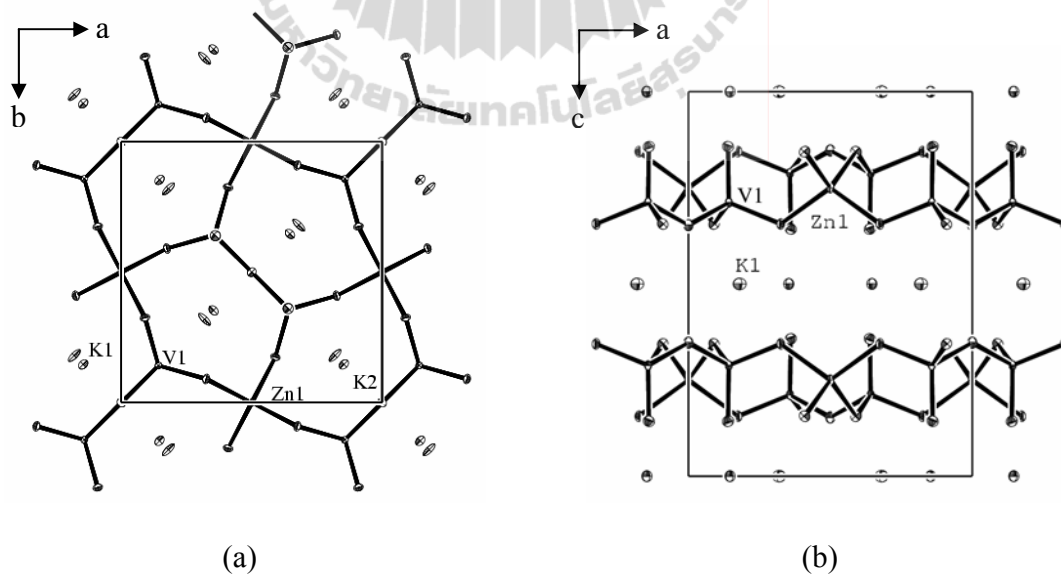


Figure 4.6 Comparing the $[ZnV_2O_7]^{2-}$ layer projected onto (a) the ab plane and (b) the ac plane, and $[(V^{4+}O)V_2O_7]^{2-}$ layer projected onto (c) the ab plane and (d) the ac plane (Chakoumakos, Custelcean, Kamiyama, Oikawa, Sales, and Lumsden, 2007).

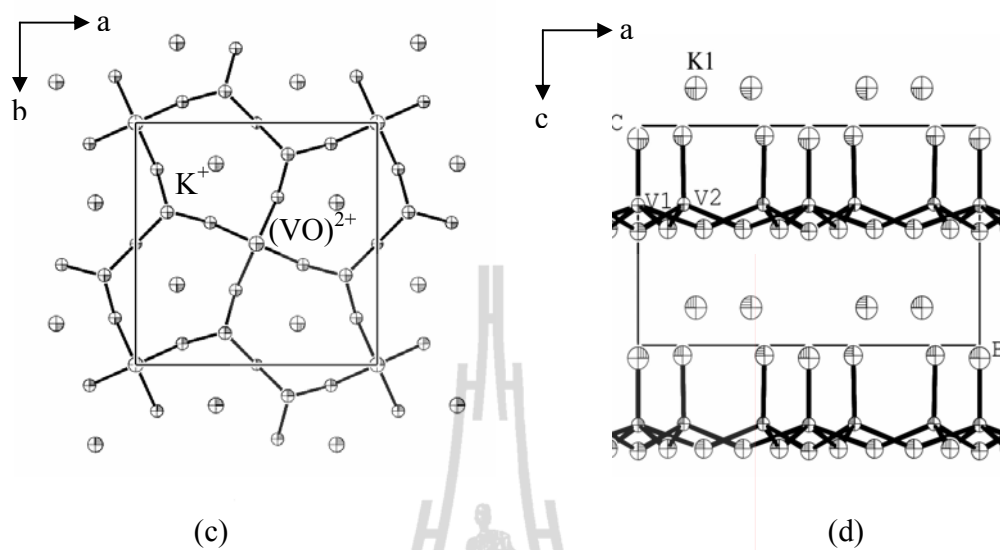


Figure 4.6 (Continued).

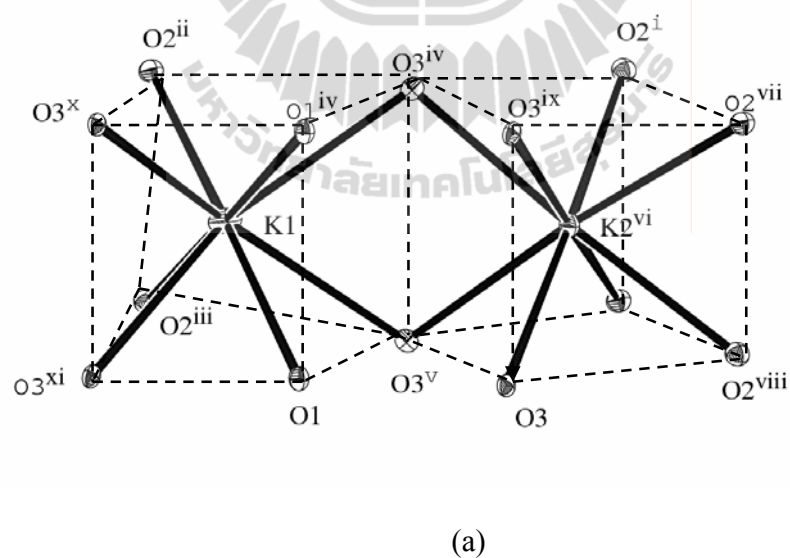


Figure 4.7 (a) Perspective view of the distorted square prismatic environments of the K atoms and projection views of (b) K(1) and (c) K(2) occupied the pentagonal channel in $\text{K}_2\text{ZnV}_2\text{O}_7$.

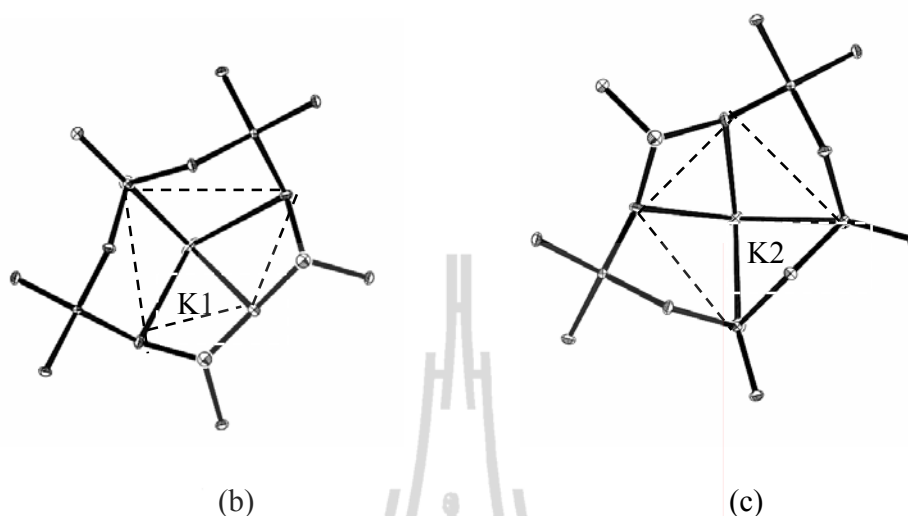


Figure 4.7 (Continued).

4.3.5 Infrared Spectroscopy

Figure 4.8 shows FT-IR spectra of all vanadates. The spectrum of CsV_3O_8 compounds, the medium and strong absorption peaks appear at 1000 and 963 cm^{-1} due to the vibration modes of two vanadyl bonds, the shorter vanadyl bond at an axial position of V^{5+}O_6 octahedra, $d[\text{V}=\text{O}(1)_t] = 1.599(9)\text{ \AA}$, whereas the longer bonds at the apical position of V^{5+}O_5 square pyramids, $d[\text{V}=\text{O}(4)_t] = 1.602(7)\text{ \AA}$, where t is a terminal O atom. The slightly different distance of the vanadyl bonds is about 0.003 \AA or Δ_ν of 37 cm^{-1} because of three associated vanadyl O atoms of MO_8 coordination with significant unequal K–O bond distances. One $d[\text{K}-\text{O}(1)^{\text{iii}}] = 3.093(9)\text{ \AA}$, with a shorter distance of 0.006 and 0.105 \AA compared to other $d[\text{K}-\text{O}(4)^{\text{iii,iv}}] = 3.098(6)$ and $3.197(6)\text{ \AA}$, respectively. These peaks compared with isostructural compounds, 1005 and 967 cm^{-1} for Rb, and 990 and 959 cm^{-1} for K, suggesting the vanadyl bond distance of CsV_3O_8 is shorter than in KV_3O_8 and longer than RbV_3O_8 , is not in agreement with that observed by Oka group (1997), those vanadyl bonds in KV_3O_8 are shortest (Table 3.6). The broad

absorption peak at 737 cm^{-1} , and a shoulder at 780 cm^{-1} is assigned to the antisymmetric stretching and bending modes of the V-O_b bond and $\text{V-O}_b\text{-V}$ bridges, however, it is very difficult to correlate and classify the O_b bond, where b are bridging O atoms, with bending modes from infrared spectroscopy.

FT-IR spectrum of $\text{K}_2\text{V}_3\text{O}_8$, the strong and very weak absorption peaks at 991 and 941 cm^{-1} assigned to the vibrational modes of two vanadyl bonds at apical positions of V^{4+}O_5 square pyramid and V^{5+}O_4 tetrahedra along the c axis, $d[\text{V}=\text{O}_t] = 1.582(6)$ and $1.628(11)\text{ \AA}$, respectively, due to the five associated apical vanadyl O atoms of pentagonal antiprismatic KO_{10} coordination environment. There are three shorter bonds, $d[\text{K-O}] = 2.769(11)$ and $2.904(11)\text{ \AA}$ and one longer bond, $d[\text{K-O}] = 3.512(6)\text{ \AA}$, related to at apical positions of square pyramids and tetrahedra, respectively. Three absorption peaks at 926, 817, and 740 cm^{-1} assigned to the antisymmetric stretching and bending modes of bridging $\text{V-O}_b\text{-V}$ units related to the 2-D vanadium and basal-plane oxygen atoms on the ab plane. The unequal $\text{V-O}(1)_b$ bond distances of $\text{V}^{4+}\text{-O}(1)_b\text{-V}^{5+}$ are $1.945(5)$ (V^{4+}) and $1.699(5)$ (V^{5+}) \AA , with the $\text{O}(1)_b$ bridge further binding the to K^+ ion of $2.875(6)$ and $3.191(6)\text{ \AA}$ and other equal $\text{V-O}(3)_b$ bond distances $\text{V}^{5+}\text{-O}(3)_b\text{-V}^{5+}$ are $1.794(4)\text{ \AA}$ with $d[\text{K-O}] = 2.794(5)\text{ \AA}$ (Figure 4.1) (Chakoumakos, Custelcean, Kamiyama, Oikawa, Sales, and Lumsden, 2007; Choi, Zhu, Musfeldt, Ragghianti, Mandrus, Sales, and Thompson, 2001; Galy and Carpy, 1975; Shi, Rocha, Lopes, and Trindade, 2005).

The FT-IR spectrum of $\text{K}_2\text{ZnV}_2\text{O}_7$, the broad bands at 936, 896 and 851 cm^{-1} correspond to the vanadate bond distances of $1.643(3)$, $1.707(2)$ and $1.8063(18)\text{ \AA}$ and the broad peak at 691 cm^{-1} is assigned to the bending mode of the bridging $\text{V-O}_b\text{-V}$ units.

4.4 Conclusions

Four layered trivanadate compounds have been prepared in high yield by hydrothermal synthesis of V_2O_5 and KOH in mole ratio 1:1, $x = 1$ in neutral media, whereas $x = 2$ in basic media with reaction temperature lower than previous reports due to zinc acetate may possible acting as catalyst and enMe as a reductant to reduce V^{5+} to V^{4+} as well as in ethanol or dicarboxylic acid. This simple, inexpensive, and environmentally friendly of hydrothermal preparation route with can be developed to prepare other layered vanadates systems.

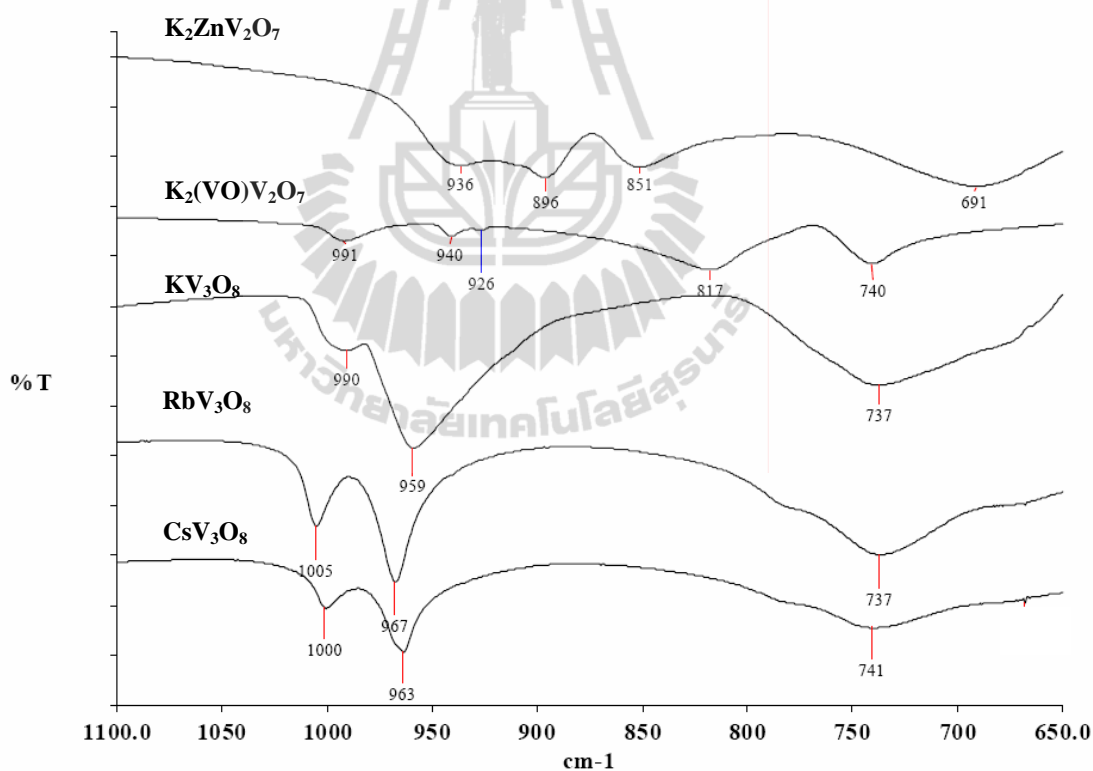


Figure 4.8 FT-IR spectra of alkali metal vanadates.

4.5 References

Bindi, L., Dusek, M., Petricek, V., and Bonazzi P. (2006). Superspace-symmetry determination and multidimensional refinement of the incommensurately

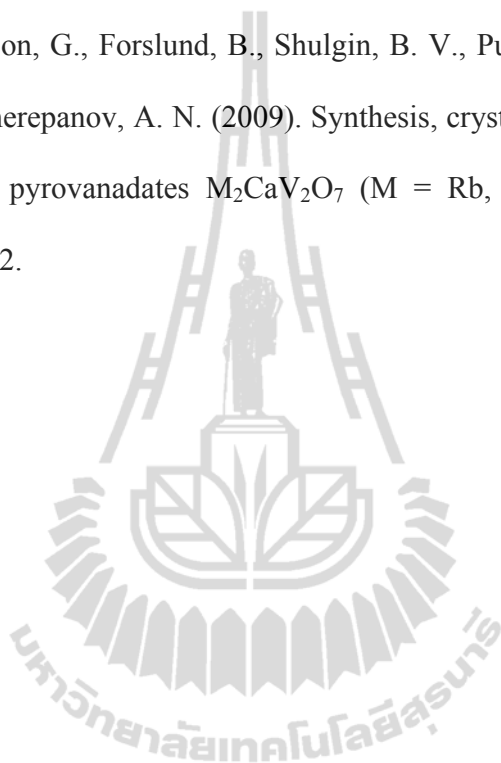
- modulated structure of natural fresnoite. **Acta Crystallographica Section B.** 62(6): 1031-1037.
- Bürgi, H.-B., and Dunitz, J. D. (1994). **Structure Correlation.** Wiley-VCH, New York. pp. 751-848.
- Chakoumakos, B. C., Custelcean, R., Kamiyama, T. Oikawa, K., Sales, B. C., and Lumsden, M. D. (2007). Structural modulation in $K_2V_3O_8$. **Journal of Solid State Chemistry.** 180(3): 812-817.
- Choi, L., Zhu, Z. T., Musfeldt, J. L., Raghianti, G., Mandrus, D., Sales, B. C., and Thompson, J. R. (2001). Local symmetry breaking in $K_2V_3O_8$ as studied by infrared spectroscopy. **Physical Review B.** 65(5): 54101-6.
- Evans, H. T., and Block, S. (1966). The crystal structures of potassium and cesium trivanadates. **Inorganic Chemistry.** 5(10): 1808-1814.
- Galy, J., and Carpy, A. (1975). Structure cristalline de $K_2V_3O_8$ ou $K_2(VO)[V_2O_7]$. **Acta Crystallographica Section B.** 31(6): 1794-1795.
- Krachodnok, S., Haller, K. J., and Williams, I. D. (2007). Hydrothermal synthesis of three-dimensional nanoporous zinc vanadates: $(\text{HenMe})_2\text{ZnV}^{4+}_4\text{V}^{5+}_4\text{O}_{20}$ and $(\text{enMe})_2\text{Zn}(\text{VO}_3)_2 \cdot 2\text{H}_2\text{O}$ containing pillared/layered structure. In **Proceeding of the German-Thai Symposium on Nanoscience and Nanotechnology (GTSNN'07).** Kasetsart University press, Bangkok. pp. 63-68.
- Law, T. S.-C., and Williams, I. D. (2000). Organic-directed synthesis of manganese vanadates with variable stoichiometry and dimensionality: 1-D $[(\text{Hen})_2\text{Mn}(\text{VO}_3)_4]$, 2-D $[(\text{H}_2\text{en})_2[\text{Mn}(\text{VO}_3)_4]$, and 3-D $[(\text{H}_2\text{en})[\text{MnF}(\text{VO}_3)_3]$. **Chemistry of Materials.** 12(1): 2070-2072.
- Li, G., Pang, S., Jiang, L., Guo, Z., and Zhang, Z. (2006). Environmentally friendly chemical route to vanadium oxide single-crystalline nanobelts as a cathode

- material for lithium-ion batteries. **The Journal of Physical Chemistry B.** 110(19): 9383-9386.
- Liu, G., and Greedan, J. E. (1995). Magnetic properties of Fresnoite-type vanadium oxides: $A_2V_3O_8$ ($A = K, Rb, NH_4$). **Journal of Solid State Chemistry.** 114(1): 499-505.
- McMurdie, H., Morris, M., Evans, E., Paretzkin, B., Wong-Ng, W., and Zhang, Y. (1986). Standard X-Ray Diffraction Powder Patterns from the JCPDS Research Associateship. **Powder Diffraction.** 1(4): 343.
- Murashova, E. V., Velikodnyi, V. K., and Trunov, V. K. (1988). Structure of the double pyrovanadate $K_2MgV_2O_7$. **Zhurnal Neorganicheskoi Khimii.** 33(6): 1593-1595.
- Oka, Y., Yao, T., and Yamamoto, N. (1997). Hydrothermal synthesis and structure refinements of alkali-metal trivanadates MV_3O_8 ($M = K, Rb, Cs$). **Materials Research Bulletin.** 32(9): 1201-1209.
- Ren, T.-Z., Yuan, Z.-Y., and Zou, X. (2007). Crystal growth of mixed-valence ammonium vanadates. **Crystal Research and Technology.** 42(4): 317-320.
- Riou, D., and Férey, G. (1995). Intercalated vanadyl vanadates: syntheses, crystal structures, and magnetic properties. **Inorganic Chemistry.** 34(26): 6520-6523.
- SADABS Version 2.03 (1998), SAINT Version 6.26a (2001a), SMART Version 5.625 (2001b), Bruker Analytical X-ray Systems Inc., Madison, Wisconsin, USA.
- Sheldrick, G.M. (1997). *SHELX-97 Program for the Solution and Refinement of Crystal Structures*, University of Göttingen, Germany.
- Sheldrick, G.M. (1997). *SHELXTL*. Version 6.1. Bruker Analytical X-ray Systems Inc., Madison, Wisconsin, USA.
- Shi, F.-N., Rocha, J., Lopes, A. B., and Trindade, T. (2005). Morphological micro-patterning of tubular-windows on crystalline $K_2V_3O_8$ sheets. **Journal of Crystal Growth.** 273(3-4): 572-576.

- Slobodin, B. V., Surat, L. L., Samigullina, R. F., Ishchenko, A. V., Shulgin, B. V., and Cherepanov, A. N. (2010). Thermochemical and luminescent properties of the $K_2MgV_2O_7$ and $M_2CaV_2O_7$ ($M = K, Rb, Cs$) vanadates. **Inorganic Materials**. 46(5): 522-528.
- Tyutyunnik, A. P., Zubkov, V. G., Surat, L. L., Slobodin, B. V., and Svensson, G. (2005). Synthesis and crystal structure of the pyrovanadate $Na_2ZnV_2O_7$. **Powder Diffraction**. 20(3):189.
- Withers, R. L., Höche, T., Liu, Y., Esmailzadeh, S., Keding, R., and Sales, S. (2004). A combined temperature-dependent electron and single-crystal X-ray diffraction study of the fresnoite compound $Rb_2V^{4+}V_2^{5+}O_8$. **Journal of Solid State Chemistry**. 177(10): 3316-3323.
- Xu, H., He, W., Wang, H., and Yan, H. (2004). Solvothermal synthesis of $K_2V_3O_8$ nanorods. **Journal of Crystal Growth**. 260(3): 447-450.
- Yahia, H. B., Guadin, E., and Darriet, J. (2007). Crystal structures of new pyrovanadates $A_2MnV_2O_7$ ($A = Rb, K$). **Zeitschrift für Naturforschung B**. 62(7): 873-880.
- Yang, H., Li, J., Zhang, X.-G., and Jin, Y.-L. (2008). Synthesis of LiV_3O_8 nanocrystallites as cathode materials for lithium ion batteries. **Journal of Materials Processing Technology**. 207(1-3): 265-270.
- Zhang, Y., Haushalter, R. C., and Clearfield, A. (1996). Hydrothermal syntheses and structural characterization of layered vanadium oxides incorporating organic cations: α -, β -($H_3N(CH_2)_2NH_3$)[V_4O_{10}] and α -, β -($H_2N(C_2H_4)_2NH_2$)[V_4O_{10}]. **Inorganic Chemistry**. 35(17): 4950-4956.
- Zhang, L., Shi, Z., Yang, G., Chen, X., and Feng, S. (2000). Hydrothermal synthesis and crystal structure of a layered vanadium oxide with an interlayer metal coordination complex: $(HenMe)_2CdV_8O_{20}$. **Journal of the Chemical Society, Dalton Transactions**. (3): 275-278.

Zhao, X., Zhang, Y., and Wang, Y. (2004). Synthesis of propylene carbonate from urea and 1,2-propylene glycol over a zinc acetate catalyst. **Industrial & Engineering Chemistry Research**. 43(15): 4038-4042.

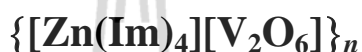
Zubkov, V. G., Tyutyunnik, A. P., Tarakina, N. V., Berger, I. F., Surat, L. L., Slobodin, B. V., Svensson, G., Forslund, B., Shulgin, B. V., Pustovarov, V. A., Ishchenko, A. V., and Cherepanov, A. N. (2009). Synthesis, crystal structure and luminescent properties of pyrovanadates $M_2CaV_2O_7$ (M = Rb, Cs). **Solid State Sciences**. 11(3): 726-732.



CHAPTER V

REVERSIBLE ORDER-DISORDER PHASE TRANSITION

IN A NEW POLYMERIC METAVANADATE:



5.1 Introduction

Noncovalent interactions are of interest in large areas of experimental theoretical research. Several studies discuss how these interactions affect the structural phase transition phenomena, and often enhance or reduce desirable physical properties. Earlier work from our group (Haller, Johnson, Feltham, Enemark, Ferraro, and Basile, 1979) documented the significant differences in the conformations of the salen ligand of Fe(NO)(salen) complex (salen = N,N'-ethylenebis(salicylideneimine)) at $-175\text{ }^\circ\text{C}$ and at $23\text{ }^\circ\text{C}$ (both $Pna2_1$) and attributed them to crystal packing and unequal interactions to the π -clouds above and below the planes of the ligands with their neighbors. The observed structural changes are consistent with the change of the spin state of Fe(NO)(salen) complex from $S = 3/2$ to $S = 1/2$ upon cooling. More recently we have investigated the reversible order-disorder structural phase transition in polymeric $[\text{Ag}(\text{bipy})(\text{NO}_3)]_n$, which shows planes of diffuse scattering at room temperature, associated with a disordered nitrate ion which becomes ordered at $-123\text{ }^\circ\text{C}$ and below. The disordering of the nitrate ions results in localized straightening of adjacent $[-\text{Ag}(\text{bipy})-]_n$ chains forcing movement along the chains producing diffuse

scattering dominated by the Ag atoms (Somphon, Haller, and Rae, 2011). The polymeric mixed-metal cyclic tetravanadates, $[M(\text{Im})_4\text{V}_2\text{O}_6]_n$ (where $M = \text{Mn}, \text{Co},$ and Ni ; $\text{Im} = \text{imidazole}$) also undergo reversible order-disorder structural phase transitions at 8 °C, -98 °C, and -173 °C for the manganese, cobalt, and nickel compounds, respectively (Chainok, Haller, Rae, Willis, and Williams, 2011). Four ordered Im ligands about the equatorial plane of the metals transform to disordered forms by rotating the Im ring planes to decrease the intermolecular N-H...O hydrogen bond interactions as temperature increases.

In addition to the structural phase transition work, we have been concerned generally with interactions in crystal engineering, for example, the intermolecular and intramolecular hydrogen bonding interactions and their relationship to crystal packing and polytypism in the 1,10-phenanthroline-1-ium salt of (2-carboxyethyl)(2-carboxylatoethyl)dichlorostannate(IV) (Somphon, Haller, Rae, and Ng, 2006), and in spectroscopy, for example, the C-H...X hydrogen bonding interactions that play an integral role in the near-infrared Raman excitonic enhancement observed in β -hematin (malaria pigment) and other related heme derivatives (Puntharod, Webster, Asghari-Khiavi, Bambery, Safinejad, Rivadehi, Langford, Haller, and Wood, 2010).

The current work continues to study the effect of supramolecular interactions on structural phase transitions with the tetraimidazolezinc(II) salt of the metavanadate polymer. Metavanadates are of interest due to potential applications in white light-emitting phosphors (Nakajima, Isobe, Tsuchiya, Ueda, and Kumagai, 2009), catalysis (Jian, Zhu, Wang, Zhang, Li, and Hu, 2006), and rechargeable lithium batteries (Muller, Valmalette, Soubeyroux, Bouree, and Gavarrri, 2001). These compounds commonly exhibit vanadium in the +5 oxidation state as corner-sharing VO_4 tetrahedra, forming infinite chains similar to those found in metasilicates (Cotton,

Wilkinson, Murillo, and Bockmann, 1998). Metavanadates are classified into two main groups based on their chain conformation, orientation, and repeating units (Liu, Lin, and Lin 2000). No helical metavanadate chains are most found in inorganic and hybrid metavanadates (Khan, Yohannes, Doedens, Golub, and O'Conner, 2005; Krachodnok, Haller, and Williams, 2011; Law and Williams, 2000; Liu, Lin, and Lin, 2000; Zhang, Haushalter, Zubieta, and O'Connor, 1996), while helical metavanadate chains are observed in only a few compounds in the literature, such as the di-, tri-, and tetranuclear tetrahedra related with 2_1 symmetry observed in $[\text{H}_3\text{N}(\text{CH}_2)_4\text{NH}_3][\text{VO}_3]_2$ (Riou and Férey, 1996), $[\text{Co}(\text{en})_3][\text{VO}_3]_3 \cdot \text{H}_2\text{O}$ (en = ethylenediamine) (Khan, Yohannes, Doedens, Golub, and O'Conner, 2005) and $\text{Ba}(\text{VO}_3)_2 \cdot \text{H}_2\text{O}$ (Ulicka, Pavelcik, and Huml, 1987), respectively, and a large repetitive sequence containing twelve tetrahedra related with 6_1 symmetry found in $[\text{Ni}(\text{en})_3][\text{VO}_3]_2$ (Liu, Lin, and Lin, 2000).

Several variable temperature and variable pressure vibrational studies on the structure of polymeric metavanadate salts are found in the literature (Onodera and Ikegami, 1980; Waal and Heyns, 1990; Shen, Ong, Kuok, and Tang, 1995). Others report the ability of hydrogen bonds to affect the phase transition behaviors. For example, NH_4VO_3 undergoes an order-disorder structural phase transition near -123 °C (Park and Shurvell 1989), the transition caused by the strong hydrogen bond between the ammoniums ions and the chains prevents the chain slipping process at 49 kbar (Adams, Haines, and Leonard, 1991) and recently, reported no evidence of any phase transition resulting in a symmetry change was detected either from X-ray data or the synchrotron data, except small energy changes about ~ 1.71 kJ mol⁻¹ related to energies characteristic for the weak C–H...O hydrogen bond interactions but not for the strong N–H...O hydrogen bond interactions with decreasing temperature destabilized the structure

(Smrčok, Bitschnau, and Filinchuk, 2009).

A pressure-induced phase transition for the cyclic tetravanadate, $[t\text{-BuNH}_3]_4[\text{V}_4\text{O}_{12}]$, which can be transformed to polymeric metavanadate, $[t\text{-BuNH}_3]_4[\text{VO}_3]$ with additional N–H...O hydrogen bond interactions found in the polymeric form (Wéry, Gutiérrez-Zorrilla, Luque, Ugalde, and Raman, 1996).

A key feature in the study of phase transitions in polymeric metavanadate salts is the effect of the size of the cation, its conformation, and the ability to hydrogen bond to the structure of the metavanadate chains. Thus, we replaced the smaller NH_4^+ monocation by the larger $[\text{Zn}(\text{Im})_4]^{2+}$ complex dication, and herein we report a reversible order-disorder phase transition in the new catena Poly[[tetraimidazolezinc(II)][hexaoxidovanadate(2-)]], $\{[\text{Zn}(\text{Im})_4][\text{V}_2\text{O}_6]\}_n$, material investigated by variable-temperature single crystal X-ray diffraction, DSC, and variable-temperature infrared spectroscopy.

5.2 Experimental

5.2.1 Synthesis and Characterization

All chemicals were of reagent grade and used without further purification. Synthesis was carried out in a PTFE-lined stainless steel reactor (Parr Instrument Company, Illinois, USA) under autogenous pressure. Powder X-ray diffraction patterns were recorded on a Philips PW 1830 diffractometer (PANalytical B.V., Almelo, The Netherlands) equipped with a Cu $K\alpha$ X-ray source ($\lambda = 1.54062 \text{ \AA}$) for the angular range $2\theta = 5\text{--}50^\circ$, with a step size of 0.05° and a counting time of 3 s per step. Elemental analysis (C, H, and N) was obtained from Medac Ltd, Surrey, UK.

$\{[\text{Zn}(\text{Im})_4][\text{V}_2\text{O}_6]\}_n$ was isolated from the hydrothermal reaction of

Zn(OAc)₂·2H₂O (0.110 g, 0.50 mol), V₂O₅ (0.091 g, 0.50 mmol), Imidazole (0.306 g, 4.5 mmol), and H₂O (2 mL, 111 mmol) in the approximate mole ratio of 1:1:9:222. After stirring in a 23 mL Teflon cup for 30 min, the pH of the reaction mixture was ~9. The cup was sealed in a Parr reactor, and heated at 110 °C for 2 days, cooled slowly to room temperature at a rate of 0.5 °C min⁻¹ to afford pure pale yellow crystals of {[Zn(Im)₄][V₂O₆]}_n (256 mg, yield ~96% based on V₂O₅). Anal. Calc. of {[Zn(Im)₄][V₂O₆]}_n: C, 26.91; H, 3.01; N, 20.92%. Found: C, 26.52; H, 2.91; N, 20.60%.

With the same starting materials proportion after 30 min stirring time by adjusting the pH to 11, the yield of {[Zn(Im)₄][V₂O₆]}_n decreases and colorless crystals of [Zn(μ-Im)₂]_n (Bauman and Wang, 1964; Xiaochun, Dan, Yexiang, and Xiaoming, 1998) also formed. No vanadate appeared in the product when the pH was adjusted to 13 after stirring 30 min.

5.2.2 Differential Scanning Calorimetry (DSC) and Thermogravimetric Analysis (TGA)

DSC measurements were performed on a heat flow calorimeter with disk-type measuring system (Mettler Toledo DSC822^e, Star-Software, V. 9.30, Greifensee, Switzerland), equipped with a standard cooling unit and purged with nitrogen gas. Measurements were performed in standard aluminium crucibles with cooling and heating rates of 5 °C min⁻¹. TGA analysis was recorded on a TGA Q5000 V2.4 Build 223 instrument in flowing nitrogen gas with a heating rate of 10 °C min⁻¹.

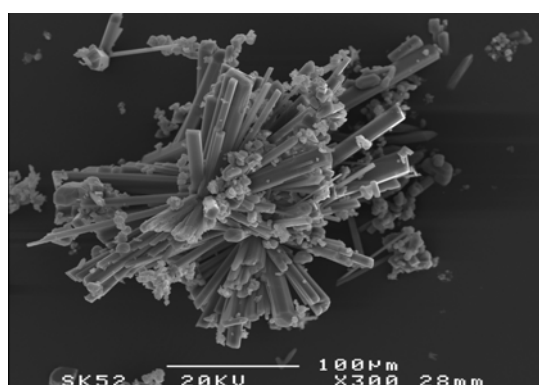
5.2.3 Variable-temperature Infrared Spectroscopy

Infrared spectra were measured on a Perkin Elmer Spectrum GX infrared spectrophotometer (700-4000 cm⁻¹, spectral resolution 4 cm⁻¹) using nujol mulls on BaF₂

windows (25 x 4 mm) separated with a 0.15 mm lead spacer using a cooled HC-32 demountable cell holder (Spectra-Tech, Inc., Tennessee, USA) with an external recirculation bath (Heto CBN 18-30, Allerød, Denmark) controlled to ± 0.1 °C (Heto HMT 200 thermostat) with 60:40 ethylene glycol:water for coolant. Temperature was monitored with a calibrated K-type thermocouple and a Jenway 2103 digital thermometer. The IR spectrum was also taken as a KBr pellet at room temperature and at the temperature of liquid nitrogen.



(a)



(b)

Figure 5.1 SEM images (a) prisms of $\{[\text{Zn}(\text{Im})_4][\text{V}_2\text{O}_6]\}_n$ and (b) needles of $[\text{Zn}(\mu\text{-Im})_2]_n$.

5.2.4 X-ray Crystallography

A single crystal of $\{[\text{Zn}(\text{Im})_4][\text{V}_2\text{O}_6]\}_n$ suitable for X-ray crystallography with size 0.10 x 0.10 x 0.30 mm was mounted on a glass fiber. Data were collected at -173 ± 2 °C on a Bruker-Nonius Smart Apex CCD diffractometer equipped with a $\text{MoK}\alpha$ X-radiation source ($\bar{\lambda} = 0.71073$ Å) and a CryoSystems low temperature device, and at 20 ± 2 °C on an Oxford Diffraction Kappa diffractometer equipped with a $\text{CuK}\alpha$ X-radiation source ($\bar{\lambda} = 1.54184$ Å). The structures were solved by direct methods and refined by full-matrix least-squares refinement on F^2 using *SHELXL* (Sheldrick, 1997). At 20 ± 2 °C, one of four crystallographically unique bridging and four terminal oxygen atoms are statistically disordered in 50:50. Hydrogen atoms were placed in geometrically idealized positions with C–H = 0.95 Å, N–H = 0.88 Å, and $U_{\text{eq}}(\text{H}) = 1.2U_{\text{eq}}(\text{C}, \text{N})$ at -173 ± 2 °C and C–H = 0.93 Å, N–H = 0.86 Å, and $U_{\text{eq}}(\text{H}) = 1.2U_{\text{eq}}(\text{C}, \text{N})$ at 20 ± 2 °C.

Molecular graphics images were created with *ORTEB-III* (Burnett and Johnson, 1996). Only the major component for the lower temperature structure is illustrated for clarity. A summary of crystal data and refinement details for $\{[\text{Zn}(\text{Im})_4][\text{V}_2\text{O}_6]\}_n$ is given in Table 5.1. Selected bond lengths of cation and anions are listed in Table 5.2. Selected bond angles of cation and anions are listed in Tables 5.3 and 5.4, respectively. Fractional coordinates and atomic displacement parameters at both temperatures are listed in Tables C1 and C2, and the asymmetric unit of the -173 ± 2 °C structure is shown in Figure C1 of Appendix C.

Table 5.1 Crystal Data and Refinement Details for $\{[\text{Zn}(\text{Im})_4][\text{V}_2\text{O}_6]\}_n$.

	-173 °C phase	20 °C phase
Crystal data		
Chemical formula	$\text{C}_{24}\text{H}_{32}\text{N}_{16}\text{O}_{12}\text{V}_4\text{Zn}_2$	$\text{C}_{24}\text{H}_{32}\text{N}_{16}\text{O}_{12}\text{V}_4\text{Zn}_2$
M_r	1071.16	1071.16
Temperature (°C)	-173±2	20±2
Crystal system, space group	Triclinic, $P\bar{1}$	Triclinic, $P\bar{1}$
Unit cell parameters (Å, °)	$a = 9.492(2)$, $\alpha = 85.956(4)$ $b = 10.156(2)$, $\beta = 110.550(5)$ $c = 21.900(5)$, $\gamma = 87.909(5)$	$a = 9.513(5)$, $92.85(5)$ $b = 10.216(6)$, $110.32(5)$ $c = 11.060(7)$, $94.48(4)$
Volume (Å ³)	1967.7(8)	1001.4(10)
Z	2	4
D_x (Mg m ⁻³)	1.808	1.776
Radiation type, wavelength (Å)	Mo, $K\alpha$, 0.71073	Cu, $K\alpha$ 1.54184
θ_{range} (°)	1.99-25.50	4.28-72.83
Absorption coefficient, μ (mm ⁻¹)	2.187	9.504
Crystal form, color	Prism, pale-yellow	Prism, pale-yellow
Crystal size	0.10 x 0.10 x 0.30	0.10 x 0.10 x 0.30
Data collection		
Diffractometer	Bruker-Nonius Smart Apex CCD	Oxford Diffraction Kappa
Data collection method	ω scans	ω scans
Absorption correction	Multi-scan	Multi-scan
T_{max} , T_{min}	0.804, 0.763	0.387, 0.368
No. of measured, independent, and observed reflections	9845, 7114, 5241	11544, 3924, 2822
Criterion for observed	$I > 2\sigma(I)$	$I > 2\sigma(I)$
R_{int}	0.0279	0.0444
θ_{max} (°)	25.50	72.83
Completeness to theta	96.9% (theta = 25.50)	98.2% (theta = 72.83)
Ranges of h , k , l	$-11 \leq h \leq 10$ $-12 \leq k \leq 12$ $-20 \leq l \leq 26$	$-11 \leq h \leq 11$ $-12 \leq k \leq 12$ $-13 \leq l \leq 13$
Refinement		
Refinement on	F^2	F^2
$R[F^2 > 2\sigma(F^2)]$, $wR_2(F^2)$, S	0.0639, 0.1455, 1.116	0.0377, 0.0895, 0.932

Table 5.1 (Continued).

	-173 °C phase	20 °C phase
No. of reflections	5241	2822
No. of parameters	662	292
H-atom treatment	Geometrically idealized	Geometrically idealized
$(\Delta/\sigma)_{\max}$	0.018	0.001
$\Delta\rho_{\max, \min, \text{err}}$ ($e \text{ \AA}^{-3}$)	1.014, -1.175, 0.153	0.412, -0.378, 0.094

5.3 Results and Discussion

5.3.1 Synthesis

$\{[\text{Zn}(\text{Im})_4][\text{V}_2\text{O}_6]\}_n$ was successfully synthesized from hydrothermal reaction of $\text{Zn}(\text{OAc})_2 \cdot 2\text{H}_2\text{O}$, V_2O_5 , imidazole, and H_2O in the mole ratio of 1:1:9:222 at 110 °C for 2 days (96% yield, based on V). The initial pH reaction was 9, thus the imidazole is neutral ($\text{p}K_{\text{a}1} = 6.95$ and $\text{p}K_{\text{a}2} = 14.5$). If the initial reaction pH was high basicity (pH range of 13) a basic pyridinic N-atom on the imidazole deprotonated to form imidazolate anion (Im^-) and it prefers to coordinate with the zinc centers forming a neutral compound in which Im^- acts as a bidentate ligand and V_2O_5 is hydrolyzed to form $[\text{VO}_3(\text{OH})]^{2-}$ which remains in solution. Therefore, isolating $\{[\text{Zn}(\text{Im})_4][\text{V}_2\text{O}_6]\}_n$ failed in highly basic media, and only crystals of the known $[\text{Zn}(\mu\text{-Im})_2]_n$ compound reported by Bauman and Wang (1964) were isolated. The crystal morphologies are shown in Figure 5.1.

5.3.2 Powder X-ray Diffraction

XRD patterns were recorded for the bulk sample of $\{[\text{Zn}(\text{Im})_4][\text{V}_2\text{O}_6]\}_n$ and compared to the simulated patterns calculated from the single crystal X-ray structural results as a check that the bulk materials do not contain multiple phases at room

temperature as shown in Figure 5.2. Figure 5.3 shows the simulated XRD pattern at 20 °C are significant differently compared to at -173 °C because pseudo inversion centers were observed at $(0,0,1/4)$, $(0,0,3/4)$, $(1/2,0,1/4)$, and $(1/2,0,3/4)$ and the crystal structure is possibly destabilized upon cooling as described below.

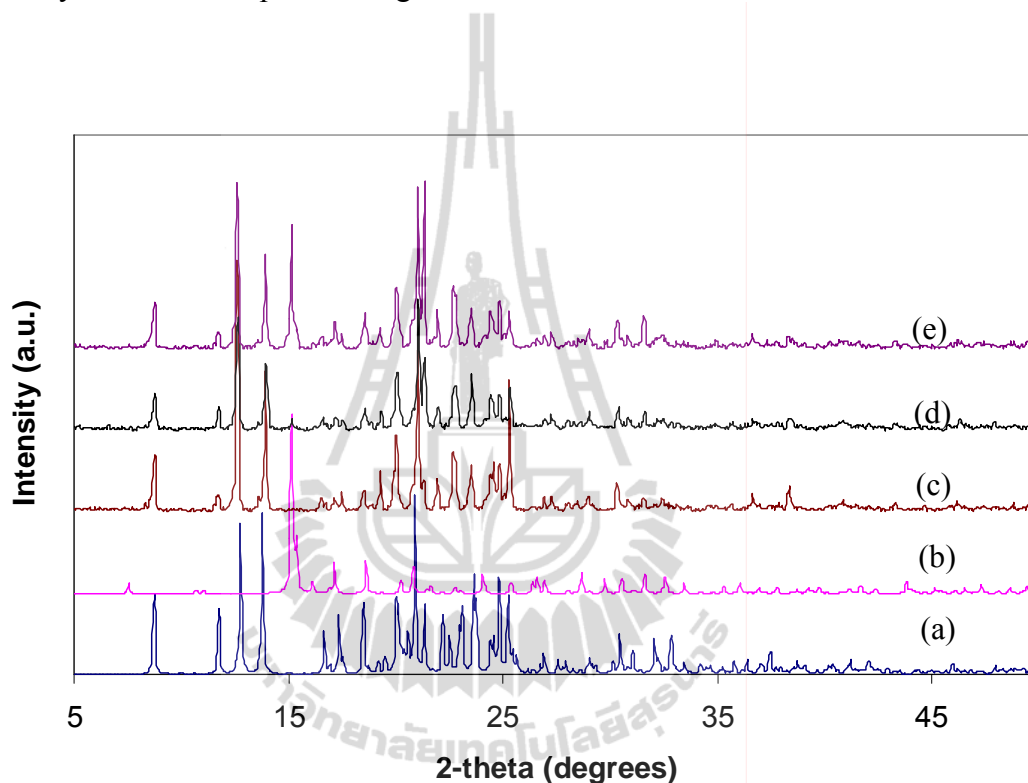


Figure 5.2 Comparison of simulated and experimental powder XRD patterns of $\{[Zn(Im)_4][V_2O_6]\}_n$: (a) calc. of $\{[Zn(Im)_4][V_2O_6]\}_n$, (b) calc. $[Zn(\mu-Im)_2]_n$, (c) measured of $\{[Zn(Im)_4][V_2O_6]\}_n$ at pH 9, (d) pH 11, and (e) pH 13.

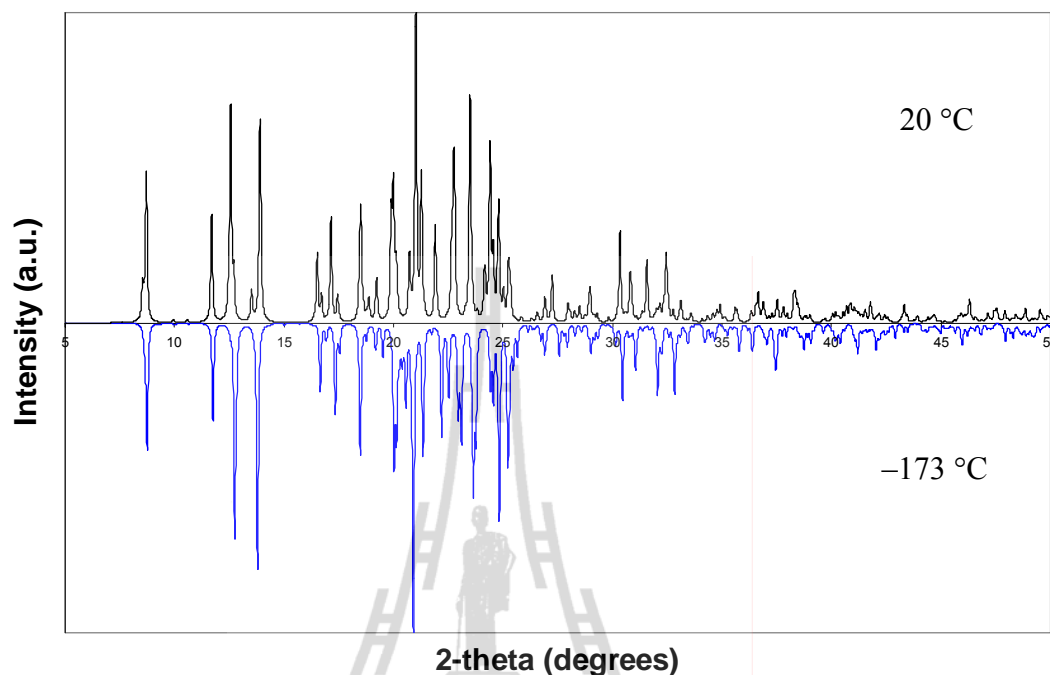


Figure 5.3 Comparison of simulated powder XRD patterns of $\{[\text{Zn}(\text{Im})_4][\text{V}_2\text{O}_6]\}_n$.

5.3.3 The Crystal Structure of $\{[\text{Zn}(\text{Im})_4][\text{V}_2\text{O}_6]\}_n$

Single crystal X-ray diffraction shows an ordered triclinic $P-1$ phase at -173 ± 2 °C and a disordered triclinic $P-1$ phase at 20 ± 2 °C. At -173 °C, the unit cell parameters are significantly different compared with at 20 °C (the c axis half of -173 °C) which is similar to those observed in hexamethylenetetraaminium 3,5-dinitrobenzoate hemideuterated water (Chen, Zhao, Ge, Xiong, and Hu, 2009 and reference therein) and polymeric $[\text{Ag}(\text{bipy})(\text{NO}_3)]_n$ (Somphon, Haller, and Rae, 2011).

The structure contains anionic metavanadate chains of corner-sharing VO_4 tetrahedra. The bond distances and angles of two temperature metavanadate forms are observed in normal ranges and similar to that found in the literature (Hawthorne and Calvo, 1977; Liu, Lin, and Lin, 2000; Khan, Yohannes, Doedens, Golub, and

O'Conner, 2005). In this work, the chains are separated by cationic distorted $[\text{Zn}(\text{Im})_4]^{2+}$ tetrahedra.

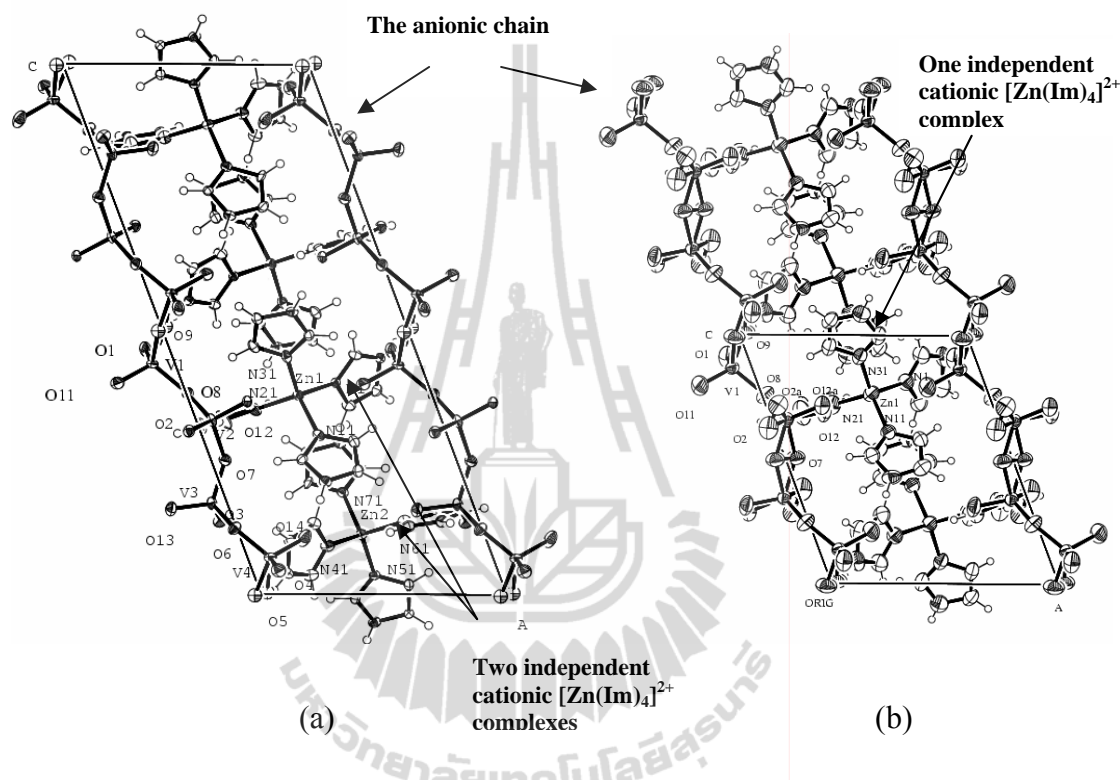


Figure 5.4 ORTEP drawing of the structures projected on the ac planes (a) at $-173\text{ }^\circ\text{C}$, and (b) at $20\text{ }^\circ\text{C}$.

At $-173\text{ }^\circ\text{C}$, the nonhydrogen atoms are crystallographic unique independence except for atom O(5) and O(9) which are disordered 50:50 at an inversion center with $d[\text{O}-\text{O}] = 0.60(2)$ and $0.46(2)\text{ \AA}$ as shown in Figure 5.4. The chains are ordered with every fourth μ -O atom lying on an inversion center, $\text{O}(5)^i-\text{V}(4)-\text{O}(6)-\text{V}(3)-\text{O}(7)-\text{V}(2)-\text{O}(8)-\text{V}(1)-\text{O}(9)^i$, and with every second and sixth μ -O atom repeated in positions alternating up and down along the chain propagation axis, placing two $[\text{V}_2\text{O}_6]^{2-}$ units and two crystallographically independent $[\text{Zn}(\text{Im})_4]^{2+}$ cations in the asymmetric unit.

The conformations of the two dimeric units as well as the zinc complex cations are quite similar. The first $[\text{V}_2\text{O}_6]^{2-}$ unit can be transformed into the second $[\text{V}_2\text{O}_6]^{2-}$ unit by pseudo inversion centers at $(0,0,1/4)$ and $(0,0,3/4)$, (at second and sixth μ -O atom). Zn(1) complex cation can be transformed to Zn(2) complex cation related by pseudo inversion centers at $(1/2,0,1/4)$, and $(1/2,0,3/4)$. The coordination geometry of V(2)O₄ tetrahedra is different compare to V(3)O₄ tetrahedra include 5° distinct of V(1)–O(8)–V(2) and V(3)–O(6)–V(4) angles of the anions and two significantly different N–Zn–N angles of the cations as listed in Tables 5.3 and 5.4.

For comparison in the –173 °C phase, the N(71)–Zn(2)–N(51) angle, 120.6(2)°, is larger than observed in zinc tetraimidazole salts of $[\text{Zn}(\text{Im})_4][\text{ClO}_4]_2$ (113.1°) and $[\text{Zn}(\text{Im})_4][\text{BF}_4]_2$ (109°) (Loeffen, Pettifer, and Tomkinson, 1996), otherwise, these are similar as found in some tetrahedral zinc complexes that exist in the literature (Bauman and Wang, 2003; Becker and Jansen, 2001; Bhosekar, Jess, Havlas, and Näther, 2007; Choi, Kim, Chang, Halasyamani, and Ok, 2009; Xiaochun, Dan, Yexiang, and Xiaoming, 1998).

As the temperature is increased, the alternating up-down positions of the chains of the ordered structure, disorder, creating additional inversion centers at every second and sixth μ -O atom positions of the –173 °C structure, by near the O(7) sites with $d[\text{O}–\text{O}] = 1.148(10)$ Å across the inversion center. Coincident with the formation of the new inversion centers, the four neighboring V = O(2),(12),(2a),(12a) terminal oxygen atoms rearrange and reorient into disordered positions, O(2) and O(12) with $d[\text{O}–\text{O}] = 1.029(8)$ and $0.749(10)$ Å, and atoms O(1) and O(11) similarly, by an approximate superimposition of the O(2)/O(12) and O(1)/O(11) positions of the –173 °C structure.

Table 5.2 Selected Bond Lengths (Å) for {[Zn(Im)₄][V₂O₆]}_n.

Triclinic at -173(2) °C				Triclinic at 20(2) °C	
Bond	Length [Å]	Bond ^a	Length [Å]	Bond	Length [Å]
Zn(1)–N(1)	2.0000(19)	Zn(2)–N(41)	2.0012(19)	Zn(1)–N(1)	2.003(3)
Zn(1)–N(11)	1.970(2)	Zn(2)–N(71)	1.969(2)	Zn(1)–N(11)	1.977(3)
Zn(1)–N(21)	1.998(2)	Zn(2)–N(61)	1.998(2)	Zn(1)–N(21)	2.013(3)
Zn(1)–N(31)	1.968(2)	Zn(2)–N(51)	1.9720(19)	Zn(1)–N(31)	1.974(3)
V(1)–O(1)	1.6322(19)	V(4)–O(4)	1.6307(19)	V(1)–O(1)	1.635(3)
V(1)–O(11)	1.6313(19)	V(4)–O(14)	1.6302(19)	V(1)–O(11)	1.618(3)
V(1)–O(8)	1.7808(18)	V(4)–O(6)	1.7794(18)	V(1)–O(8)	1.772(2)
V(1)–O(9)	1.790(2)	V(4)–O(5)	1.789(2)	V(1)–O(9)	1.770(2)
V(1)–O(9) ⁱ	1.786(4)	V(4)–O(5) ⁱⁱ	1.782(4)	V(1)–O(9) ⁱ	1.785(3)
V(2)–O(2)	1.6474(19)	V(3)–O(3)	1.6474(19)	V(2)–O(2)	1.640(2)
				V(2)–O(2A)	1.643(2)
V(2)–O(12)	1.6249(19)	V(3)–O(13)	1.6255(19)	V(2)–O(12)	1.634(2)
				V(2)–O(12A)	1.636(2)
V(2)–O(8)	1.7806(18)	V(3)–O(6)	1.7796(18)	V(2)–O(8)	1.782(3)
V(2)–O(7)	1.8387(18)	V(3)–O(7)	1.7594(19)	V(2)–O(7)	1.839(3)
				V(2)–O(7) ⁱⁱ	1.732(4)
				O(2)–O(2A)	1.029(8)
				O(12)–O(12A)	0.749(10)
				O(7)–O(7) ⁱⁱ	1.148(10)
				O(9)–O(9) ⁱ	0.646(12)
N(1)–C(2)	1.3219(16)	N(41)–C(42)	1.3220(16)	N(1)–C(2)	1.314(2)
N(1)–C(5)	1.3952(16)	N(41)–C(45)	1.3954(16)	N(1)–C(5)	1.371(2)
C(2)–N(3)	1.3502(16)	C(42)–N(43)	1.3500(16)	C(2)–N(3)	1.329(2)
N(3)–C(4)	1.3756(17)	N(43)–C(44)	1.3755(17)	N(3)–C(4)	1.354(2)
C(4)–C(5)	1.3656(17)	C(44)–C(45)	1.3659(17)	C(4)–C(5)	1.346(2)
N(11)–C(12)	1.3215(16)	N(71)–C(72)	1.3219(16)	N(11)–C(12)	1.315(2)
N(11)–C(15)	1.3946(17)	N(71)–C(75)	1.3947(16)	N(11)–C(15)	1.376(2)
C(12)–N(13)	1.3488(16)	C(72)–N(73)	1.3495(16)	C(12)–N(13)	1.328(2)
N(13)–C(14)	1.3754(17)	N(73)–C(74)	1.3758(17)	N(13)–C(14)	1.354(2)

^aSelected bond lengths related by pseudo inversion centers at ($1/2, 0, 1/4$), and ($1/2, 0, 3/4$) for [Zn(Im)₄]²⁺ cations and at ($0, 0, 1/4$) and ($0, 0, 3/4$) for [V₂O₆]²⁻ anions. Symmetry code: At -173(2) °C: (i) -x, -y, -z+1; (ii) -x, -y, -z. At 20(2) °C: (i) -x, -y, -z+2; (ii) -x, -y, -z+1.

Table 5.2 (Continued).

Bond	Triclinic at $-173(2)$ °C		Triclinic at $20(2)$ °C		
	Length [Å]	Bond ^a	Length [Å]	Bond	Length [Å]
C(14)–C(15)	1.3652(17)	C(74)–C(75)	1.3651(17)	C(14)–C(15)	1.343(2)
N(21)–C(22)	1.3214(17)	N(61)–C(62)	1.3221(17)	N(21)–C(22)	1.311(2)
N(21)–C(25)	1.3940(17)	N(61)–C(65)	1.3944(17)	N(21)–C(25)	1.371(2)
C(22)–N(23)	1.3497(17)	C(62)–N(63)	1.3500(17)	C(22)–N(23)	1.327(2)
N(23)–C(24)	1.3755(17)	N(63)–C(64)	1.3758(17)	N(23)–C(24)	1.353(2)
C(24)–C(25)	1.3652(17)	C(64)–C(65)	1.3658(17)	C(24)–C(25)	1.345(2)
N(31)–C(32)	1.3219(17)	N(51)–C(52)	1.3228(16)	N(31)–C(32)	1.316(2)
N(31)–C(35)	1.3947(16)	N(51)–C(55)	1.3948(16)	N(31)–C(35)	1.371(2)
C(32)–N(33)	1.3495(16)	C(52)–N(53)	1.3498(16)	C(32)–N(33)	1.328(2)
N(33)–C(34)	1.3756(17)	N(53)–C(54)	1.3762(17)	N(33)–C(34)	1.355(2)
C(34)–C(35)	1.3655(17)	C(54)–C(55)	1.3654(17)	C(34)–C(35)	1.342(2)

The introduction of additional inversion centers at 20 °C cuts the unit translation in the chain direction in half, thereby cutting the cell volume in half, transforming into the disordered structure. The phase transition in this metavanadate polymeric salt is due to the temperature dependent small reorientation of the anionic polymeric chains with the V–O–V angles expanded along the *c* axis are driving forces to the small reorientation and rearrangement of the cations within a 3-D supramolecular cationic network, the N–Zn–N angles of the single independent cation become similar to the mean N–Zn–N angles at -173 °C (see in Tables 5.3 and 5.4) through the significantly different weak C–H...O, and weaker N–H... π and C–H... π hydrogen bonding interactions as described below.

Table 5.3 Selected Bond Angles (°) for the Cationic $[\text{Zn}(\text{Im})_4]^{2+}$ Complexes.

Triclinic at $-173(2)$ °C			
	Angle [°]		Angle [°] ^a
N(11)–Zn(1)–N(1)	102.2(2)	N(71)–Zn(2)–N(41)	105.2(3)
N(21)–Zn(1)–N(1)	110.8(2)	N(61)–Zn(2)–N(41)	104.4(3)
N(31)–Zn(1)–N(1)	112.3(2)	N(51)–Zn(2)–N(41)	112.8(3)
N(21)–Zn(1)–N(11)	110.2(2)	N(61)–Zn(2)–N(71)	108.1(2)
N(31)–Zn(1)–N(11)	112.9(2)	N(51)–Zn(2)–N(71)	120.6(2)
N(31)–Zn(1)–N(21)	108.4(2)	N(51)–Zn(2)–N(61)	104.5(2)
Triclinic at $-173(2)$ °C		Triclinic at $20(2)$ °C	
	Mean Angle [°]		Angle [°]
N(11)–Zn(1)–N(1)	103.7 ± 1.5		103.85(11)
N(21)–Zn(1)–N(1)	107.6 ± 3.2		106.90(12)
N(31)–Zn(1)–N(1)	112.6 ± 0.0		110.55(12)
N(21)–Zn(1)–N(11)	109.2 ± 1.0		110.31(13)
N(31)–Zn(1)–N(11)	116.8 ± 3.9		118.10(12)
N(31)–Zn(1)–N(21)	106.4 ± 1.7		106.67(12)

^aSelected bond angles related by pseudo inversion centers at $(\frac{1}{2}, 0, \frac{1}{4})$, and $(\frac{1}{2}, 0, \frac{3}{4})$.

Table 5.4 Selected Bond Angles (°) for the Anionic $[\text{V}_2\text{O}_6]^{2-}$ Chains.

Triclinic at $-173(2)$ °C				Triclinic at $20(2)$ °C	
	angle [°]		angle [°] ^a		angle [°]
O(1)–V(1)–O(11)	109.4(2)	O(4)–V(4)–O(14)	108.8(3)	O(1)–V(1)–O(11)	108.15(16)
O(1)–V(1)–O(8)	108.2(2)	O(4)–V(4)–O(6)	107.3(2)	O(1)–V(1)–O(8)	108.18(14)
O(1)–V(1)–O(9) ⁱ	114.4(5)	O(4)–V(4)–O(5)	113.6(4)	O(1)–V(1)–O(9) ⁱ	116.4(4)
O(1)–V(1)–O(9)	104.1(5)	O(4)–V(4)–O(5) ⁱⁱ	104.6(4)	O(1)–V(1)–O(9)	102.2(4)
O(11)–V(1)–O(8)	110.8(2)	O(14)–V(4)–O(6)	110.6(2)	O(11)–V(1)–O(8)	110.61(15)
O(11)–V(1)–O(9)	115.6(4)	O(14)–V(4)–O(5) ⁱⁱ	118.4(3)	O(11)–V(1)–O(9)	119.3(3)
O(11)–V(1)–O(9) ⁱ	101.2(4)	O(14)–V(4)–O(5)	98.9(4)	O(11)–V(1)–O(9) ⁱ	99.1(3)
O(8)–V(1)–O(9)	108.4(5)	O(6)–V(4)–O(5) ⁱⁱ	106.5(4)	O(9)–V(1)–O(8)	107.6(5)
O(8)–V(1)–O(9) ⁱ	112.7(5)	O(6)–V(4)–O(5)	117.2(4)	O(8)–V(1)–O(9) ⁱ	114.0(5)
O(2)–V(2)–O(12)	108.3(3)	O(3)–V(3)–O(13)	108.6(3)	O(2)–V(2)–O(12)	130.1(4)

Table 5.4 (Continued).

Triclinic at -173(2) °C				Triclinic at 20(2) °C	
angle [°]		angle [°] ^a		angle [°]	
				O(2)–V(2)–O(12A)	106.8(5)
				O(2A)–V(2)–O(12)	107.7(4)
				O(2A)–V(2)–O(12A)	81.2(5)
O(2)–V(2)–O(8)	112.2(2)	O(3)–V(3)–O(6)	107.5(2)	O(2)–V(2)–O(8)	116.1(3)
				O(2A)–V(2)–O(8)	105.0(2)
O(2)–V(2)–O(7)	108.7(2)	O(3)–V(3)–O(7)	108.9(2)	O(2)–V(2)–O(7)	108.2(3)
				O(2A)–V(2)–O(7) ⁱⁱ	109.5(3)
O(12)–V(2)–O(7)	106.3(3)	O(13)–V(3)–O(7)	113.7(3)	O(12)–V(2)–O(7)	83.6(3)
				O(12)–V(2)–O(7) ⁱⁱ	116.4(3)
				O(12A)–V(2)–O(7)	104.2(4)
				O(12A)–V(2)–O(7) ⁱⁱ	127.7(4)
O(12)–V(2)–O(8)	111.9(3)	O(13)–V(3)–O(6)	105.9(2)	O(12)–V(2)–O(8)	104.9(3)
				O(12A)–V(2)–O(8)	113.3(4)
O(8)–V(2)–O(7)	109.2(2)	O(7)–V(3)–O(6)	112.1(2)	O(8)–V(2)–O(7)	107.6(2)
				O(7) ⁱⁱ –V(2)–O(8)	112.6(2)
V(1) ⁱ –O(9)–V(1)	165.1(6)	V(4) ⁱⁱ –O(5)–V(4)	160.6(5)	V(1)–O(9)–V(1) ⁱ	159.0(4)
V(2)–O(8)–V(1)	138.33(19)	V(4)–O(6)–V(3)	133.33(19)	V(1)–O(8)–V(2)	140.57(17)
V(3)–O(7)–V(2)	135.6(2)			V(2) ⁱⁱ –O(7)–V(2)	142.7(3)

^aSelected bond angles related by pseudo inversion centers at $(0,0,1/4)$ and $(0,0,3/4)$.

Symmetry code: At -173(2) °C: (i) $-x,-y,-z+1$; (ii) $-x,-y,-z$. At 20(2) °C: (i) $-x,-y,-z+2$; (ii) $-x,-y,-z+1$.

There are no electrostatic forces between cations and anions due to the steric effect of the imidazole ligands on the cations, therefore, only the relative complex system of hydrogen bonding interactions as listed in Table 5.5 supports the structure. Figure 5.5 shows a 3-D supramolecular network formed by intermolecular connections between the cations and anions through eight strong N–H...O hydrogen bond interactions at both temperatures which are not significantly different. Its network stability is reinforced significantly different by six and seven weak C–H...O hydrogen bond interactions related the Zn(1) and Zn(2) cations to anions at -173 °C, no

C(25)–H(25)⋯O(8) and C(55)–H(55)⋯O(6) were observed, whereas the fourteen weak hydrogen bond interactions at 20 °C are similar to the Zn(2) cation of –173 °C are shown in Figure 5.6.

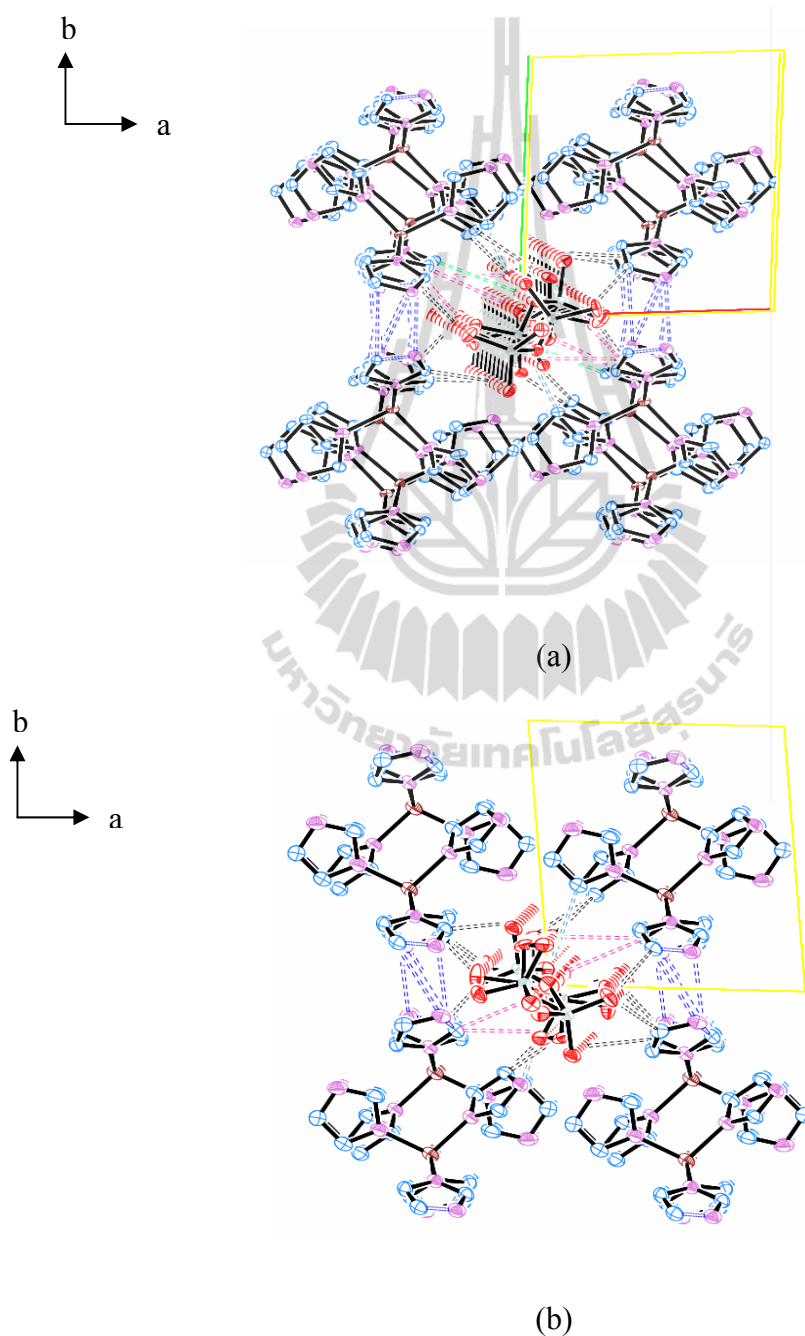


Figure 5.5 A 3-D supramolecular network in $\{[\text{Zn}(\text{Im})_4][\text{V}_2\text{O}_6]\}_n$ projection to the ab plane (a) at $-173\text{ }^\circ\text{C}$ and (b) at $20\text{ }^\circ\text{C}$. Hydrogen atoms are omitted for clarity.

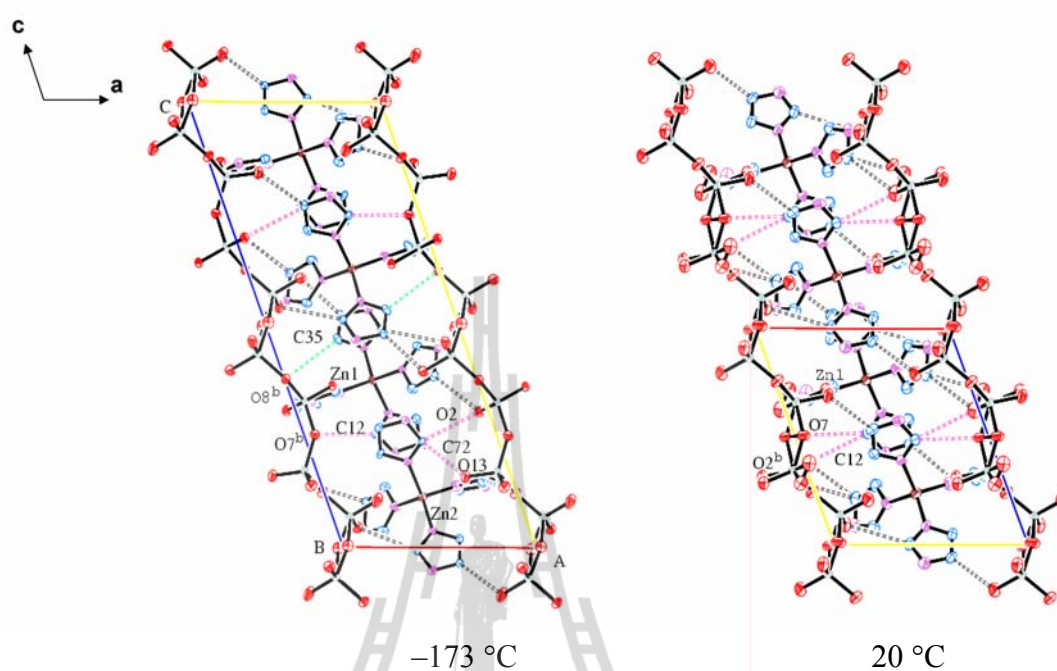


Figure 5.6 Weak C–H...O hydrogen bond interactions projected on the *ac* plane at $-173\text{ }^{\circ}\text{C}$ (left) and $20\text{ }^{\circ}\text{C}$ (right). Hydrogen atoms are omitted for clarity.

Figure 5.7 and Table 5.6 show the intercation interactions forming the 2-D supramolecular layers on the *bc* plane at $-173\text{ }^{\circ}\text{C}$ and at $20\text{ }^{\circ}\text{C}$ which are significantly different and that these interactions can be divided into two types;

(i) they related on top and bottom of anionic polymeric metavanadate propagations, two are parallel and two are tilted offset displaced (*off*) N–H... π hydrogen bond interactions ($d[\text{N13}–\text{H13}\cdots\pi_{\text{R8}}] = 3.09(1)\text{ \AA}$ and $d[\text{N73}–\text{H73}\cdots\pi_{\text{R2}}] = 3.19\text{ \AA}$; two $d[\text{N33}–\text{H33}\cdots\pi_{\text{R4}}] = 3.11(1)\text{ \AA}$; dihedral angles = $5.0(6), 0.0(6)^{\circ}$), whereas at $20\text{ }^{\circ}\text{C}$, observed all four parallel *off* N–H... π interactions (two $d[\text{N13}–\text{H13}\cdots\pi_{\text{R2}}] = 3.21(1)\text{ \AA}$ and two $d[\text{N33}–\text{H33}\cdots\pi_{\text{R4}}] = 3.22\text{ \AA}$; dihedral angles = $0.0(2), 0.0(3)^{\circ}$).

(ii) they occupied in between the anions, each multifold aryl embrace interconnected their neighbors formed two different motif types of edge-to-face (*ef*)

C–H... π hydrogen bond interactions, $-6ef-2ef-4ef-2ef-$ motif correspond to the Zn...Zn distances of ~ 5.8 , ~ 6.8 , ~ 5.6 and ~ 6.8 Å at -173 °C, whereas multifold aryl embraces decrease with increasing temperature are as observed $-4ef-2ef-4ef-2ef-$ motif at 20 °C correspond to the Zn...Zn distances of ~ 5.8 , ~ 6.8 , ~ 5.8 and ~ 6.8 Å at 20 °C.

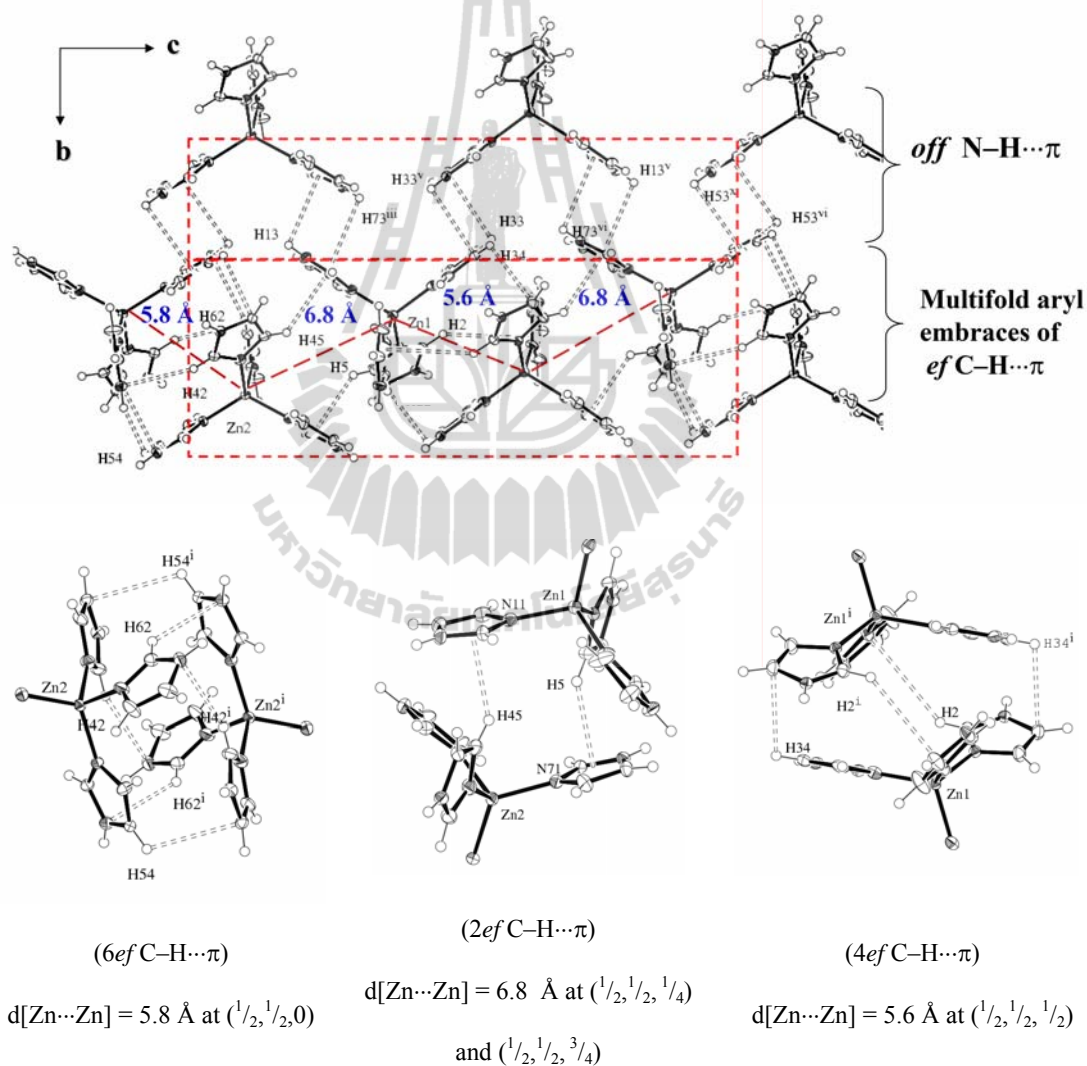


Figure 5.7 A 2-D supramolecular cationic layers formed through weaker N–H... π and C–H... π hydrogen bond interactions projected on the bc plane (a) at -173 °C and (b) at 20 °C. The anionic chains are omitted for clarity.

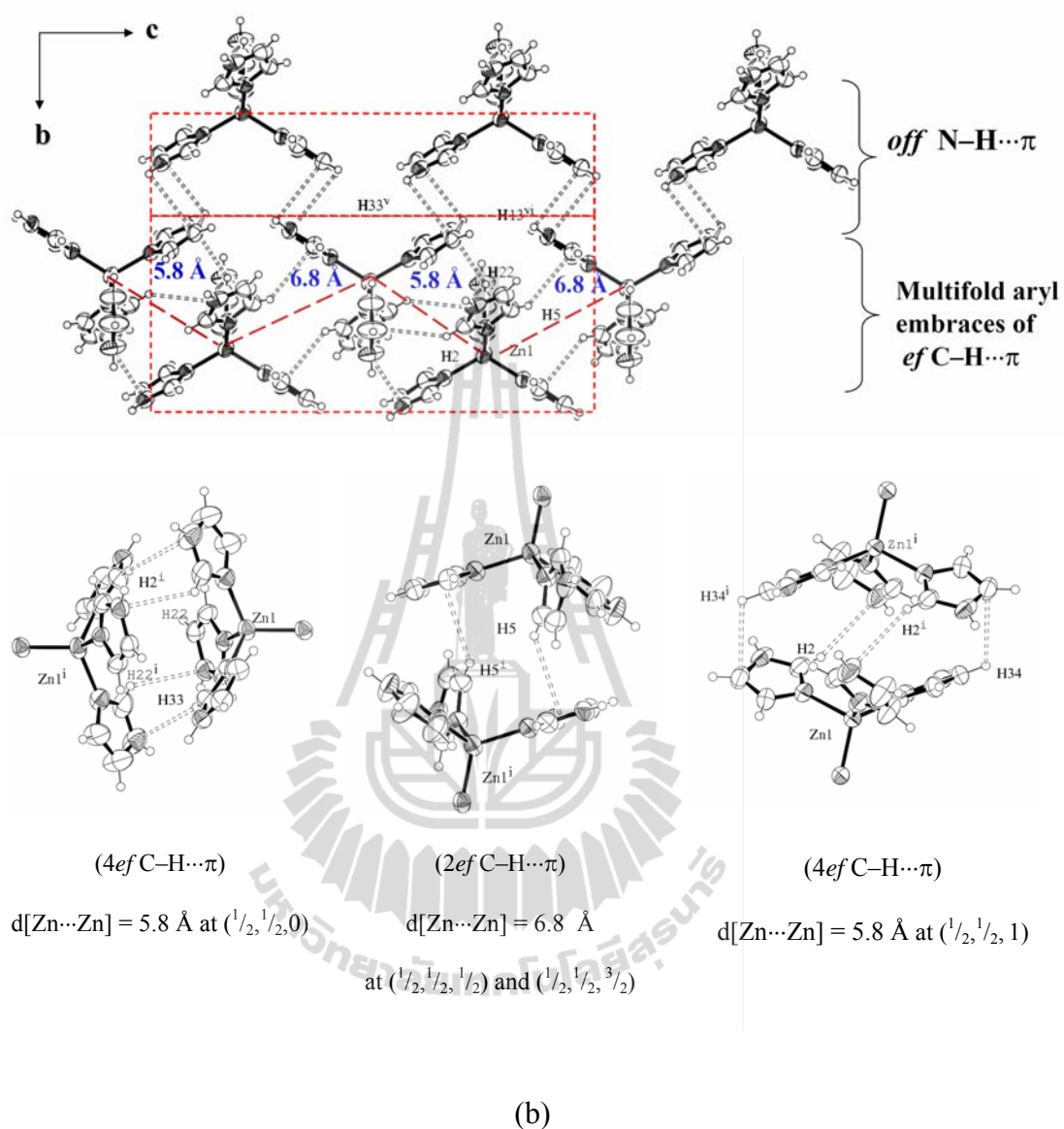


Figure 5.7 (Continued).

The 2-D supramolecular cationic layers further hydrogen-bonded to neighbors through two tilted *off* C-H... π hydrogen bond interactions at $-173 \text{ }^\circ\text{C}$ while observed two parallel *off* C-H... π and four *ef* C-H... π hydrogen bonding interactions related to eight-fold aryl embrace, (2*off*)(4*ef*), from the four cations interconnections $(\frac{1}{2}, 0, \frac{1}{2})$ at $20 \text{ }^\circ\text{C}$ are illustrated in Figures 5.8 and 5.9. All weaker hydrogen bond interactions are

listed in Table 5.6.

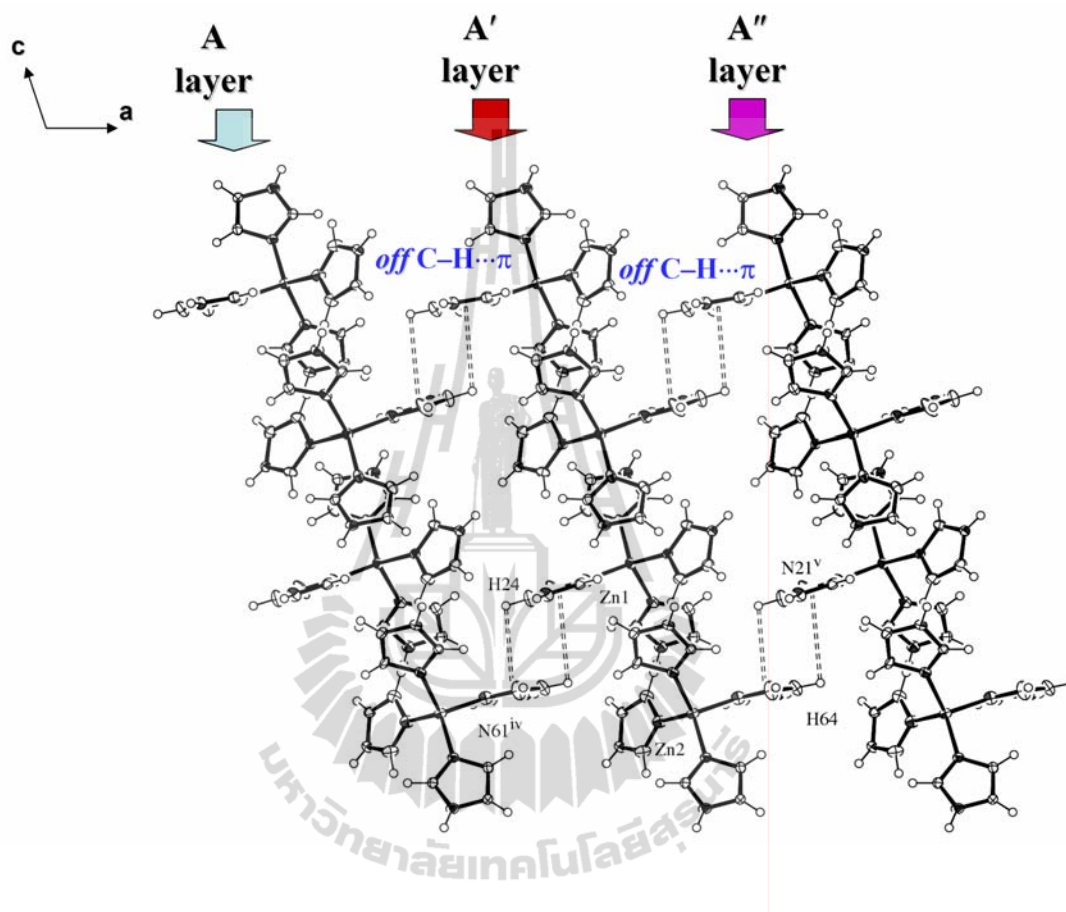


Figure 5.8 A 3-D supramolecular cationic network via weaker C–H \cdots π hydrogen bond interactions projected on the *ac* plane at -173 °C. The anionic chains are omitted for clarity.

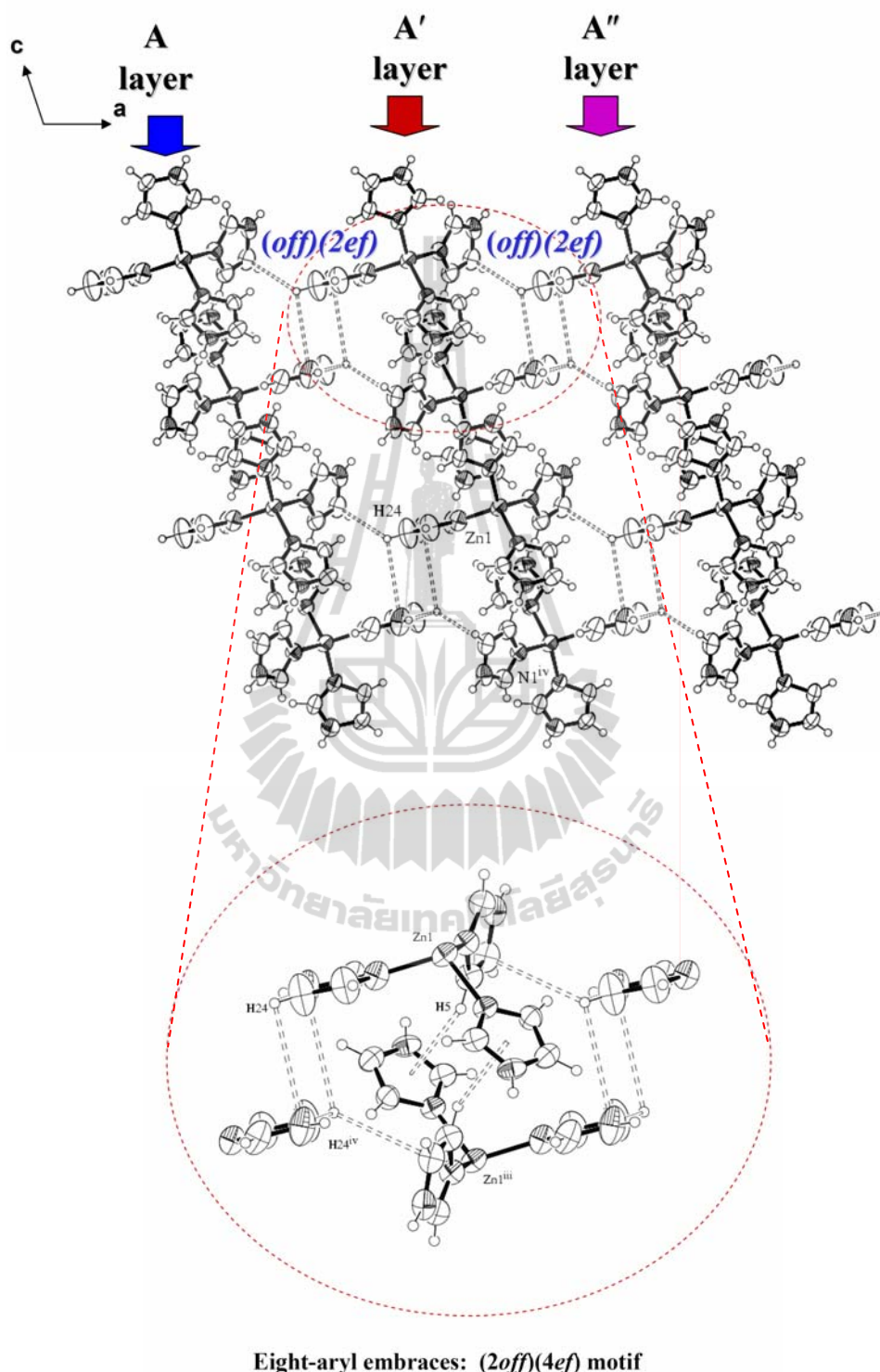


Figure 5.9 A 3-D supramolecular cationic network via weaker C–H... π H-bond interactions projected on the *ac* plane at 20 °C, showing eight-fold aryl embraces. The anionic chains are omitted for clarity.

Table 5.5 Hydrogen Bond Interactions between Cations and Anions for $\{[\text{Zn}(\text{Im})_4][\text{V}_2\text{O}_6]\}_n$.

-173 °C (related with the Zn(1) cation)					-173 °C (related with the Zn(2) cation)					20 °C				
D-H...A	d(D-H)	d(H...A)	d(D...A)	∠(DHA)	D-H...A	d(D-H)	d(H...A)	d(D...A)	∠(DHA)	D-H...A	d(D-H)	d(H...A)	d(D...A)	∠(DHA)
N(3)-H(3)...O(1) ⁱ	0.88	1.87	2.732(6)	166.2	N(43)-H(43)...O(4) ^{vii}	0.88	1.85	2.712(6)	165.5	N(3)-H(3)...O(1) ⁱ	0.86	1.87	2.713(4)	168.5
N(13)-H(13)...O(14) ⁱⁱ	0.88	1.82	2.691(6)	171.9	N(73)-H(73)...O(11) ^{iv}	0.88	1.86	2.735(6)	174.1	N(13)-H(13)...O(11) ⁱⁱ	0.86	1.86	2.715(4)	175.5
N(23)-H(23)...O(2)	0.88	1.84	2.715(7)	171.7	N(63)-H(63)...O(3) ^v	0.88	1.79	2.664(6)	173.8	N(23)-H(23)...O(2) ⁱⁱⁱ	0.86	2.09	2.908(7)	157.7
										N(23)-H(23)...O(2A) ⁱⁱⁱ	0.86	1.75	2.608(5)	172.5
										N(23)-H(23)...O(average)			2.758	
N(33)-H(33)...O(12) ⁱⁱⁱ	0.88	1.82	2.690(6)	170.0	N(53)-H(53)...O(13) ^{viii}	0.88	1.99	2.870(8)	177.1	N(33)-H(33)...O(12) ^{iv}	0.86	2.24	3.091(8)	171.8
										N(33)-H(33)...O(12A) ^{iv}	0.86	1.68	2.537(7)	171.8
										N(33)-H(33)...O(average)			2.814	
C(4)-H(4)...O(2) ^{iv}	0.95	2.38	3.290(7)	159.1	C(44)-H(44)...O(3) ⁱⁱ	0.95	2.40	3.234(7)	146.3	C(4)-H(4)...O(2) ^v	0.93	2.44	3.306(7)	154.3
										C(4)-H(4)...O(2A) ^v	0.93	2.39	3.220(6)	147.7
										C(4)-H(4)...O(average)			3.263	
C(12)-H(12)...O(7) ⁱⁱ	0.95	2.39	3.266(7)	153.1	C(72)-H(72)...O(2) ^{iv}	0.95	2.33	3.141(7)	143.6	C(12)-H(12)...O(7)	0.93	2.52	3.380(6)	154.7
					C(72)-H(72)...O(13) ^v	0.95	2.62	3.209(8)	120.2	C(12)-H(12)...O(2) ⁱⁱ	0.93	2.41	3.234(8)	147.2
					C(74)-H(74)...O(12)	0.95	2.20	3.130(8)	166.2	C(14)-H(14)...O(12) ^{vi}	0.93	2.45	3.304(9)	152.1
C(14)-H(14)...O(13) ^v	0.95	2.39	3.265(8)	152.6						C(14)-H(14)...O(12A) ^{vi}	0.93	2.30	3.197(9)	163.1
										C(14)-H(14)...O(average)			3.251	
					C(65)-H(65)...O(6) ^{iv}	0.95	2.52	3.315(6)	141.1	C(25)-H(25)...O(8)	0.93	2.59	3.429(5)	149.5
					C(52)-H(52)...O(4)	0.95	2.34	3.198(7)	149.9	C(32)-H(32)...O(1) ^{vii}	0.93	2.40	3.290(4)	159.9
C(32)-H(32)...O(1) ^v	0.95	2.31	3.239(7)	166.9	C(54)-H(54)...O(14) ^{ix}	0.95	2.12	3.039(7)	161.0	C(34)-H(34)...O(11) ^{viii}	0.93	2.18	3.088(4)	163.7
C(34)-H(34)...O(11) ^{vi}	0.95	2.31	3.234(7)	164.5										
C(35)-H(35)...O(8) ⁱⁱ	0.95	2.60	3.311(7)	132.3										

Symmetry code: (i) $-x+1, -y, -z+1$; (ii) $x, y+1, z$; (iii) $-x+1, -y+1, -z+1$; (iv) $x+1, y, z$; (v) $x+1, y+1, z$; (vi) $-x, -y+1, -z+1$; (vii) $-x, -y+1, -z$; (viii) $-x, -y, -z$; (ix) $-x+1, -y, -z$.

Symmetry code: (i) $-x+1, -y+1, -z+2$; (ii) $-x, -y, -z+1$; (iii) $y+1, z$; (iv) $-x+1, -y, -z+2$; (v) $x+1, y+1, z$; (vi) $-x+1, -y, -z+1$; (vii) $x+1, y, z$; (viii) $-x, -y, -z+2$.

Table 5.6 N–H... π and C–H... π Hydrogen Bond Intercation Interactions of $\{[\text{Zn}(\text{Im})_4][\text{V}_2\text{O}_6]\}_n$.

D–H...A	d[D–H] (Å)	d[H...A] (Å)	d[D...A] (Å)	Dihedral angle (°)
–173 °C				
C2–H2... $\pi_{\text{R}3}^{\text{i}}$	0.95	3.58(1)	4.361(8)	57.6(4)
C5–H5... $\pi_{\text{R}8}$	0.95	2.73(1)	3.345(9)	63.9(4)
N13–H13... $\pi_{\text{R}8}^{\text{ii}}$	0.88	3.09(1)	3.151(10)	5.0(6)
C24–H24... $\pi_{\text{R}7}^{\text{iii}}$	0.95	3.33(1)	3.424(10)	9.6(2)
N33–H33... $\pi_{\text{R}4}^{\text{iv}}$	0.88	3.11(1)	3.105(14)	0.0(6)
N33 ^d –H33 ^{iv} ... $\pi_{\text{R}4}$	0.88	3.11(1)	3.105(14)	0.0(6)
C34–H34... $\pi_{\text{R}1}^{\text{i}}$	0.95	3.10(1)	3.419(8)	35.2(5)
C42–H42... $\pi_{\text{R}7}^{\text{v}}$	0.95	2.89(1)	3.757(8)	71.1(5)
C45–H45... $\pi_{\text{R}2}$	0.95	2.85(8)	3.466(9)	67.5(4)
N53–H53... $\pi_{\text{R}6}^{\text{vi}}$	0.88	3.22(9)	3.222(10)	0.0(5)
N53 ^{vi} –H53 ^{vi} ... $\pi_{\text{R}6}$	0.88	3.22(9)	3.222(10)	0.0(5)
C54–H54... $\pi_{\text{R}5}^{\text{v}}$	0.95	3.10(1)	3.564(8)	45.0(5)
C62–H62... $\pi_{\text{R}6}^{\text{v}}$	0.95	2.79(1)	3.401(8)	64.8(3)
C64–H64... $\pi_{\text{R}3}^{\text{vii}}$	0.95	3.44(1)	3.338(11)	9.6(2)
N73–H73... $\pi_{\text{R}2}^{\text{viii}}$	0.88	3.19(1)	3.124(13)	5.0(6)
20 °C				
C2–H2... $\pi_{\text{R}3}^{\text{ix}}$	0.93	3.27(1)	4.080(5)	66.1(3)
C5–H5... $\pi_{\text{R}2}^{\text{i}}$	0.93	2.94(1)	3.499(5)	64.5(2)
N13–H13... $\pi_{\text{R}2}^{\text{x}}$	0.86	3.21(1)	3.215(6)	0.0(2)
C22–H22... $\pi_{\text{R}4}^{\text{ix}}$	0.93	2.84(1)	3.445(6)	66.1(2)
C24–H24... $\pi_{\text{R}1}^{\text{vii}}$	0.93	3.15(1)	3.668(7)	66.1(2)
C24–H24... $\pi_{\text{R}3}^{\text{xi}}$	0.93	3.51(1)	3.521(13)	0.0(2)
N33–H33... $\pi_{\text{R}4}^{\text{xii}}$	0.86	3.22(1)	3.218(5)	0.0(3)
C34–H34... $\pi_{\text{R}1}^{\text{ix}}$	0.93	3.22(1)	3.637(5)	44.8(2)

Symmetry code: (i) $-x+1, -y+1, -z+1$; (ii) $x, y-1, z$; (iii) $x+1, y, z$; (iv) $-x+1, -y+2, -z+1$; (v) $-x+1, -y+1, -z$; (vi) $-x+1, -y, -z$; (vii) $x-1, y, z$; (viii) $x, y+1, z$; (ix) $-x+1, -y+1, -z+2$; (x) $-x+1, -y, -z+1$; (xi) $-x, -y+1, -z+1$; (xii) $-x+1, -y, -z+2$.

Notation: Imidazole ring

R1 = N(1)-C(5), R2 = N(11)-C(15), R3 = N(21)-C(25), R4 = N(31)-C(35); R5 = N(41)-C(45), R6 = N(51)-C(55), R7 = N(61)-C(65), and R8 = N(71)-C(75).

5.4.4 Differential Scanning Calorimetry and Thermogravimetric Analysis

It is clear from the DSC measurements (Figures 5.10 and 5.11 and Table 5.7) that this compound undergoes a reversible first-order phase transition at 1.69 °C (exothermic transition, $\Delta H = -1.103 \text{ kJ mol}^{-1}$, and $\Delta S = -4.00 \text{ J K}^{-1} \text{ mol}^{-1}$) and at 3.90 °C (endothermic transition, $\Delta H = +1.253 \text{ kJ mol}^{-1}$ and $\Delta S = 4.52 \text{ J K}^{-1} \text{ mol}^{-1}$) upon 1st cooling and 1st heating, respectively, with a hysteresis of ~2 K (with a rate of $5 \text{ }^\circ\text{C min}^{-1}$).

Upon heating, the DSC curve shows the 2nd endothermic peaks appear about 170 °C, and a TGA curve shows the 1st weight loss step about 150 °C, respectively, assigned to the imidazole ligand and oxygen atoms of anionic chains started to decompose from the structure with significantly different temperature loss due to the rate of heating of TGA ($10 \text{ }^\circ\text{C min}^{-1}$) faster than the DSC twice ($5 \text{ }^\circ\text{C min}^{-1}$). Continuous heating until 751 °C, the organic ligands are lost completely include eight oxygen atoms with a total loss of 62.653% (calc. 61.795%). The residual 37.347% (calc. 36.936%) corresponds to the $\text{Zn}_2\text{V}_3\text{O}_7$ compound (Figure 5.12 and Table 5.8).

Table 5.7 Thermochemical Properties of $\{[\text{Zn}(\text{Im})_4][\text{V}_2\text{O}_6]\}_n$.

	T_i (K)	T_f (°C)	T_m (°C)	ΔH (kJ mol ⁻¹)	ΔS (J K ⁻¹ mol ⁻¹)
Phase transition (1st peak)					
1 st cooling	275.86	0.34	1.84	-1.10	-4.00
2 nd cooling	275.97	0.65	1.92	-1.07	-3.90
1 st heating	276.12	5.24	4.05	+1.25	+4.52
2 nd heating	276.12	5.21	4.04	+1.25	+4.52
Decomposition					
2 nd peak	462.86	198.23	193.27	+109.08	+233.94
3 rd peak	503.47	235.93	231.72	+27.73	+54.94
4 th peak	544.92	303.63	293.92	-33.93	-59.85

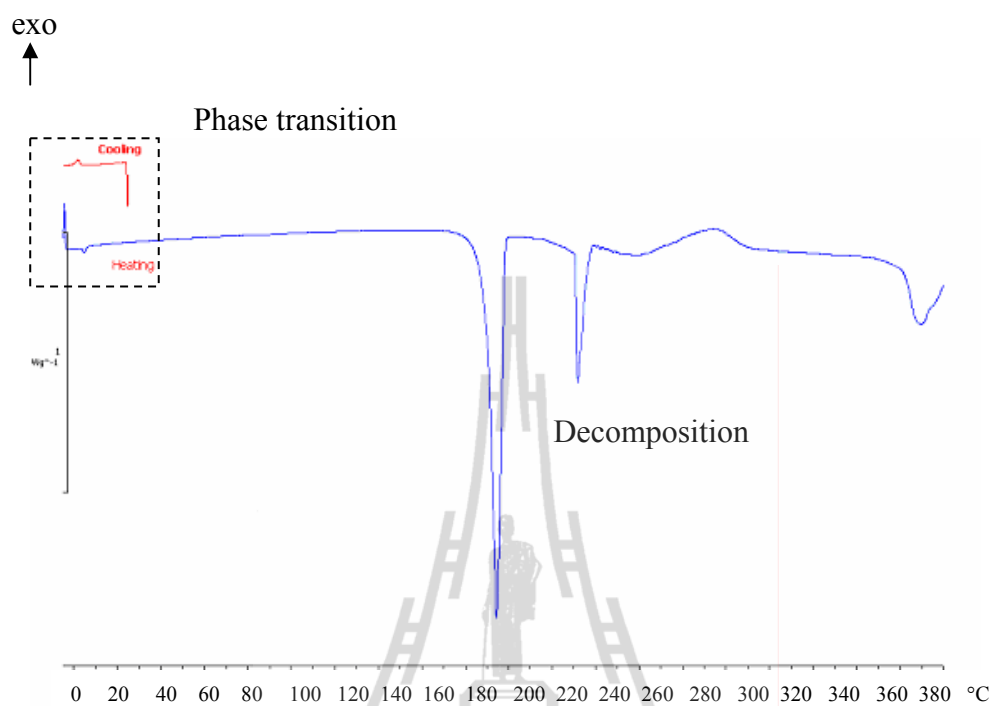


Figure 5.10 DSC curves of $\{[Zn(Im)_4][V_2O_6]\}_n$.

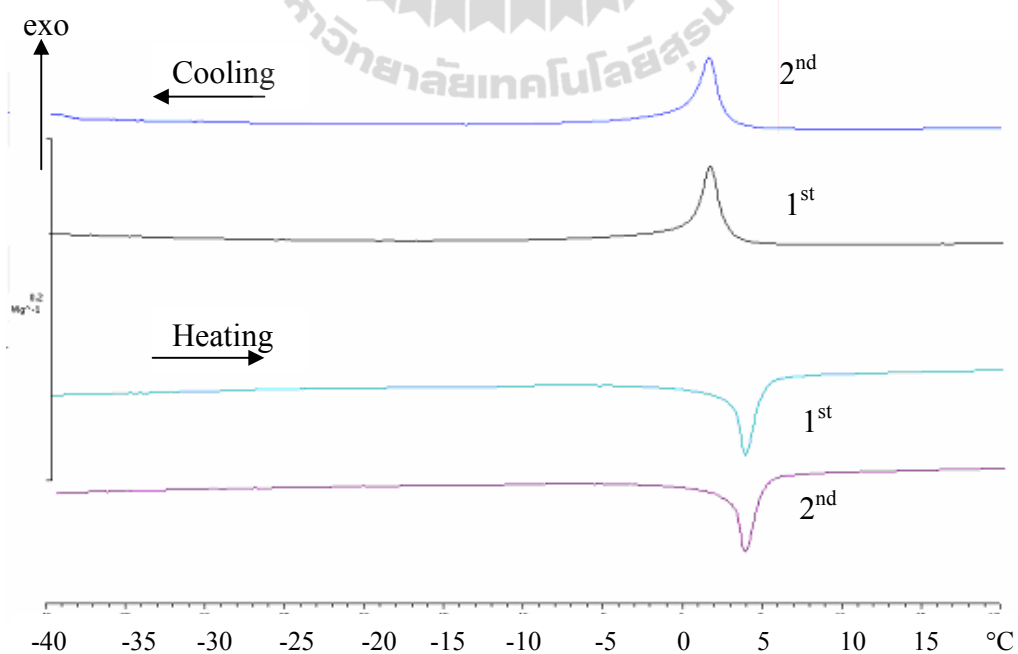


Figure 5.11 DSC curves of $\{[Zn(Im)_4][V_2O_6]\}_n$ with a cooling and heating rate of 5 °C min⁻¹.

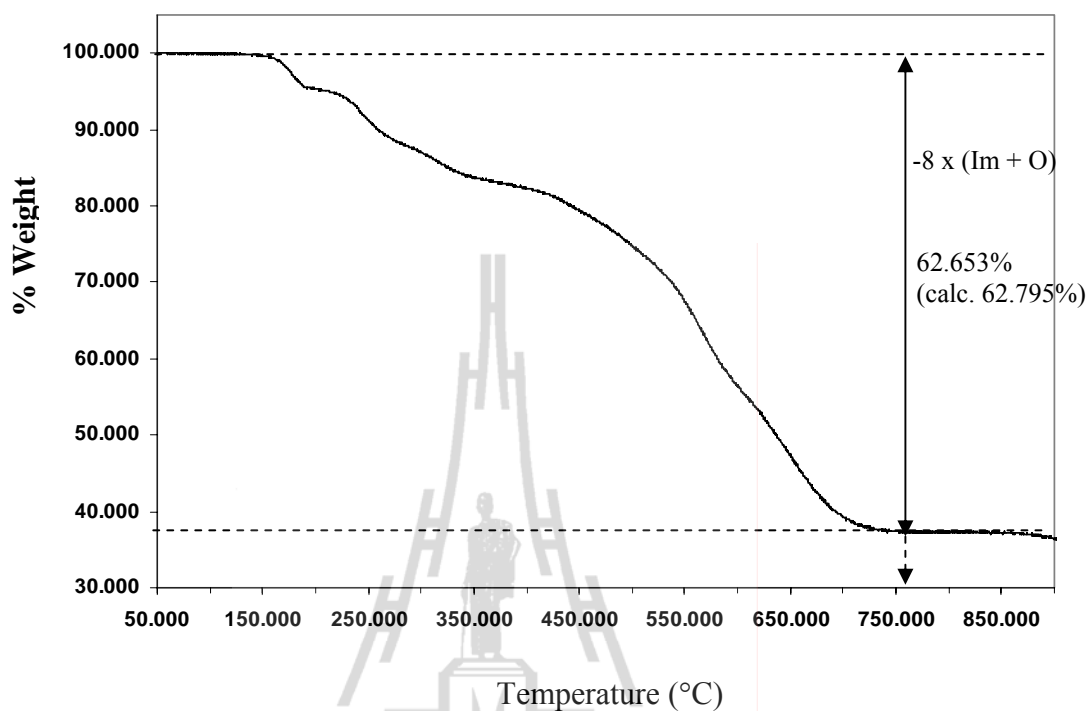


Figure 5.12 TGA curve of $\{[\text{Zn}(\text{Im})_4][\text{V}_2\text{O}_6]\}_n$.

Table 5.8 Decomposition as a Function of Temperature.

	%Weight loss			Temperature (°C)	Composition
	Calc.	Measured	Error		
Decomposition	62.794	62.653	0.141	128.572-751.471	8 x (Im + O)
Residual	36.936	37.347	0.411	>751.471	$\text{Zn}_2\text{V}_3\text{O}_7$

5.4.5 Variable-temperature Infrared Spectroscopy

The results of single crystal X-ray diffraction and DSC are in good agreement with the vibrational spectra using a KBr pellet at room temperature (RT) and in liquid nitrogen (LT). Figure 5.13(c) and Table 5.9 show an additional shoulder of $\nu_s(\text{VO}_2)$ and $\nu_{\text{as}}(\text{V-O-V})$ stretching modes at 948 and 624 cm^{-1} , respectively, and the intensity of

$\nu_{\text{as}}(\text{VO}_2)$ stretching modes at 866, 831, and 755 cm^{-1} increase 14% similar to that seen in KVO_3 , RbVO_3 , CsVO_3 and NH_4VO_3 (Onodera and Ikegami, 1980), $[\text{Ni}(\text{en})_3][\text{VO}_3]_2$ (Liu, Lin, and Lin, 2000) and $[\text{Co}(\text{en})_3][\text{VO}_3]_3 \cdot \text{H}_2\text{O}$ (Khan, Yohannes, Doedens, Golub, and O'Conner, 2005). We suggest that as the temperature decreases, this transition is relevant to the disordered anionic chains transforming order form as observed in NH_4VO_3 (Onodera and Ikegami, 1980; Park and Shurvell, 1989). Figures 5.13(a) and (b), and Table 5.10 show two peaks and a shoulder of the $\nu(\text{NH})$ and $\nu(\text{CH})$ stretching modes in the regions of 3170-3100 cm^{-1} and of 2850-2800 cm^{-1} at RT splitting with minor blue shift of the three peaks at 3153, 3134, and 3115 cm^{-1} , and 2833, 2818, and 2802 cm^{-1} , respectively, and some additional shoulders appear at 2951 and 2747 cm^{-1} and others shift to high frequencies as expected for two additional bifurcated N23-H23...O2/O2A and N33-H33...O12/O12A hydrogen bonds at RT remain one hydrogen bond of each and significantly different weak C-H...O hydrogen bonds between cations and the anions upon cooling.

The bands at 1300-1200 cm^{-1} and 1100-1060 cm^{-1} are comprised of the $\delta(\text{CH})$ bending mode and some additional shoulders at 1276 and 1204 cm^{-1} with blue shift and the intensity of combination $\nu(\text{Ring})$ stretching mode, $\delta(\text{NH})$ and $\delta(\text{CH})$ bending modes at 1105 cm^{-1} increasing by 56% and a peak at 1078 cm^{-1} at RT splits with red shift into two peaks at 1078 and 1075 cm^{-1} as observed the significantly different weaker N/C-H... π hydrogen bond interactions at both temperatures.

Figures C2 and C3 show no evidence of vibrational phase transition mechanism observed using nujol mulls (Appendix C).

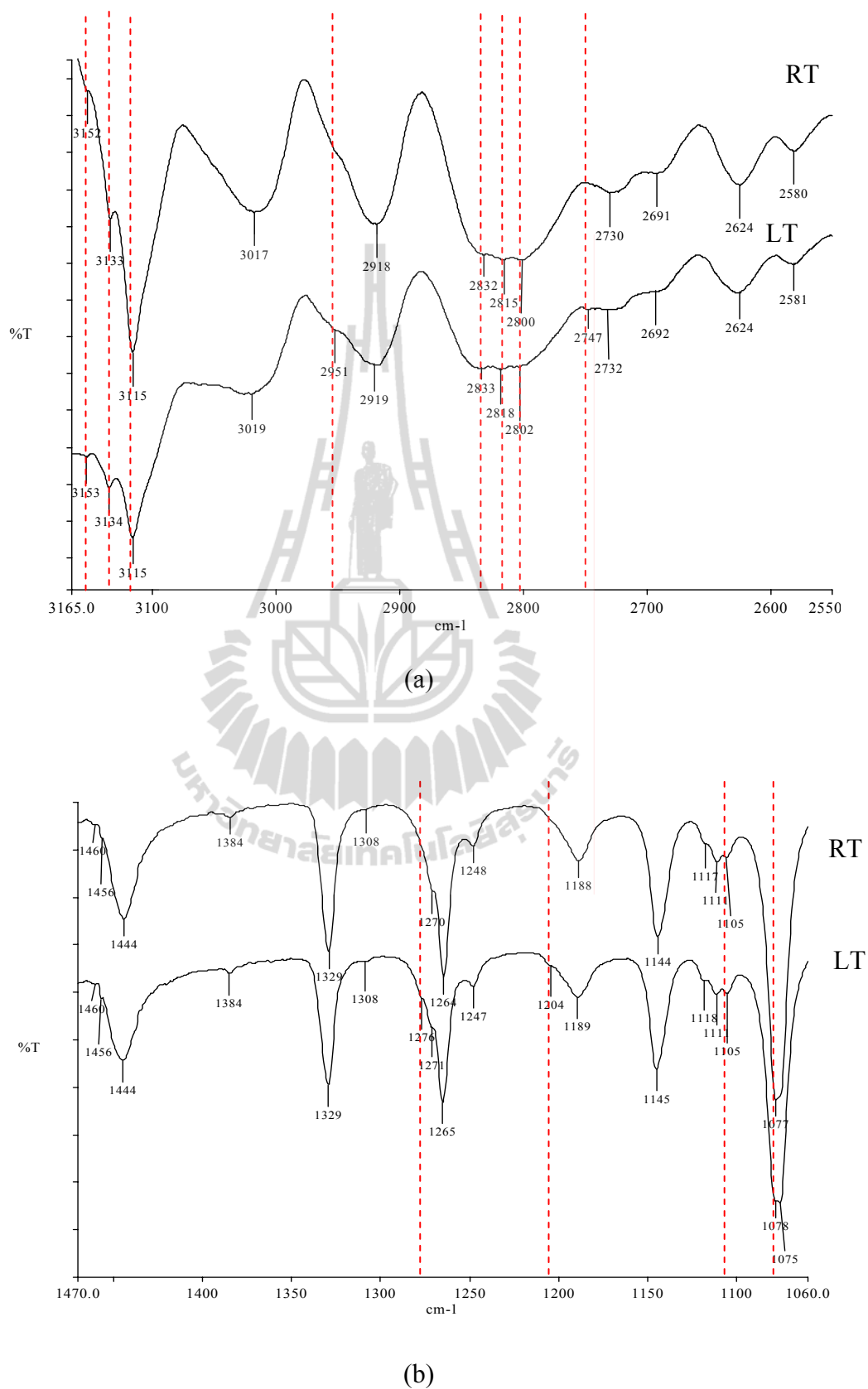


Figure 5.13 The infrared spectra of $\{[Zn(Im)_4][V_2O_6]\}_n$ (pressed KBr pellet).

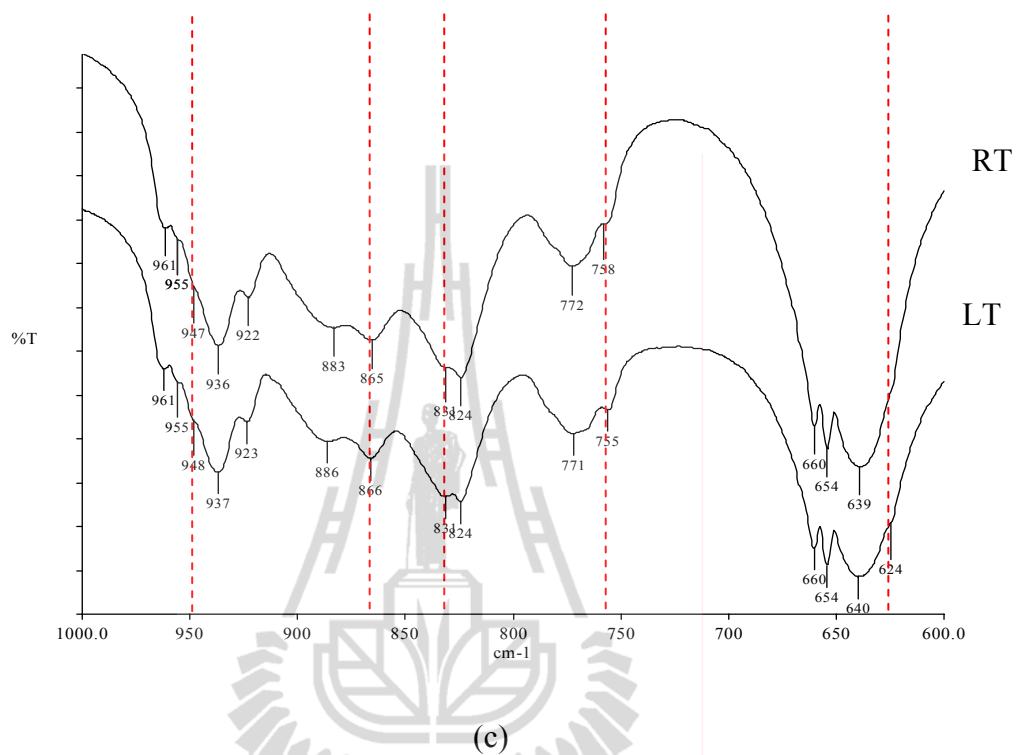


Figure 5.13 (Continued).

Table 5.9 Observed Frequencies (cm^{-1}) and Intensities for the $\{\text{VO}_3\}_n^{n-}$ Chain in MVO_3 .

^b K ⁺	^b Rb ⁺	^b Cs ⁺	^b [NH ₄] ⁺	^c [Ni(en) ₃] ²⁺	^d [Co(en) ₃] _{1/3} ²⁺	[Zn(Im) ₄] ²⁺		^a Assignment
						(This Work)		
						RT	LT	
960 w	957 w					961 vw	961 vw	ν _s (VO ₂)
						955 sh	955 sh	
		948 w			946 s		948 sh	
935 s	935 s		935 s	938		936 s	937 s	
		920 s				922 w	923 w	
890 w	895 w	905 w	895 w	905	908 vs, 891 sh			
						883 vw	886 vw	ν _{as} (VO ₂)
850 s	863 s	860 s	850 s			865 w	866 m	
			840			831 sh	831 vw	
						824 w	824 w	
					797 m	772 m	771 m	
					746 s	758 sh	755 vw	
693 s	685 s	690 s	690 s	655	643 s	660 m,sp	660 m,sp	ν _{as} (V–O–V)
						654 m,sp	654 m,sp	
						639 s	640 s	
							624 sh	
495 w	485 w	475 w	495 w					ν _s (V–O–V)

^aRelative intensities and shape of peak are indicated by vs = very strong, s = strong, m = medium, w = weak, vw = very weak, and sh = shoulder, and sp = shape, respectively.

^bFrom Onodera and Ikegami (1980) at 20 °C.

^cFrom Liu, Lin, and Lin (2000) at 20 °C.

^dFrom Khan, Yohannes, Doedens, Golub, and O'Conner (2005) at 20 °C.

Table 5.10 Observed Frequencies (cm^{-1}) and Intensities for the Imidazole in $[\text{Zn}(\text{Im})_4][\text{X}]_2$.

^b ClO_4	^c ClO_4	^c BF_4	$[\text{V}_2\text{O}_6]^{2-}$ (This Work)		^a Assignment
			RT	LT	
3380					v(NH)
3160			3152 sh	3153 vw	
3145					
3131			3135 vw	3134 vw	v(CH)
	3113	3114	3115 s	3115 s	
			3017 s	3019 m	
				2951 sh	
	2954	2954	2918 s	2916 m	
	2849	2849	2832 sh, 2815, 2800 vw	2833, 2818, 2802 vw	
			2730, 2691 vw	2747 sh, 2725, 2691 vw	
			2624, 2580 w	2624, 2581 w	
1431	1429	1430	1444 s	1444 s	v(Ring)
1331	1329	1329	1329 s	1329 s	
1267	1264	1264	1270 sh, 1264 s	1277, 1270 sh, 1264 s	δ (CH)
1230			1248 vw	1248 vw, 1204 sh	
			1188 m	1188 m	Combinations of
			1144 s	1144 s	v(Ring),
			1118 sh, 1111, 1105 vw	1118 sh, 1111, 1105 vw	δ (NH), and
			1078 vs	1078, 1075 vs	δ (CH)

^aRelative intensities and shape of peak are indicated by vs = very strong, s = strong, m = medium, w = weak, vw = very weak, and sh = shoulder, and sp = shape, respectively.

^bFrom Hodgson, Percy, and Thornton (1980) at 20 °C.

^cFrom Loeffen, Pettifer, and Tomkinson (1996) at 20 °C.

5.5 Conclusions

DSC measurements reveal that a new tetraimidazolezinc(II) metavanadate undergoes a reversible order-disordered phase transition at 2 °C and 4 °C with small enthalpy energy of $\sim 1 \text{ kJ mol}^{-1}$ upon cooling and heating, respectively. Combined single crystal X-ray diffraction and variable-temperature infrared spectroscopy studies at room and low temperatures suggested that the cause of the phase transition at $\sim 3 \text{ }^\circ\text{C}$ due to the order-disorder anionic polymeric chains at the additional inversion centers and the small reorientation of the anions with their skeleton expanded along *c* axis, are driving forces for the small reorientation and rearrangement of a 3-D supramolecular cationic network through different weak C–H \cdots O hydrogen bonding interactions between cations and anions and concerted aryl embraces of weaker *off* N–H $\cdots\pi$, *off* C–H $\cdots\pi$ and *ef* C–H $\cdots\pi$ hydrogen bond interactions among the cations themselves as the temperature increases. Good agreement with the infrared spectra using a KBr pellet pressed at RT and liquid nitrogen temperature is found, otherwise, with nujol mulls no evidence of a phase transition occur over the ranges of 6 °C to $-1 \text{ }^\circ\text{C}$. On the other hand, due to the large size and the hydrogen bond capability of multifunctional groups of imidazole on the zinc tetraimidazole dication, the phase transition is observed from X-ray diffraction, DSC and infrared spectroscopy different to the ammonium monocation in NH_4VO_3 , presented only the strong N–H \cdots O hydrogen bonds and the phase change occurred near $-123 \text{ }^\circ\text{C}$ using Raman spectroscopy or no evidence of any phase transition in NH_4VO_3 due to the total energy changes at 20 °C and $-173 \text{ }^\circ\text{C}$ about $\sim 1.71 \text{ kJ mol}^{-1}$ as relevant to weak C–H \cdots O hydrogen bond interactions by X-ray and synchrotron diffractions.

5.6 References

- Adams, D. M., Haines, J., and Leonard, S. (1991). The pressure-induced disordering of ammonium metavanadate. **Journal of Physics: Condensed Matter**. 3(17): 2859-2865.
- Bauman, J. E., and Wang, J. C. (1964). Imidazole complexes of nickel(II), copper(II), zinc(II), and silver(I). **Inorganic Chemistry**. 3(3), 368-373.
- Becker, M., and Jansen, M. (2001). Zinc cyanamide, Zn(CN₂). **Acta Crystallographica Section C**. 57(4): 347-348.
- Bhosekar, G., Jess, I., Havlas, Z., and Näther, C. (2007). Structures and properties of three polymorphic modifications based on tetrahedral building blocks of dichlorobis(pyridazine-N) zinc(II). **Crystal Growth & Design**. 7(12): 2627-2634.
- Burnett, M. N., and Johnson, C. K. (1996). *ORTEP-III: Oak Ridge Thermal Ellipsoid Plot Program for Crystal Structure Illustration*, Report ORNL-6895, Oak Ridge National Laboratory, Oak Ridge, Tennessee.
- Bürgi, H.-B., and Dunitz, J. D. (1992). **Structure Correlation**. Wiley-VCH, New York. pp. 807-808.
- Chainok, K., Haller, K. J., Rae, A. D., Willis, A. C., and Williams, I. D. (2011). Investigation of the structure and phase transitions of the polymeric inorganic-organic hybrids: [M(Im)₄V₂O₆]_∞, M = Mn, Ni, Co; Im = imidazole. **Acta Crystallographica Section B**. 67(1): 41-52.
- Chen, L.-Z., Zhao, H., Ge, J.-Z., Xiong, R.-G., and Hu, H.-W. (2009). Observation of deuteration effects in co-crystal system: hexamethylenetetraminium 3,5-dinitrobenzoate hemideuterated water. **Crystal Growth & Design**. 9(9):

3828-3831 and reference therein.

Choi, M.-H., Kim, S.-H., Chang, H.-Y., Halasyamani, P. S., and Ok, K. M. (2009).

New noncentrosymmetric material-[N(CH₃)₄]ZnCl₃: polar chains of aligned ZnCl₄ tetrahedra. **Inorganic Chemistry**. 48(17): 8376-8382.

Cotton, F. A., Wilkinson, G., Murillo, C. A., and Bochmann, M. (1998). **Advanced Inorganic Chemistry**. 6th edition, John Wiley & Sons, Inc., New York. pp. 715-958.

DeBord, J. R. D., Zhang, Y., Haushalter, R. C., Zubieta, J., and O'Connor, C. J. (1996). One-dimensional vanadium oxide chains containing covalently bound copper coordination complexes: hydrothermal synthesis and characterization of Cu(en)[VO₃]₂, Cu(2,2'-bipy)[VO₃]₂, and Cu(2,2'-bipy)₂[VO₃]₂. **Journal of Solid State Chemistry**. 122(2): 251-258.

Guthrie, J. P., and Pike, D. C. (1987). Hydration of acylimidazoles: tetrahedral intermediates in acylimidazole hydrolysis and nucleophilic attack by imidazole on esters. The question of concerted mechanisms for acyl transfers. **Canadian Journal Chemistry**. 65(8): 1951-1969.

Haller, K. J., Johnson, P. L., Feltham, R. D., Enemark, J. H., Ferraro, J. R., and Basile, L. J. (1979). Effects of temperature and pressure on the molecular and electronic structure of N,N'-ethylenebis(salicylideneiminato)nitrosyliron, Fe(NO)(salen). **Inorganica Chimica Acta**. 33(1): 119-130.

Hawthorne, F. C. and Calvo, C. (1977). The crystal chemistry of the M⁺VO₃ (M⁺ = Li, Na, K, NH₄, Tl, Rb, and Cs) pyroxenes. **Journal of Solid State Chemistry**. 22(1): 157-170.

Hodgson, J. B., Percy, G. C., and Thornton, D. A. (1980). The infrared spectra of

imidazole complexes of first transition series metal(II) nitrates and perchlorates. **Journal of Molecular Structure.** 66(1): 81-92.

Ishii, D., Yaamada, T., Nakagawa, M., Iyoda, T., and Yoshida, H. (2006). Thermally induced structural transformation in a hydrogen-bonded supramolecular single-crystal DSC-FT-IR studies. **Journal of Thermal Analysis and Calorimetry.** 86(3): 681-685.

Jian, M., Zhu, L., Wang, J., Zhang, J., Li, G., and Hu, C. (2006). Sodium metavanadate catalyzed direct hydroxylation of benzene to phenol with hydrogen peroxide in acetonitrile medium. **Journal of Molecular Catalysis A: Chemical.** 253(1-2): 1-7.

Jiménez, P., Roux, M. V., and Turrión, C. (1987). Thermochemical properties of N-heterocyclic compounds. I. Enthalpies of combustion, vapour pressures and enthalpies of sublimation, and enthalpies of formation of pyrazole, imidazole, indazole, and benzimidazole. **Journal of Chemical Thermodynamics.** 19(9): 985-992.

Khan, M. I., Yohannes, E., Doedens, R. J., Golub, V. O., and O'Conner, C. J. (2005). Templated synthesis of a chiral solid: Synthesis and characterization of $[\text{Co}(\text{en})_3][\text{VO}_3]_3 \cdot \text{H}_2\text{O}$, containing a new type of chiral vanadium oxide chain. **Inorganic Chemistry Communication.** 8(9): 841-845.

Krachodnok, S., Haller, K. J., and Williams, I. D. (2011). Hydrothermal synthesis and crystal structures of hybrid organic-inorganic materials of divalent metal vanadates. (*unpublished results*).

Law, T. S.-C., and Williams I. D. (2000). Organic-directed synthesis of manganese vanadates with variable stoichiometry and dimensionality: 1-D

[(Hen)₂Mn(VO₃)₄], 2-D [(H₂en)₂[Mn(VO₃)₄], and 3-D [(H₂en)[MnF(VO₃)₃].

Chemistry of Materials. 12(1): 2070-2072.

- Li, G., Pang, S., Jiang, L., Guo, Z., and Zhang, Z. (2006). Environmentally friendly chemical route to vanadium oxide single-crystalline nanobelts as a cathode material for lithium-ion batteries. **The Journal of Physical Chemistry B.** 110(19): 9383-9386.
- Liu, G., and Greedan, J. E. (1995). Magnetic properties of fresnoite-type vanadium oxides: M₂V₃O₈ (M = K, Rb, NH₄). **Journal of Solid State Chemistry.** 114(1): 499-505.
- Liu, S.-X., Lin, B.-Z., and Lin, S. (2000). Hydrothermal synthesis and characterization of metavanadate containing spiral chain: [Ni(en)₃][VO₃]₂. **Inorganic Chimica Acta.** 304(1): 33-37.
- Loeffen, P. W., Pettifer, R. F., and Tomkinson, J. (1996). Vibrational force field of zinc tetraimidazole from inelastic neutron scattering. **Chemical Physics.** 208(3): 403-420.
- Muller, C., Valmalette, J.-C., Soubeyroux, J.-L., Bouree, F., and Gavarri, J.-R. (2001). Structural disorder and ionic conductivity in LiVO₃: a neutron powder diffraction study from 340 to 890 K. **Journal of Solid State Chemistry.** 156(2): 379-389.
- Nakajima, T., Isobe, M., Tsuchiya, T., Ueda, Y., and Kumagai, T. (2009). A revisit of photoluminescence property for vanadate oxides MVO₃ (M: K, Rb and Cs) and M₃V₂O₈ (M: Mg and Zn). **Journal of Luminescence.** 129(12): 1598-1601.
- Oka Y., Yao, T., and Yamamoto, N. (1997). Hydrothermal synthesis and structure refinements of alkali-metal trivanadates MV₃O₈ (M = K, Rb, Cs). **Material**

Research Bulletin. 32(9): 1201-1209.

Onodera, S., and Ikegami, Y. (1980). Infrared and Raman spectra of ammonium, potassium, rubidium, and cesium metavanadates. **Inorganic Chemistry.** 19(3): 615-618.

Park, Y.S., and Shurvell, H. F. (1989). The Raman spectrum of ammonium metavanadate. **Journal of Raman Spectroscopy.** 20(10): 673-681.

Puntharod, R., Webster, G. T., Asghari-Khiavi, M., Bambery, K. R., Safinejad, F., Rivadehi, S., Langford, S. J., Haller, K. J., and Wood, B. R. (2010). Supramolecular Interactions playing an integral role in the near-infrared Raman “excitonic” enhancement observed in β -Hematin (malaria pigment) and other related heme derivatives. **The Journal of Physical Chemistry B.** 114(3): 12104-12115.

Riou, D., and Férey, G. J. (1996). Hydrothermal synthesis and structure determination of 1,4-diamonobutane metavanadate. **Journal of Solid State Chemistry.** 124(1): 151-154.

Seo, D.-K., and Whangbo, M.-H. (1996). Origin of the structural phase transitions and the anomalous electrical and magnetic properties of the magnetic metal $\text{NaV}_6\text{O}_{11}$. **Journal of the American Chemical Society.** 118(16): 3951-3958.

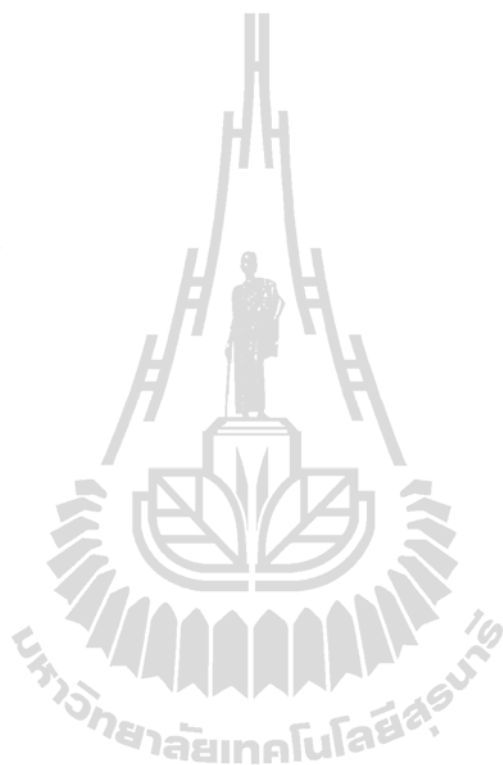
Sheldrick, G.M. (1997). *SHELX-97 Program for the Solution and Refinement of Crystal Structures*, University of Göttingen, Germany.

Shen, Z. X., Ong, C. W., Kuok, M. H., and Tang, S. H. (1995). High-pressure phase transitions and pressure-induced amorphization in LiVO_3 . **Journal of Physics: Condensed Matter.** 7(5): 939-946.

Somphon, W., Haller, K. J., Rae, A. D., and Ng, S. W. (2006). Packing and polytypism

- in 1,10-phenanthroline-1-ium(2-carboxyethyl)(2-carboxylatoethyl)dichlorostannate(IV). **Acta Crystallographica Section B**. 62(3): 255-261.
- Somphon, W., Haller, K. J., and Rae, A. D., (2011). The Order-Disorder Phase Transition of Polymeric $[\text{Ag}(\text{bipy})\text{NO}_3]_n$. **Acta Crystallographica Section B**. for publication.
- Smrcčok, L', Bitschnau, B., and Filinchuk, Y. (2009). Low temperature powder diffraction and DFT solid state computational study of hydrogen bonding in NH_4VO_3 . **Crystal Research and Technology**. 44(9): 978-984.
- Ulicka, L., Pavelcik, F., and Huml, K. (1987). Structure of barium metavanadate monohydrate. **Acta Crystallographica Section C**. 439(12): 2266-2268.
- Waal, D. D., and Heyns, A. M. (1990). Infrared spectra of the ammonium ion in ammonium metavanadate NH_4VO_3 . **Spectrochimica Acta**. 46A(11): 1639-1648.
- Wéry, A. S. J., Gutiérrez-Zorrilla, J. M., Luque, A., Ugalde, M., and Raman, P. (1996). Phase transitions in metavanadates. Polymerization of tetrakis(tert-butylammonium)-cycle-tetrametavanadate. **Chemistry of Materials**. 8(1): 408-413.
- Xiaochun, H., Dan, L. Yexiang, T., and Xiaoming, C. (1998). Synthesis and crystal structure of $[\text{Zn}(\text{Im})_2]_n$. **Acta Scientiarum Naturalium Universitatis Sunyatseni**. 37(1): 55-58.
- Yang, H., Li, J., Zhang, X.-G., and Jin, Y.-L. (2008). Synthesis of LiV_3O_8 nanocrystallites as cathode materials for lithium ion batteries. **Journal of Materials Processing Technology**. 207(1-3): 265-270.
- Ye, H.-Y., Chen, L.-Z., and Xiong, R.-G. (2010). Reversible phase transition of

pyridine-3-carboxylic acid perchlorate. **Acta Crystallographica Section B.**
66(3): 387-395.



CHAPTER VI

CONCLUSIONS

6.1 Conclusions

The successful syntheses of helical chiral network or open framework structures offer a fascinating example of hybrid organic-inorganic materials.

Five new hybrid organic-inorganic vanadate compounds, namely (en)Zn₂V₂O₇, (en)Zn(VO₃)₂, (Hen)₂Cd(VO₃)₄, (HenMe)₂Zn(V₂O₅)₄, and (enMe)₂Zn(VO₃)₂·2H₂O (en = ethylenediamine and enMe = propane-1,2-diamine), were isolated from the hydrothermal reaction at 110 °C of V₂O₅-M(OAc)₂-H₂O system (M = Zn, Cd) in a mole ratio of 1:1:111 with varied amounts of en and enMe, and reaction pH.

The (en)Zn₂V₂O₇ structure consists of a layer structure composed of polymeric helical chains of –vanadium tetrahedra–zinc trigonal bipyramids– as the inner strand and –zinc tetrahedra–en–zinc trigonal bipyramids– as the outer strand pitched together with zinc sites and propagated by a 2₁ screw axis. The layers are further linked through the VO₄ pillars forming a 3-D chiral helical network, the flexibility of the en bridging ligand is essential for formation of the helix with shows high thermal stability of 283 °C, even through its thermal stability is lower than (en)Mn₂V₂O₇ by about 33 °C with en acting as pillars.

(HenMe)₂Zn(V₂O₅)₄ exhibits mixed-valence [(V⁴⁺O)(V⁵⁺O₄)]₅ layers which are composed of a combination of an equal number of V⁵⁺O₄ tetrahedra and V⁴⁺O₅ square pyramids perpendicular to the *b* axis. The layers are linked together with the pillared

zinc octahedral complexes forming an open 3-D framework with exhibits a high thermal stability of 338 °C.

The others, $(\text{Hen})_2\text{Cd}(\text{VO}_3)_4$, $(\text{en})\text{Zn}(\text{VO}_3)_2$, and $(\text{enMe})_2\text{Zn}(\text{VO}_3)_2 \cdot 2\text{H}_2\text{O}$, are composed of polymeric metavanadate chains with corner-sharing VO_4 tetrahedra propagation along the chain axis. The metavanadate chains are cross-linked with the metal octahedral complex linkers forming 1-D double chains, 2-D double layers, and an open 3-D framework. The double chains of $(\text{Hen})_2\text{Cd}(\text{VO}_3)_4$ and the layers of $(\text{en})\text{Zn}(\text{VO}_3)_2$ are further hydrogen bonded, $\text{N}-\text{H}\cdots\text{O}$ interactions, to neighbors producing a 2-D supramolecular layer and a 3-D supramolecular network. Furthermore, $\text{O}-\text{H}\cdots\text{O}$ hydrogen bond interactions with a $R_4^3(10)$ motif are found between water molecules and framework in $(\text{enMe})_2\text{Zn}(\text{VO}_3)_2 \cdot 2\text{H}_2\text{O}$.

Addition of alkali metal salts into the same system, three neutral and one mixed-valence layered alkali metal trivanadate compounds, $\text{M}_x\text{V}_3\text{O}_8$ (M = alkali metal), have been prepared in high yield and high crystallinity at lower reaction temperatures than previously reported in neutral media at 110 °C for 2 days for $x = 1$ and $\text{M} = \text{K}, \text{Rb}, \text{Cs}$ and in basic media at 140 °C for 2 days for $x = 2$ and $\text{M} = \text{K}$. Unreacted $\text{Zn}(\text{OAc})_2$ may act as catalyst or HOAc/OAc^- acts as a buffer and product yields increase with increasing reaction temperature up to 200 °C in obtaining of monopotassium salts and enMe acts to adjust pH and as a reducing agent in producing the dipotassium salt. The yield of the dipotassium salt decreased with black crystals of $(\text{HenMe})_2\text{Zn}(\text{V}_2\text{O}_5)_4$ and the colorless needles of $\text{K}_2\text{ZnV}_2\text{O}_7$ also formed when doubling the mole ratio of zinc salt and heating at 110 °C. The MV_3O_8 ($\text{M} = \text{K}, \text{Rb}, \text{Cs}$) crystallize in the monoclinic space group $P2_1/m$ and are layers composed of corner-sharing VO_6 octahedra and V_2O_8 units, two edge-sharing VO_5 square pyramids.

The $\text{K}_2\text{ZnV}_2\text{O}_7$ crystallizes in a tetragonal space group $P4_2/mnm$. The $\text{K}_2\text{ZnV}_2\text{O}_7$ unit cell parameters are different from the known $\text{K}_2(\text{VO})\text{V}_2\text{O}_7$ structure with approximate doubling of the c axis while the ab plane is constant when replacing the VO_5 square pyramids of the $[(\text{V}^{4+}\text{O})\text{V}^{5+}_2\text{O}_7]^{2-}$ layer with the distorted ZnO_4 tetrahedra, and relative orientation of all vanadyl bonds of the $\text{K}_2(\text{VO})\text{V}_2\text{O}_7$ layer are in the same direction while only vanadyl groups of pyrovanadates of the $\text{K}_2\text{ZnV}_2\text{O}_7$ layer are alternating two up and two down. In addition, the different potassium crystallographic independent sites and coordination environments are one with pentagonal antiprismatic KO_{10} , and two with distorted square prismatic KO_8 coordination environments, respectively. The connections and orientations of the vanadyl and vanadate groups from structural analysis are in good agreement with infrared results.

Use of the planar cyclic diamine, imidazole (Im), in the synthesis gave a high yield of a new polymeric metavanadate, $\{[\text{Zn}(\text{Im})_4][\text{V}_2\text{O}_6]\}_n$. DSC measurements reveal a new $\{[\text{Zn}(\text{Im})_4][\text{V}_2\text{O}_6]\}_n$ undergoes a reversible ordered-disordered phase transition at 2 °C (exothermic transition) and 4 °C (endothermic transition) with a small enthalpy energy of $\sim 1 \text{ kJ mol}^{-1}$ and a small entropy of $\sim 4 \text{ J mol}^{-1} \text{ K}^{-1}$ upon cooling and heating. Combined single crystal X-ray diffraction studies shows the structure consists of anionic polymeric metavanadate chains and cationic $[\text{Zn}(\text{Im})_4]^{2+}$ complexes are between the anions with an ordered triclinic $P\bar{1}$ phase at $-173(2) \text{ }^\circ\text{C}$ and a disordered triclinic $P\bar{1}$ phase at $20(2) \text{ }^\circ\text{C}$ (the c axis half of $-173 \text{ }^\circ\text{C}$). The reorientation of anions and skeleton expansion/contraction along the c axis. The small rearrangement of the 3-D supramolecular cationic network through weak $\text{C-H}\cdots\text{O}$ hydrogen bonding interactions between cations and anions and concerted aryl embraces of weaker *off* $\text{N-H}\cdots\pi$, *off*

and *ef* C–H... π hydrogen bond interactions among the cations themselves as the phase transition occurs. The different interactions correlate with the differences in the variable-temperature infrared spectra.

Due to the hydrogen bonded capabilities of multifunctional groups of imidazole on the zinc tetraimidazole dication, thus, the phase transition with small total energy change can be observed through weaker supramolecular interactions by using single crystal X-ray diffraction, DSC and infrared spectroscopy. Comparison with NH_4VO_3 which shows only strong N–H...O hydrogen bonds and a phase change near $-123\text{ }^\circ\text{C}$ using Raman spectroscopy or no evidence of any phase transition in NH_4VO_3 due to the total energies changes at $20\text{ }^\circ\text{C}$ and $-173\text{ }^\circ\text{C}$ about $\sim 1.71\text{ kJ mol}^{-1}$ as relevant to weak C–H...O hydrogen bond interactions by X-ray and Synchrotron diffractions.

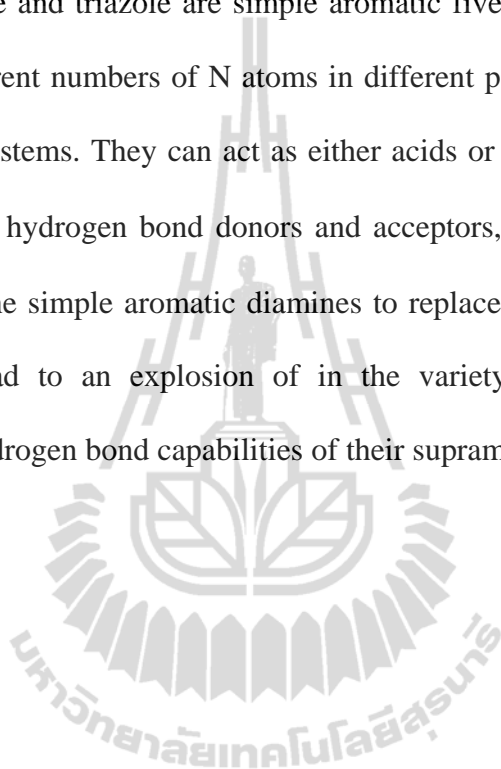
6.2 Suggestions for the Further Work

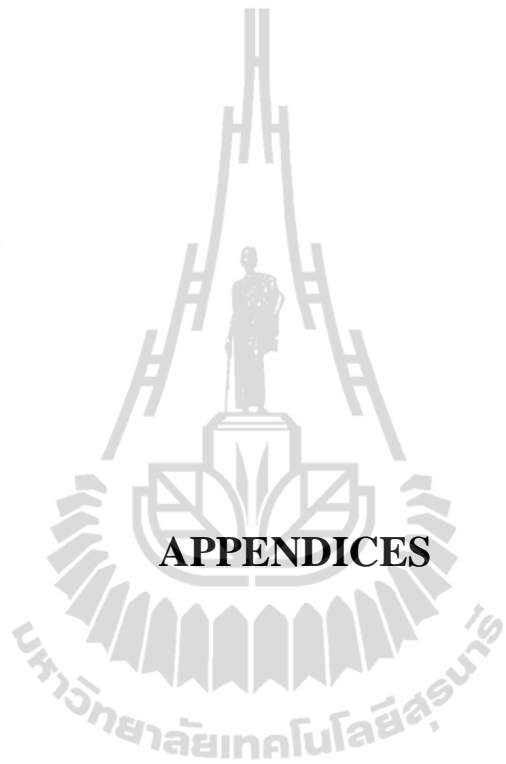
The exploration of layered mixed-metal vanadium oxide and hybrid organic-inorganic main group vanadates with potential applications for light emitting devices, cathode materials for Li-ion batteries, and magnetism have resulted in considerable interest. Therefore, we will further study those properties by photoluminescence, electrochemical measurement, and magnetic susceptibility.

Many critical parameters can be affected for isolating the desired product under hydrothermal conditions with pure phase and high product yield. Such as the kind of reagent source and the mole ratio of reagents, the reaction pH, temperature and times.

Additional syntheses with varied reaction temperature and time and the mole ratio of metal sources could be possible to obtain the pure phase compounds of $\text{K}_2\text{ZnV}_2\text{O}_7$, $(\text{en})\text{Zn}(\text{VO}_3)_2$ and $(\text{Hen})_2\text{Cd}(\text{VO}_3)_4$ with high yield.

Consider the chemistry of organic reagents, for example, their shapes, geometries, and conformations, and their pK_a or pK_b , affect the design and controlling synthesis of hybrid organic-inorganic materials. The aromatic diamines such as imidazole, pyrazole and triazole are simple aromatic five-membered heterocyclic ring systems with different numbers of N atoms in different positions that are important in many biological systems. They can act as either acids or bases. They are planar, rigid systems, and good hydrogen bond donors and acceptors, and weak π hydrogen bond acceptors. Using the simple aromatic diamines to replace the chain-aliphatic diamines is expected to lead to an explosion of in the variety of structures utilizing the multifunctional hydrogen bond capabilities of their supramolecular interactions.





APPENDICES

APPENDIX A

SUPPORTING INFORMATION CHAPTER III

Table A1 Atomic Coordinates ($\times 10^4$) and Equivalent Isotropic Displacement Parameters ($\text{\AA}^2 \times 10^3$) for **3a**. $U(\text{eq})$ is Defined as One Third of the Trace of the Orthogonalized U^{ij} Tensor.

	x	y	z	$U(\text{eq})$
Zn(1)	-5401(1)	3760(1)	2656(1)	16(1)
Zn(2)	2285(1)	1564(1)	7385(1)	15(1)
V(1)	3812(1)	5596(1)	8983(1)	11(1)
V(2)	-252(1)	7892(1)	6935(1)	12(1)
O(1)	1377(5)	6443(5)	8427(4)	18(1)
O(2)	-1623(5)	8791(5)	7982(4)	16(1)
O(3)	1226(5)	-809(4)	6532(5)	23(1)
O(4)	4954(5)	509(4)	8698(4)	16(1)
O(5)	3570(5)	3820(5)	8170(4)	22(1)
O(6)	1840(5)	2022(4)	4921(4)	19(1)
O(7)	5182(5)	6641(5)	8116(4)	20(1)
N(1)	345(6)	1867(5)	8631(5)	14(1)
C(2)	-1214(7)	3090(7)	7952(6)	19(1)
C(3)	-2782(7)	2664(6)	6179(6)	18(1)
N(4)	-4102(6)	4015(5)	5294(5)	16(1)

Table A2 Atomic Coordinates ($\times 10^4$) and Equivalent Isotropic Displacement Parameters ($\text{\AA}^2 \times 10^3$) for **3b**. $U(\text{eq})$ is Defined as One Third of the Trace of the Orthogonalized U_{ij} Tensor.

	x	y	z	$U(\text{eq})$
Zn(1)	9439(1)	5524(1)	3371(1)	9(1)
V(1)	7970(1)	3773(1)	2613(1)	7(1)
V(2)	2514(1)	4389(1)	1043(1)	8(1)
O(1)	8126(3)	2988(1)	3573(2)	12(1)
O(2)	8685(3)	4426(1)	4119(2)	9(1)
O(3)	5080(3)	3864(1)	1591(2)	12(1)
O(4)	136(3)	3779(1)	1175(2)	11(1)
O(5)	2371(3)	4715(1)	-904(2)	12(1)
O(6)	2352(3)	5069(1)	2425(2)	10(1)
C(1)	6411(4)	6699(2)	4203(3)	13(1)
C(2)	7581(4)	6987(2)	2733(3)	13(1)
N(1)	6330(4)	5889(1)	4148(3)	10(1)
N(2)	9869(4)	6625(1)	2779(3)	12(1)

Table A3 Atomic Coordinates ($\times 10^4$) and Equivalent Isotropic Displacement Parameters ($\text{\AA}^2 \times 10^3$) for **3c**. $U(\text{eq})$ is Defined as One Third of the Trace of the Orthogonalized U_{ij} Tensor.

	x	y	z	$U(\text{eq})$
Cd(1)	0	0	5000	33(1)
V(1)	-2170(2)	1782(1)	3473(2)	31(1)
V(2)	2240(2)	1148(1)	1937(2)	32(1)
O(1)	-1448(11)	1196(3)	5023(7)	39(1)
O(2)	2227(12)	453(3)	3200(8)	42(1)
O(3)	-4773(11)	1473(4)	2170(8)	44(2)
O(4)	-2637(12)	2572(3)	4220(9)	49(2)
O(5)	236(10)	1854(3)	2398(8)	38(1)
O(6)	1360(11)	847(3)	102(7)	42(1)
N(1)	2860(13)	310(4)	7152(8)	35(2)
N(2)	7683(13)	1734(4)	7942(9)	36(2)
C(1)	4133(15)	988(5)	6934(11)	38(2)
C(2)	6179(14)	1126(4)	8346(10)	35(2)

Table A4 Atomic Coordinates ($\times 10^4$) and Equivalent Isotropic Displacement Parameters ($\text{\AA}^2 \times 10^3$) for **3d**. $U(\text{eq})$ is Defined as One Third of the Trace of the Orthogonalized U_{ij} Tensor.

	x	y	z	$U(\text{eq})$
Zn(1)	0	10000	10000	11(1)
V(1)	2842(2)	8060(1)	10854(1)	14(1)
V(2)	8125(2)	7217(1)	11428(1)	16(1)
V(3)	12133(3)	7650(1)	13210(1)	17(1)
V(4)	7437(2)	8031(1)	8859(1)	14(1)
O(1)	2230(11)	9111(4)	10870(5)	20(1)
O(2)	7560(11)	6211(4)	11405(5)	23(2)
O(3)	12789(11)	8653(4)	13310(5)	22(2)
O(4)	4688(10)	8065(4)	8249(5)	19(2)
O(5)	1289(10)	7471(4)	11667(5)	17(1)
O(6)	2248(10)	7695(4)	9630(5)	21(2)
O(7)	5601(10)	7953(4)	11389(5)	19(1)
O(8)	8937(10)	7452(4)	12959(5)	19(1)
O(9)	7802(10)	7476(5)	9973(5)	22(2)
O(10)	1795(11)	10954(4)	10930(5)	19(1)
N(1)	2273(15)	10082(8)	8987(7)	26(2)
N(2)	5099(13)	9921(6)	7445(6)	20(2)
C(1)	1430(19)	10120(9)	7869(8)	28(3)
C(2A)	2870(20)	10347(14)	7181(11)	65(5)
C(2B)	2740(60)	9720(20)	7110(30)	52(8)
C(3)	1910(18)	10196(9)	6044(8)	33(3)

Table A5 Atomic Coordinates ($\times 10^4$) and Equivalent Isotropic Displacement Parameters ($\text{\AA}^2 \times 10^3$) for **3e**. $U(\text{eq})$ is Defined as One Third of the Trace of the Orthogonalized U_{ij} Tensor.

	x	y	z	$U(\text{eq})$
Zn(1)	2589(1)	3956(1)	7578(1)	14(1)
V(1)	5230(1)	5584(1)	8429(1)	11(1)
V(2)	-322(1)	2542(1)	6550(1)	11(1)
O(1)	6737(2)	5522(2)	8180(3)	27(1)
O(2)	-1653(3)	3178(2)	6567(2)	27(1)
O(3)	4523(2)	4541(2)	8113(2)	22(1)
O(4)	5000	5916(3)	10000	20(1)
O(5)	794(3)	3249(2)	7129(3)	35(1)
O(6)	-549(2)	1474(2)	7446(2)	21(1)
O(7)	0	2223(3)	5000	26(1)
N(1)	3211(3)	2621(2)	8396(3)	17(1)
N(2)	1916(3)	4206(2)	9375(3)	19(1)
N(3)	1946(3)	5302(2)	6824(3)	16(1)
N(4)	3209(3)	3752(2)	5767(3)	18(1)
C(1)	3155(4)	2729(3)	9752(3)	20(1)
C(2)	1930(4)	3265(3)	10017(4)	24(1)
C(3)	3222(4)	1776(3)	10459(4)	22(1)
C(4)	1961(4)	5226(3)	5465(3)	19(1)
C(5)	3176(4)	4705(3)	5144(3)	20(1)
C(6)	1833(4)	6182(3)	4803(4)	21(1)
O(1W)	9367(3)	4996(2)	8037(3)	24(1)
O(2W)	5688(3)	3009(2)	6939(3)	22(1)

Table A6 XRD Pattern Searching from PDF Database Library.**Pattern: 00-049-0805 Fe_{0.02}V₂O₅^a**

2θ (°)	^b _i	<i>h</i>	<i>k</i>	<i>l</i>	Comments
15.344	10	2	0	0	Strongest line.
20.352	100	0	0	1	
21.765	15	1	0	1	
26.189	45	1	1	0	
30.917	40	4	0	0	
32.412	10	0	1	1	
34.331	20	3	1	0	
41.384	20	0	0	2	
42.195	10	1	0	2	
47.228	10	6	0	0	
51.285	20	0	2	0	

^aMaingot, S., Baddour, R., Pereira-Ramos, J., Baffier, N., and Willmann, P. (1993). A new iron V₂O₅ bronze as electrode material for rechargeable lithium Batteries. **Journal of Electrochemical Society**. 140(11): L158-L160.

^bRelative intensity.

Pattern: 01-089-0610 Mg_{0.01}V₂O₅^a (Orthorhombic, *Pmn*2₁)

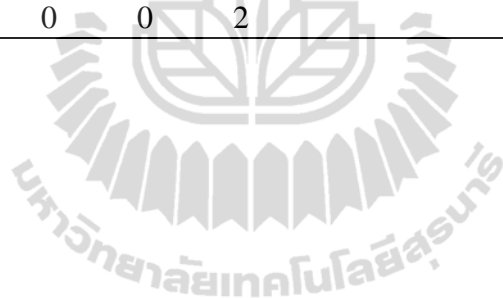
2θ (°)	^b _i	<i>h</i>	<i>k</i>	<i>l</i>	Comments
15.339	448	2	0	0	Strongest line.
20.244	999	0	1	0	
21.671	311	1	1	0	
25.497	44	2	1	0	
26.079	720	1	0	1	
30.961	504	3	1	0	Line with multiple indexes.
30.961	504	4	0	0	
32.294	248	0	1	1	

^aShklover, V., Haibach, T., Ried, F., Nesper, R., and Novak, P. (1996). Crystal structure of the product of Mg²⁺ insertion into V₂O₅ single crystals. **Journal of Solid State Chemistry**. 123(2): 317-323. Calculated from ICSD using POWD-12++.

^bRelative intensity.

Pattern: 01-089-0610 Mg_{0.01}V₂O₅ (Continued).

2θ (°)	i	h	k	l	Comments
33.236	89	1	1	1	
34.213	267	3	0	1	
35.933	29	2	1	1	
37.274	28	4	1	0	
40.077	5	3	1	1	
41.157	110	0	2	0	
41.927	57	1	2	0	
44.169	6	2	2	0	
44.308	3	5	1	0	
45.345	115	4	1	1	
46.806	7	5	0	1	
47.202	163	6	0	0	
47.720	97	3	2	0	
48.700	87	0	2	1	
49.376	24	1	2	1	
51.069	162	0	0	2	



APPENDIX B

SUPPORTING INFORMATION CHAPTER IV

Table B1 Anisotropic Displacement Parameters ($\text{\AA}^2 \times 10^3$) for CsV_3O_8 . The Anisotropic Displacement Factor Exponent Takes the Form: $-2\pi^2[h^2a^{*2}U^{11} + \dots + 2hka^*b^*U^{12}]$.

	U^{11}	U^{22}	U^{33}	U^{23}	U^{13}	U^{12}
Cs(1)	7(1)	12(1)	23(1)	0	1(1)	0
V(1)	3(1)	7(2)	20(2)	0	1(1)	0
V(2)	3(1)	6(1)	22(1)	-1(1)	2(1)	0(1)
O(1)	7(3)	2(3)	22(4)	-1(3)	-1(2)	0(2)
O(2)	8(5)	4(6)	19(6)	0	-4(3)	0
O(3)	5(5)	11(6)	16(6)	0	-3(4)	0
O(4)	8(3)	11(4)	18(4)	0(3)	4(2)	2(2)
O(5)	10(3)	9(4)	26(4)	1(3)	4(3)	-1(2)

Table B2 Anisotropic Displacement Parameters ($\text{\AA}^2 \times 10^3$) for $\text{K}_2\text{ZnV}_3\text{O}_8$. The Anisotropic Displacement Factor Exponent Takes the Form: $-2\pi^2[h^2a^{*2}U^{11} + \dots + 2hka^*b^*U^{12}]$.

	U^{11}	U^{22}	U^{33}	U^{23}	U^{13}	U^{12}
K(1)	16(1)	16(1)	13(1)	0	0	12(1)
K(2)	10(1)	10(1)	11(1)	0	0	3(1)
Zn(1)	5(1)	5(1)	10(1)	0	0	0
V(1)	5(1)	5(1)	8(1)	0(1)	0(1)	0(1)
O(1)	8(1)	8(1)	12(2)	0	0	-1(2)
O(2)	12(1)	12(1)	10(2)	1(1)	1(1)	0(1)
O(3)	6(1)	10(1)	11(1)	-1(1)	0(1)	1(1)

APPENDIX C

SUPPORTING INFORMATION CHAPTER V

Table C1 Atomic Coordinates ($\times 10^4$) and Equivalent Isotropic Displacement Parameters ($\text{\AA}^2 \times 10^3$) for $\{[\text{Zn}(\text{Im})_4][\text{V}_2\text{O}_6]\}_n$ at $-173\text{ }^\circ\text{C}$. $U(\text{eq})$ is Defined as One Third of the Trac of the Orthogonalized U_{ij} Tensor.

	x	y	z	$U(\text{eq})$
Zn(1)	4550(2)	6236(1)	3759(1)	16(1)
Zn(1A)	4943(10)	6581(9)	3865(5)	22(3)
Zn(2)	5005(2)	3343(1)	1134(1)	16(1)
Zn(2A)	5330(11)	3659(10)	1206(5)	21(3)
V(1)	-923(1)	-930(1)	4334(1)	17(1)
O(1)	-978(5)	-2455(3)	4610(2)	29(1)
O(11)	-2639(3)	-280(4)	3968(2)	28(1)
V(2)	635(1)	215(1)	3275(1)	19(1)
O(2)	-463(5)	1590(3)	3065(2)	21(1)
O(2A)	630(40)	1500(20)	3693(16)	21(5)
O(12)	2363(3)	599(6)	3631(2)	27(1)
O(12A)	2413(11)	-240(40)	3485(19)	21(5)
V(3)	-624(1)	-362(1)	1701(1)	19(1)
O(3)	-540(6)	-1766(3)	1378(3)	26(1)
O(3A)	440(30)	-1749(18)	1954(17)	21(5)
O(13)	-2374(3)	30(6)	1596(3)	27(1)
O(13A)	-2384(13)	-700(40)	1477(19)	21(5)
V(4)	926(1)	857(1)	686(1)	18(1)
O(4)	1065(5)	2386(2)	443(2)	30(1)
O(14)	2617(3)	159(5)	1055(3)	43(2)
O(5)	276(10)	-184(9)	30(4)	29(2)
O(6)	-80(5)	892(3)	1234(2)	23(1)

Table C1 (Continued).

	x	y	z	<i>U</i> (eq)
O(7)	576(4)	-534(4)	2527(1)	24(1)
O(7A)	-570(20)	370(30)	2451(4)	21(5)
O(8)	70(4)	-943(3)	3779(2)	21(1)
O(9)	189(11)	-167(10)	5043(4)	29(2)
N(1)	6265(4)	4862(4)	3999(3)	14(1)
C(2)	7495(5)	4665(5)	4529(2)	20(2)
N(3)	8454(6)	3711(5)	4468(3)	16(2)
C(4)	7809(7)	3256(7)	3861(3)	23(2)
C(5)	6460(7)	3971(6)	3574(3)	23(2)
N(1A)	6580(20)	5140(20)	4079(16)	13(3)
C(2A)	7770(30)	4930(30)	4624(15)	13(3)
N(3A)	8650(30)	3860(30)	4615(19)	13(3)
C(4A)	7990(40)	3340(40)	4030(20)	13(3)
C(5A)	6710(40)	4130(40)	3698(16)	13(3)
N(11)	4774(6)	7268(4)	3006(2)	19(2)
C(12)	3729(6)	8035(6)	2543(3)	18(2)
N(13)	4334(6)	8613(8)	2127(3)	21(2)
C(14)	5837(6)	8200(8)	2331(3)	21(2)
C(15)	6111(6)	7359(6)	2881(3)	22(2)
N(11A)	5020(40)	7520(20)	3060(9)	13(3)
C(12A)	3990(30)	8230(40)	2563(17)	13(3)
N(13A)	4630(40)	8720(50)	2141(16)	13(3)
C(14A)	6140(40)	8310(60)	2380(20)	13(3)
C(15A)	6380(30)	7560(40)	2951(18)	13(3)
N(21)	2577(3)	5399(4)	3484(3)	22(2)
C(22)	2409(6)	4113(4)	3481(3)	20(2)
N(23)	931(5)	3888(5)	3291(3)	24(2)
C(24)	122(7)	5090(5)	3168(3)	27(2)
C(25)	1144(5)	6039(6)	3288(3)	37(3)
N(21A)	3002(19)	5690(30)	3616(10)	13(3)
C(22A)	2970(20)	4390(20)	3706(16)	13(3)
N(23A)	1570(30)	4070(20)	3653(17)	13(3)

Table C1 (Continued).

	x	y	z	$U(\text{eq})$
C(24A)	670(20)	5210(30)	3520(20)	13(3)
C(25A)	1550(30)	6230(20)	3500(19)	13(3)
N(31)	4665(5)	7312(5)	4486(2)	19(1)
C(32)	5897(5)	7774(5)	4892(2)	17(2)
N(33)	5562(6)	8475(5)	5330(3)	19(1)
C(34)	4035(5)	8466(7)	5200(3)	18(2)
C(35)	3479(6)	7742(6)	4675(3)	21(2)
N(31A)	5020(30)	7560(20)	4621(9)	13(3)
C(32A)	6190(30)	8120(30)	5013(15)	13(3)
N(33A)	5820(40)	8700(40)	5475(14)	13(3)
C(34A)	4330(40)	8510(50)	5377(19)	13(3)
C(35A)	3830(30)	7800(50)	4845(19)	13(3)
N(41)	3435(6)	4846(5)	911(4)	21(2)
C(42)	2303(7)	5150(6)	352(3)	24(2)
N(43)	1411(6)	6179(6)	394(3)	18(2)
C(44)	1991(7)	6575(7)	1017(3)	19(2)
C(45)	3239(8)	5743(8)	1333(3)	23(2)
N(41A)	3570(40)	4990(40)	920(20)	13(3)
C(42A)	2330(40)	5380(50)	420(18)	13(3)
N(43A)	1460(30)	6270(50)	580(20)	13(3)
C(44A)	2160(50)	6470(50)	1230(20)	13(3)
C(45A)	3460(50)	5680(60)	1437(18)	13(3)
N(51)	4931(5)	2397(5)	368(2)	16(1)
C(52)	3781(5)	1905(5)	-76(2)	17(2)
N(53)	4220(5)	1320(6)	-520(3)	20(2)
C(54)	5746(5)	1439(6)	-356(3)	14(2)
C(55)	6180(6)	2106(6)	194(3)	20(2)
N(51A)	5400(30)	2540(20)	517(10)	13(3)
C(52A)	4180(20)	2190(30)	53(15)	13(3)
N(53A)	4550(30)	1550(40)	-395(13)	13(3)
C(54A)	6090(40)	1470(40)	-212(16)	13(3)
C(55A)	6620(30)	2090(40)	352(16)	13(3)
N(61)	6958(4)	4213(4)	1380(3)	23(2)

Table C1 (Continued).

	x	y	z	<i>U</i> (eq)
C(62)	7049(6)	5504(4)	1291(3)	21(2)
N(63)	8478(5)	5811(5)	1387(3)	21(1)
C(64)	9359(7)	4643(5)	1547(3)	27(2)
C(65)	8421(5)	3653(6)	1542(4)	32(2)
N(61A)	7250(20)	4540(30)	1350(13)	13(3)
C(62A)	7460(20)	5780(30)	1506(16)	13(3)
N(63A)	8930(30)	5980(20)	1783(17)	13(3)
C(64A)	9730(17)	4810(30)	1810(20)	13(3)
C(65A)	8690(30)	3920(20)	1540(20)	13(3)
N(71)	4899(6)	2379(5)	1927(2)	18(2)
C(72)	6013(6)	1681(6)	2393(3)	16(2)
N(73)	5506(6)	1165(7)	2856(3)	16(2)
C(74)	3999(6)	1546(9)	2677(4)	20(2)
C(75)	3618(6)	2310(8)	2098(4)	22(2)
N(71A)	5160(40)	2650(40)	1974(13)	13(3)
C(72A)	6290(30)	1940(40)	2426(18)	13(3)
N(73A)	5780(40)	1300(50)	2864(18)	13(3)
C(74A)	4260(40)	1620(60)	2680(20)	13(3)
C(75A)	3870(30)	2460(50)	2130(20)	13(3)

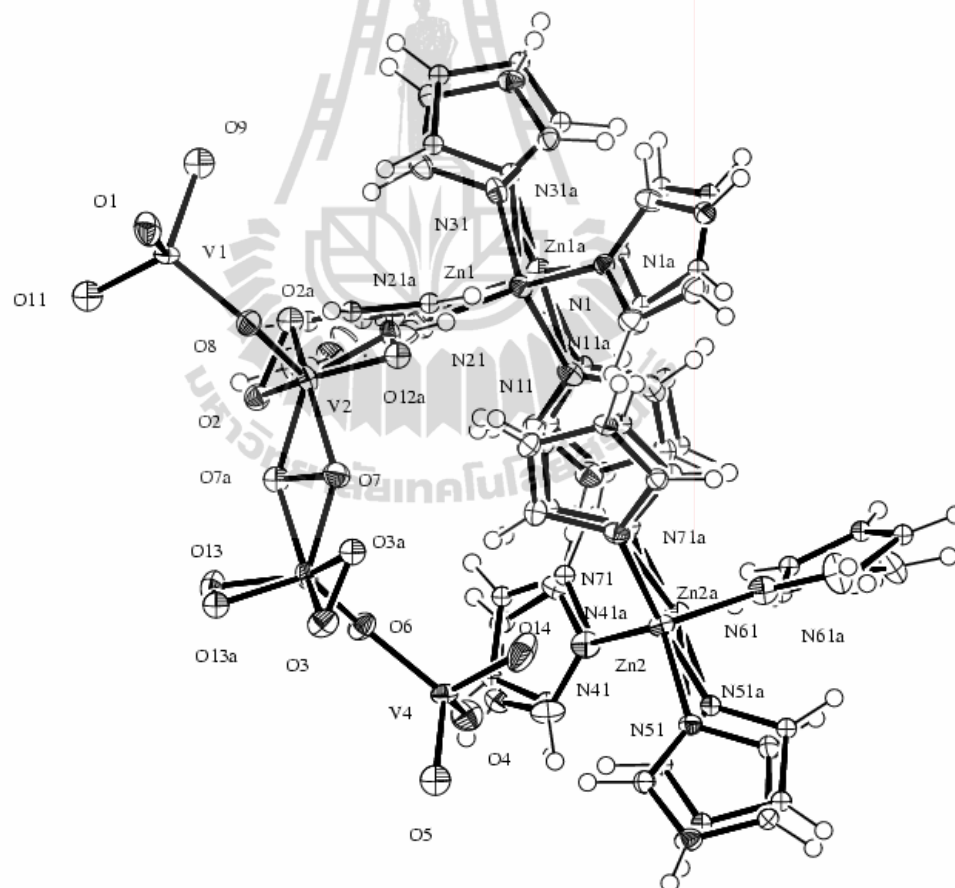
Table C2 Atomic Coordinates ($\times 10^4$) and Equivalent Isotropic Displacement

Parameters ($\text{\AA}^2 \times 10^3$) for $\{[\text{Zn}(\text{Im})_4][\text{V}_2\text{O}_6]\}_n$ at 20 °C. $U(\text{eq})$ is Defined as One Third of the Trace of the Orthogonalized U^{ij} Tensor.

	x	y	z	$U(\text{eq})$
Zn(1)	4801(1)	3480(1)	7626(1)	52(1)
V(1)	-879(1)	828(1)	8635(1)	39(1)
V(2)	696(1)	-317(1)	6574(1)	40(1)
O(9)	262(10)	243(9)	10099(8)	73(2)
O(8)	134(3)	809(3)	7560(2)	60(1)
O(7)	459(6)	416(5)	5038(3)	60(1)
O(1)	-955(3)	2364(3)	9079(3)	68(1)
O(11)	-2586(3)	152(3)	7920(3)	77(1)
O(12)	2482(3)	136(8)	6891(8)	66(2)
O(12A)	2491(4)	-521(12)	7164(8)	94(3)
O(2)	-226(7)	-1793(3)	6241(7)	76(2)
O(2A)	568(8)	-1751(3)	7158(6)	63(1)
N(1)	6496(3)	4923(3)	8097(2)	52(1)
C(2)	7620(3)	5206(3)	9200(3)	59(1)
N(3)	8540(3)	6218(3)	9118(3)	61(1)
C(4)	7998(4)	6606(3)	7902(3)	64(1)
C(5)	6731(4)	5805(3)	7275(3)	61(1)
N(11)	4932(3)	2514(3)	6081(2)	48(1)
C(12)	3836(3)	1826(3)	5137(3)	54(1)
N(13)	4363(3)	1307(3)	4275(3)	57(1)
C(14)	5861(3)	1675(3)	4670(3)	59(1)
C(15)	6216(3)	2422(3)	5789(3)	52(1)
N(21)	2877(3)	4352(2)	7155(3)	60(1)
C(22)	2792(4)	5626(3)	7225(5)	74(1)
N(23)	1376(4)	5891(3)	6951(4)	86(1)
C(24)	489(4)	4735(3)	6682(7)	97(2)
C(25)	1425(3)	3786(4)	6830(5)	82(1)
N(31)	4913(3)	2487(3)	9138(3)	50(1)
C(32)	6085(3)	2017(3)	9968(3)	56(1)

Table C2 (Continued).

	x	y	z	<i>U</i> (eq)
N(33)	5690(3)	1412(3)	10854(3)	60(1)
C(34)	4198(3)	1490(3)	10584(3)	56(1)
C(35)	3719(3)	2159(3)	9526(3)	55(1)

**Figure C1** The asymmetric unit of $\{[Zn(Im)_4][V_2O_6]\}_n$ at $-173(2)^\circ\text{C}$.

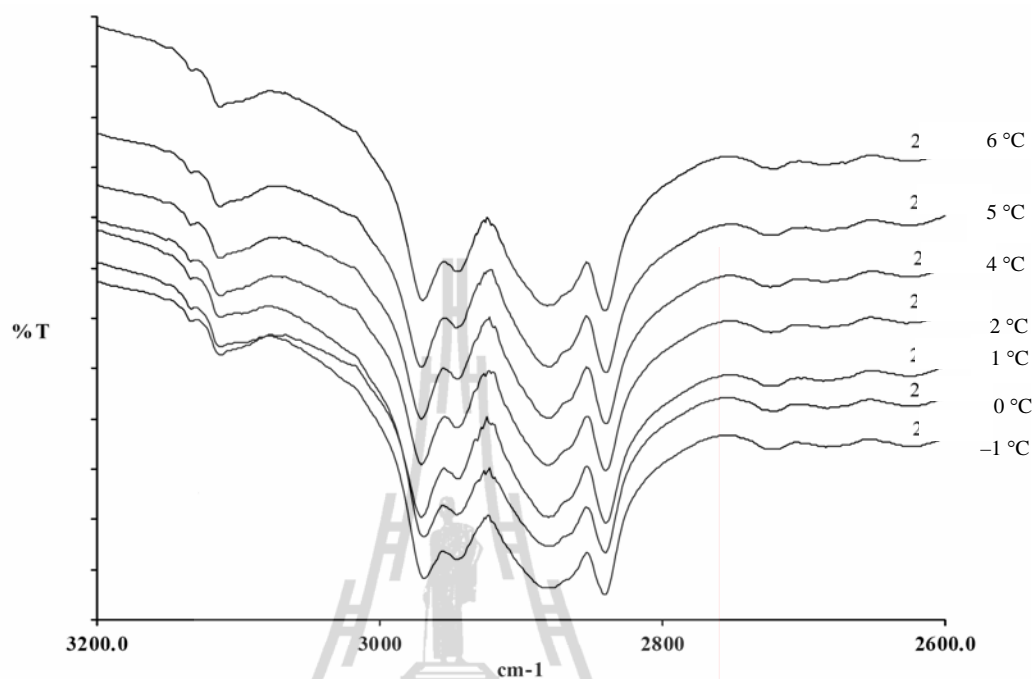


Figure C2 IR spectra of $\{[Zn(Im)_4][V_2O_6]\}_n$ (nujol mulls) in the region 3200-2600 cm^{-1} at various temperatures.

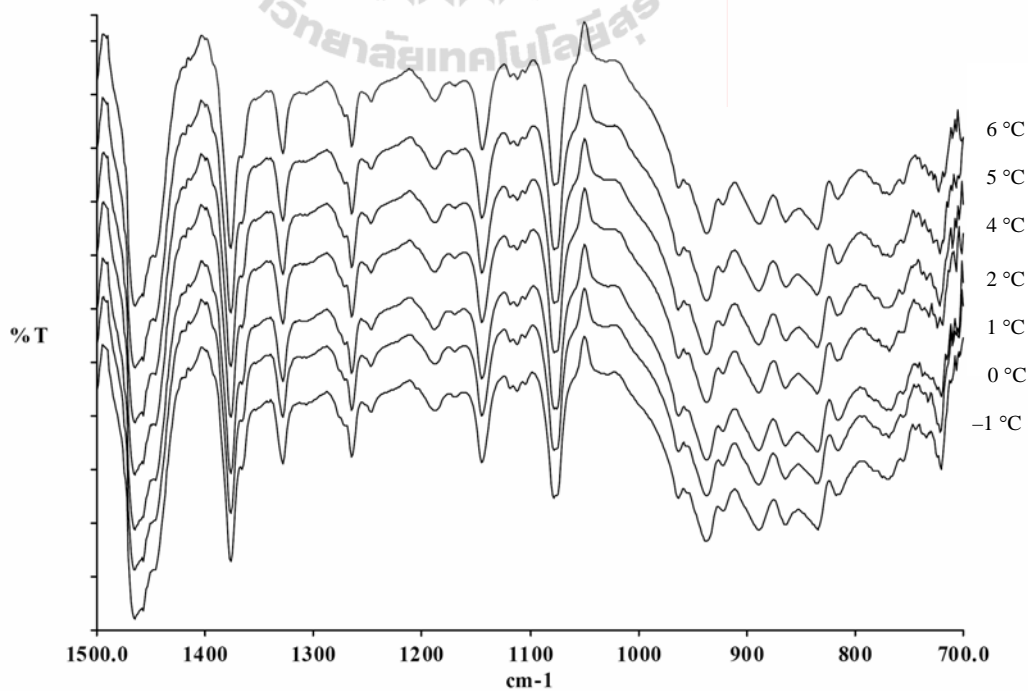


Figure C3 IR spectra of $\{[Zn(Im)_4][V_2O_6]\}_n$ (nujol mulls) in the region 1500-700 cm^{-1} at various temperatures.

APPENDIX D

CONFERENCE PRESENTATIONS

D.1 Proceeding

1. **Krachodnok, S.**, and Haller, K. J. Supramolecular structure analysis: detection of a novel carbonyl-carbonyl interaction in the structure of pyridine-3,5-dicarboxylic acid. The 9th Annual National Symposium on Computational Science & Engineering, 23-25 March 2005, Mahidol University, Thailand. pp. 464-470.

2. **Krachodnok, S.**, Haller, K. J., and Williams, I. D. Hydrothermal synthesis of three-dimensional nanoporous zinc vanadates: $\text{Zn}(\text{HenMe})_2\text{V}^{4+}_4\text{V}^{5+}_4\text{O}_{20}$ and $\text{Zn}(\text{enMe})_2(\text{VO}_3)_2 \cdot 2\text{H}_2\text{O}$ containing pillared/layered structure. The German-Thai Symposium on Nanoscience and Nanotechnology, 27-28 September 2007, Chonburi, Thailand. pp. 63-68.

3. **Krachodnok, S.**, Haller, K. J., Sung, H. H.-Y., Shek, F. L.-Y., and Williams, I. D. Hydrothermal synthesis and characterization of a three-dimensional nanoporous zinc vanadate containing pillared structure. The 1st SUT Graduate Conference, 1-2 November 2007, Suranaree University of Technology, Nakhon Ratchasima. CD-SUT-GRAD059.

4. **Krachodnok, S.**, Haller, K. J., and Williams, I. D. Zinc helices in 3D network of $\text{Zn}_2(\text{en})\text{V}_2\text{O}_7$. Smart/Intelligent Materials and Nano Technology & 2nd International Workshop on Functional Materials and Nanomaterials, 22-25 April 2008, Chaing Mai. pp. 332.

5. **Krachodnok, S.**, Haller, K. J., Sung, H. H.-Y., Shek, F. L.-Y., and Williams, I. D. Supramolecular structure of zinc-2-methyl-imidazole–decavanadate. The 34th Congress on Science and Technology of Thailand 2008, 31 October-2 November 2008, Queen Sirikit National Convention Center, Bangkok. http://www.scisoc.or.th/stt/34/author/S/C2_C0245.html.

D.2 Abstract

1. **Krachodnok, S.**, Chainok, K., and Haller, K. J. Hydrothermal synthesis and characterization of $[\text{NH}_3\text{CH}_2\text{CH}_2\text{NH}_3]^{2+}[(\text{VO})_2(\text{VO}_4)_2]^{2-}$. The 29th Congress on Science and Technology of Thailand, 20-22 October 2003, Khon Kaen University, Thailand.

2. **Krachodnok, S.**, and Haller, K. J. The crystal structure of pyridine-3,5-dicarboxylic acid. The 6th Conference of the Asian Crystallographic Association, 27-30 June 2004, Hong Kong, China.

3. **Krachodnok, S.**, and Haller, K. J. Novel Carbonyl-carbonyl interaction in the structure of dinicotinic acid. The 4th National Symposium on Graduate Research, 10-11 October 2004, Chiang Mai, Thailand.

4. **Krachodnok, S.**, and Haller, K. J. Organically templated transition metal vanadium arsenates. RGJ-Ph.D. Congress VI, 28-30 April 2005, Pattaya, Thailand.

5. **Krachodnok, S.**, and Haller, K. J. A new organically templated vanadium arsenate. XX Congress of the International Union of Crystallography, 23-31 August 2005, Florence, Italy.

6. **Krachodnok, S.**, and Haller, K. J. Hydrothermal synthesis and characterization of a new organically templated vanadium arsenate. The 31st Congress on Science and Technology of Thailand, 18-20 October 2005, Suranaree University of Technology, Thailand.

7. **Krachodnok, S.**, and Haller, K. J. Hydrothermal synthesis and structural characterization of an open-framework arsenic vanadate: $\text{As}_2\text{V}_{10}\text{O}_{26}$. The 2006 Meeting of the American Crystallographic Association, 22-27 July 2006, Honolulu, Hawaii.

8. **Krachodnok, S.**, Chainok, K., Haller, K. J., Sung, H. H.-Y., Shek, F. L.-Y., and Williams, I. D. Synthesis and structures of organically modified zinc vanadates. Joint Conferences of the Asian Crystallographic Association and the Crystallographic Society of Japan, 20-23 November 2006, Epochal Tsukuba, Japan.

9. Suwanwisut, W., Dokpong, P., **Krachodnok, S.**, Puntharod, R., and Haller, K. J. Hydrothermal synthesis of organically modified metal vanadate compounds. The 32nd Congress on Science and Technology of Thailand, 10-12 October 2006, Queen Sirikit National Convention Center, Bangkok, Thailand.

10. **Krachodnok, S.**, Haller, K. J., Sung, H. H.-Y., Shek, F. L.-Y., and Williams, I. D. Synthesis and crystal structure of 2-methylimidazolium tetra-(2-methylimidazole)zinc(II) decavanadate. The 33rd Congress on Science and Technology of Thailand 2007, 18-19 October 2007, Walailuk University, Nakhon Sri Thummarat, Thailand.

11. Palasak, P., **Krachodnok, S.**, and Haller, K. J. Hydrothermal synthesis of cadmium vanadate compounds modified by imidazole. The 33rd Congress on Science and Technology of Thailand 2007, 18-19 October 2007, Walailuk University, Nakhon Sri Thummarat, Thailand.

12. Orrasa In-noi, **Krachodnok, S.**, Haller, K. J., Sung, H. H.-Y., Shek, F. L.-Y., and Williams, I. D. Hydrothermal synthesis and characterization of a three-dimensional supramolecular structure of zinc vanadate: $\text{Zn}(2\text{-EtIm})_2(\text{VO}_3)_2$. The 33rd

Congress on Science and Technology of Thailand 2007, 18-19 October 2007, Walailuk University, Nakhon Sri Thummarat, Thailand.

13. **Krachodnok, S.**, Haller, K. J., Sung, H. H.-Y., Shek, F. L.-Y., and Williams, I. D. Layered and network structures of hybrid zinc vanadates containing bridging azole ligands. The 8th Conference of the Asia Crystallographic Association, 4-7 November 2007, Taiwan.

14. In-noi, O., **Krachodnok, S.**, Haller, K. J., Sung, H. H.-Y., Shek, F. L.-Y., and Williams, I. D. A Three-dimensional supramolecular structure of zinc vanadate: $\text{Zn}(2\text{-EtIm})_2(\text{VO}_3)_2$. The 8th Conference of the Asia Crystallographic Association, 4-7 November 2007, Taiwan.

15. **Krachodnok, S.**, Haller, K. J., and Williams, I. D. Syntheses and structures of organic-inorganic hybrid zinc vanadates. RGJ-Ph.D. Congress IX, 4-6 April 2008, Pattaya, Thailand.

16. **Krachodnok, S.**, Haller, K. J., and Williams, I. D. Concerted aryl interactions in zinc-imidazole-oxovanadate hybrid organic-inorganic materials. XXI Congress of the International Union of Crystallography, 23-31 August 2008, Osaka, Japan.

17. **Krachodnok, S.**, Haller, K. J., and Williams, I. D. Concerted aryl interactions in zinc-imidazole complex hybrid oxovanadates. The 2009 Meeting of the American Crystallographic Association, 25-30 July 2009, Toronto, Canada.

18. **Krachodnok, S.**, Haller, K. J., and Williams, I. D. Synthesis and crystal structures of layered polyvanadates, $\text{K}_x\text{V}_3\text{O}_8$ ($x = 1$ and 2). German-Thai Symposium on Nanoscience and Nanotechnology 2009, 21-22 September 2009, Chaing Mai, Thailand.

19. **Krachodnok, S.**, Haller, K. J., and Williams, I. D. Cation-cation supramolecular interactions in zinc-imidazole-oxovanadate compounds. Joint Conference of the Asian Crystallographic Association and Chinese Crystallographic Society, 22-25 October 2009, Beijing, China.

20. **Krachodnok, S.**, Haller, K. J., and Williams, I. D. Synthesis and crystal structure of tris(ethylenediamonium) decavanadate dihydrate, $(\text{enH}_2)_3[\text{V}_{10}\text{O}_{28}] \cdot 2\text{H}_2\text{O}$. Pure and Applied Chemistry International Conference (PACCON2010), 21-23 January 2010, Sunee Grand Hotel and Convention Center, Ubon Ratchathani, Thailand.

21. **Krachodnok, S.**, Haller, K. J., and Williams, I. D. Order-disorder structure in a new zinc oxovanadate, $[\text{Zn}(\text{Im})_4][\text{V}_2\text{O}_6]$. 14th International Annual Symposium on Computational Science and Engineering (ANSCSE14), 23-26 March 2010, Mae Fah Luang University, Chiang Rai, Thailand.

22. **Krachodnok, S.**, Haller, K. J., and Williams, I. D. Reversible phase transition in a new polymeric zinc metavanadate, $[\text{Zn}(\text{Im})_4][\text{V}_2\text{O}_6]_n$. The Tenth Conference of the Asian Crystallographic Association, 31 October-3 November 2010, Busan, Korea.

CURRICULUM VITAE

SAMROENG KRACHODNOK

Born, Citizenship, and Martial Status: 10 September 1977, Khon Kaen; Thai; Single

Education:

2010 Ph.D. Candidate, Chemistry, Suranaree University of Technology, Thailand

1996-99 B.Sc., Chemistry, Khon Kaen University, Thailand

Work Experiences and Position:

2000-03 Quality Assurance Engineering, Nidec Precision (Thailand) Company, Limited, Ayuttaya.

2006-7 Training on a Bruker-Nonius Smart Apex CCD diffractometer at HKUST, and workshop on the EXAFS data analysis at NSRC, Nakhon Ratchasima.

2009-2011 Teaching the undergraduate student laboratory courses at SUT.

Scholarship/Awards:

2003-08 RGJ-TRF (3.C.TS/45B.1) and collaboration with the RGC-HKUST.

2004, 2007-10 Bursary Student Grant from the 6th and 8th AsCA2006 (Hong Kong), 2007 (Taiwan), 2010 (Korea); the 21th IUCr2008 (Japan); the 2009 ACA (Canada).

Publications:

Krachodnok, S., and Haller, K. J. (2005). *Acta Crystallographica Section A. 61*: C306;

Krachodnok, S., Haller, K. J., and Williams, I. D. (2008). *Acta Crystallographica*

Section A. 64: C409; **Krachodnok, S., Haller, K. J., and Williams, I. D. (2008).**

***Advanced Materials Research. 55-57*: 669-672.**